Propagation of Urban Transportation Noise

LUI WAI KEUNG

A thesis submitted in partial fulfillment of the requirements for the
Degree of Doctor of Philosophy

Department of Mechanical Engineering
The Hong Kong Polytechnic University

August 2004

CERTIFICATE OF ORIGINALITY

I hereby declare that this thesis is my own work and that, to the best of my knowledge and belief, it reproduces no material previously published or written, nor material that has been accepted for the award of any other degree or diploma, except where due acknowledgement has been made in the text.

____________________(Signed)

Lui Wai Keung ________(Name of student)

Abstract

In the present study, the particular condition of sound propagation confined to the hornlike geometry enveloped by the road surface and tire belt is investigated in details. A simplified model based on the study of sound diffracted by a sphere above a ground surface is proposed to simulate this so-called horn effect. In a parametric study, it has been shown that an increase in the thickness and porosity of a porous layer, or the use of a double layer of porous road pavement, will lead to the reduction of the horn amplification of sound. However, a decrease in the flow resistivity of a porous road pavement does little to reduce the horn amplification of sound. It has also been demonstrated that the horn effect over a porous road pavement is less dependent on the angular position of the source on the surface of tires.

In the present context of booming railway networks, there is a great concern about noise due to moving trains. Comparative studies have been conducted to investigate the applicability of oversea prediction schemes for the calculation of noise levels caused by passing trains that run on a viaduct. The results from an outdoor field measurement are compared with the calculated results of the prediction schemes. Calculation of Railway Noise (CRN) developed in UK, Nordic Prediction Method for Train Noise (NMT), CSTB 92 and ISO 9613 provided in the Mithra software are the schemes used for the comparisons. Among these schemes, CRN gives the best agreement with the measured results, although it does not provide a term for correcting the vertical directivity characteristic of a passing train.

In order to study the source characteristics of a passing train, four sets of noise measurements for different train operational conditions have been conducted at three different sites, including ballast tracks at grade and railway on a concrete viaduct. The measured sound exposure levels are used to deduce the vertical directivity pattern for different railway systems. It is found that the vertical directivity of different railway systems shows a rather similar pattern. The vertical directivity of train noise is shown to increase up to about 30° before reducing to a minimum at 90°. A multipole expansion model is proposed to account for the vertical radiation directivity of the train noise. An empirical formula is derived and compares well with the experimental data. The empirical model is found to be applicable to different train/rail systems at train speeds ranging up to 120 km/h in this study.

A new methodology for the prediction of noise levels inside the balconies is proposed. It is based on the well-known prediction scheme – the Calculation of Road Traffic Noise developed in the UK. Field measurements on four different types of balcony have been conducted to validate the scheme. It is shown that balcony of different architectural features can offer considerable screening effects in protecting dwellings against road traffic noise. An effective noise-shielding effect is achieved when the incident angle of traffic noise is large and without ceiling reflection. The noise screening effects decrease with an increase of height above the balcony floor. Furthermore, it is found that the effectiveness of a parapet or side wall against road traffic noise depends on their orientations with the affecting roads.

Publications arising from the thesis

1. W. K. Lui and K. M. Li, "Scattering of sound by a penetrable sphere above a plane boundary," *Journal of the Acoustical Society of America* **112**, No. 5 Pt. 2, 2215. The First Pan-American/Iberian Meeting on Acoustics, Cancun, Mexico, Dec 2002.

2. W. K. Lui, K. M. Li, K. K. Lau and K. S. Chan, "A Study of the Use of Balconies in Screening Road Traffic Noise," Inter-noise 2003, Seogwipo, Korea, August 2003.

3. K. M. Li, W. K. Lui, K. K. Lau and K. S. Chan, "A simple formula for evaluating the acoustic effect of balconies in protecting dwellings against road traffic noise," *Applied. Acoustics 64*, 633-653 (2003).

4. K. M. Li, W. K. Lui and G. H. Frommer, "The diffraction of sound by an impedance sphere in the vicinity of a ground surface ground," J. Acoust. Soc. Am. **115**, 42-56 (2004).

5. K. M. Li and W K Lui, "A study of the horn effect above a porous road pavement", ICA 2004, Kyoto, Japan, April 2004.

6. W. K. Lui and K. M. Li, "A theoretical study of the horn amplification of sound radiated from tires above a porous road pavement," J. Acoust. Soc. Am. **116, 1-10** (2004).

7. K. M. Li, W. K. Lui and G. H. Frommer, "The scattering of sound by a hard sphere above an impedance ground", Acta Acust. **90**, 251-262 (2004).

8. W. K. Lui, K. M. Li, Pui Lun Ng and G H Frommer, "A comparative study of different numerical models for predicting train noise in high-rise cities," submitted to *Journal of the Acoustical Society of America*, 2004.

9. W. K. Lui, K. M. Li, C. W. M. Leung, and G. H. Frommer, "An energy approach for modeling the characteristics of wheel/rail rolling noise," submitted to Acta Acust., 2004.

Acknowledgements

The work reported in this thesis was completed during the author's employment as a Research Assistant (February 2001 – July 2004) in the Department of Mechanical Engineering at the Hong Kong Polytechnic University. Most of the work was funded jointly by the Innovation and Technology Commission of the Hong Kong Special Administrative Region and the Mass Transit Railway Corporation Limited, through the award of a grant from the Innovation and Technology Fund under the University-Industry Collaboration Programme.

Herein I would like to express my earnest thanks to my research supervisor, Dr. K M Li, for his brilliant ideas, genuine expertise and outstanding support which were always available from him. His great intellect, wisdom and invaluable guidance not only have had a tremendous effect on my academic progress, but also have broadened my perception on the scientific world and enriched my personal development.

I am grateful to my Industrial Supervisor, Dr. Glenn Frommer from the MTR Corporation Ltd. He provided me with the test sites, facilities and much expert advice for conducting large-scale outdoor measurement of trains noise. The professional advice and reviews offered by Dr. K K Lau are gratefully acknowledged. Dr. Lau has spent many hours discussing with me, particularly on the project for the study of balconies in shielding road traffic noise. A special acknowledgement goes to Dr. G Lo for her invaluable comments on my thesis. I would also like to express my thanks to my colleagues, C N Tang, Catherine Leung, Man Wong, Kelvin Kwok, Mike Law, Coriolanus Lam, Franco Ng and Raymond Tang for their valuable assistance in conducting field measurements.

Last but not least, I would to like to thank my parents for their patience and loving care shown to me. Their strong support and recognition of my scientific endeavours gave me with strength to complete this thesis.

Table of Contents

Part I

Chapter 1 – Introduction

Chapter 2 – Diffraction of Sound by a Hard Sphere

Chapter 3 – Diffraction of Sound by an Impedance Sphere

Chapter 4 – The Horn Effect above a Porous Road Pavement

Part II

Chapter 5 – Comparative Study of Different Prediction Schemes for Train Noise

Chapter 6 – Modeling the Characteristics of Wheel/Rail Rolling Noise

Part III

Chapter 7 – Prediction of Traffic Noise Levels inside a Balcony

Chapter 8 – Conclusions and Suggestions for Future Research

Nomenclature

b	Radius of sphere
ϕ	Scalar velocity potential or azimuthal angle subtended from the train segment to nearest point of the source line to the receiver
ϕ^T	Total sound field
k	Wave number of sound
ω	Angular frequency of sound
c	Speed of sound in air
S	Source point
P	Field point
O and O'	Origin and image origin
R_o	Radial distance of source point from the origin
θ_o	Polar angle of source point
φ_o	Azimuthal angle of source point
R	Radial distance of field point from the origin or slant distance from the nearest point of the source line to the receiver
θ	Polar angle of field point or angle of elevation
φ	Azimuthal angle of field point
ϕ^i	Incident sound field
ϕ^s	Scattered sound field
δ_{m0}	Kronecker delta function
a_{mn}	Coefficient of incident sound wave
b_{mn}	Coefficients of scattering sound wave
$d/2$	Centre of sphere above a flat ground
ϕ_r^i	Sound field contributed by an image source
R_o'	Distance from the center of the real sphere to the image source
θ_1	Polar angle measured from the center of the real sphere to the image source
ϕ_r^s	Scattering sound field from the image sphere
Q_1	Spherical wave reflection coefficient for the point source reflection on the impedance ground
R_2	Distance between the image source and field point
α_1	Angle of incidence of the reflected wave
β	Specific admittance of the reflecting ground
Q_2	Spherical wave reflection coefficient for a scattered wave reflection on an impedance ground

f	Frequency of sound
σ_e	Effective flow resistivity
α_e	Effective rate of change of porosity with depth
$\rho. \rho_o$	Complex densities of air
ρ_l	Complex densities of sphere
ζ, m_l	Density ratio
η, n_l	Index of refraction
c_1	Speed of sound inside sphere
β_e	Effective acoustic admittance of sphere
β_s	Specific normalized acoustic admittance of sphere
β_g	Effective admittance of porous layers above a hard-backed layer
l_1 and l_2	Thickness of the first and second porous layers
Z_c	Characteristic impedance of a porous pavement
γ	Specific heat ratio
N_{pr}	Prandtl number
R_s	Airflow resistivity of a porous layer
Ω	Porosity of the air-filled connected pores
q^2	Tortuosity
Z	Normalized surface impedance
R_3	Separation distance between the center of the image sphere and the field point
d	Distance of receiver from the contact point of a sphere/tire on the ground or length of the train
o	Offset distance from the center of the sphere/tire
h	Height of the receiver above the origin
S	Nearest point of the source line to the receiver or effective source point of a road sub-segment
n	Normal distance from the source line to receiver
ψ	Polar angle made with the z-axis
l	Center of the train from the S
dx	Train segment
x	Distance of train segment from the S along the source line
r	Shortest distance from the train segment to the receiver
W	A-weighted sound power radiated by the train
I	A-weighted sound intensity radiated by the train
$f(\phi)$	Dimensionless function to characterise the horizontal directivity of noise radiated from a passing train

$g(\theta)$	Dimensionless function to characterise the vertical directivity of noise radiated from a passing train
L	A-weighted sound pressure level
L_w	Source strength of train noise
L_h	Horizontal component of train noise
L_v	Vertical component of train noise
SEL	A-weighted sound exposure level
v	Speed of train
D_h	Normalized horizontal directivity
D_v	Normalized vertical directivity
I_c	Image receiver in the balcony ceiling
I_b	Image receiver in the balcony back wall
I_s	Image receiver in the balcony side wall
$\wp$	Overall noise level at a reception point inside a balcony
L_0	Direct noise level from road traffic noise source
L_i	Incident noise level due to road traffic noise
α	Sound absorption coefficient of the reflecting surface
$\overline{L}_i$	Noise level contributed by the reflection of traffic noise on the balcony facade
L_s	Combined noise level at the reception point due to the road segment

Chapter 1

Introduction

1.1 Objectives

The objectives of this thesis are divided into three parts. The first part of the objectives is to develop a theoretical model for a particular problem of so-called horn effect caused by the noise radiation confined to a space formed between the tire belt and road surface. Particular attention will be paid to study the influence of acoustical properties of a porous road pavement on the noise reduction to the horn effect. The second part of the objectives is to devise and conduct experiments to measure the passing train noise which allows identification of the noise emission characteristics of moving trains. The data forms the basis of validation with theoretical and numerical models to be developed in this thesis. Moreover, the applicability of different numerical models for predicting train noise in a high-rise city will be assessed by a comparative study for predicting the train noise radiated from an elevated viaduct. Lastly, a numerical and an experimental study will be conducted to evaluate the acoustic effect of balconies in protecting dwellings against road traffic noise. The prediction scheme is devised to incorporate in one of the prediction models currently in use for the assessment of the road traffic noise.

1.2 Background and motivation of the study

There has been a continual and sustained economic growth in Hong Kong in the past forty years. To meet the demands of the ever-growing population, new town development programs and urban renewal projects have been implemented to make more land available for housing resources and various other urban uses. We have also witnessed the construction of more roads, flyovers, railway lines, and a new airport. These highly publicized infrastructure projects will help to enhance the flexibility and mobility for citizens of Hong Kong. An efficient transport system is an important factor for the economic success of Hong Kong. In recent decades, the volume of traffic grows steadily in Hong Kong. We have seen an alarmingly increase in speed, power, and, in some cases, sheer volume of cars, goods vehicles, trains, and aircraft. Apart from the increase in traffic congestion and air pollution, there is a significant rise in environmental noise all over the city. This has no doubt added to the stress of our daily lives.

Since the airport moved to Chek Lap Kok in 1997, the nuisance from the aircraft noise has now become less important in comparison with the land tranportation noise. The most dominant source of urban transportation noise is now due to road traffic. According to the case study of transport in Hong Kong given by Cullinane [25], Hong Kong has one of the highest vehicle densities in the world. In 1998, there were 268 motor vehicles per kilometer of road in Hong Kong, compared with 219 in Singapore (Hong Kong Transport Department, 2001) and 187 in London (UK Department of the Environment, Transport and the Regions, 1998). The public transport is hugely important, accounting for around 90% of motorized journeys. It consists of a mixture of road and rail based modes [24].

It is recognized that electrified railway not only helps to alleviate the air pollution problem but also provides a fast and efficient mass transport system that lessens the need for road transport and, hence, reduces the overall road traffic volume. This, in turn, will lead to the reduction of air and noise pollution caused by vehicles in road traffic. Indeed, the Hong Kong Government has indicated in its year policy address that railway services would be enhanced and improved to provide a less polluting mode of transport in the turn of the century. However, railway transportation must face a challenge, if not properly designed, maintained and operated, it would cause a great concern from noise and vibration viewpoints. The problem is even more acute for those sections of railway tracks running on a viaduct above the ground level in the vicinity of high-rise buildings. The reasons are simple: the scarcity of suitable land has encouraged building development to go up in the vertical dimension. It is not uncommon to find residential and commercial tower blocks of over 40 storeys with height over 100 m or even more. The lack of available land space means that buildings are tall and located very close to the viaducts. This inevitably leads to high noise levels radiating from the elevated railways to the neighboring residents.

The noise nuisance caused by the vehicles running smoothly on a road is mainly contributed by the rolling noise due to the interaction between a tire and the surface of a road [45]. In a particular condition, the radiated sound from the noise source is amplified at the hornlike geometry formed between the tire belt and road surface before propagating away to the roadside. This so-called horn effect [97] can substantially amplify the noise level at the noise receiver. Although there have been developments in the numerical and experimental modeling of the horn effect, they do not provide satisfactory predictions. In addition they fail to consider the influence of the acoustical properties of a porous road surface on the horn effect. The researchers simply neglect the advanced development of the porous ground models in recent years. In fact, porous road surfaces are widely used to reduce noise from road/tire interaction [8][56][58][59][68]. They act together to reduce air-pimping noise and noise propagating away from the vehicles to the roadside. More importantly, many numerical models assume that the surface is locally reacting for the representation of the acoustical absorbing material. This assumption is only valid for a limited range of absorbing surfaces and frequencies. A more realistic model is to include surfaces of extended reaction. Improved models for extended reaction grounds have been suggested in a recent study [73].

Although there are simple schemes for prediction of railway noise (CRN [29] and NMT [20]), they are largely empirical and aimed primarily for the sub-urban situations. It is strongly believed that these schemes are not sufficient for urban environments where many high-rise buildings and multiple reflections/scattering of sound are detrimental in predicting the noise levels. Besides the source characteristics of the train noise are different in various countries, these empirical schemes do not provide the prediction of train noise propagated from an elevated viaduct to its neighborhood buildings. As the construction of more railway lines is imminent and comparatively less attention has been paid to address the noise issue, these compounding factors make the noise abatement program a complicated and challenging task.

It is well known that the interaction of wheel and rail dominates the noise generation from the railway operation at normal speeds and remain significant even for high-speed trains [103]. Squeal noise, generated as a railcar negotiates a curve of short radius, will not be considered in this thesis because the problem is relatively less important in Hong Kong. It is also known that an elevated viaduct may radiate noise because of its structural vibration caused by a running train. However, it has been demonstrated in a recent report [34] that structure-borne noise is relatively insignificant in comparison with that due to the wheel/rail interaction. In view of these studies, it is reasonable to focus our attention on the rolling noise in this thesis. The rolling noise from trains is often modeled by a line of incoherent dipole source which need be verified by field measurements. Often, the vertical directivity pattern of train noise is always neglected in the existing prediction schemes which is crucial in modelling the sound field in high-rise cities. Outdoor measurements need to be deployed to find out the vertical directivity pattern of train noise.

There is a growing awareness of the use of direct and indirect measures to mitigate land transportation noise. These measures include the use of drainage asphalt pavements and porous road surfaces to reduce the tire noise, integrated building layout design for new housing estates and the adoption of podium structures as barriers to screen noise sensitive areas have been used as a tactical means to prevent road traffic noise from reaching residential blocks. Nevertheless, the indirect measures are not applicable in a built-up city because the residential blocks are high-rise and unavoidably placed very close or even next to a road, due to confined land space. Balconies have been considered as a possible measure to prevent the intrusion of road traffic noise into the residence because the noise screening effect is there even if the balcony door is opened for leisure and ventilation. However, to the best knowledge of author, there is no scheme available to incorporate any of the simple yet accurate prediction models currently in use for the assessment of road traffic noise. Therefore, it is preferable to establish a methodology to model the propagation of traffic noise from the road to a balcony. The methodology is preferable to be based on the source levels estimated by the existing prediction scheme for the road traffic noise. In fact, the same principles can also be incorporated in the numerical schemes for the prediction of train noise.

1.3 Literature Review

1.3.1 Diffraction of sound by a spherical object

The study of acoustic diffraction by an object can be traced back as far as the late 19th century and the early 20th century. Such eminent scientists as Rayleigh, Helmholtz, Kirchhoff and Born have contributed to this field of classical physics [9][81][95]. Their analytical techniques and solutions to problems form the core of the mathematical physics of wave propagation. At that time, researchers were especially interested in spherical objects in the frequency domain and for a plane incident wave. This is because the plane wave has its singularity at infinity and is perpendicular to the direction of propagation that somehow maximizes the simplicity of the incident field. Moreover, the situation becomes simpler when the scatter exhibits some kind of spherical symmetry as a relatively simple scattering model can be derived. These studies have been extended in search for the exact analytic solutions for a plane wave incident on a spherical object near a hard, soft and impedance plane boundary. Addition theorems for the spherical wave functions and Helmholtz integral equation [36][37][38][51] [98] are often used in these analyses.

In practice, many problems ask for a solution of scattering problem with an incident wave emanates from a finite point located outside the scattering region. These include theoretical analysis of experimental data obtained within a laboratory, medical diagnostic techniques, nondestructive evaluation and testing of composite materials, seismic wave exploration and many more in engineering applications. Most of the work for point sources can be found in the literature of seismology and in books on wave propagation, a list of these articles is given in [27]. The exact analytic solution for acoustic diffraction from a spherical object has been fully investigated and can be found in textbooks, see for example, Jones [61]. Recently, Dassios and his colleagues undertook a series of studies on the problems of scattering by a point source excitation [26][27]. In these studies, Dassios and his co-workers provided analytic approximations for many different boundary conditions at low frequencies. They also developed the transmission conditions of acoustic scattering of a point source by: a soft or hard sphere, a sphere with an impedance boundary condition on its surface, a penetrable sphere which could have either a lossy or lossless interior, a soft or hard small sphere with a lossy coating and the corresponding problem with a resistive core surface, and a sphere coated with a penetrable spherical shell.

In the late 1940s, Weiner [112] conducted an experimental investigation of an incident plane wave scattered by a rigid sphere in air. Similar experimental studies of the acoustic scattering by a solid sphere immersed in water were also carried out by Hampton and McKinny [42]. On the other hand, Harbold and Steinberg [43] explored the creeping wave theory for sound diffracted by a hard sphere experimentally. More recently, Huang and Gaunaurd [51] examined the acoustic point source scattering by a spherical elastic shell submerged beneath a free surface in underwater acoustics. In spite of these earlier experimental and theoretical studies done by the researchers, few experimental results could be found in the published literature for comparison with the theoretical predictions developed for acoustic scattering of a rigid sphere irradiated by spherical waves emanating from a point source in outdoor environments. Even though many applications of scattering theory such as underwater acoustics, medical imaging, nondestructive testing and seismic wave exploration involve the use of point-source irradiation, exact analytic solutions and their experimental validation for a more general problem of acoustic scattering by an absorbing sphere above a hard ground or an impedance ground with a point source incidence are very few in the published literature.

1.3.2 Modeling the effect of ground

The propagation of sound in an outdoor environment is influenced by many external factors such as the meteorological effects, refraction, turbulence, air absorption and ground effect. The most state-of-the-arts reviews of outdoor sound propagation can be found in the articles of Embleton [33], Piercy [91] and Attenborough [6]. However, the most comprehensive collection of reviews on outdoor sound propagation is referred to a handbook of acoustics recently published by Crocker [22].

In fact, the ground surface has the most important influence on the propagation of outdoor sound and has been studied extensively. When sound propagates from source to receiver within a few meters of a reflecting plane, direct and reflected sound contributions interfere. If the reflecting plane has finite impedance then a phase change occurs on reflection. The combined effect of this phase change and the path length difference between direct and reflected sound may cancel each other out over a useful range of frequencies for noise control. Typically, the reflecting plane is the surface of the ground. In the absence of topography and barriers, the interference between the direct and reflected sound is an important source of the attenuation of outdoor sound. It is also known that the result of this interference is sensitive to the acoustical properties of the ground.

The condition of the ground can either be modeled as a locally reacting or extended reacting boundary [83]. For a locally reacting ground, the speed of sound in the ground surface is small compared with that in the air, thus the sound waves at any angle of incidence travel normally to the ground surface. The surface impedance is basically independent of the incident angle of the incoming wave for a locally reacting ground but the opposite conditions apply to an extended reacting ground. A locally reacting ground is usually used for predicting sound propagation outdoors because of its simplicity. A general solution for sound propagating over locally reacting ground was firstly given out by Rudnick [96]. Further researches on the development of possible theoretical models for this kind of calculation were then carried out by Lawhead and Rudnick [72] and Ingard [52]. Among them, Chien and Soroka [18][19] developed a more general asymptotic solution for the velocity potential of a sound field generated by a point source above a plane of constant normal impedance which can be expressed as a form of Weyl-van der Pol formula.

Though, many numerical models assume that the surface is locally reacting for the representation of the acoustical absorbing material. This assumption is only valid for a limited range of absorbing surfaces and frequencies. Some surfaces which have a relatively low flow resistance [5], may allow the sound waves to transmit into the ground. In this case an extended reaction ground model may be required. In 1969, Delany and Bazley [28] developed empirical power-law relationships to define the measured characteristic impedance and propagation constant of a large range of absorbent materials in terms of their ratio of flow resistivity to frequency. Later on, Attenborough [3] developed a more comprehensive model that involved five parameters to predict the acoustical characteristics of rigid fibrous absorbent sands and soils. In 1992, Attenborough [4] simplified the five parameter model into a two parameter approximation, using only porosity and flow resistivity, for normal surface impedance of a non hard-backed layer structure. These two parameters, porosity and flow resistivity, can be evaluated by obtaining the best-fit between the theoretical and experimental data. Recently, Li [73] has developed a Green's function for a monopole source above previous surface of multiple layers to improve the models for extended reaction grounds.

1.3.3 The horn effect of tire/road rolling noise

The generation of sound due to the rolling mechanisms of a tire on the surface of a road has been studied for several decades [45][57][71][87]. Despite these efforts, there is still no acceptable model for predicting the noise radiated from a specific combination of tires and roads. In fact, sound generation and radiation are very complicated processes which depend on such inter-dependent factors as the vibration patterns of the tire, the deflections of the tire and the resulting air displacements at the gap formed between the tire and surface of road [45]. In this particular condition, the radiated sound is confined to a hornlike space enveloped by the road surface and the tire belt before propagating away from the noise sources. This leads to a substantial amplification of the radiated sound power and can cause an increase in noise levels at the noise receiver. This particular condition of sound radiation from the rolling tire, the so-called horn effect, was firstly brought up by Schaaf and

Ronneberger [97]. They demonstrated the effect experimentally by simply representing the interspaces between the tire and road as a semi-infinite wedge. The sound amplification was explained by the contributions of the multiple image sources on the tire and road which are evenly distributed over the circle on which the image sources lie. In 1996, Iwao *et al.* [57] carried out experiments using a real tire to confirm the phenomenon of horn amplification. Recently, Graf et al. [40] showed by experimental measurements that the effect of the horn amplification accounted for about 10-20 dB, with the maximum amplification occurring at the plane of the tire.

In 2000, Kropp *et al.* [66] suggested a theoretical model based on multipole synthesis [85]. The model can provide a reasonable prediction of noise levels at mid and high frequencies for a tire placed on a hard surface. However, it overestimates the horn amplification effect at low frequencies. Since the Kropp model is a two-dimensional one, it can only be valid for estimating the amplification of sound when the receiver is located in the plane of a tire. The model was also used to simulate the horn effect over an impedance surface. However, the predictions could not provide consistent agreements with the experimental results. Recently, Graf et al. [40] used a three-dimensional (3D) model of a tire by virtue of the boundary element method (BEM) to study the dependence of horn effect on different geometrical parameters such as the effect of the radius of curvature of the shoulders, the load, the width of the tire and the source/receiver configurations. Although BEM [35][40] can be used for this purpose, it can be a time-consuming tool for predicting the horn effect for practical geometries. Moreover, BEM cannot be used in a parametric study of the influence of porous ground on the horn amplification. Meanwhile, researchers have endeavored to develop three-dimensional (3D) analytical models based on the modal decomposition of the sound pressure [2] and on the asymptotic theories [69] for modeling the horn effect. However, these models either do not consider the effect of impedance ground or are somewhat inadequate in light of the recent advances in predicting the propagation of sound outdoors [5][33][73]. It is also worth pointing out that the two asymptotic models presented by Kuo *et al.* [69], a ray theory for high frequencies and a compact body scattering model for low frequencies, were found to be accurate on a typical tire at frequencies of above 3 kHz and below 300 Hz, respectively. However, at the frequencies of practical interest (approximately 500 - 2500 Hz), the asymptotic models fail to provide satisfactory predictions.

Porous road surfaces are widely used for the road pavement due to their distinguished noise reduction property in reducing both air-pumping noise and noise propagating away from the vehicles [8][56][58][59][68]. It is considered to have an effect on the air-pumping noise generation mechanism since the presence of the porous surface permits instantaneous pressure release from the tire/road cavity. The propagation is influenced primarily by ground effect whereby sound traveling directly to the receiver and sound reflected from the porous road surface may interfere destructively in certain frequency bands. For a realistic situation, the effect of sound field over a single or double porous layer above a hard-backed layer can be evaluated by the improved models for extended reaction grounds based on the approximate analytical solutions suggested in a recent study [73].

1.3.4 Railway noise prediction models

There are many schemes available to predict railway noise. In general, prediction models are based on the pure theory and a number of empirical formulae. A propagation model can be regarded as consisting of two main parts: a model with a description of the noise source and the propagation model. In Europe, many countries have developed their own prediction models such as German VDI 2714/2720 model, Dutch rail traffic model SRMII, Nordic models from Scandinavia, French models from the Guide du Bruit and Mithra-Fer, Calculation of Railway Noise (CRN) from UK and models from Austria, Germany, Switzerland and Netherlands [67]. Greece [7] and United State [106] have also developed their own prediction models recently. In Asia, Japan developed various models to predict railway noise for the open terrain [77] and built-up areas [86]. Besides the mentioned prediction models, the international ISO 9613-2 standard for the propagation of outdoor sound [53][54] can also be adopted for the prediction of train noise.

Since most of the formulations in the prediction models are based on the results of local measurements, the models are generally not possible to be used in other countries because of the different radiation characteristics of the noise due to various vehicles, rails and trackforms used in the railway system. Wolde et al. [102] pointed out that the choice of source height influences the prediction of sound propagation in all cases and especially in the case of obstacles between the source point and the receiver point. However, there is no simple and generally valid rule governing the height of the acoustical source in rolling noise prediction. In 1995, van Leeuwen [108] surveyed 14 models for predicting the effect of placing a noise barrier alongside a railway line. He compared the source locations, barrier attenuations and the insertion losses provided by a 2m high barrier for different prediction models. In this survey, he also gave an overview of the differences in attenuation between reflective and absorptive barrier of various prediction schemes..

Apart from the differences in noise radiation characteristics, the predicted noise levels are invariably different for various prediction models due to the different schemes used to account for the factors influencing the noise propagation. In 1999, van Leeuwen [107] conducted a suvery to compare the European prediction models for railway noise. These models are from Austria, Denmark, France, Germany, Netherlands, Norway, Sweden, Switzerland and UK. The propagatoin part of the ISO 9613-2 was also considered. He pointed out that the inherent differences in various models are due to the fact that the models were developed by different institiutions. All these institutions had their own points of view in acoustial matters, which did not necessarily match those of the neighboring countries. In addition, most countries have their own regualtions, acts and laws, which influence the prediciton standard. In his survey, the assumption of source positions, the levels of noise emitted by passing trains, the radiaiton characteristics of the source and the propagation models were compared between different prediction models. In the part of noise propagation, he studied the differences in geometrial spreading, atmospherical attenuation, ground attenuation, screening attenution, reflection and meteorological correction between the models.

Among the prediction models mentioned, CRN [29] is widely used in United Kingdom and in Hong Kong. It is an empirical scheme developed by virtue of a set of experimental measurements. In fact, it is intended only for ranges out to 300 m and for propagation over flat grass covered land. Its original development is certainly not aimed at the urban situations. A similar scheme, Nordic Prediction Method for Train Noise [20] is also aimed primarily at the sub-urban situations where multiple reflections/scattering of sound is not significant. Although, the prediction schemes are possible for the prediction of railway noise, they are aimed primarily for the rural areas. Moreover, these empirical schemes do not provide the prediction of train noise propagated from an elevated viaduct to its neighborhood buildings. Therefore, it is doubtful whether the methods can be applied to the urban situations.

1.3.5 The radiation characteristic of wheel/rail rolling noise

Many factors can affect the sound power level of the rolling noise due to the railway operation. The most important factors are train speed and roughness of wheels and rails. Different types of trains, bogies, wheels, rails, sleepers and track beds will also cause differences [31][102][113]. Although there are many other noise sources, mechanisms associated with the interaction of the wheel and the rail dominate the noise production in railway operations at normal speeds and remain significant even for high-speed trains. Rolling noise occurs on straight track and is predominantly caused by uneveness of the wheel and rail surfaces which induce a vertical relative vibration [103]. Furthermore, King [63] showed that the aerodynamic noise from a train is unimportant at speeds below 240 km/h. Zhang et al. [113] reported that the wheel/rail rolling noise could be modeled as an array of point sources together with its dipole horizontal directivity and some kind of vertical directivity depending on the railway system. They suggested that several source heights are required to obtain a good source model. Based on their model analyses, they concluded that the source locations of the rolling noise should be below the wheel axles even though the source heights for the rolling noise are not yet confirmed.

Most of the researches on outdoor sound propagation consider the noise source to be sufficiently far from the receivers to act as a point monopole. However, most situations may require modeling of sources as dipoles or quadrupoles or as combination of these. Peters [88] suggested that the rolling noise from a train could be modeled as a line of incoherent dipole sources. Many previous theoretical and experimental studies [12][88][94] have shown that the noise profile which is the time signature of a passing train can either be modeled by using a spherical, dipole or cosine radiation model. The different radiation characteristics are all given under the assumption of wheel/rail being the primary noise source for trains.

In the 1990s, Hohenwarter [46] carried out a large number of measurements at a short distance for different elevation angles of up to 50°. He found that, in most cases, electrically hauled trains radiate sound with dipole characteristics. However, in accordance with Kruze's [70] measurements and the Austrian model [67], the directivity can be composed of a combination of monopole and dipole characteristics. Kurze [70] showed in his measurements that there is no relevant directivity of sound radiation at various vertical heights. Notwithstanding, Chew [15][16][17] showed that noise radiating from the mass rapid transit system in Singapore exhibits a pattern of vertical directivity. Measurements made of both track at grade and track on an elevated viaduct showed that train noise increased by about 6 dB(A) following with an increase in elevation angle from 8° to 30° [15]. In another set of field measurements carried out on an overhead bridge, Chew [16] found that train noise was at a maximum near the vertical and decreased by about 10 dB in the horizontal direction. All in all, the most important rolling noise can be modeled by a continuous line of incoherent point sources, together with either a spherical, dipole or combined spherical/dipole horizontal directivity.

1.3.6 Noise screening effect of a balcony

A balcony is a building feature on the floor with access of doors to the outdoor environment. It is generally constructed with a cantilever protruding from the building façade built together with parapets or railings on the perimeter of the cantilever. It provides a leisure and ventilation to the residents in the apartment. It can also provide an acoustical protection from the land transportation noise in a high-rise residential building as advocated by the study [14]. In most of the previous studies, investigations of the sound levels on balconies were carried out by using indoor scale model experiments [41][82] or full-scale field experiments [80][104]. From these studies, it is generally accepted that balconies can be employed to protect weak points on the facades of dwellings against traffic noise. The protection increases with increased incident angle and balcony depth. It is frequency dependent when the direct path between the source and receiver is partially screened. The performance is, however, degraded by the reflection of sound from the ceiling. The use of sound absorptive material on the parapets and ceiling of the balcony was shown to produce substantial noise reductions.

A numerically intensive scheme – the boundary element method, has been used by Hothersall et al. [50] for the two-dimensional study of sound fields in the region of balconies of a tall building close to a roadway. The effects of shielding of the source by the balcony wall are found to be largely cancelled by the strong reflected sound from the ceiling and rear wall of the balcony. It is also found that the treatment of the ceiling or the rear wall of the balcony is most efficient in noise reduction, producing values of between about 5 and 8 dB for a broad band spectrum characteristic of A-weighted road traffic noise measured at the positions 0.5m from the rear wall of the balcony and 1.5m above the balcony floor. Kropp et al. [64][65] developed a three-dimensional theoretical model to predict the sound field inside non-rigid cavities in the low and middle frequencies below 1 kHz. The model can be used for balconies including an arbitrary distribution of absorbing areas in the form of a locally reacting surface expressed by its impedance. Best results are achieved when treatment is giving to the ceiling and the rear wall of the balcony. With the application of different sound absorbing materials, an insertion loss between 4 and 7 dB can be expected inside a room behind the balcony while the window (door) to the balcony is open. The efficiency of the treatment depends on the balcony position: the higher the balcony is above the ground, the better the attenuation as a result of increased shielding against the direct sound at high elevation. Jiang et al. [60] also carried out a study on noise reduction by a balcony in a high-rise building. By dividing the façade of the balcony into smaller patches, they calculated the balcony insertion loss by taking into account the averaged reflected and diffracted sound energy at the façade. Their numerical model was somewhat simplified by only considering a point source and a balcony of cantilever type enclosed with parapets. They provided no experimental results to validate their numerical model.

Recently, Cheung et al. [14] studied the noise reduction to the road traffic noise provided by the balconies in their scale model tests. The average measured noise reduction provided by the balconies with reflective ceiling was only 1.6 dB. If a balcony without ceiling was tested, an additional 5 dB reduction could be obtained. More recently, Hossam El-dien and Woloszyn [47][49] proposed an architectural concept by using an inclined parapet to increase the shielding effect to protect the balcony back wall from the excessive traffic noise in a free field. Furthermore, they studied the effect of noise reduction offered by balconies with inclined ceilings. In their study, three inclined ceilings at angles 5°, 10°, and 15° were tested with different balcony depths by using a Pyramid Tracing model [48]. The maximum reduction is obtained at the higher floors and from balcony with 2m in depth or more.

1.4 Scope of work and structure of thesis

The purpose of this thesis is to investigate the noise problems caused by the road traffic and operation of railways. In particular, the noise radiations caused by the horn effect due to the rolling tire and by the wheel/rail interaction will be studied. Theoretical models and extensive experimental measurements will be devised to provide the tools to understand the problems.

The ability to model the sound propagation is vastly important in predicting the noise effects on a noise sensitive receiver at the roadsides. The economic benefit of the work will result from the optimum use of porous materials for road pavements in conjunction with other noise mitigation measures. In particular, balcony is considered as a viable architectural feature to protect the residential blocks against the land transportation noise in a high-rise urban environment. Social benefits are the potential for low-cost noise reduction and the improvement of environmental conditions near noise sources.

It is clear that source characteristics influence the propagation of sound, especially, in the case of obstacles between the source and noise sensitive receivers. Outdoor measurements will be conducted to characterize the sound sources of moving trains. Attentions will be paid to the determination of the vertical directivity pattern of the source, which was not included in most prediction schemes. Its influence is particularly significant in dense high-rise cities. This will allow flexibility in such a way that even the noise source characteristics may vary with the physical conditions of the wheels and rail tracks after prolonged period of operation, the accuracy of the noise prediction model can be maintained by a regular source-monitoring scheme.

In order to achieve these objectives, the thesis will be divided into eight chapters:

Chapter 1 - Outline the objectives and background of the current studies. Reviews are given on the studies of sound diffraction by a spherical object, effect of ground on the sound propagation, horn effect, different train noise prediction models, source characteristics of train noise and noise screening effect of balconies.

Charter 2 and 3 - Theoretical models based on wave field expansions, image method and addition theorem are developed. They consider the case of sound diffraction by a hard sphere, an absorbing sphere with a locally reacting boundary or an extended reaction boundary placed above an outdoor ground surface of finite impedance. Comparative results between the theoretical predictions and experimental data are given in these chapters.

Chapter 4 - A simplified model based on the study of sound diffracted by a sphere is proposed to investigate the influence of a porous road pavement on the sound amplification due to the horn-like geometry in the tire/road gap. Comparative validations of the predicted results with the published numerical and experimental results are given. Parametric studies of porous road pavement on the horn effect are presented.

Chapter 5 - Large-scale outdoor field measurements are carried out on a residential building to assess the noise levels caused by passing trains that run on a viaduct. The experimental results are compared with different schemes for predicting noise from trains.

Chapter 6 - Theoretical models for predicting sound energy radiating from a passing train are discussed. A multipole expansion model is proposed to account for the vertical radiation directivity of the wheel/rail rolling noise. An empirical formula is derived and compared with the experimental data.

Chapter 7 - This chapter describes a prediction scheme pertaining to the propagation of traffic noise from a road to a balcony and explores the screening effect of a balcony. A new methodology is developed that focuses on the prediction of traffic noise levels inside a balcony by incorporating geometrical acoustic principle into a well-known prediction model – the Calculation of Road Traffic Noise (CRTN). Field measurements in different balcony types have been conducted to validate the proposed methodology.

Chapter 8 – Conclusions to all the relevant theories and the findings in this thesis are given. Furthermore, some prospective developments are suggested by virtue of the present study.

Chapter 2

Diffraction of Sound by a Hard Sphere

2.1 Introduction

The study of acoustic diffraction by an object has attracted the attention of researchers since the late 19th century. Researchers are especially interested in the phenomenon of sound diffraction by spheres because of the relatively simple mathematical models that can be derived. The theoretical models have been used in many applications in fields as diverse as engineering, biology, marine studies and medicine. In the past decades, there was significant interest in finding the analytical solutions for a plane wave incident on a spherical object [42][112], and the studies have recently been extended to include the presence of a hard, soft or impedance plane boundary [36][37][38][51][98]. More recently, Dassios et al. [27] undertook a series of studies on the problems of diffraction by point source excitation. In their work, they propose analytical approximations for most, if not all, possible boundaries at low frequencies. A full list of their articles and other references are given in Ref. [27].

Despite an exact analytical solution for acoustic diffraction by a sphere irradiated by a point source can be found in many textbooks (see, for example Ref. [61]), exact analytical solutions and their experimental validation for the acoustic diffraction by a hard sphere above a hard ground or an impedance ground with a point source incidence are scarce in the published literature except the work done by Huang and Gaunaurd [51].for the acoustic point source scattering by a spherical elastic shell submerged beneath a free surface in underwater acoustics. The current study is motivated by the need of developing an accurate numerical model pertaining to the diffraction of sound by a finite obstacle irradiated by a point source above an impedance ground. One of our objectives aspires to provide a model study for exploiting, for example, the sound radiation from tires above a porous road pavement. The sound field behind a hard sphere above an impedance ground is chosen because an exact analytic solution can be obtained straightforwardly.

In Sec. 2.2, the analytical solutions for the sound fields due to a point source irradiated on a hard sphere were reviewed. The image method and an appropriate addition theorem [10][11][23][100] as presented by Huang and Gaunaurd [36][37][38][51] will be presented. We also endeavor to explain the physical parameters involved in the mathematical model. Section 2.3 presents an extension of the Huang and Gaunaurd model for predicting the sound field for a hard sphere insonified by a point source above a hard ground and an impedance ground respectively. To incorporate the scattering effect of a plane boundary, an asymptotic solution [18][19] for the reflection of a spherical wave from a locally reacting surface is used. In Sec. 2.4, numerical calculations and experimental results are presented for validation of the proposed analytical models.

2.2 Sound diffraction by a hard sphere in a free space

Suppose an acoustically hard sphere of radius b is placed in an unbounded homogeneous medium. It is insonified by a point source and the total sound field is governed by a time-harmonic wave equation expressed in terms of a scalar velocity potential, ϕ as

$$\nabla^2\phi + k^2\phi = -\delta(x - x_s), \tag{2.1}$$

where $k = \omega/c$ is the wave number, ω the angular frequency of the source, and c the sound speed in the medium. Equation (2.1) is known as the Helmholtz or reduced wave equation, in which the time-dependent factor $e^{-i\omega t}$ has been suppressed for brevity. The problem can be best tackled by choosing a spherical coordinate system with the origin selected at the center of the sphere as shown in Fig. 2.1. The source point S is located at $(R_o, \theta_o, \varphi_o)$, and the field point P is situated at (R, θ, φ). We are primarily interested in the situation where source and receiver are located at the external positions of the sphere, i.e. $R_o, R \geq b$ (the radius of the sphere).

The incident sound field ϕ^i can be represented by a series of associated Legendre polynomials and spherical Bessel functions (see Ref. [61]) as,

$$\phi^i = \sum_{n=0}^{\infty}\sum_{m=0}^{n} a_{mn} h_n^{(1)}(kR_o) j_n(kR) P_n^m(\cos\theta_o) P_n^m(\cos\theta)\cos m(\varphi - \varphi_o) \quad (2.2)$$

for $R < R_o$, where $j_n()$ and $h_n^{(1)}()$ are, respectively, the spherical Bessel functions of the first and third kinds, and $P_n^m()$ are the associated Legendre functions expressed in terms of hypergeometric functions as

$$p_n^m(z) = \frac{1}{(-m)}\left(\frac{z+1}{z-1}\right)^{(1/2)m} F(-n, n+1; 1-m; \frac{1}{2} - \frac{1}{2}z). \quad (2.3)$$

$$F(\alpha, \beta; \gamma; z) = 1 + \frac{\alpha\beta}{1!\gamma} + \frac{\alpha(\alpha+1)\beta(\beta+1)}{2!\gamma(\gamma+1)} + \cdots. \quad (2.4)$$

The coefficient a_{mn} in Eq. (2.2) is determined according to

$$a_{mn} = \frac{i(n-m)!(2n+1)(2-\delta_{m0})k}{4\pi(n+m)!}, \quad (2.5)$$

and δ_{m0} is a Kronecker delta function that vanishes if $m \neq 0$. Equation (2.2) gives an exact formulation for the study of the sound field in the entire free space. We note that in Eq. (2.2), the roles of R and R_o can be interchanged when $R > R_o$ because of the reciprocity condition between source and receiver.

The scattered sound field ϕ^s can be treated as if it were a problem involving a spherical radiator. As a result, the sound field scattered from the surface of the sphere can be given by outgoing spherical Hankel functions and associated Legendre polynomials

$$\phi^s = \sum_{n=0}^{\infty}\sum_{m=0}^{n} b_{mn} h_n^{(1)}(kR_o) h_n^{(1)}(kR) P_n^m(\cos\theta) P_n^m(\cos\theta_o)\cos m(\varphi - \varphi_o) \quad (2.6)$$

for $R < R_o$, where the unknown scattering coefficients b_{mn} are to be determined by imposing proper boundary conditions on the surface of the sphere. The formula is appropriate because it represents an outgoing wave spreading spherically at a large distance from the center of the sphere.

The total sound field ϕ can now be found by adding the incident and scattered sound field by the principal of superposition,

$$\phi = \phi^i + \phi^s . \quad (2.7)$$

When the spherical boundary at $R = b$ is hard, the acoustic particle velocity normal to scattering surface is required to vanish,

$$\frac{\partial\phi}{\partial R} = 0 , \quad (2.8)$$

the unknown coefficient b_{mn} in Eq. (2.6) can be determined by

$$b_{mn} = -\frac{j_n'(kb)}{h_n^{(1)\prime}(kb)} a_{mn} \quad (2.9)$$

where the primes denote the derivative with respect to their arguments.

In the free space, the total sound field in the presence of a hard sphere irradiated by a point source can be written in a spherical coordinate system as

$$\phi = \sum_{n=0}^{\infty} \sum_{m=0}^{n} [a_{mn} j_n(kR) + b_{mn} h_n^{(1)}(kR)] h_n^{(1)}(kR_o) P_n^m(\cos\theta_o) P_n^m(\cos\theta) \cos m(\varphi - \varphi_o) \quad (2.10)$$

for $R < R_o$.

2.3 Sound diffraction by a hard sphere above an outdoor ground

It is well known that the sound field near an outdoor ground surface is affected by the wave propagation mechanisms over the ground determined by the acoustical properties, principally its acoustic impedance [33]. In fact, the acoustical characteristics of the ground determine the phase and amplitude of the reflected waves, which will inevitably interfere with the direct waves to produce an intricate sound field. A competent model for determining the acoustical properties of the ground is therefore as crucial as a scattering model for predicting a sound field induced by a scatterer above an impedance ground. The current scattering problem can be modeled by considering a sphere of radius b at a distance $d/2$ above a flat ground. Again, a spherical polar co-ordinate system is used with the center of the hard sphere chosen as the origin. The sound waves emanate from a point source that is positioned at a finite distance from the ground and irradiating on the sphere. The geometrical configuration of the problem is shown in Fig. 2.2. The sound field anywhere in the ambient medium is inherently contributed by the direct radiation from the source and the exterior radiation (diffraction) from the sphere, as well as by the reflection from the ground.

2.3.1 Diffraction above a hard ground

The sound field produced due to a sphere irradiated by a point source in a free field can be computed by using Eq. (2.10). The contributions due to the reflected sound waves can be readily found by applying the image method in accordance with the theory of geometrical acoustics. In this case, the problem is tackled by expressing the sound field in four components: the direct source, scattered waves from the sphere, waves disseminating from the image source and the image sphere (see Fig. 2.2). The sound field contributed by an image source in a hard ground can be expanded in an infinite series of associated Legendre functions and spherical Bessel functions as

$$\phi_r^i = \sum_{n=0}^{\infty}\sum_{m=0}^{n} a_{mn} h_n^{(1)}(kR_n^{'}) j_n(kR) P_n^m(\cos\theta_1) P_n^m(\cos\theta) \cos m(\varphi - \varphi_o) \quad (2.11)$$

for $R < R_o^{'}$, where $R_o^{'}$ is the distance and θ_1 is the polar angle measured from the center of the real sphere to the image source, and the constant a_{mn} is given by Eq. (2.5). Noting $\theta_o' = \pi - \theta_o$, invoking the identity of Legendre functions $P_n^m(\cos\theta_o') = (-1)^{m+n} P_n^m(\cos\theta_o)$ and taking the center of the image sphere as origin, the contribution due to the scattering sound field from the image sphere in a hard ground can be represented in an analogous form

$$\phi_r^s = \sum_{q=0}^{\infty}\sum_{m=0}^{q} (-1)^{m+q} b_{mq} h_q^{(1)}(kR_o) h_q^{(1)}(kR_3) P_q^m(\cos\theta_o) P_q^m(\cos\theta') \cos m(\varphi - \varphi_o), \quad (2.12)$$

where the unknown coefficients b_{mq} have to be determined from the boundary condition on the spherical surface. By the principle of superposition, we can express the total sound field as the sum of direct source, scattered waves from the real sphere, image source and scattered waves from the image sphere,

$$\phi^T = \phi^i + \phi^s + \phi_r^i + \phi_r^s. \quad (2.13)$$

Since the sound field contributed from an image sphere is still expressed in terms of spherical polar coordinates where the origin is at the center of the image sphere 'O'', we need to express this solution in a real spherical coordinate system with the origin at the center of the 'real' sphere 'O'. The analysis can be simplified somewhat by employing the translational addition theorem [23][100] for the spherical wave functions as presented by Huang and Gaunaurd [36][37][38][51]. For the case of vertical translation, we have a simplified formulation for the addition theorem [10][11]:

$$h_q^{(1)}(kR_3)P_q^m(\cos\theta') = \sum_{n=m}^{\infty} A_{mn}^{mq}(kd)j_n(kR)P_n^m(\cos\theta), \qquad (2.14)$$

where the translation coefficients

$$A_{mn}^{mq}(kd) = (-1)^m i^{n-q}(2n+1)\sum_p i^p a(m,q,-m,n,p) \begin{bmatrix} \mathrm{h}_p^{(1)}(kd) \\ j_p(kd) \end{bmatrix}, \quad \begin{bmatrix} R \le d \\ R > d \end{bmatrix} \qquad (2.15)$$

with $p = q+n, q+n-2, \ldots, |q-n|$ and the Gaunt coefficients given by

$$a(m,q,-m,n,p) = (2p+1)\left[\frac{(q+m)!(n-m)!}{(q-m)!(n+m)!}\right]^{\frac{1}{2}} \begin{bmatrix} q & n & p \\ 0 & 0 & 0 \end{bmatrix} \begin{bmatrix} q & n & p \\ m & -m & 0 \end{bmatrix}. \qquad (2.16)$$

The Gaunt coefficients are expressed as products of the Wigner 3-j symbols [the last two terms of Eq. (2.16)]. The Wigner 3-j symbol, which is associated with the coupling of two angular momentum eigenvectors, is defined in the Van der Waerden form [32] by

$$\begin{aligned} \begin{bmatrix} j_1 & j_2 & j_3 \\ m_1 & m_2 & m_3 \end{bmatrix} &= (-1)^{j_1-j_2-m_1-m_2}\,\Delta(j_1 \quad j_2 \quad j_3) \\ &\times \sqrt{(j_1+m_1)!(j_1-m_1)!(j_2+m_2)!(j_2-m_2)!(j_3+m_1+m_2)!(j_3-m_1-m_2)!} \\ &\times \sum_n \frac{(-1)^n}{n!(j_1+j_2-j_3-n)!(j_1-m_1-n)!(j_2+m_2-n)!(j_3-j_2+m_1+n)!(j_3-j_1+m_2+n)!} \end{aligned} \quad ,(2.17)$$

where the 'triangle relation' is defined by

$$\Delta(j_1 \quad j_2 \quad j_3) = \sqrt{\frac{(j_1 + j_2 - j_3)!(j_1 - j_2 + j_3)!(-j_1 + j_2 + j_3)!}{(j_1 + j_2 + j_3 + 1)!}} . \qquad (2.18)$$

The summation index n assumes all integer values for which the factorial arguments are not negative. The Gaunt coefficients can be either directly calculated using Eq. (2.16) or evaluated by the recursion relation proposed by Bruning and Lo [10][11]. However, use of the recursion relation is preferred as there is no need to calculate any Wigner 3-j symbol that can substantially reduce the computational time. When the translation for the spherical wave functions is along the vertical z-axis, the recursion relation is given by

$$\alpha_{p-3}a_{p-4} - (\alpha_{p-2} + \alpha_{p-1} - 4m^2)a_{p-2} + \alpha_p a_p = 0 , \qquad (2.19)$$

where

$$a_p \equiv a(m,n,-m,\nu,p) , \quad p = n+\nu, n+\nu-2, \ldots, |n-\nu| , \qquad (2.20)$$

and

$$\alpha_p = \frac{[(n+\nu+1)^2 - p^2][p^2 - (n-\nu)^2]}{4p^2 - 1} \qquad (2.21)$$

The recursion relation is most conveniently employed in the backward direction, since we can find simple starting values for the coefficients. The first two values at $p = n + \nu$ and $p = n + \nu - 2$ are

$$a_{n+\nu} = \frac{(2n-1)!!(2\nu-1)!!}{(2n+2\nu-1)!!} \frac{(n+\nu)!}{(n-m)!(\nu+m)!} , \qquad (2.22)$$

$$a_{n+\nu-2} = \frac{(2n+2\nu-3)}{(2n-1)(2\nu-1)(n+\nu)} [n\nu - m^2(2n+2\nu-1)] a_{n+\nu} , \qquad (2.23)$$

where $(2q-1)!! = (2q-1)(2q-3)\ldots 3 \cdot 1$; $(0)!! \equiv (-1)!! \equiv 1$. This recursion relation can give all a_p coefficients and thus all $A_{m\nu}^{mn}$.

The total sound field due to a hard sphere irradiated by a point source above a hard ground can now be expressed in a real spherical coordinate system which consists of four components: the direct waves from source and sphere, and the scattered waves from the image source and image sphere. Mathematically, the sound field can be written in a form as

$$\begin{aligned}\phi^T &= \sum_{n=0}^{\infty}\sum_{m=0}^{n} a_{mn} h_n^{(1)}(kR_o) j_n(kR) P_n^m(\cos\theta) P_n^m(\cos\theta_o)\cos m(\varphi-\varphi_o)\\ &+ \sum_{n=0}^{\infty}\sum_{m=0}^{n} a_{mn} h_n^{(1)}(kR'_n) j_n(kR) P_n^m(\cos\theta) P_n^m(\cos\theta_1)\cos m(\varphi-\varphi_o)\\ &+ \sum_{n=0}^{\infty}\sum_{m=0}^{n} b_{mn} h_n^{(1)}(kR_o) h_n^{(1)}(kR) P_n^m(\cos\theta) P_n^m(\cos\theta_o)\cos m(\varphi-\varphi_o)\,.\\ &+ \sum_{q=0}^{\infty}\sum_{m=0}^{q} (-1)^{m+q} b_{mq} h_q^{(1)}(kR_o) P_q^m(\cos\theta_o)\cdot\\ &\sum_{n=m}^{\infty} A_{mn}^{mq}(kd) j_n(kR) P_n^m(\cos\theta)\cos m(\varphi-\varphi_o)\end{aligned} \tag{2.24}$$

The unknown coefficients b_{mn} can be determined by applying the Neumann boundary condition, $\partial\phi^T/\partial R = 0$, on the surface of the hard sphere. After equating the coefficients of $P_n^m(\cos\theta)\cos m(\varphi-\varphi_o)$ and some tedious manipulations, a set of infinite and coupled linear complex equations can be formed for solving b_{mn}. The set of complex equations can be written in a form:

$$\begin{aligned}& b_{mn} h_n^{(1)}(kR_o) P_n^m(\cos\theta_o) + T_n \sum_{q=0}^{\infty} (-1)^{m+q} b_{mq} h_q^{(1)}(kR_o) P_q^m(\cos\theta_o) A_{mn}^{mq}(kd)\\ &= -a_{mn} T_n [h_n^{(1)}(kR_o) P_n^m(\cos\theta_o) + h_n^{(1)}(kR'_o) P_n^m(\cos\theta_1)]\end{aligned} \tag{2.25}$$

It can be expressed in a more compact form by using matrix notations as

$$\mathbf{XB} = \mathbf{C}\ , \tag{2.26}$$

where **B** is the matrix of the unknown coefficients b_{mn}, the diagonal elements of **X** are

$$X_{mn} = h_n^{(1)}(kR_o) P_n^m(\cos\theta_o) + T_n (-1)^{m+n} h_n^{(1)}(kR_o) P_n^m(\cos\theta_o) A_{mn}^{mn}(kd) \quad ,(2.27)$$

the off-diagonal elements of **X** are

$$X_{nq} = T_n(-1)^{m+q} h_q^{(1)}(kR_o) P_q^m(\cos\theta_o) A_{mn}^{mq}(kd)\,, \tag{2.28}$$

and the elements of the vector **C** are

$$C_n = -a_{mn} T_n [h_n^{(1)}(kR_o) P_n^m(\cos\theta_o) + h_n^{(1)}(kR_o^{'}) P_n^m(\cos\theta_1)]\,, \tag{2.29}$$

with
$$T_n = \frac{j_n'(kb)}{h_n'(kb)}\,. \tag{2.30}$$

The system of complex equations in (2.25) can be truncated to an order of N, that is the number of sums from n or $q = 0$ to N, depending on the degree of accuracy required. Thus, the matrix **X** is a $(N+1-m)\times(N+1-m)$ complex matrix, **B** and **C** are complex vectors of dimension $(N+1-m)$ for each m where m ranges from 0 to N.

The scattering effect from the sphere after reflection on the ground is directly related to the translation coefficients $A_{mn}^{mq}(kd)$ as shown in Eqs. (2.24) and (2.25). It can be conceived that the scattering effect of the image sphere to the total sound field becomes less important when it is not too close to the ground. Since the translation coefficients $A_{mn}^{mq}(kd)$ are proportional to $h_p^{(1)}(kd)$ for $R \le d$ or $j_p(kd)$ for $R > d$ as shown in Eq. (2.14), the scattering effect from image sphere depends on both the wave number and the separation distance d between the real sphere and image sphere. In a limiting case of $kd >> 1$, the spherical Bessel functions can be simplified by means of asymptotic expansions to give

$$h_n^{(1)}(kd) \approx i^{-(n+1)} \frac{e^{ikd}}{kd}\,, \tag{2.31}$$

$$j_n(kd) \approx \frac{\cos[kd - (n+1)\dfrac{\pi}{2}]}{kd}\,. \tag{2.32}$$

Consider an example of an urban scenario: an enclosed section of an elevated road or a railway viaduct located in close proximity to residential buildings. These flyovers and viaducts are usually built at a height of over 10 m above porous road pavement. In this case, the viaduct or the flyover is an "obstacle" to the traffic noise having dominant frequencies at about 500 to 2000 Hz. Obviously, the condition of $kd >> 1$ can be satisfied easily in this case.

Since the two spherical Bessel functions in Eqs. (2.31) and (2.32) are decreasing with increasing kd and their magnitudes are less than one for $kd >> 1$, it is reasonable to make the following approximation. The off-diagonal elements X_{nq} of Eq. (2.28) can be negligible compared to the diagonal element X_{nn} of Eq. (2.27) in the matrix $\mathbf{X}$ such that the linear complex equation Eq. (2.25) for b_{mn} can be decoupled and b_{mn} can be found directly as

$$b_{mn} = \frac{C_n}{X_{nn}} = \frac{-a_{mn}T_n\{h_n^{(1)}(kR_o)P_n^m(\cos\theta_o) + h_n^{(1)}(kR_o')P_n^m(\cos\theta_1)]}{h_n^{(1)}(kR_o)P_n^m(\cos\theta_o) + T_n(-1)^{m+n}h_n^{(1)}(kR_o)P_n^m(\cos\theta_o)A_{mn}^{mn}(kd)} . \quad (2.33)$$

When the sphere is far off the surface of the hard ground, the separation distance d and the distance R_o' from the center of real sphere to the image source become very large such that the spherical Hankel function $h_n^{(1)}(kR_o')$ and translation coefficient $A_{mn}^{mn}(kd)$ tend to zero. Thus Eqs. (2.24) and (2.33) can be reduced to Eqs. (2.10) and (2.9), respectively. These equations are the known expressions for a hard sphere in an unbounded medium. In the next section, we shall turn our attention to consider a more complicated situation where the ground has finite impedance.

2.3.2 Diffraction above an impedance ground

When a sound wave propagates near an impedance ground, the acoustical properties of the impedance ground are very important in determining the structure and nature of the sound field as it is effected by the direct and boundary-reflected sound waves. To incorporate the effect of ground impedance on radiation from a spherical source, we use an approximate analytical solution proposed in Refs. [18][19][92][93] for the reflection of a spherical wave from a locally reacting plane surface. The sound field due to the presence of a point source above an impedance ground can be expressed in the classical Weyl-van der Pol formula

$$\phi_T^i = \frac{e^{ikR_1}}{4\pi R_1} + Q_1 \frac{e^{ikR_2}}{4\pi R_2}, \tag{2.34}$$

where Q_1 is the spherical wave reflection coefficient for the point source reflection on the impedance ground. Knowing the distance R_2 between the image source and field point, the angle of incidence of the reflected wave α_1 (see Fig. 2.2), and the specific admittance of the reflecting ground β, the spherical wave reflection coefficient can be determined by

$$Q_1 = V_1 + (1 - V_1)F(w_1), \tag{2.35}$$

where

$$V_1 = \frac{\cos\alpha_1 - \beta}{\cos\alpha_1 + \beta} \tag{2.36}$$

is the plane wave reflection coefficient, and the function $F(w_1)$ is known as the boundary loss factor given by

$$F(w_1) = 1 + i\sqrt{\pi}\, w_1 e^{-w_1^2} \operatorname{erfc}(-iw_1), \tag{2.37}$$

in which erfc( ) is the complementary error function and the parameter w_1, the numerical distance w_1 is calculated by

$$w_1 = +\sqrt{\tfrac{1}{2}ikR_2}(\cos\alpha_1 + \beta) \quad . \tag{2.38}$$

Since the scattered waves from the sphere are spherically spreading waves, the approximate formulation presented in Refs. [18][19][92][93] can be adopted to solve the multi-scattering problem in the presence of an impedance ground which has previously been used by Hasheminejad [44] to find the modal acoustic force on a spherical radiator near a locally reacting boundary. Following similar arguments in Secs. 2.2 and 2.3, a heuristic formula for the multi-scattering sound field due to the presence of an impedance ground can be estimated by

$$\phi_T^s = \phi^s + Q_2\phi_r^s, \tag{2.39}$$

where ϕ^s and ϕ_r^s are given by Eqs. (2.6) and (2.12) respectively. The spherical wave reflection coefficient Q_2 for a scattered wave reflection on an impedance ground is given by

$$Q_2 = V_2 + (1 - V_2)F(w_2), \tag{2.40}$$

where V_2 is the plane wave reflection coefficient,

$$V_2 = \frac{\cos\alpha_2 - \beta}{\cos\alpha_2 + \beta}. \tag{2.41}$$

The boundary loss factor, $F(w_2)$, is given by

$$F(w_2) = 1 + i\sqrt{\pi}\,w_2 e^{-w_2^2} erfc(-iw_2), \tag{2.42}$$

where the corresponding numerical distance w_2 is determined by

$$w_2 = +\sqrt{\tfrac{1}{2}ikR_3}(\cos\alpha_2 + \beta) \ . \tag{2.43}$$

In Eqs. (2.40) - (2.43), R_3 is the distance between the center of the image sphere and the field point, and α_2 is the angle of incidence of the scattered wave on the impedance ground (see Fig. 2.2). By expressing the solution in the real spherical coordinate system, the total sound field can be written as

$$
\begin{aligned}
\phi^{T} &= \sum_{n=0}^{\infty}\sum_{m=0}^{n} a_{mn} h_n^{(1)}(kR_o) j_n(kR) P_n^m(\cos\theta) P_n^m(\cos\theta_o)\cos m(\varphi-\varphi_o) \\
&+ Q_1 \sum_{n=0}^{\infty}\sum_{m=0}^{n} a_{mn} h_n^{(1)}(kR_o^{'}) j_n(kR) P_n^m(\cos\theta) P_n^m(\cos\theta_1)\cos m(\varphi-\varphi_o) \\
&+ \sum_{n=0}^{\infty}\sum_{m=0}^{n} b_{mn} h_n^{(1)}(kR_o) h_n^{(1)}(kR) P_n^m(\cos\theta) P_n^m(\cos\theta_o)\cos m(\varphi-\varphi_o) \quad , \qquad (2.44) \\
&+ Q_2 \sum_{q=0}^{\infty}\sum_{m=0}^{q} (-1)^{m+q} b_{mq} h_q^{(1)}(kR_o) P_q^m(\cos\theta_o) \cdot \\
&\sum_{n=m}^{\infty} A_{mn}^{mq}(kd) j_n(kR) P_n^m(\cos\theta)\cos m(\varphi-\varphi_o)
\end{aligned}
$$

where a_{mn} is given by Eq. (2.5) and the unknown scattering coefficients b_{mn} have to be determined by the application of Neumann boundary condition on the surface of the hard sphere. Eventually, we can get another set of coupled linear complex equations for solving b_{mn},

$$
\begin{aligned}
& b_{mn} h_n^{(1)}(kR_o) P_n^m(\cos\theta_o) + Q_2 T_n \sum_{q=0}^{\infty} (-1)^{m+q} b_{mq} h_q^{(1)}(kR_o) P_q^m(\cos\theta_o) A_{mn}^{mq}(kd) \\
&= -a_{mn} T_n [h_n^{(1)}(kR_o) P_n^m(\cos\theta_o) + Q_1 h_n^{(1)}(kR_o^{'}) P_n^m(\cos\theta_1)]
\end{aligned}
, \quad (2.45)
$$

which can also be conveniently put in a matrix form as

$$\mathbf{YB} = \mathbf{D} . \qquad (2.46)$$

The diagonal elements of **Y** are

$$Y_{nn} = h_n^{(1)}(kR_o) P_n^m(\cos\theta_o) + Q_2 T_n (-1)^{m+n} h_n^{(1)}(kR_o) P_n^m(\cos\theta_o) A_{mn}^{mn}(kd) \quad ,$$

(2.47)

the off-diagonal elements of **Y** are

$$Y_{nq} = Q_2 T_n (-1)^{m+q} h_q^{(1)}(kR_o) P_q^m(\cos\theta_o) A_{mn}^{mq}(kd) , \qquad (2.48)$$

and the elements of the vector **D** are

$$D_n = -a_{mn} T_n [h_n^{(1)}(kR_o) P_n^m(\cos\theta_o) + Q_1 h_n^{(1)}(kR_o^{'}) P_n^m(\cos\theta_1)] , \qquad (2.49)$$

where T_n is given by Eq. (2.30). In a similar fashion as shown in the last section, the system of complex equations in Eq. (2.45) can be truncated to an order of N, that is the number of sums from n or $q = 0$ to N, depending on the degree of accuracy required. The complex matrix $\mathbf{Y}$ has an order of $(N+1-m)\times(N+1-m)$ and the complex vectors $\mathbf{B}$ and $\mathbf{D}$ have dimensions $(N+1-m)$ for each m where m ranges from 0 to N.

Using the same arguments in the previous section, an approximation can be made, the off-diagonal elements Y_{nq} of Eq. (2.48) are negligibly small compared with the diagonal element Y_{nn} of Eq. (2.47) in the matrix Y provided that $kd >> 1$. The linear complex equation Eq. (2.45) for b_{mn} can then be decoupled and they can be solved directly as

$$b_{mn} = \frac{D_n}{Y_{nn}} = \frac{-a_{mn} T_n [h_n^{(1)}(kR_o) P_n^m(\cos\theta_o) + Q_1 h_n^{(1)}(kR_o') P_n^m(\cos\theta_1)]}{h_n^{(1)}(kR_o) P_n^m(\cos\theta_o) + Q_2 T_n (-1)^{m+n} h_n^{(1)}(kR_o) P_n^m(\cos\theta_o) A_{mn}^{mn}(kd)} \quad .(2.50)$$

Considering the limiting case when the sphere is very far away from the impedance ground, the contribution from the image source and image sphere to total the sound field are negligible such that Eqs. (2.44) and (2.50) can be reduced to Eqs. (2.10) and (2.9) respectively. It is reassuring to start from a more general situation that leads to an expression for the scattering of sound by a hard sphere in a boundless medium.

In the following sections, we shall present the calculated results that will be used to compare with experimental data. The comparisons provide a validation of the proposed theoretical formulation for the scattering of sound by a hard spherical obstacle in the context of outdoor sound propagation. Although a boundary element formulation (BEM) [13] may be developed to compute the scattering by obstacles with an irregular shape above an impedance ground, we prefer to use the techniques of separation of variables together with the appropriate wave field expansions as detailed above. It is because the BEM scheme gives little physical insight into the phenomenon of the effect of multiple-scattering. In addition, the required computational times become increasingly demanding at higher frequencies. We remark that there is a lack of experimental data to support the theoretical formulations of the acoustic diffraction by an spherical object above a finite impedance ground. In the following section, we shall show the validity of our theoretical formulation by comparing its predictions with experimental data.

2.4 Experiments and numerical results

2.4.1 Instrumentation

A series of indoor experiments were conducted in an anechoic chamber 6 m × 6 m × 4 m (high) in size for the validation of the theoretical models introduced in Secs. 2.2 and 2.3. The anechoic chamber used in the experiments has been designed with a cut-off frequency of 75Hz and a NC rating of NC-25 respectively. The point source was produced by means of a tube of 1 m in length and 3 cm in internal diameter. It was driven by a Tannoy loudspeaker powered by a power amplifier (B&K 2713) connected to a maximum length sequence system analyzer (MLSSA) with an MLS card installed in a PC. The MLSSA system was used as a source signal generator as well as a signal processing analyzer for all the experimental measurements. The acoustic signals were taken by a BSWA TECH MK224 ½-in condenser microphone coupled with a BSWA TECH MA201 preamplifier that was connected to the MLS card through a BSWA TECH MC102 amplifier.

2.4.2 Diffraction by a hard sphere in free field

In order to complete the study of the acoustic scattering by a hard sphere, a set of appropriate experimental measurements in a free space has been carried out which was used to validate our theoretical formulations. The experimental data was presented and compared with theoretical predictions for future reference. A sphere of radius 0.1 m was made of hardwood and varnished to provide a smooth hard surface. It was used in these measurements. The sphere was bolted with a small hook and hung in the anechoic chamber by suspending a fine nylon thread fixed in position by means of stands as shown in Fig. 2.3. A specifically designed device, calibrated with angles and radial dimensions, was used to measure the positions of both the source and receiver points. The experimental data of different source/receiver configurations are plotted in Fig. 2.4, in which the theoretical predictions for the same geometrical configurations are shown. For a consistent presentation, relative sound pressure levels are used throughout in this chapter. The relative sound pressure level is defined as the ratio of the total sound field relative to the reference free-field level measured at 1 m from the source.

In Fig. 2.4, we show the spectra of relative sound-pressure levels with the source S located at (0.4 m, 90°, 0°) and receiver P located at four locations of (0.19 m, 90°, 60°), (0.24 m, 90°, 60°), (0.2 m, 90°, 120°) and (0.15 m, 90°, 180°) respectively. In general, the theoretical predictions are in accord with the experimental measurements for different experimental configurations despite the fact that the experimental results show a trend of noticeable differences in magnitude (the experimental results are always lower than predictions) at the high frequency regime. These discrepancies are mainly due to the limitations of our experimental set-up because a long tube was used to represent a point source. This set-up was inadequate especially at high frequencies because the point source was neither omni-directional nor adequate in producing sufficient signal levels for accurate indoor measurements. It is not surprising to see that the frequency spectra become plain as the subtended angle between the source and receiver increases. This is because the interference effect of the direct wave on the scattered sound at field points becomes less effective when the subtended angle increases. In such a situation, the receiver is located in the shadow zone. With these enlightening results, we feel confident in using the validated model for the prediction of acoustic scattering by a hard sphere in the presence of a ground.

2.4.3 Diffraction by a hard sphere above a hard ground

A vanished hardwood board of 0.02 m in thickness and with a transmission loss of about 23 dB(A) was used to model the hard ground, and a hardwood sphere of radius 0.127 m, varnished to provide a smooth surface, was used in our experiments for the study of diffraction by a hard sphere above a hard ground. The sphere was hung above the hard ground in the same way as described in the previous section. Two sets of measurements were presented in this case. The center of the sphere was set at 0.22 m and 0.287 m above the hard ground surface for the first and second set of measurements respectively. In the first set of measurements (Fig. 2.5), the spectra of relative sound-pressure levels were obtained with the source situated at (0.35 m, 90°, 0°) and receivers at (0.2 m, 90°, 60°), (0.25 m, 90°, 120°), (0.25 m, 90°, 180°) and (0.3 m, 90°, 180°) respectively. In the second set of measurements (Fig. 2.6), the spectra of relative sound-pressure levels were obtained with the source at (0.35 m, 90°, 0°) and receivers at (0.25 m, 90°, 60°), (0.2 m, 90°, 120°), (0.2 m, 90°, 180°) and (0.3 m, 90°, 180°) respectively. In these figures, the experimental results are plotted in solid lines. The dashed lines represent the theoretical prediction derived from an exact solution method by solving the complex linear equation Eq. (2.26) for the unknowns b_{mn}. The dotted lines represent the theoretical result obtained by an approximate method of using Eq. (2.33) to determine b_{mn}. In the numerical analyses, we have used $N = 30$ throughout in order to obtain the numerical results calculated by using exact solution method. We can see that the experimental results show close agreement with the predictions based on the analytical models discussed in Sec. 2.3. The predicted results obtained by using the exact solution and the approximate solution are consistent (two curves are always coincident) as shown in Figs. 2.5 and 2.6. However, the computational time needed to obtain the same prediction result by using the approximation solution method is much less than that by using the exact solution method. We developed a MATLAB program for each model and used a desktop computer with CPU of 1.8 GHz to carry out the computations. The program takes about 1 s for the approximate model comparing with 60 s for the exact solution to obtain a predicted result at a source frequency of 1000 Hz. It can also be observed in Figs. 2.5 and 2.6 that the patterns of the spectra become more intricate compared to a sphere in free field, it is because in the presence of a hard ground, the reflected waves produced will interact with the direct and scattered waves to form a more complicated sound field.

2.4.4 Diffraction by a hard sphere above an impedance ground

The ground with impedance was simulated by laying a thick carpet on the hardwood board. The carpet can be regarded as a locally reacting ground, and a two-parameter model [4] was used to predict the effective admittance

$$\beta_e = \frac{1}{0.436(1+i)(\sigma_e/f)^{1/2} + 19.48 i \alpha_e / f}, \tag{2.51}$$

where f is the frequency, σ_e is the effective flow resistivity, and α_e is the effective rate of change of porosity with depth of the material. Prior measurements were conducted to characterize the acoustical properties of the carpet. Figure 2.7 shows a typical result of theoretical prediction by the Weyl-van der Pol formula and experimental measurements for characterizing the impedance (admittance) of the carpet. The measurement was carried out with a point source near an impedance surface and without the presence of a scattering sphere. These measurement results were subsequently fitted with the two-parameter model, and the best-fit parameters were found to be σ_e = 10 kPa s m^{-2} and α_e = 80 m^{-1}. These acoustical parameters were used in our subsequent predictions of acoustic diffraction by a hard sphere above an impedance ground. In this case, the sphere of radius 0.127 m was hung above the impedance ground in the same way as described in the previous sections. Two sets of experimental data were also presented. In the first set of measurements, the center of the sphere was set at 0.212 m above the impedance ground surface and it was set at 0.277 m above the ground surface for the second set of measurements. In the first set of measurements (Fig. 2.8), the spectra of relative sound-pressure levels were obtained with the source at (0.35 m, 90°, 0°) and receivers at (0.25 m, 90°, 60°), (0.2 m, 90°, 120°), (0.25 m, 90°, 120°) and (0.3 m, 90°, 180°) respectively. Figure 2.9 displays the results of the second set of measurements. In the second set of measurements, the spectra of relative sound-pressure levels were taken with the source at (0.35 m, 90°, 0°) and receivers at (0.25 m, 90°, 60°), (0.25 m, 90°, 120°), (0.3 m, 90°, 120°) and (0.3 m, 90°, 180°) respectively. In these figures, the experimental results are plotted in solid lines, the dashed lines represent the theoretical prediction derived from an exact solution method and the dotted lines represent the theoretical results obtained by the approximation scheme. In general, the experimental results agree reasonably well with the predictions made by the theoretical models developed in Sec. 2.3.2, although the experimental results show a trend of observable differences in magnitude at high frequencies. The discrepancies in magnitude at high frequencies could be attributed to the insufficient energy content of the waves after reflection from the impedance ground that weakens the total sound field. Once again, the prediction results obtained by using the approximate solution is a good representation to that obtained by exact solution as evinced from the comparisons shown in Figs 2.8 and 2.9. The computational time needed to calculate the numerical results can be reduced substantially by using the approximate scheme.

2.5 Summary

The classical formulation of acoustic diffraction by an acoustically hard sphere insonified by a point source has been validated by indoor measurements. The theoretical analysis has been extended for the study of acoustic diffraction by a hard sphere above an acoustically hard and an impedance ground by using the classical method of images and translational addition theorems for the spherical wave functions. The effect of an impedance ground on the boundary-reflected sound fields can be incorporated into the exact analytical model through the use of the Weyl-van der Pol formula, which is an approximate analytical solution for the reflection of a spherical wave from a locally reacting ground. The analytical solutions for a hard sphere irradiated by a point source above a hard and an impedance ground can be expressed in four terms: contributions from the source and the sphere, and contributions from the image source and the image sphere. An approximate method has been proposed to obtain the scattering coefficients for a sphere not too close to the ground, which can substantially reduce the computational time for the calculation of the total sound fields. The predictions made by the analytical models were plotted against the experimental results of different configurations and good agreements of comparisons are obtained. It has been shown that the numerical result predicted by the approximate method agree closely with the prediction made by the exact solution method. As expected, the experimental and theoretical results reveal that the sound fields become more intricate in the presence of an outdoor ground surface.

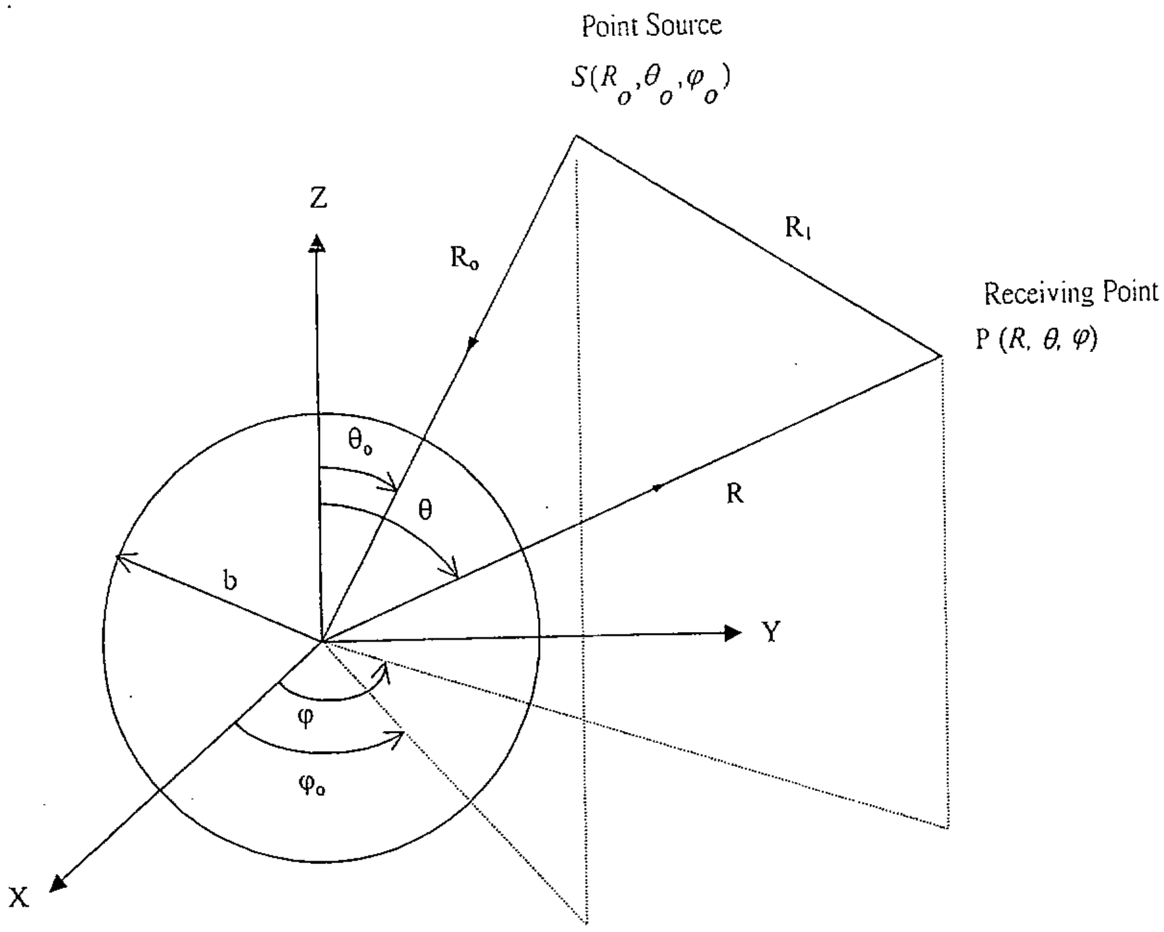

Figure 2.1. Illustration of the geometrical configuration of the diffraction problem by a sphere irradiated by a point source.

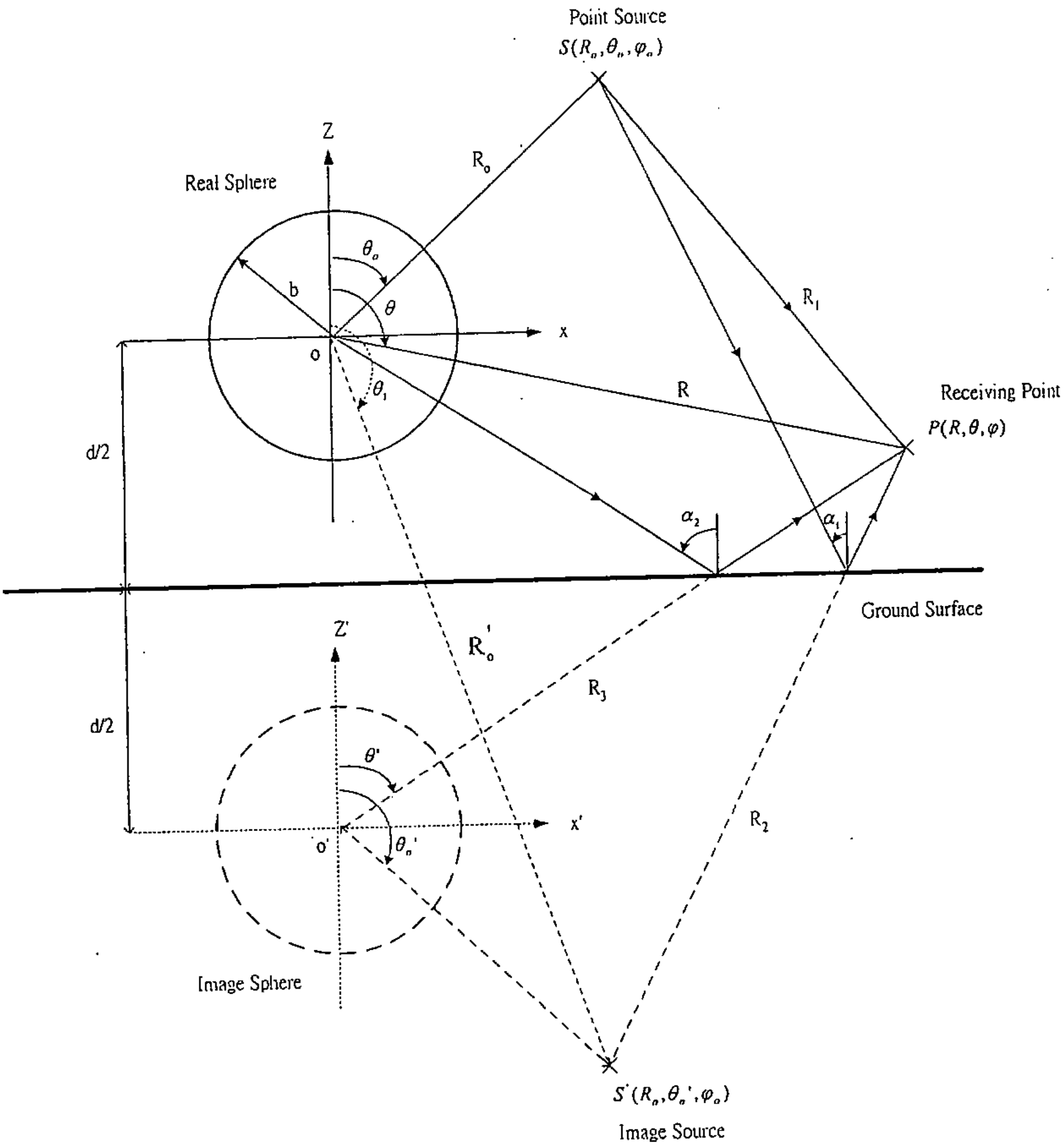

Figure 2.2. Illustration of the geometrical configuration of the acoustic diffraction problem by a sphere above a flat ground irradiated by a point source.

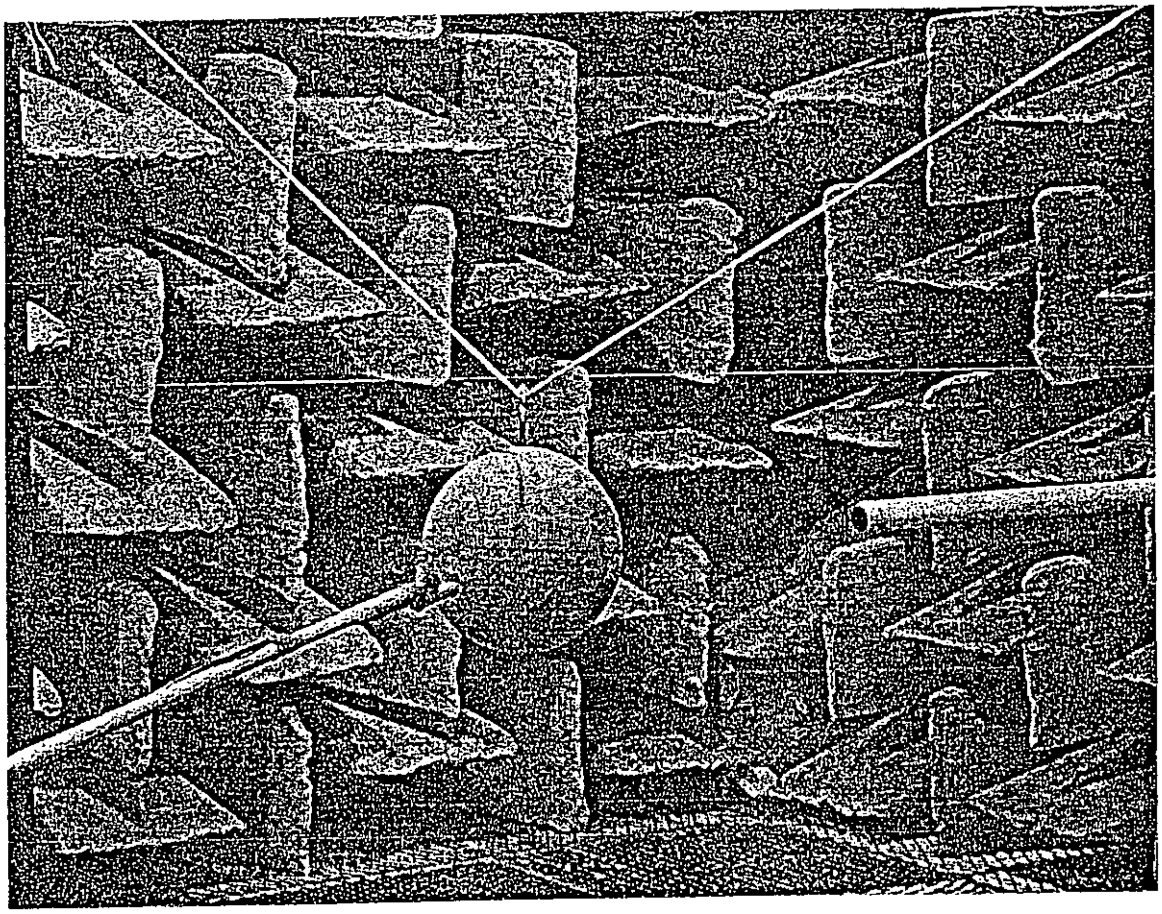

Figure 2.3. The experimental setup in an anechoic chamber for the measurement of sound diffraction by a hard sphere in free field. The sphere is bolted with a small hook and hung in the anechoic chamber by suspending a fine nylon thread fixed in position by means of stands.

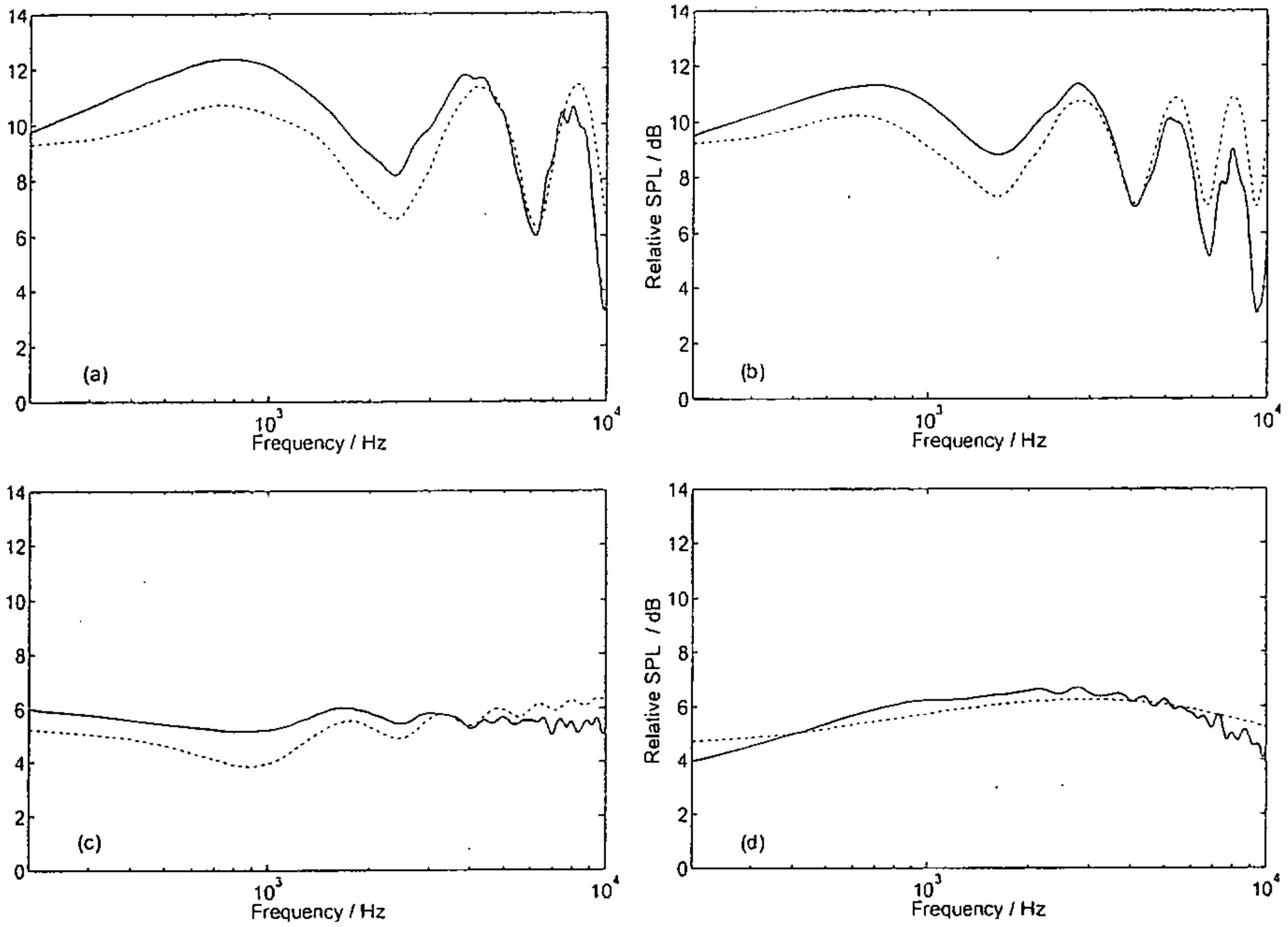

Figure 2.4. Experimental results and theoretical predictions for acoustic diffraction by a hard sphere of radius 0.1 m. Source: $R_0 = 0.4$ m, $\theta_0 = 90°$, $\phi_0 = 0°$. Receiver: (a) $R = 0.19$ m, $\theta = 90°$, $\phi = 60°$; (b) $R = 0.24$ m, $\theta = 90°$, $\phi = 60°$; (c) $R = 0.2$ m, $\theta = 90°$, $\phi = 120°$; (d) $R = 0.15$ m, $\theta = 90°$, $\phi = 180°$. (Dotted line: theoretical predictions; solid line: experimental results).

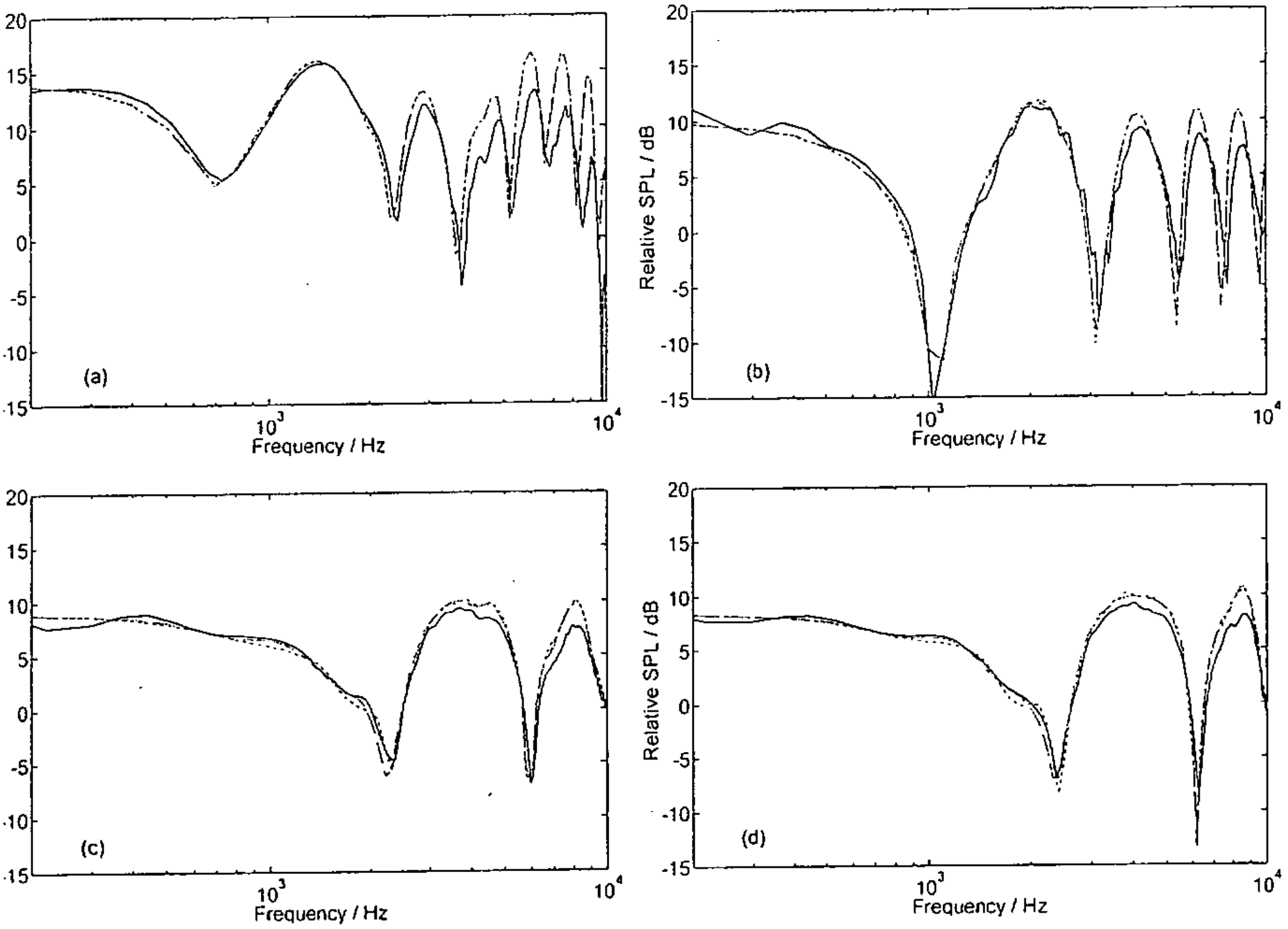

Figure 2.5. Experimental results and theoretical predictions for acoustic diffraction by a hard sphere of radius 0.127 m above a hard ground. The sphere center is 0.22 m above the hard ground. Source: $R_o = 0.35$ m, $\theta_o = 90°$, $\phi_o = 0°$. Receiver: (a) $R = 0.2$ m, $\theta = 90°$, $\phi = 60°$; (b) $R = 0.25$ m, $\theta = 90°$, $\phi = 120°$; (c) $R = 0.25$ m, $\theta = 90°$, $\phi = 180°$; (d) $R = 0.3$ m, $\theta = 90°$, $\phi = 180°$. (Dotted line: theoretical predictions – approximation; dashed line: theoretical predictions – exact solution; solid line: experimental results).

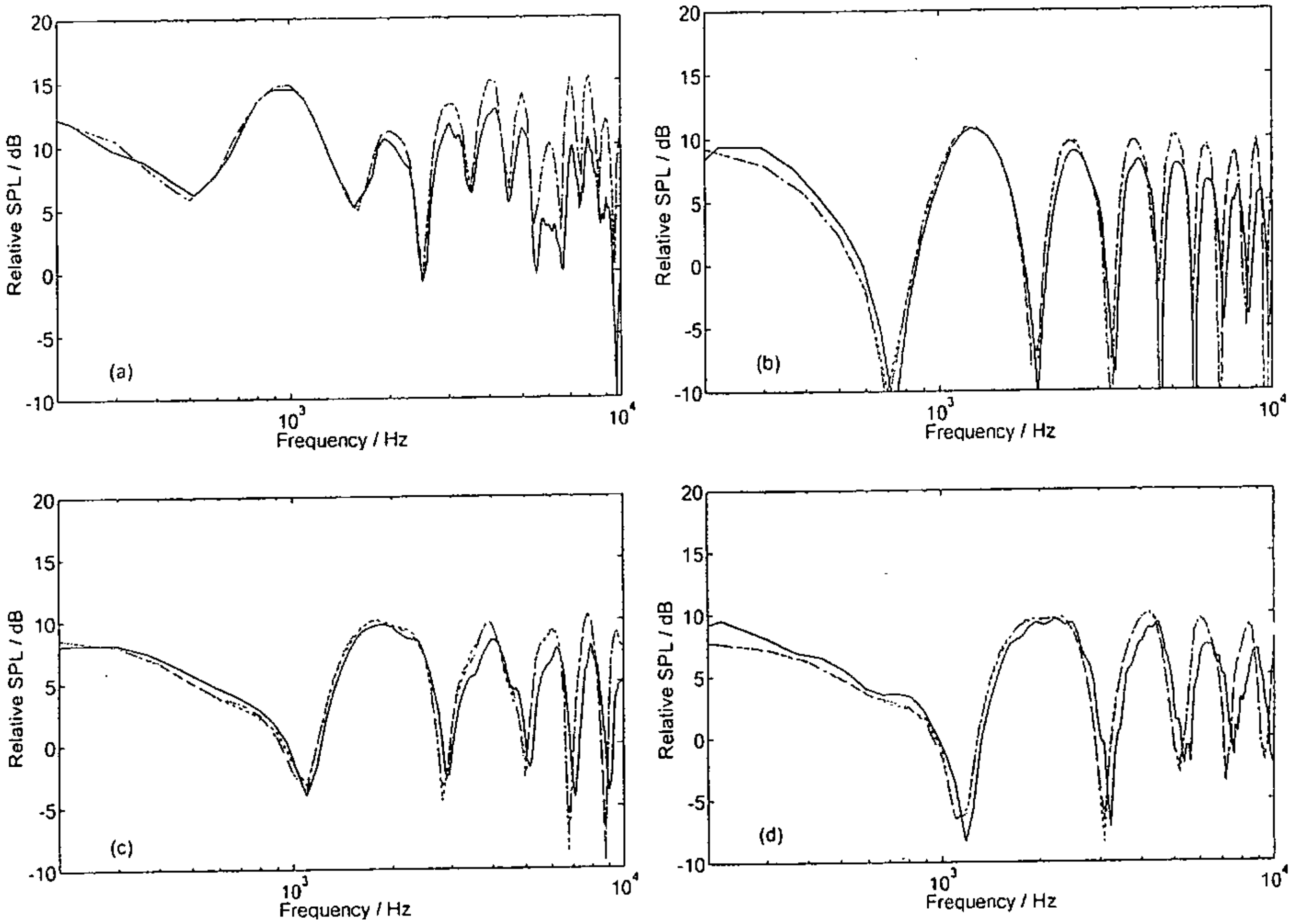

Figure 2.6. Experimental results and theoretical predictions for acoustic diffraction by a hard sphere of radius b = 0.127 m above a hard ground. The sphere center is 0.287 m above the hard ground. Source: R_o = 0.35m, θ_o = 90°, ϕ_o = 0°. Receiver: (a) R = 0.25m, θ = 90°, ϕ = 60°; (b) R = 0.2 m, θ = 90°, ϕ = 120°; (c) R = 0.2m, θ = 90°, ϕ = 180°; (d) R = 0.3m, θ = 90°, ϕ = 180°. (Dotted line: theoretical predictions – approximation; dashed line: theoretical predictions – exact solution; solid line: experimental results).

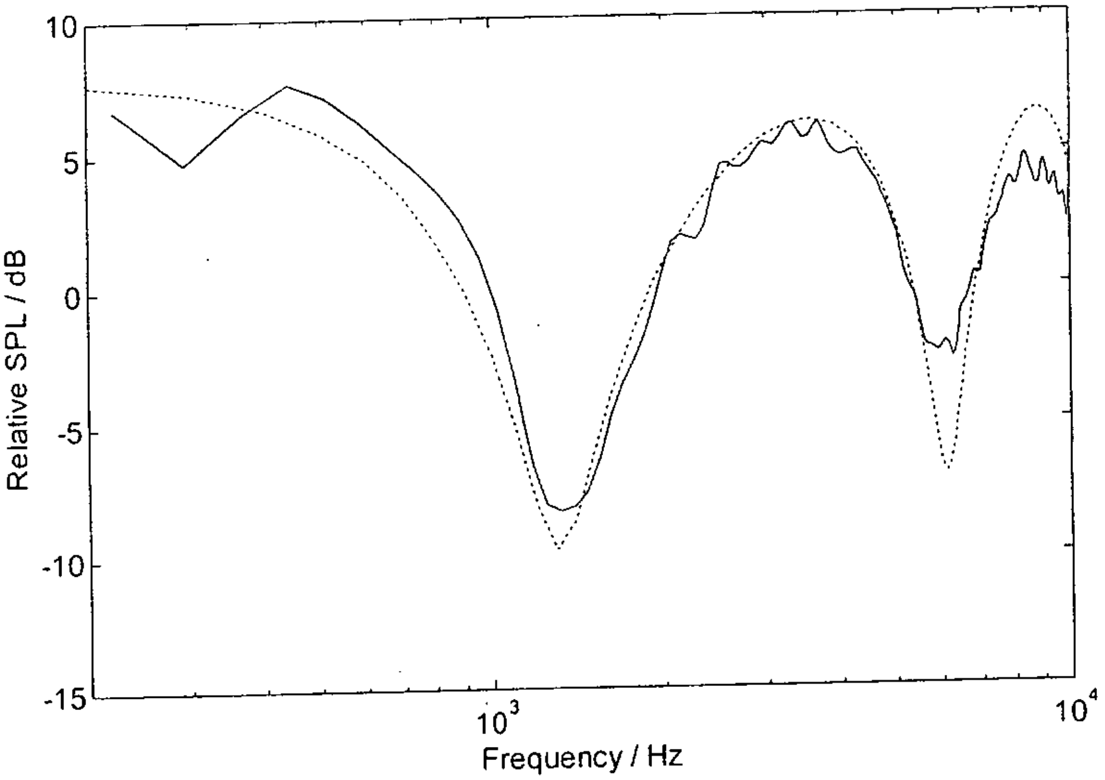

Figure 2.7. Characterization of a thick carpet. Source height = 0.16 m, receiver height = 0.16 m and range = 1 m. The best-fit parameters are found to be σ_e = 10 kPa s m^{-2} and α_e = 80 m^{-1}. (Dotted line: theoretical predictions by Weyl-van der Pol formula and two-parameter model; solid line: experiment results).

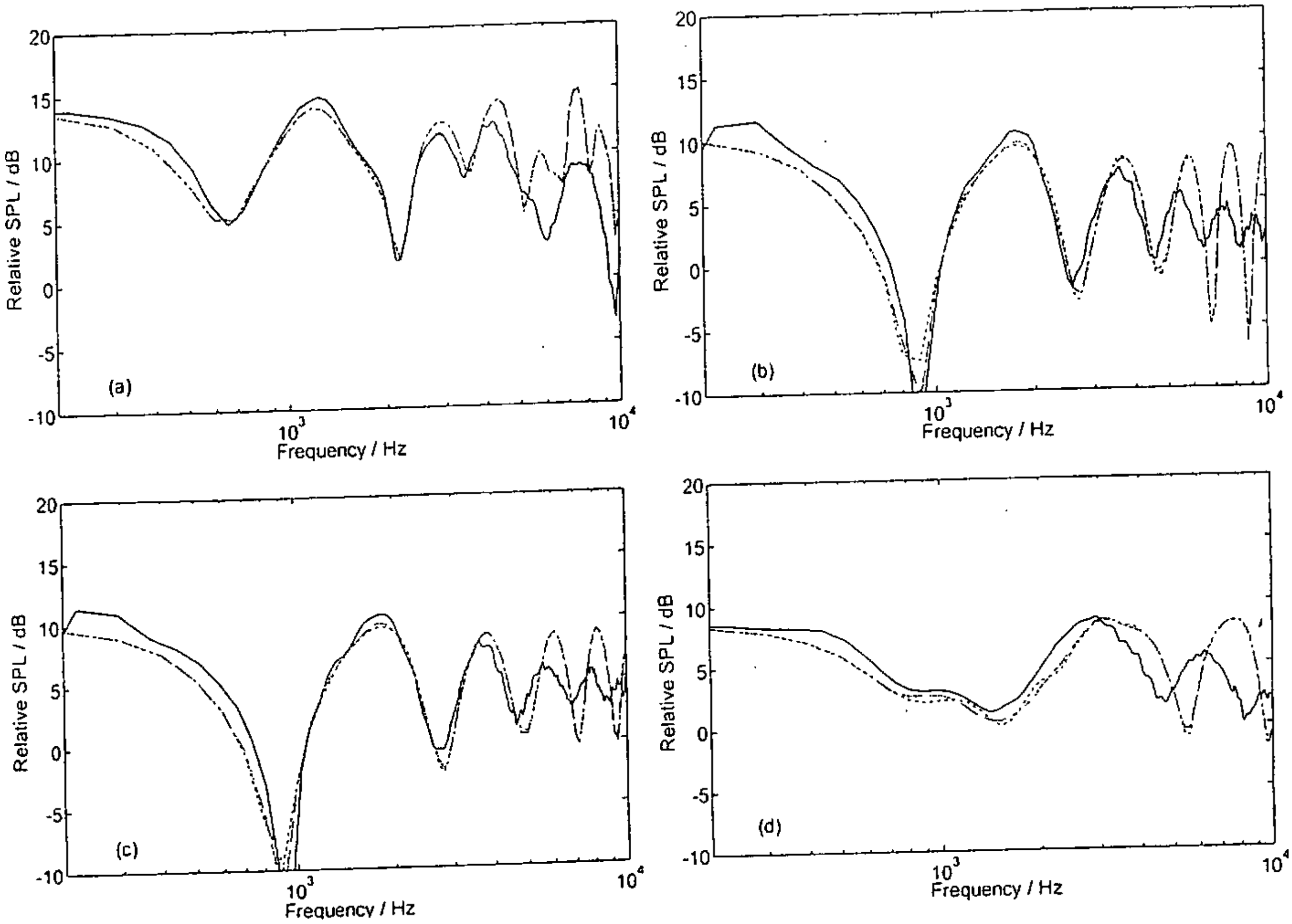

Figure 2.8. Experimental results and theoretical predictions for acoustic diffraction by a hard sphere of radius b = 0.127 m above an impedance ground. The sphere center is 0.212 m above the impedance ground. Source: R_o = 0.35 m, $\theta_o = 90°$, ϕ_o = 0°. Receiver: (a) R = 0.25 m, $\theta = 90°$, $\phi = 60°$; (b) R = 0.2 m, $\theta = 90°$, $\phi = 120°$; (c) R = 0.25 m, $\theta = 90°$, $\phi = 120°$; (d) R = 0.3 m, $\theta = 90°$, $\phi = 180°$. (Dotted line: theoretical predictions – approximation; dashed line: theoretical predictions – exact solution; solid line: experimental results).

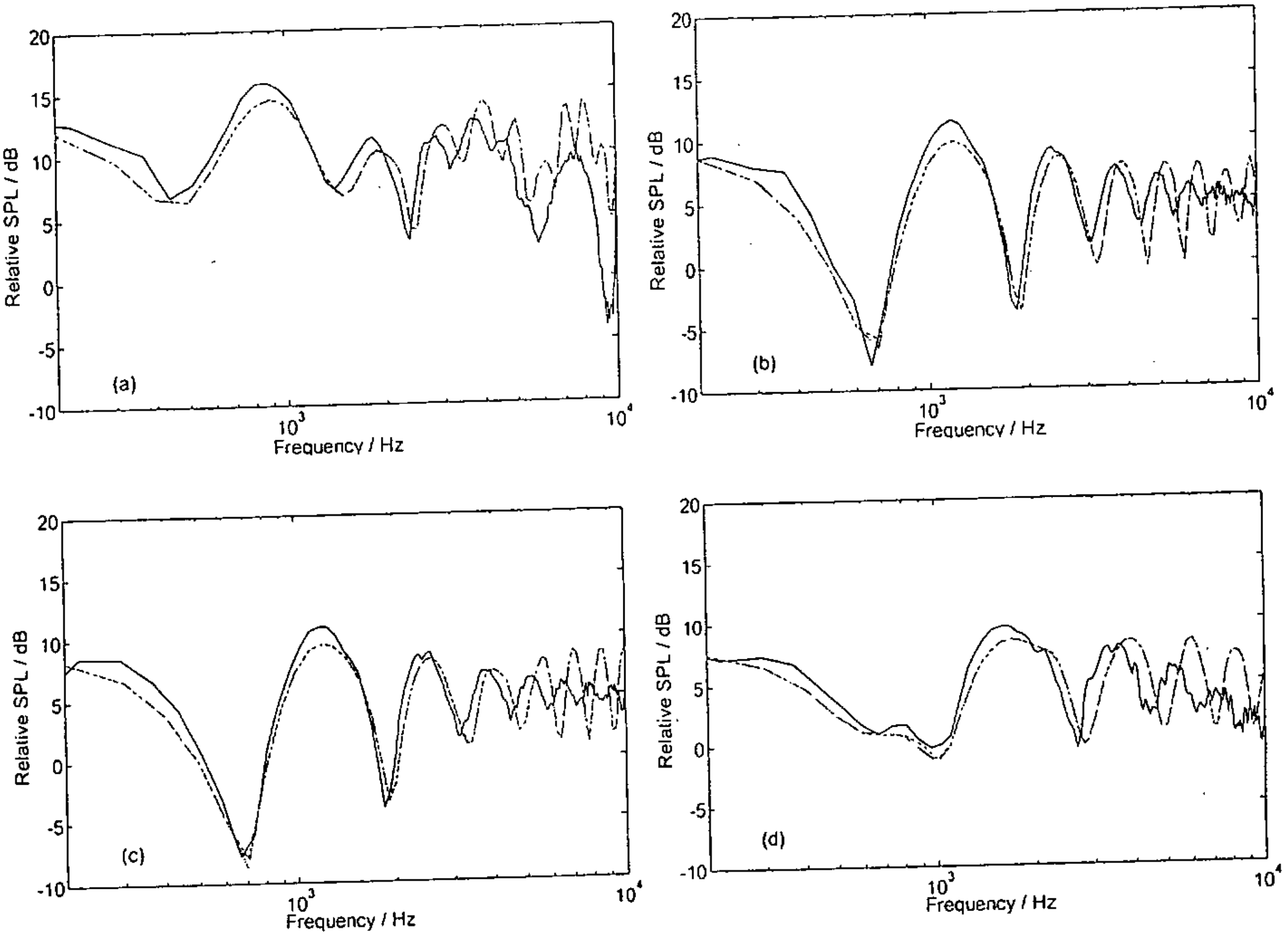

Figure 2.9. Experimental results and theoretical predictions for acoustic diffraction by a hard sphere of radius b = 0.127 m above an impedance ground. The sphere center is 0.277 m above the ground surface. Source: R_o = 0.35 m, θ_o = 90°, ϕ_o = 0°. Receiver: (a) R = 0.25 m, θ = 90°, ϕ = 60°; (b) R = 0.25 m, θ = 90°, ϕ = 120°; (c) R = 0.30 m, θ = 90°, ϕ = 120°; (d) R = 0.3 m, θ = 90°, ϕ = 180°. (Dotted line: theoretical prediction – approximation; dashed line: theoretical prediction – exact solution; solid line: experimental result).

Chapter 3

Diffraction of Sound by an Impedance Sphere

3.1 Introduction

The problem of acoustic diffraction by a hard spherical object above a ground surface has been studied both theoretically and experimentally in Chapter 2. Here, previous analyses are extended to allow the prediction of sound fields in the presence of an absorbing sphere near a flat ground of different boundary conditions. Despite the fact that point-source radiation has a broad application in the fields of underwater acoustics, medical imaging, nondestructive testing and seismic wave exploration [27], there are relatively few theoretical and experimental studies exploiting the phenomenon of sound diffracted by an absorbing spherical object above an outdoor ground surface of finite impedance. A notable exception is the work of Huang and Gaunaurd [51] on acoustic point source scattering by a spherical elastic shell submerged beneath a free surface in underwater acoustics. The exact analytical solution for this relatively simple case is needed because it will provide a benchmark for other more complicated and theoretically intractable numerical schemes. The analytical solutions developed in the present work can also be useful in assessing other numerical models used in related fields such as acoustical oceanography and others.

Section 3.2 of this chapter outlines analytical solution of acoustic diffraction by an absorbing sphere excited by a point source. Attempts are made to explain the physical parameters involved in the mathematical model. In Sec. 3.3 the problem is extended to include the presence of a hard ground as well as an impedance ground.

The image method and appropriate addition theorem [10][11][23][100] presented by Huang and Gaunaurd [36][37][38][51] will be employed to tackle the multi-scattering problem. The effect of ground impedance on the reflected sound waves is incorporated in the numerical model using an asymptotic solution [18][19][92][93] developed for the reflection of a spherical wave from a locally reacting surface. In Sec. 3.4, experimental measurements of the present study are presented. They are used to validate the theoretical models for various receiver locations around the sphere above the hard and impedance ground.

3.2 Sound diffraction by an impedance sphere in a free space

Consider an absorbing sphere made of either locally reacting material or extended reaction material irradiated by a point source in an unbounded homogeneous medium, the total sound field is governed by the Helmholtz equation as given in Eq. (2.1). The incident sound field due to the acoustic radiation from a point source can be represented by spherical Bessel functions and associated Legendre polynomials as

$$\phi^i = \sum_{n=0}^{\infty}\sum_{m=0}^{n} a_{mn} h_n^{(1)}(kR_o) j_n(kR) P_n^m(\cos\theta) P_n^m(\cos\theta_o)\cos m(\varphi-\varphi_o) \quad (3.1)$$

for $R < R_o$, where the coefficient a_{mn} in Eq. (3.1) is determined according to

$$a_{mn} = \frac{i(n-m)!(2n+1)(2-\delta_{m0})k}{4\pi(n+m)!}. \quad (3.2)$$

Mathematically, the sound scattered by an absorbing sphere can be expressed in the same form as Eq. (2.6)

$$\phi^s = \sum_{n=0}^{\infty}\sum_{m=0}^{n} b_{mn} h_n^{(1)}(kR_o) h_n^{(1)}(kR) P_n^m(\cos\theta) P_n^m(\cos\theta_o)\cos m(\varphi-\varphi_o) \quad (3.3)$$

for $R < R_o$. The unknown scattering coefficients b_{mn} are to be determined by imposing proper boundary conditions on the surface of the sphere. For an absorbing sphere irradiated by a point source, an interior sound field is established inside the sphere which can be determined in a similar form as Eq. (3.1),

$$\phi^{in} = \sum_{n=0}^{\infty}\sum_{m=0}^{n} c_{mn} h_n^{(1)}(kR_o) j_n(k_1 R) P_n^m(\cos\theta) P_n^m(\cos\theta_o)\cos m(\varphi - \varphi_o) \quad (3.4)$$

for $R < b$ (the radius of the sphere). In the above equation, k_1 is the wave number inside the sphere and the unknown coefficient c_{mn} has to be determined by imposing the boundary conditions on the spherical surface. The analytical solution of the total sound field is mathematically represented by the same form as Eq. (2.10)

$$\phi = \sum_{n=0}^{\infty}\sum_{m=0}^{n} [a_{mn} j_n(kR) + b_{mn} h_n^{(1)}(kR)] h_n^{(1)}(kR_o) P_n^m(\cos\theta_o) P_n^m(\cos\theta)\cos m(\varphi - \varphi_o) \quad (3.5)$$

for $R < R_o$. The symbols used in Eqs. (3.1) to (3.5) are of the same definitions as given in Sec. 2.2.

3.2.1 Diffraction by an extended reaction sphere

For an extended reaction sphere, the acoustic pressure and normal particle velocity should be continuous. This implies

$$\phi^i + \phi^s = \phi^{in} \quad (3.6)$$

and

$$\frac{1}{\rho}\frac{\partial}{\partial R}(\phi^i + \phi^s) = \frac{1}{\rho_1}\frac{\partial}{\partial R}\phi^{in} \quad (3.7)$$

on the surface of the sphere, i.e. $R = b$. The complex densities of air and the sphere are denoted by ρ and ρ_1, respectively. The condition for acoustic pressure continuity demands

$$a_{mn} j_n(kb) + b_{mn} h_n^{(1)}(kb) = c_{mn} j_n(k_1 b)\ . \quad (3.8)$$

The need for continuity of particle velocity at the surface of the sphere gives

$$a_{mn} j'_n(kb) + b_{mn} h'^{(1)}_n(kb) = \frac{\rho}{\rho_1}\frac{k_1}{k} c_{mn} j'_n(k_1 b). \tag{3.9}$$

After some mathematical manipulations, we can express b_{mn} and c_{mn} in terms of a_{mn}, as follows:

$$b_{mn} = -\frac{j'_n(kb) - \zeta\eta \dfrac{j'_n(k_1 b)}{j_n(k_1 b)} j_n(kb)}{h^{(1)\prime}_n(kb) - \zeta\eta \dfrac{j'_n(k_1 b)}{j_n(k_1 b)} h^{(1)}_n(kb)} a_{mn} \tag{3.10}$$

and $$c_{mn} = \frac{-ia_{mn}}{(kb)^2[h^{(1)\prime}_n(kb) j_n(k_1 b) - \zeta\eta j'_n(k_1 b) h^{(1)}_n(kb)]}, \tag{3.11}$$

where ζ is the density ratio and η is the index of refraction of the spherical surface. These parameters are given by

$$\zeta = \frac{\rho}{\rho_1} \quad \text{and} \quad \eta = \frac{k_1}{k} = \frac{c}{c_1}, \tag{3.12}$$

where c and c_1 are the velocity of sound in air and inside the sphere, respectively. The primes in the spherical Bessel functions of Eqs. (3.10) and (3.11) denote the derivatives with respect to their arguments. It is now convenient to introduce a term called effective acoustic admittance β_e, which is related to the specific normalized acoustic admittance β_s of the sphere. They are determined by

$$\beta_s = \zeta\eta, \tag{3.13}$$

and $$\beta_e = \beta_s \frac{j'_n(k_1 b)}{j_n(k_1 b)}. \tag{3.14}$$

3.2.2 Diffraction by a locally reacting sphere

Suppose a sphere is made of a material such that the sound speed in the sphere is much smaller than the sound speed in air, the argument $k_1 b$ will be very large and the ratio $j_n'(k_1 b)/j_n(k_1 b)$ can be approximated by $-i$. The approximation can be shown by knowing that

$$\frac{j_n'(Z)}{j_n(Z)}=\frac{j_{n-1}(Z)-j_{n+1}(Z)}{2j_n(Z)}, \tag{3.15}$$

and by applying the asymptotic expansion to the spherical Bessel function $j_n(Z)$ to get

$$\begin{aligned}\frac{j_n'(Z)}{j_n(Z)} &\approx \frac{\cos(Z-\frac{n-1}{2}\pi-\frac{\pi}{4})-\cos(Z-\frac{n+1}{2}\pi-\frac{\pi}{4})}{2\cos(Z-\frac{n}{2}\pi-\frac{\pi}{4})} \\ &=\tan[\frac{n\pi}{2}+(\frac{\pi}{4}-Z)]\end{aligned} \tag{3.16}$$

After using the addition formula of a tangent function, Eq. (3.16) can now be expressed as

$$\frac{j_n'(Z)}{j_n(Z)}\approx\frac{1-\tan Z}{1+\tan Z}, \text{ for n is an even integer }, \tag{3.17}$$

or

$$\frac{j_n'(Z)}{j_n(Z)}\approx-\frac{1+\tan Z}{1-\tan Z}, \text{for n is an odd integer}. \tag{3.18}$$

By invoking the tangent function in terms of real and imaginary parts, and by taking the limiting values of hyperbolic functions, we can show that the tangent function $\tan Z$ is equal to i and the approximation of $j_n'(k_1 b)/j_n(k_1 b)\approx -i$ is now evident. With such an approximation, the scattering coefficients can be reduced:

$$b_{mn}=-\frac{j_n'(kb)+i\beta_s j_n(kb)}{h_n^{(1)}{}'(kb)+i\beta_s h_n^{(1)}(kb)}a_{mn}. \tag{3.19}$$

This type of boundary is called a locally reacting boundary because the sound waves at any angle of incidence will be strongly refracted along the radius and thus travel normally to the spherical surface. Indeed, if we apply an impedance boundary condition at the surface of the sphere,

$$\frac{\partial\phi}{\partial R}+ik\beta_s\phi=0 \tag{3.20}$$

at $R = b$, then we can deduce the same scattering coefficient as shown in Eq. (3.19) above. This implies that a local reaction model would be a good approximation for the extended reaction model when the propagation constant of the porous materials is sufficiently large. We shall elaborate on this argument in the following paragraphs by providing some numerical examples. It is worth pointing out that in the extreme case, when β_s approaches zero, the scattering coefficient b_{mn} of Eq. (3.19) will be reduced to

$$b_{mn}=-\frac{j_n'(kb)}{h_n^{(1)\prime}(kb)}a_{mn}, \tag{3.21}$$

which corresponds to the scattering coefficients of a hard sphere insonified by a monopole point source, see Eq. (2.9).

3.2.3 Numerical validation of the approximation

The validity of computing sound fields by approximating a sphere of an extended reaction boundary as a locally reacting one when the propagation constant of the sphere is large can be assessed numerically by employing a single-parameter model [28]. The model, which is also known as the Delaney and Bazley model, describes the propagation constant and normalized surface impedance of fibrous porous materials as follows:

$$\frac{k_1}{k}=1+0.0858\left(\frac{f}{\sigma_e}\right)^{-0.7}+i0.175\left(\frac{f}{\sigma_e}\right)^{-0.59}, \tag{3.22}$$

$$Z_s = \frac{\rho_1 c_1}{\rho c} = 1 + 0.0511(\frac{f}{\sigma_e})^{-0.75} + i0.0768(\frac{f}{\sigma_e})^{-0.73} , \quad (3.23)$$

where f is the sound wave frequency and σ_e is the effective flow resistivity which has a unit of Pa s m^{-2}. It is chosen because of its simplicity as only a single parameter is needed to compute the relevant parameters for either a locally reacting boundary or an extended reaction one. We note that there are other more sophisticated models involving two or more parameters, but Delaney and Bazley model is sufficient in this section. With the numerical simulations, we can estimate the lower limit of the effective flow resistivity at which an extended reaction model can be adequately approximated by a locally reacting model.

Figure 3.1 shows the numerical comparisons of the sound diffracted by a sphere with a radius of 0.1 m in the absence of other reflecting surfaces. In the plots, the dotted lines represent the predicted sound fields in the vicinity of an extended reaction sphere and the solid lines are the corresponding predictions for a locally reacting sphere. In Figs. 3.1 (d) and (h), we also show the respective plots for an acoustically hard sphere of the same radius. In these plots, the sound fields are determined by using Eq. (3.5) with the scattering coefficient determined either by Eq. (3.10) or Eq. (3.19) for an extended reaction material or locally reacting material, respectively. For a consistent presentation, the relative sound pressure level is used throughout the current study. It is defined as the ratio of the total sound field relative to the reference free-field level measured at 1 m from the source. Two representative receiver locations are chosen in the plots: one located in the illuminated zone with R = 0.15 m, θ = 90°, ϕ = 30°, [see Figs. 3.1 (a) – (d)] and the other located in the shadow zone with R = 0.15 m, θ = 90°, ϕ = 150° [see Figs. 3.1 (e) – (h)]. Different values of the effective flow resistivity σ_e of 5, 25, 50, and 100 kPa s m^{-2} are selected in our numerical simulations in order to estimate an approximate lower limit of the effective flow resistivity at which an extended reaction model can be approximated by a local reaction model. For the material used with $\sigma_e \geq 50$ kPa s m^{-2}, it is found that the predicted sound fields from both types of surfaces are in close agreement with each other (see Fig. 3.1). These comparisons suggest that a locally reacting model is an adequate approximation if the effective flow resistivity of the absorbing sphere is greater than 50 kPa s m^{-2}.

3.3 Sound diffraction by an impedance sphere above an outdoor ground

It has been discussed in Sec. 2.3 that the sound wave propagation mechanisms, and hence the sound field above an outdoor ground, are inevitably affected by the acoustical properties of the ground surface, principally the acoustic impedance of the ground. The acoustical characteristics of the ground determine the phase and amplitude of reflected waves, which interfere with direct waves to produce an intricate sound field. The current scattering problem can be tackled by following the approach presented in Sec. 2.3. The geometrical configuration of the scattering problem is shown in Fig. 2.2.

3.3.1 Diffraction above a hard ground

Following the same argument as discussed in Sec. 2.3.1, the total sound field due to an impedance sphere irradiated by a point source above a hard ground can be expressed in a real spherical coordinate system as

$$\begin{aligned}\phi^T &= \sum_{n=0}^{\infty}\sum_{m=0}^{n} a_{mn} h_n^{(1)}(kR_o) j_n(kR) P_n^m(\cos\theta) P_n^m(\cos\theta_o)\cos m(\varphi-\varphi_o)\\ &+\sum_{n=0}^{\infty}\sum_{m=0}^{n} a_{mn} h_n^{(1)}(kR_o^{'}) j_n(kR) P_n^m(\cos\theta) P_n^m(\cos\theta_1)\cos m(\varphi-\varphi_o)\\ &+\sum_{n=0}^{\infty}\sum_{m=0}^{n} b_{mn} h_n^{(1)}(kR_o) h_n^{(1)}(kR) P_n^m(\cos\theta) P_n^m(\cos\theta_o)\cos m(\varphi-\varphi_o)\ ,\\ &+\sum_{q=0}^{\infty}\sum_{m=0}^{q} (-1)^{m+q} b_{mq} h_q^{(1)}(kR_o) P_q^m(\cos\theta_o)\cdot\\ &\quad\sum_{n=m}^{\infty} A_{mn}^{mq}(kd) j_n(kR) P_n^m(\cos\theta)\cos m(\varphi-\varphi_o)\end{aligned} \tag{3.24}$$

where the translation coefficients $A_{mn}^{mq}(kd)$ is given by Eq. (2.14).

For an absorbing sphere with a locally reacting boundary, the unknown coefficients b_{mn} can be determined by the following equation,

$$\frac{\partial\phi^T}{\partial R} + ik\beta_s\phi^T = 0\ , \quad \text{at } R = b, \tag{3.25}$$

where β_s is the specific normalized acoustic impedance of the sphere as defined in Eq. (3.13). After equating the coefficients of $P_n^m(\cos\theta)\cos m(\varphi-\varphi_o)$ and some tedious manipulations, a set of infinite and coupled linear complex equations can be formed for solving b_{mn}. The set of complex equations can be written in the same form as Eq. (2.25):

$$\begin{aligned}&b_{mn} h_n^{(1)}(kR_o) P_n^m(\cos\theta_o) + T_n \sum_{q=0}^{\infty} (-1)^{m+q} b_{mq} h_q^{(1)}(kR_o) P_q^m(\cos\theta_o) A_{mn}^{mq}(kd)\\ &= -a_{mn} T_n [h_n^{(1)}(kR_o) P_n^m(\cos\theta_o) + h_n^{(1)}(kR_o^{'}) P_n^m(\cos\theta_1)]\end{aligned} \tag{3.26}$$

Following the same approach done in Sec. 2.3.1, Eq. (3.26) can conveniently be expressed in a more compact form by using matrix notations as

$$\mathbf{XB} = \mathbf{C}\ , \tag{3.27}$$

where the diagonal elements of **X** are

$$X_{nn} = h_n^{(1)}(kR_o)P_n^m(\cos\theta_o) + T_n(-1)^{m+n}h_n^{(1)}(kR_o)P_n^m(\cos\theta_o)A_{mn}^{mn}(kd)\,, \qquad (3.28)$$

the off-diagonal elements of **X** are

$$X_{nq} = T_n(-1)^{m+q}h_q^{(1)}(kR_o)P_q^m(\cos\theta_o)A_{mn}^{mq}(kd)\,, \qquad (3.29)$$

and the elements of the vector **C** are

$$C_n = -a_{mn}T_n[h_n^{(1)}(kR_o)P_n^m(\cos\theta_o) + h_n^{(1)}(kR_o')P_n^m(\cos\theta_1)]\,, \qquad (3.30)$$

with $$T_n = \frac{j_n'(kb) + i\beta_s j_n(kb)}{h_n^{(1)\prime}(kb) + i\beta_s h_n^{(1)}(kb)}\,. \qquad (3.31)$$

The system of complex equations in Eq. (3.26) can be truncated to an order of N depending on the degree of accuracy required. The order N is the maximum number of terms required in the summation series. Thus, the matrix **X** is a $(N+1-m)\times(N+1-m)$ complex matrix, and **B** and **C** are complex vectors of dimension $(N+1-m)$ for each m where m ranges from 0 to N.

For an absorbing sphere of an extended reaction boundary, it is requisite that the following conditions on the sphere interface be satisfied

$$\phi^T = \phi^{in}\,, \qquad (3.32)$$

$$\frac{\partial\phi^T}{\partial R} = \zeta\frac{\partial\phi^{in}}{\partial R}\,. \qquad (3.33)$$

After equating the coefficients of $P_n^m(\cos\theta)\cos m(\varphi-\varphi_0)$ for the above equations, we have

$$\begin{aligned}
&a_{mn}j_n(kb)[h_n^{(1)}(kR_o)P_n^m(\cos\theta_o) + h_n^{(1)}(kR_o')P_n^m(\cos\theta_1)] \\
&+ b_{mn}h_n^{(1)}(kR_o)h_n^{(1)}(kb)P_n^m(\cos\theta_o) \\
&+ \sum_{q=0}^{\infty}(-1)^{m+q}b_{mq}h_q^{(1)}(kR_o)j_n(kb)P_q^m(\cos\theta_o)A_{mn}^{mq}(kd) \\
&= c_{mn}h_n^{(1)}(kR_o)j_n(k_1b)P_n^m(\cos\theta_o)
\end{aligned} \qquad (3.34)$$

to satisfy the condition of acoustic pressure continuity and

$$
\begin{aligned}
& a_{mn} j_n'(kb)[h_n^{(1)}(kR_o)P_n^m(\cos\theta_o) + h_n^{(1)}(kR_o')P_n^m(\cos\theta_1)] \\
& + b_{mn} h_n^{(1)}(kR_o) h_n^{(1)\prime}(kb) P_n^m(\cos\theta_o) \\
& + \sum_{q=0}^{\infty} (-1)^{m+q} b_{mq} h_q^{(1)}(kR_o) j_n'(kb) P_q^m(\cos\theta_o) A_{mn}^{mq}(kd) \\
& = \beta_s c_{mn} h_n^{(1)}(kR_o) j_n'(k_1 b) P_n^m(\cos\theta_o)
\end{aligned}
\tag{3.35}
$$

to assure the continuity of particle velocity at the surface of the sphere. A set of infinite and coupled linear complex equations in the same form as Eq. (3.26) can then be formed for solving b_{mn} after equating Eqs. (3.34) and (3.35). The equations can also be conveniently put in matrix notations in the forms of Eqs. (3.27) – (3.31). However, in this case T_n is given by

$$
T_n = \frac{j_n'(kb) - \beta_e j_n(kb)}{h_n^{(1)\prime}(kb) - \beta_e h_n^{(1)}(kb)}
\tag{3.36}
$$

where β_e is the effective acoustic admittance as defined in Eq. (3.14).

Adhering to the arguments in Sec. 2.3.1 that when $kd >> 1$, we can make the following approximation. The off-diagonal elements X_{nq} of Eq. (3.29) are negligible compared to the diagonal element X_{nn} in the matrix X in Eq. (3.28). As a result, Eq. (3.26) can be decoupled, leading to a direct solution for scattering coefficient b_{mn}, as follows:

$$
b_{mn} = \frac{C_n}{X_{nn}} = \frac{-a_{mn} T_n [h_n^{(1)}(kR_o)P_n^m(\cos\theta_o) + h_n^{(1)}(kR_o')P_n^m(\cos\theta_1)]}{h_n^{(1)}(kR_o)P_n^m(\cos\theta_o) + T_n(-1)^{m+n} h_n^{(1)}(kR_o)P_n^m(\cos\theta_o)A_{mn}^{mn}(kd)} .
\tag{3.37}
$$

When the sphere is far away from the hard ground surface, the separation distance d and the distance R_o' from the center of the real sphere to the image source will be very large such that both the spherical Hankel function $h_n^{(1)}(kR_o')$ and translation coefficient $A_{mn}^{mn}(kd)$ tends to zero. Thus, Eq. (3.24) can be reduced to Eq. (3.5) and

Eq. (3.37) can be simplified to either Eq. (3.10) or Eq. (3.19) depending on the boundary condition of the absorbing sphere. These equations are the known expressions for an absorbing sphere in an unbounded medium.

3.3.2 Diffraction above an impedance ground

The total sound field due to an impedance sphere irradiated by a point source above an impedance ground, which is composed of four terms, can be expressed exactly in similar form as Eq. (3.24) except for the addition of Q_1 and Q_2 as multipliers for the second and fourth terms respectively. The reflection coefficients Q_1 and Q_2 can be determined in accordance to Sec. 2.3.2. We can now get another set of coupled linear complex equations for solving the scattering coefficients b_{mn} which are valid for an absorbing sphere of either a locally reacting boundary or an extended reaction boundary,

$$\begin{aligned} &b_{mn}h_n^{(1)}(kR_o)P_n^m(\cos\theta_o)+Q_2T_n\sum_{q=0}^{\infty}(-1)^{m+q}b_{mq}h_q^{(1)}(kR_o)P_q^m(\cos\theta_o)A_{mn}^{mq}(kd) \\ &=-a_{mn}T_n[h_n^{(1)}(kR_o)P_n^m(\cos\theta_o)+Q_1h_n^{(1)}(kR_o^{'})P_n^m(\cos\theta_1)] \end{aligned} . \quad (3.38)$$

The complex equations can be expediently put in a matrix form similar to Eq. (3.27). The diagonal elements of **X** in this case are

$$X_{nn}=h_n^{(1)}(kR_o)P_n^m(\cos\theta_o)+Q_2T_n(-1)^{m+n}h_n^{(1)}(kR_o)P_n^m(\cos\theta_o)A_{mn}^{mn}(kd)\ , \quad (3.39)$$

the off-diagonal elements of **X** are

$$X_{nq}=Q_2T_n(-1)^{m+q}h_q^{(1)}(kR_o)P_q^m(\cos\theta_o)A_{mn}^{mq}(kd), \quad (3.40)$$

and the elements of the vector **C** are

$$C_n=-a_{mn}T_n[h_n^{(1)}(kR_o)P_n^m(\cos\theta_o)+Q_1h_n^{(1)}(kR_o^{'})P_n^m(\cos\theta_1)], \quad (3.41)$$

where T_n is determined either by Eq. (3.31) for an absorbing sphere with a locally reacting boundary or by Eq. (3.36) for an extended reaction boundary. In a similar fashion as shown in the last section, the system of complex equations in Eq. (3.38) can be truncated to an order of N, that is the number of sums from n or $q = 0$ to N, depending on the degree of accuracy required. The complex matrix **X** has an order of $(N+1-m)\times(N+1-m)$ and the complex vectors **B** and **C** have dimensions $(N+1-m)$ for each m where m ranges from 0 to N.

Using the same arguments in the previous section, an approximation can be made. The off-diagonal elements X_{nq} of Eq. (3.40) are negligibly small compared with the diagonal element X_{nn} of Eq. (3.39) in the matrix X provided that $kd >> 1$. The linear complex equation Eq. (3.38) for b_{mn} can then be decoupled and the scattering coefficient can be solved directly as

$$b_{mn} = \frac{C_n}{X_{nn}} = \frac{-a_{mn}T_n[h_n^{(1)}(kR_o)P_n^m(\cos\theta_o) + Q_1 h_n^{(1)}(kR_o^{'})P_n^m(\cos\theta_1)]}{h_n^{(1)}(kR_o)P_n^m(\cos\theta_o) + Q_2 T_n(-1)^{m+n} h_n^{(1)}(kR_o)P_n^m(\cos\theta_o)A_{mn}^{mn}(kd)}. \quad (3.42)$$

Considering the limiting case when the sphere is very remote from the impedance ground, the contribution from the image source and image sphere to the total sound field are negligible such that Eq. (3.42) can be reduced to Eq. (3.10) or Eq. (3.19) respectively, depending on the boundary condition of the absorbing sphere. It is reassuring to start from a more general situation that leads to an expression for the scattering of sound by an absorbing sphere in an unbounded medium.

3.4 Experiments and numerical results

The indoor experiments conducted for the current study were done in the anechoic chamber with the same instrumentation as described in Sec. 2.4.

3.4.1 Characterization and acoustic measurement of a sphere in a free field

To confirm that the theoretical models introduced in Secs. 3.2 and 3.3 are competent for studying acoustic scattering by an absorbing sphere, a set of experimental measurements was carried out for comparison with the theoretical predictions. A foam sphere with a radius of 0.1 m and density of 18.4 kg/m^3, which was made of open-cell polyurethane, was used in the experiments of the current study. Beginning with the in-depth experimental validations, preliminary free field measurements were conducted to characterize the acoustical properties of the foam sphere. The sphere was suspended in an anechoic chamber by means of two small hooks bolted at the tips of the sphere and fixed in position using fine threads that were tightly fastened to two poles erected remotely from the sphere as shown in Fig. 3.2. A specifically designed device, calibrated with angles and radial dimensions, was used to measure the positions of both the source and receiver points.

The acoustic impedance of the foam sphere was determined by comparing the experimental data with the theoretical predictions at a given source/receiver configuration, cf. Eq. (3.5). Because the polyurethane foam used for the sphere is relatively dense, we assume that the acoustical impedance can be modeled as a locally reacting type. It is well established that a two-parameter model developed by Attenborough [4] is generally applicable to calculate the acoustic impedance of many locally reacting materials. The specific normalized admittance of the foam sphere is calculated by

$$\beta_s = \frac{1}{0.436(1+i)(\sigma_e/f)^{1/2} + 19.48 i\alpha_e/f}, \tag{3.43}$$

where f is the frequency, σ_e is the effective flow resistivity, and α_e is the effective rate of change of porosity with depth of the material. Knowing the parametric values of σ_e and α_e, we can calculate β_e and apply Eqs. (3.5), (3.10), and (3.19) to compute the corresponding sound field at a given geometrical configuration. By adjusting the parametric values of the Attenborough model, we can deduce a set of σ_e and α_e such that the predicted sound levels give a best fit curve with the experimental data.

The acoustic characterization of the polyurethane sphere was implemented for different source/receiver configurations. The best-fit parameters were found to be σ_e = 100 kPa s m^{-2} and α_e = 10 m^{-1} (see Fig. 3.3 for some typical characterization results). In the plots, we display the spectra of relative sound pressure levels with the source, S, located at R_o = 0.15 m, θ_o = 90°, ϕ_o = 30°, and the receiver, P, at the following six locations: (a) R = 0.15m, θ = 90°, ϕ = 30°; (b) R = 0.15 m, θ = 90°, ϕ = 60°; (c) R = 0.15 m, θ = 90°, ϕ = 90°; (d) R = 0.3 m, θ = 90°, ϕ = 120°; (e) R = 0.15 m, θ = 90°, ϕ = 150°; (f) R = 0.3 m, θ = 90°, ϕ = 180°. It is not surprising to see that the experimental results can generally be predicted by the theoretical calculations. As expected, the frequency spectra become rather flat as the subtended angle between the source and receiver increases. This is because the interference effect of the direct wave on the scattered sound at the field points becomes less effective when the subtended angle increases. In such a situation, the receiver is located in the shadow zone. With these enlightening results, we feel confident about extending the model for the prediction of acoustic diffraction by an absorbing sphere in the presence of a reflecting ground.

3.4.2 Diffraction by a locally reacting sphere above a hard ground

In this set of experiments, the foam sphere was suspended above a hard ground in the same way as described in the previous section. A vanished hardwood board of 0.02 m in thickness and with a transmission loss of about 23 dB(A) was used to simulate the hard ground. In Fig. 3.4, the spectra of relative sound-pressure levels were obtained with the source situated at $R_0 = 0.4$ m, $\theta_0 = 90°$, $\phi_0 = 0°$ and receivers at (a) $R = 0.15$ m, $\theta = 90°$, $\phi = 30°$; (b) $R = 0.15$ m, $\theta = 90°$, $\phi = 60°$; (c) $R = 0.25$ m, $\theta = 90°$, $\phi = 90°$; (d) $R = 0.25\ m$, $\theta = 90°$, $\phi = 120°$; (e) $R = 0.25$ m, $\theta = 90°$, $\phi = 150°$; (f) $R = 0.25$ m, $\theta = 90°$, $\phi = 180°$. In these figures, the experimental results are plotted in solid lines. The dashed lines represent the theoretical predictions derived from an exact solution method by solving Eq. (3.27), and the dotted lines represent the theoretical result obtained by an approximate method using Eq. (3.37). The predicted results from these two methods are very close to within the thickness of the curves shown in the figures. The predicted sound field (dash-dotted line) at each receiver position above a hard ground in the absence of the sphere is also given in the figures. They serve to show how the sphere perturbs the sound field above a hard plane. In the numerical analyses, we have used $N = 30$ [the number of sums for the summation series in Eq. (3.26)] throughout in order to obtain the numerical results calculated by using an exact solution method. We can see that the experimental results show close agreement with the predictions based on the analytical models discussed in Sec. 3.3. However, the computational time needed to obtain the same prediction result by using the approximation solution method is much faster than by using the exact solution method. We developed a MATLAB program for each model and used a desktop computer with CPU of 1.8 GHz to carry out the computations. The program takes 1 s for the approximate model compared with 60 s for the exact solution to obtain a predicted result at a source frequency of 1000 Hz. Understandably, the interference patterns of the spectra are more intricate in this case, as the reflected waves can interact with both the direct and scattered waves to create a more complicated sound field even when the measuring point is in the shadow zone.

3.4.3 Diffraction by a locally reacting sphere above an impedance ground

The impedance ground was simulated by laying a thick carpet on a hardwood board. The carpet used for the present experiments is actually the one used in Sec. 2.4.4 and the acoustical parameters of the carpet were $\sigma_e = 10$ kPa s m^{-2} and $\alpha_e = 80$ m^{-1}. The foam sphere was suspended above the impedance ground in the same way as described in the previous sections. Two sets of experiments were carried out in this case. In the first set of measurements, the center of the sphere was set at 0.176 m above the impedance ground; for the second set of experiments, at 0.26 m above the ground. In the first set of measurements (Fig. 3.5), the spectra of relative sound pressure levels were obtained with the source at $R_o = 0.35$m, $\theta_o = 90°$, $\phi_o = 0°$ and receivers at (a) $R = 0.15$ m, $\theta = 90°$, $\phi = 30°$; (b) $R = 0.15$ m, $\theta = 90°$, $\phi = 60°$; (c) $R = 0.15$ m, $\theta = 90°$, $\phi = 90°$; (d) $R = 0.30$ m, $\theta = 90°$, $\phi = 120°$; (e) $R = 0.30$ m, $\theta = 90°$, $\phi = 150°$; (f) $R = 0.30$ m, $\theta = 90°$, $\phi = 180°$. Figure 3.6 shows the results of the second set of measurements. The spectra of relative sound pressure levels were taken with the source at $R_o = 0.4$m, $\theta_o = 90°$, $\phi_o = 0°$ and receivers at (a) $R = 0.2$ m, $\theta = 90°$, $\phi = 30°$; (b) $R = 0.2$ m, $\theta = 90°$, $\phi = 60°$; (c) $R = 0.2$ m, $\theta = 90°$, $\phi = 90°$; (d) $R = 0.3$ m, $\theta = 90°$, $\phi = 120°$; (e) $R = 0.30$ m, $\theta = 90°$, $\phi = 150°$; (f) $R = 0.35$ m, $\theta = 90°$, $\phi = 180°$. In these figures, the experimental results are plotted in solid lines. The dashed lines represent the theoretical predictions derived from an exact solution method, and the dotted lines represent the theoretical results obtained by the approximation scheme. The computed results from both prediction methods agree to within the thickness of the lines shown in the figures. We also remark that the predicted sound field in the absence of the sphere above an impedance plane is also shown (dash-dotted lines) in Figs. 3.5 and 3.6. These predictions are shown for assessing the relative importance of the contribution from the ground reflected waves as compared with those scattered by the sphere.

The predictions made by the theoretical model developed in Sec. 3.3.2 agree reasonably well with the experimental results. Not surprisingly, the theoretical predictions are in accord with the patterns observed from experimental measurements in spite of the fact that the experimental results show a trend of noticeable differences in magnitude (the experimental results are always lower than predictions) at high frequency region. These discrepancies are probably due to experimental limitations, especially the production of a point source by a long tube. The point source at high frequency may not be omni-directional and the energy content of the source may not be sufficiently higher than the background noise level. Similar to the case of sound diffraction near a hard ground, the interference patterns of the spectra are more intricate compared to the sound diffraction by an absorbing sphere in a free field as the total sound field is made up of reflected waves, direct waves and scattered waves to give a more complicated acoustic environment.

3.5 Summary

The theoretical formulations of acoustic diffraction by an absorbing sphere of different boundary conditions insonified by a point source have been discussed. The acoustical properties of the sphere made of open-cell polyurethane foam have been characterized by indoor measurements and used *a posteriori* to validate the theoretical models. The theoretical analyses have been extended to the study of acoustic diffraction by an absorbing sphere of different boundary conditions above an acoustically hard and an impedance ground. Exact analytical solutions have been derived using the classical method of images and translational addition theorems for the spherical wave functions. The effect of the impedance surface on the ground-reflected sound fields can be incorporated into the exact analytical model through the use of the Weyl-van der Pol formula, which is an approximate analytical solution for the reflection of a spherical wave from a locally reacting plane. The analytical solutions developed in the presence of a hard or an impedance ground can be expressed in four terms: contributions from the source and the sphere, and contributions from the image source and the image sphere. An approximate method has been proposed to obtain the scattering coefficients for a sphere located not too close to the ground, which can substantially reduce the computational time of the total sound field calculation. Experimental results have been used to validate the theoretical predictions made by the analytical models and good agreement was observed. It has also been shown that the numerical results predicted by the approximate method agree to within the thickness of lines with the predictions made by the exact solution method. Not surprisingly, the numerical simulations and experimental results reveal that the sound fields become more intricate in the presence of a reflecting ground. The results of the current study can serve as a benchmark for solutions obtained by other numerical or asymptotic approaches.

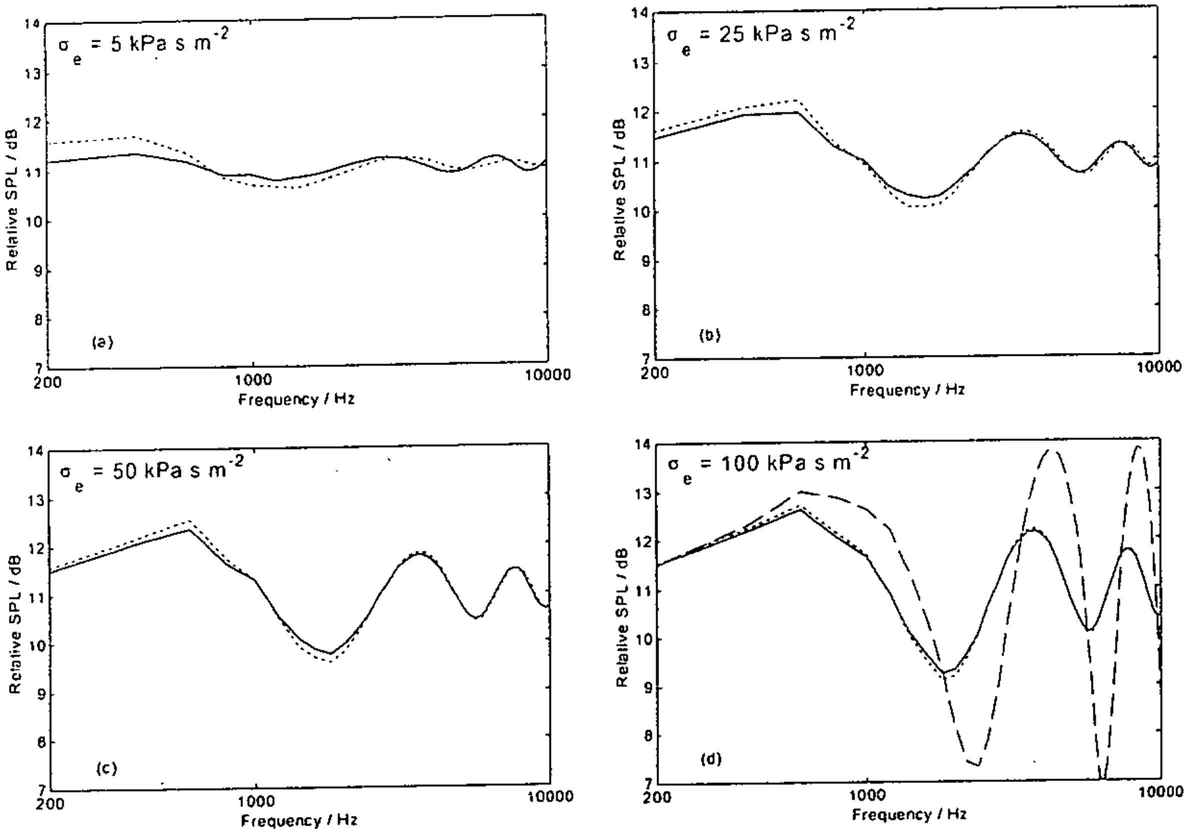

Figure 3.1 (a) – (d). Numerical comparisons for the acoustic diffraction by a sphere with a radius of 0.1 m using the Delaney and Bazley locally reacting model and an extended reaction model. Different values of effective flow resistivity σ_e are used for comparison. Solid line: locally reacting model. Dotted line: extended reaction model. Source: R_0 = 0.4 m, θ_0 = 90°, ϕ_0 = 0°. Receiver locations: (a) – (d), R = 0.15 m, θ = 90°, ϕ = 30°. The dashed line in (d) represents the relative SPL for an acoustically-hard sphere with σ_e = 30,000kPa s m^{-2}.

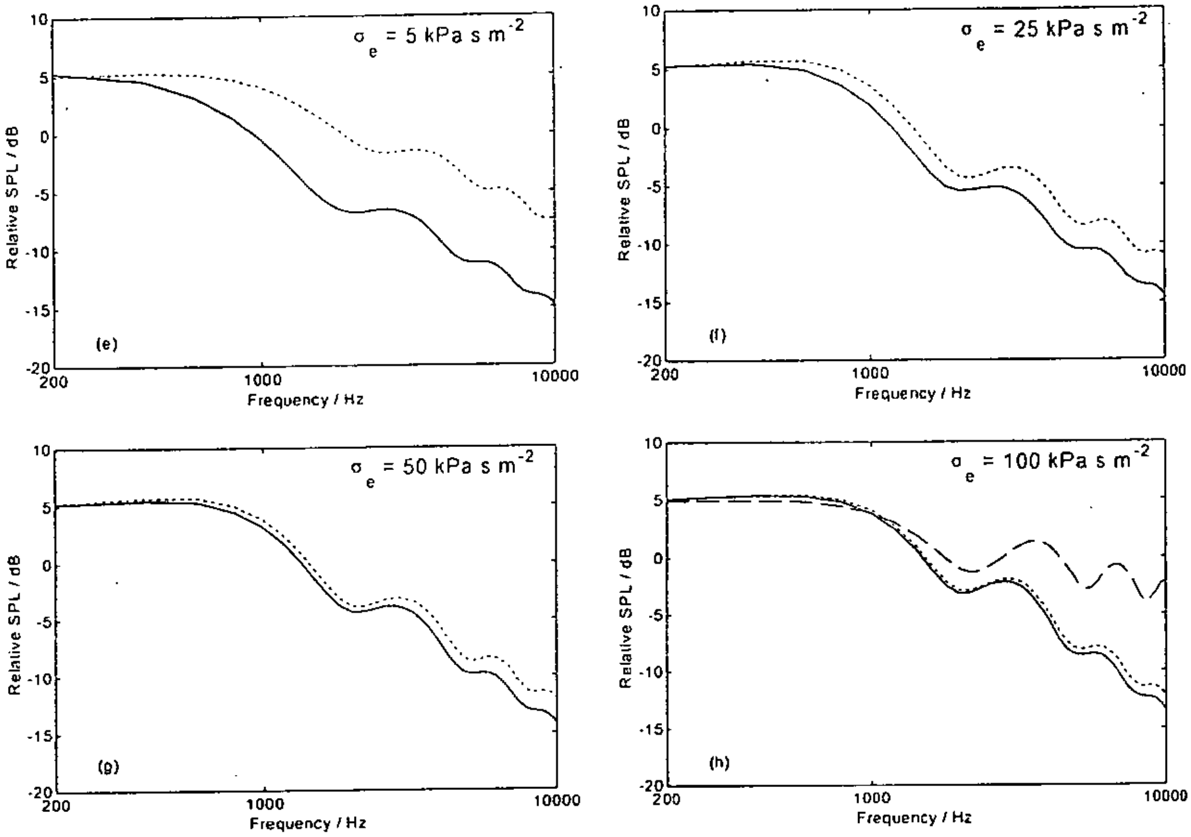

Figure 3.1 (e) – (h). Numerical comparisons for the acoustic diffraction by a sphere with a radius of 0.1 m using the Delaney and Bazley locally reacting model and an extended reaction model. Different values of effective flow resistivity σ_e are used for comparison. Solid line: locally reacting model. Dotted line: extended reaction model. Source: $R_0 = 0.4$ m, $\theta_0 = 90°$, $\phi_0 = 0°$. Receiver locations: (e) – (h), $R = 0.15$ m, $\theta = 90°$, $\phi = 150°$. The dashed line in (h) represents the relative SPL for an acoustically-hard sphere with $\sigma_e = 30{,}000$kPa s m^{-2}.

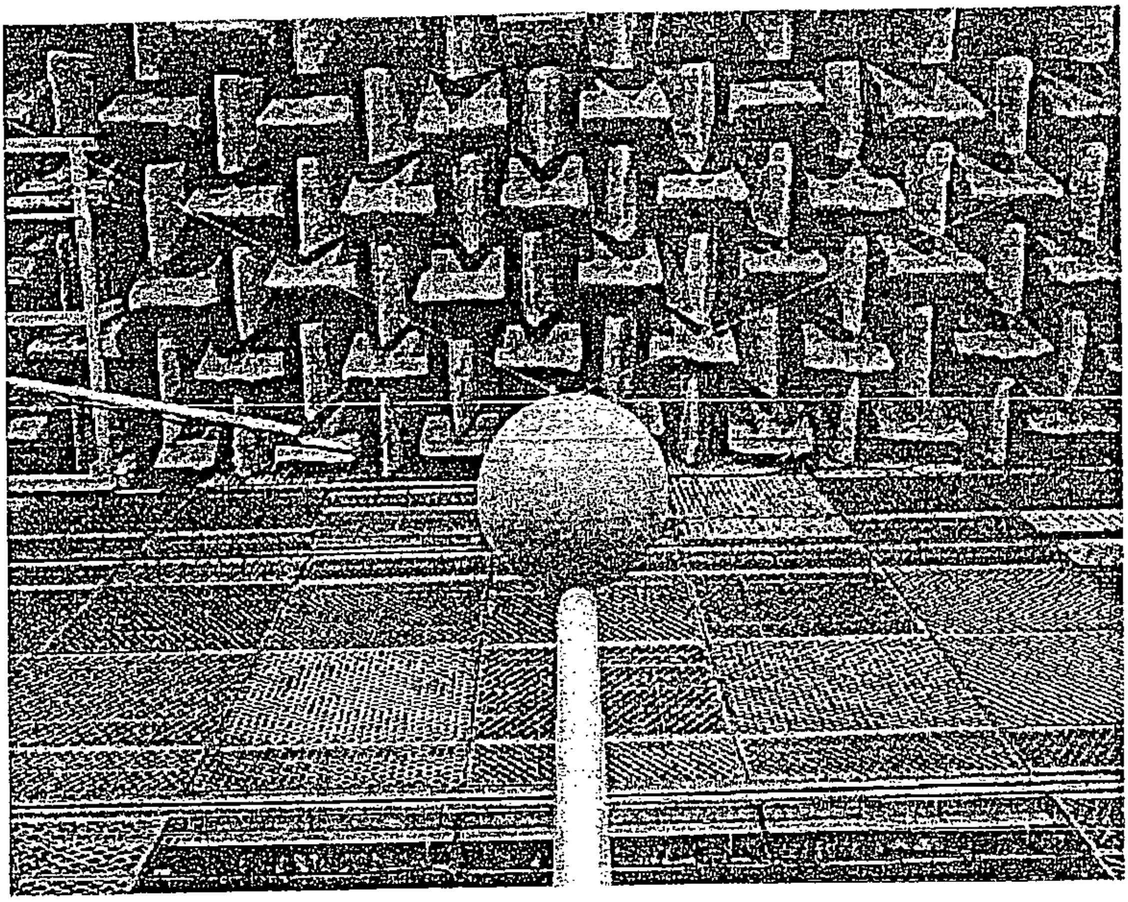

Figure 3.2. The experimental setup in an anechoic chamber for the measurement of sound diffraction by an absorbing sphere in a free field. The sphere is bolted with small hooks and hung in the anechoic chamber by suspending fine threads fixed in position by means of poles.

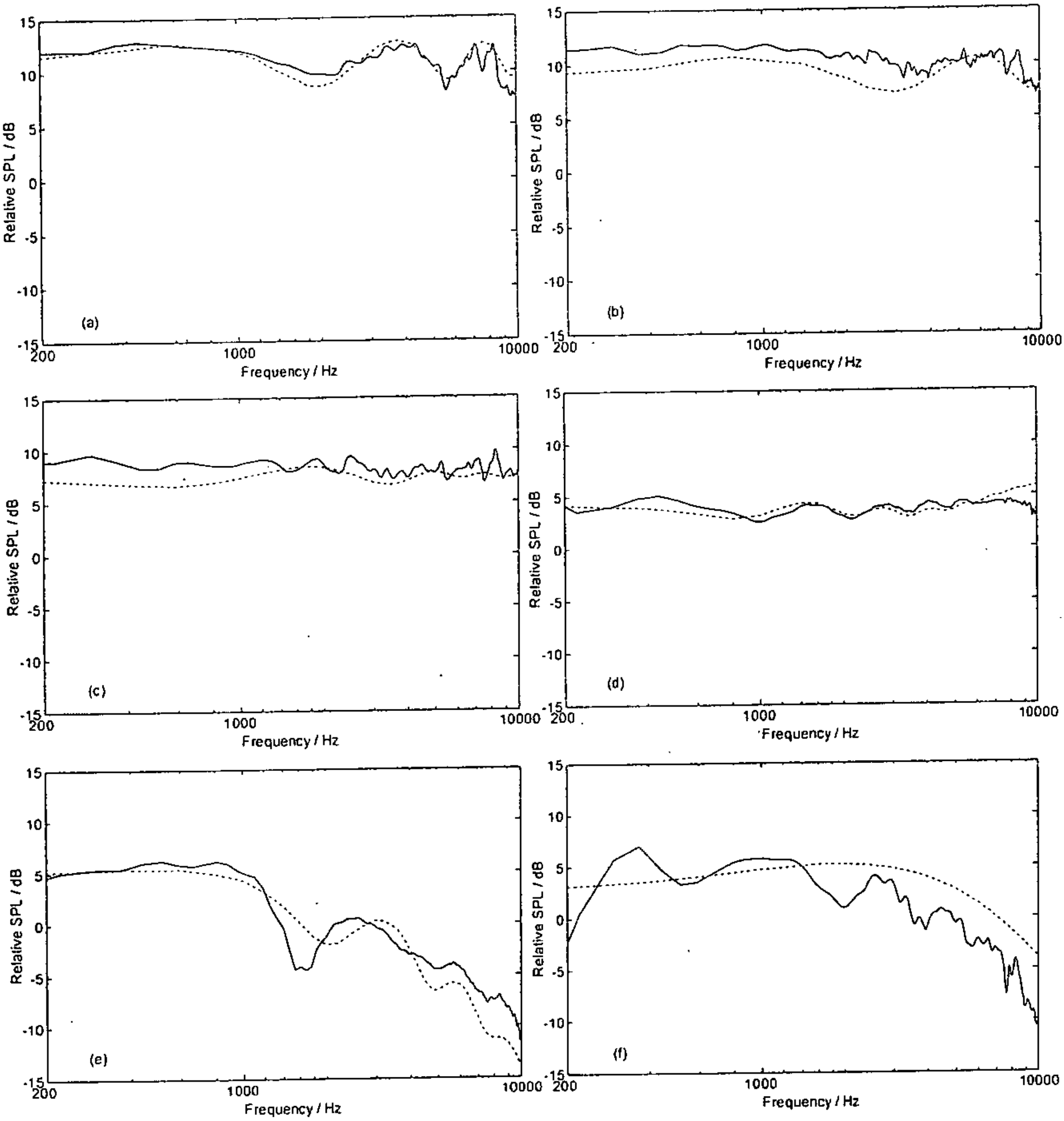

Figure 3.3. Experimental results and theoretical predictions for acoustic diffraction by a locally reacting sphere with a radius of 0.1m in a free space. Source: R_o=0.4m, θ_o=90°, ϕ_o=0°. Receiver: (a) R = 0.15 m, θ = 90°, ϕ = 30°; (b) R = 0.15 m, θ = 90°, ϕ = 60°; (c) R = 0.15 m, θ = 90°, ϕ = 90°; (d) R = 0.3 m, θ = 90°, ϕ = 120°; (e) R = 0.15 m, θ = 90°, ϕ = 150°; (f) R = 0.3 m, θ = 90°, ϕ = 180°. (Dotted line: the theoretical prediction using the two parameters model with the best-fit parameters are found to be σ_e = 100 kPa s m^{-2} and α_e = 10 m^{-1}; solid line: experimental result).

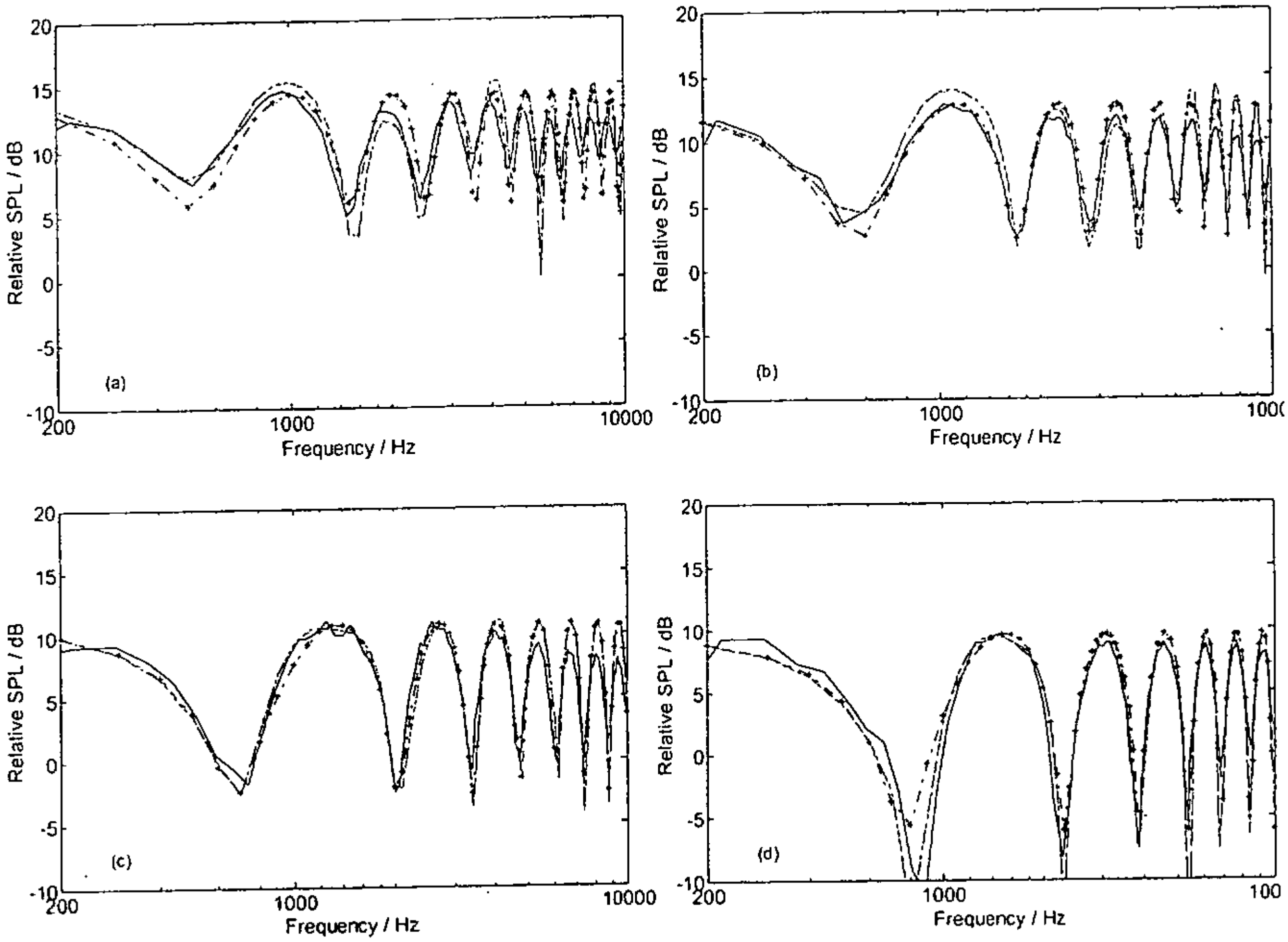

Figure 3.4 (a) – (d). Experimental results and theoretical predictions for acoustic diffraction by a locally reacting sphere with a radius of 0.1m above a hard ground. The center of the sphere is 0.275 m above the hard ground. Source: $R_0 = 0.4$ m, $\theta_0 = 90°$, $\phi_0 = 0°$. Receiver: (a) $R = 0.15$ m, $\theta = 90°$, $\phi = 30°$; (b) $R = 0.15$ m, $\theta = 90°$, $\phi = 60°$; (c) $R = 0.25$ m, $\theta = 90°$, $\phi = 90°$; (d) $R = 0.25$ m, $\theta = 90°$, $\phi = 120°$. (Dotted line: theoretical prediction – approximation; dashed line: theoretical prediction - exact solution; solid line: experimental result; dash-dotted line with mark: predicted sound field without presence of sphere).

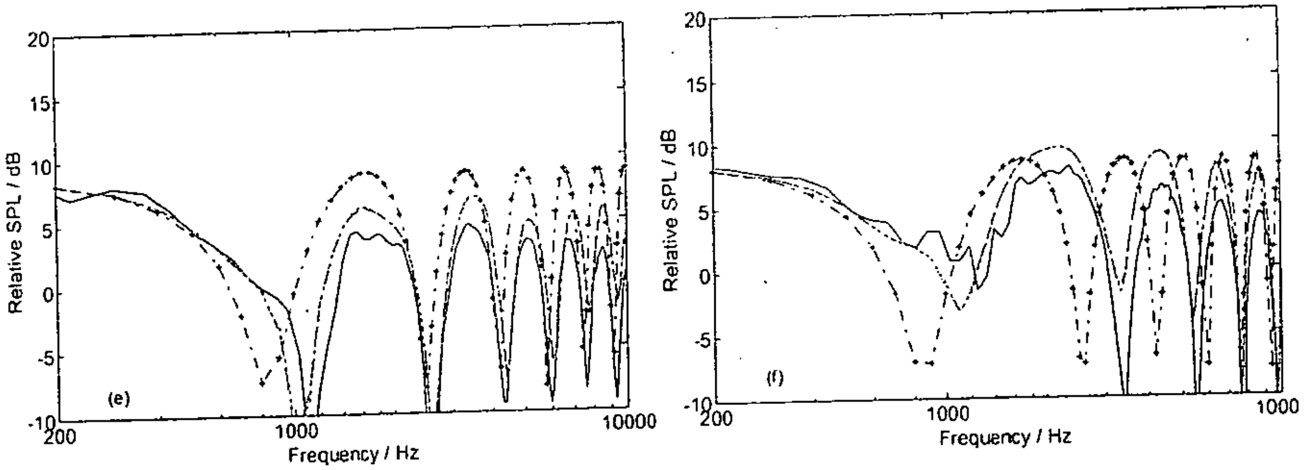

Figure 3.4 (e) – (f). Experimental results and theoretical predictions for acoustic diffraction by a locally reacting sphere with a radius of 0.1m above a hard ground. The center of the sphere is 0.275 m above the hard ground. Source: $R_0 = 0.4$ m, $\theta_0 = 90°$, $\phi_0 = 0°$. Receiver: (e) $R = 0.25$ m, $\theta = 90°$, $\phi = 150°$; (f) $R = 0.25$ m, $\theta = 90°$, $\phi = 180°$. (Dotted line: theoretical prediction – approximation; dashed line: theoretical prediction - exact solution; solid line: experimental result; dash-dotted line with mark: predicted sound field without presence of sphere).

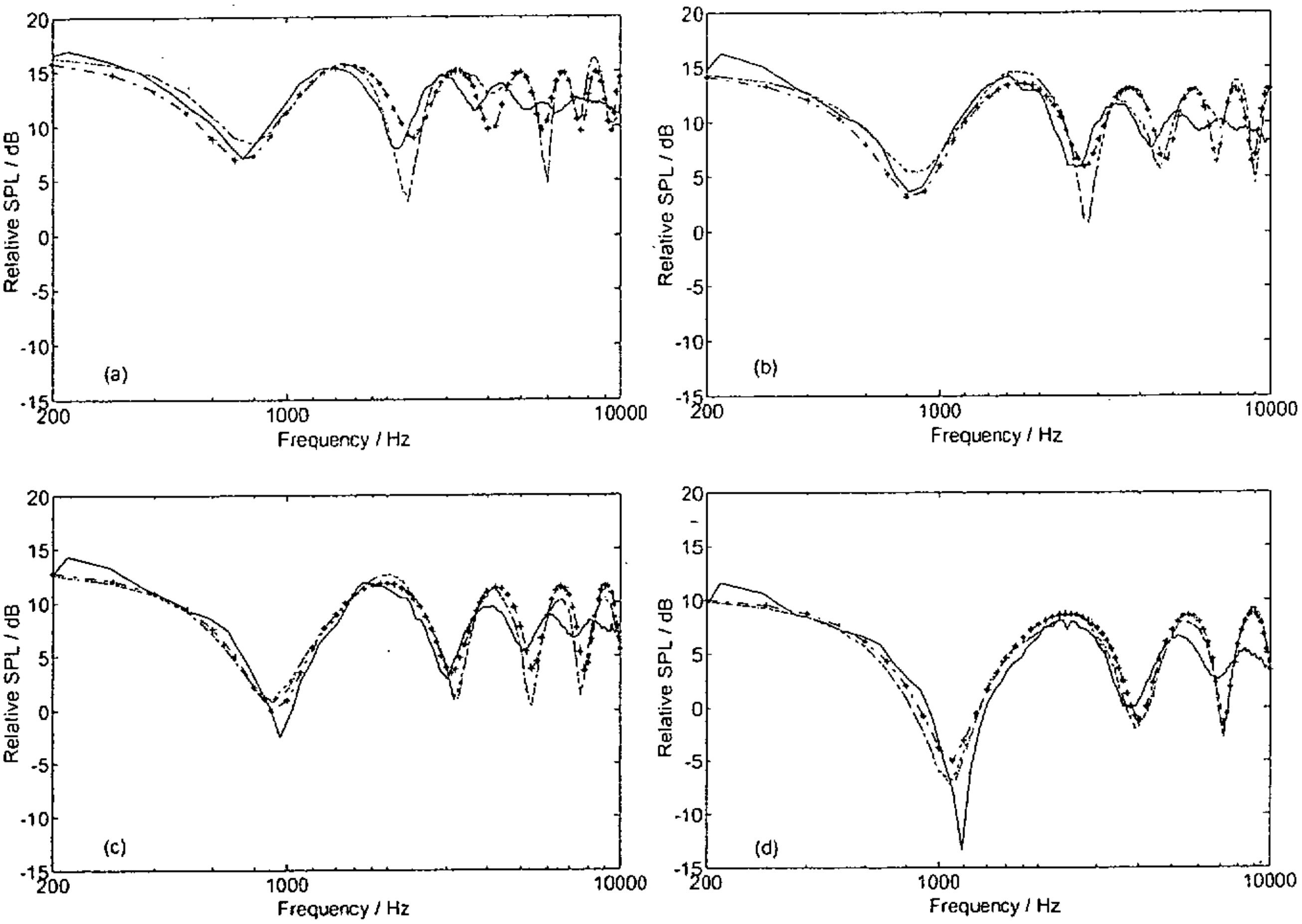

Figure 3.5 (a) – (d). Experimental results and theoretical predictions for acoustic diffraction by a locally reacting sphere with a radius of 0.1 m above an impedance ground. The center of the sphere is 0.176 m above the impedance ground. Source: R_o = 0.35 m, θ_o = 90°, ϕ_o = 0°. Receiver: (a) R = 0.15 m, θ = 90°, ϕ = 30°; (b) R = 0.15 m, θ = 90°, ϕ = 60°; (c) R = 0.15m, θ = 90°, ϕ = 90°; (d) R = 0.30 m, θ = 90°, ϕ = 120°. (Dotted line: theoretical prediction - approximation; dashed line: theoretical prediction - exact solution; solid line: experimental result; dash-dotted line with legend: predicted sound field without presence of sphere).

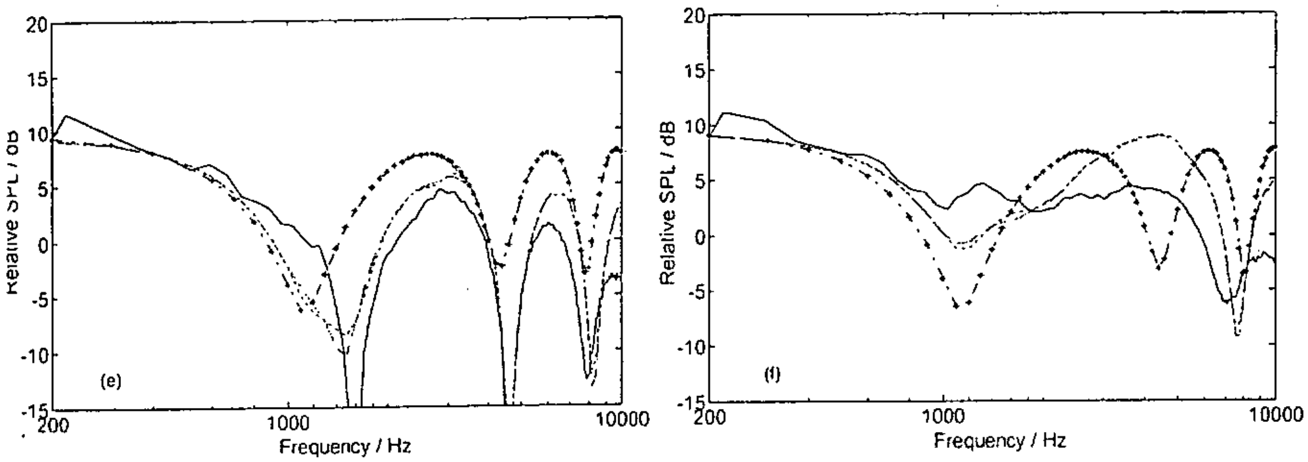

Figure 3.5 (e) – (f). Experimental results and theoretical predictions for acoustic diffraction by a locally reacting sphere with a radius of 0.1 m above an impedance ground. The center of the sphere is 0.176 m above the impedance ground. Source: R_o = 0.35 m, $\theta_o = 90°$, $\phi_o = 0°$. Receiver: (e) R = 0.30 m, $\theta = 90°$, $\phi = 150°$; (f) R =0.30 m, $\theta = 90°$, $\phi =180°$. (Dotted line: theoretical prediction - approximation; dashed line: theoretical prediction - exact solution; solid line: experimental result; dash-dotted line with legend: predicted sound field without presence of sphere).

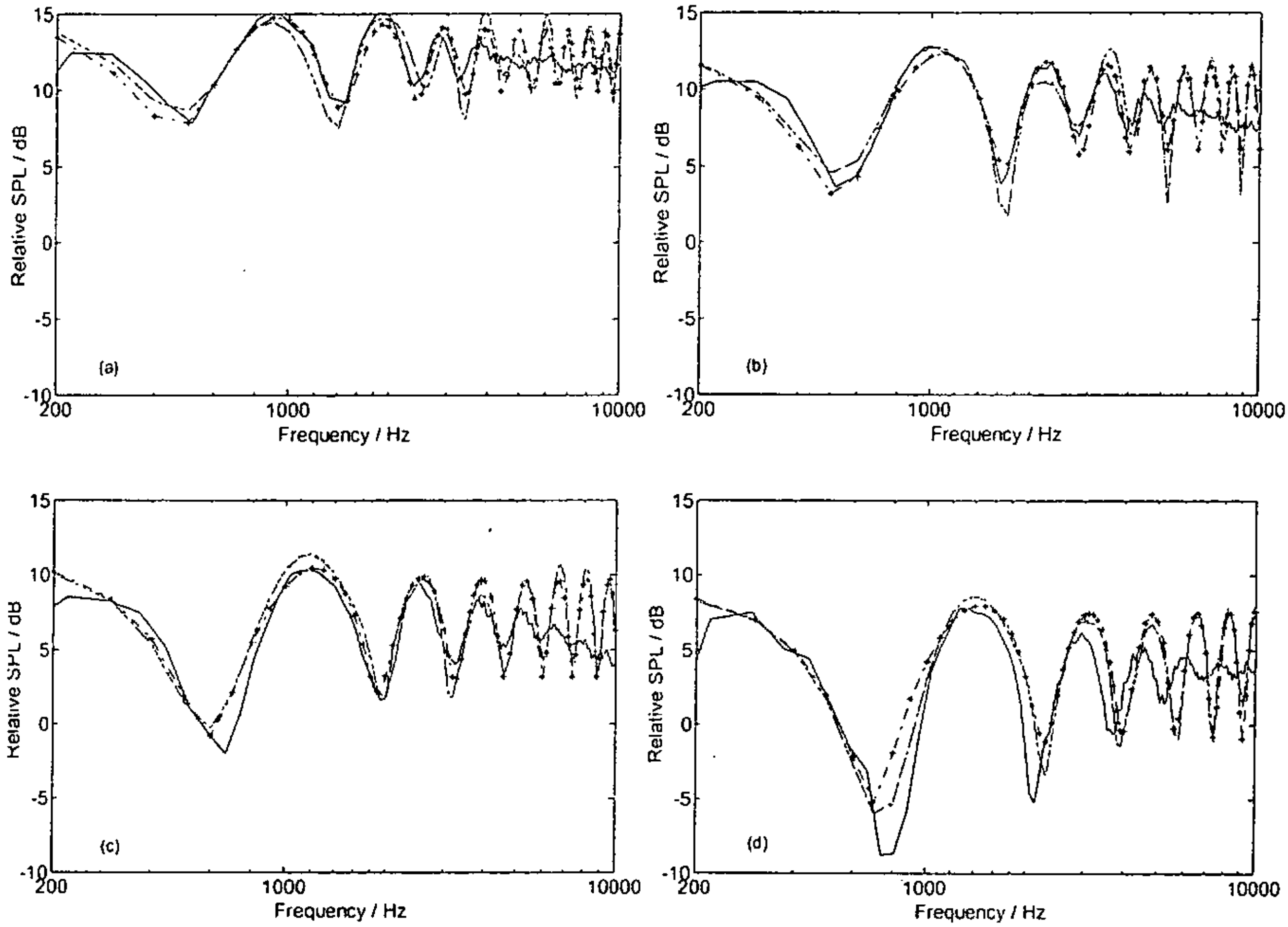

Figure 3.6 (a) – (d). Experimental results and theoretical predictions for acoustic diffraction by a locally reacting sphere with a radius of 0.1 m above an impedance ground. The center of the sphere is 0.26 m above the impedance ground. Source: R_o = 0.4 m, θ_o = 90°, ϕ_o = 0°. Receiver: (a) R = 0.2 m, θ = 90°, ϕ = 30°; (b) R = 0.2 m, θ = 90°, ϕ = 60°; (c) R = 0.2 m, θ = 90°, ϕ = 90°; (d) R = 0.3 m, θ = 90°, ϕ = 120°. (Dotted line: theoretical prediction - approximation; dashed line: theoretical prediction – exact solution; solid line: experimental result; dash-dotted line with legend: predicted sound field without presence of sphere).

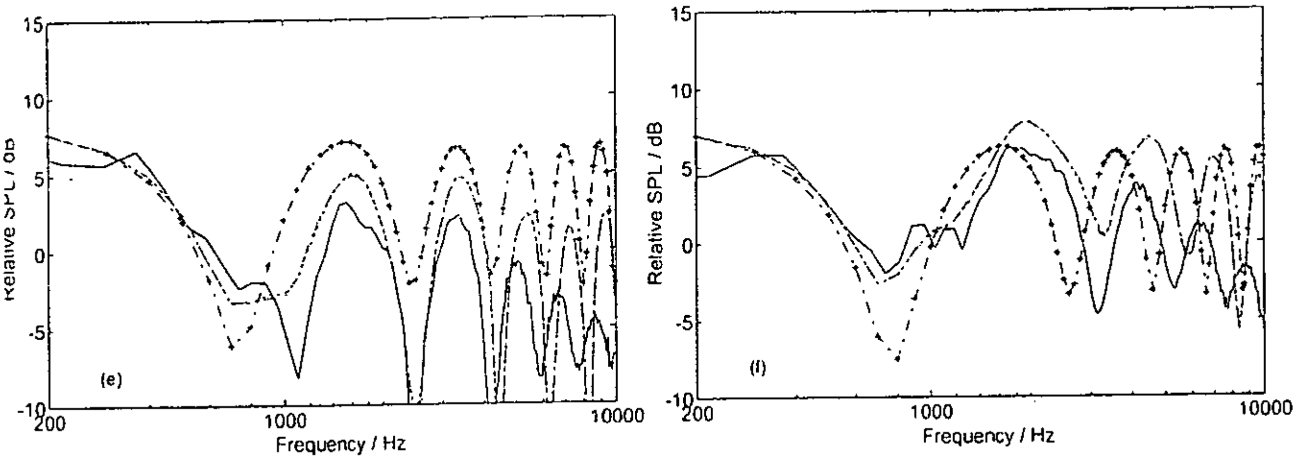

Figure 3.6 (e) – (f). Experimental results and theoretical predictions for acoustic diffraction by a locally reacting sphere with a radius of 0.1 m above an impedance ground. The center of the sphere is 0.26 m above the impedance ground. Source: $R_o = 0.4$ m, $\theta_o = 90°$, $\phi_o = 0°$. Receiver: (e) $R = 0.30$ m, $\theta = 90°$, $\phi = 150°$; (f) $R = 0.35$ m, $\theta = 90°$, $\phi = 180°$. (Dotted line: theoretical prediction - approximation; dashed line: theoretical prediction – exact solution; solid line: experimental result; dash-dotted line with legend: predicted sound field without presence of sphere).

Chapter 4

The Horn Effect above a Porous Road Pavement

4.1 Introduction

The mechanisms of the generation of rolling noise caused by the interaction between a tire and the surface of a road [45][57][71][87] have received considerable attention over the past few decades. The noises come from the vibrations of tires, the deflections from the surface of the tires and the resulting displacement of air in the gap between the tire and the road [45]. In this case, the propagation of noise is thus confined to a small area enveloped by the surface of the road and the tire belt, forming a hornlike geometry. This hornlike configuration leads to a substantial amplification of the sound that is radiated. Schaaf and Ronneberger [97] demonstrated this effect experimentally, and theoretically identified this so-called "horn effect" by a simple image source model. The phenomenon of the horn effect amplification was also confirmed experimentally by Iwao *et al.* [57].

Although there are various numerical methods by virtue of the boundary element method (BEM) [35][40] and analytical models based on asymptotic theories [69], modal decomposition of the sound pressure [2] and multipole synthesis [66] developed to account for the horn effect, they do not provide satisfactory predictions because of the intrinsic limitations. Moreover, in view of the increase in interest in using porous pavement [8][56][59], especially double-layer porous pavement [58][68] to reduce tire/road noise, it is thus desirable to offer a simplified theoretical model to allow highway designers to carry out a parametric study when selecting appropriate materials for porous road pavement. The purpose of the current study is to explore a simplified theoretical model to account for the amplification of noise due to the propagation of sound in the tire/road gap over a porous road pavement. The theoretical model is centered on the analytical formulation to study the sound diffracted by a sphere above an impedance ground as presented in Chapter 2 and 3. In Sec. 4.2, we explain and justify the choice of our analytical model, as there are many other numerical models [40][66][69] devoted to the study of the acoustic interaction between tires and road. Section 4.3 gives numerical predictions based on our analytical formulation. These numerical results are compared with the published experimental data and theoretical predictions based on other computationally intensive schemes. A parametric study of the influence of porous ground on the horn effect is discussed in Sec. 4.4. Finally, in Sec. 4.5, we offer some concluding remarks.

4.2 Theoretical formulation

4.2.1 Justification for the use of a simple theoretical model

The dependence of the horn effect on different geometrical parameters such as the radius of the curvature of the tire shoulders, the load, the width of the tire and the geometrical configurations of the source/receiver have been investigated through experiments, the formulation of exact boundary element (BEM) [40] and other asymptotic theories [69]. The experimental measurements showed that the effect of the horn amplification accounted for about 10 - 20 dB, with the maximum amplification occurring at the plane of the tire. In view of the fact that the amplification of sound reaches a maximum at the plane of the tire, as shown by the published experimental results [40][66][69], we hypothesize that the horn effect induced by the semi-closed space formed between the curved surface of a sphere and the ground surface is similar to that created by the hornlike geometry formed between the tire belt and the surface of the road. Although this hypothesis may at first appear questionable, we will validate it through detailed comparisons of the numerical predictions using the published experimental data described in Sec. 4.3 below.

4.2.2 Review of sound diffracted by a sphere above an extended reaction ground

When an object is subject to radiation from a point source located at $\mathbf{x}_s$, the total sound field at point $\mathbf{x}$ is governed by the Helmholtz equation, expressed in terms of a scalar velocity potential, ϕ, as follows:

$$\nabla^2\phi + k_o^2\phi = -\delta(\mathbf{x} - \mathbf{x}_s), \tag{4.1}$$

For a sphere resting on a ground surface, the total sound field at the receiver is contributed by the direct waves, by scattered waves from the sphere, and by waves disseminating from the image source and the image sphere, as shown in Fig. 4.1. The origin is taken as the center of the sphere. In this situation, the acoustical properties of the porous medium are crucial in determining the sound field produced due to the combination of direct and boundary-reflected sound waves. In Chapter 2 and 3, we developed a numerical scheme to compute the diffraction of sound by a sphere located above an impedance ground. The scheme was based on the expansion of the wave field in terms of a series of associated Legendre functions. Here, we extend the solution to model the corresponding sound field above an extended reaction ground. In particular, the road pavement is modeled as either a single or double porous layer above a hard-backed layer. In fact, Bérengier *et al.* [8] used a hard-back layer model to study the acoustical characteristics and propagation effects of porous road pavements.

The effect of a single or double porous layer above a hard-backed layer on the radiation from a point source can be modeled by an approximate analytical solution developed by Li *et al.* [73] for the reflection of a spherical wave. By introducing an effective admittance, β_g, the sound field contributed from the point source above a hard-backed layer surface can be approximated by

$$\phi_T^i = \frac{e^{ik_oR_1}}{4\pi R_1} + Q_1 \frac{e^{ik_oR_2}}{4\pi R_2}, \tag{4.2}$$

where

$$Q_1 = V + (1-V)F(w), \tag{4.3}$$

$$V = \frac{\cos\alpha_1 - \beta_g}{\cos\alpha_1 + \beta_g}, \tag{4.4}$$

$$F(w) = 1 + i\sqrt{\pi}we^{-w^2}\operatorname{erfc}(-iw), \tag{4.5}$$

$$w = +\sqrt{\tfrac{1}{2}ik_oR_2}(\cos\alpha_1 + \beta_g) \ . \tag{4.6}$$

For a single porous layer above a hard-backed layer, the effective admittance is

$$\beta_g = -im_1\sqrt{n_1{}^2 - \sin^2\alpha_1}\,\tan(k_ol_1\sqrt{n_1{}^2 - \sin^2\alpha_1}) \ , \tag{4.7}$$

and for a double layer with a hard backing, the effective admittance can be determined according to

$$\beta_g = -im_1\sqrt{n_1{}^2 - \sin^2\alpha_1}\left\{\frac{\tan(k_ol_1\sqrt{n_1{}^2 - \sin^2\alpha_1}) + \bar{g}_1\tan(k_ol_2\sqrt{n_2{}^2 - \sin^2\alpha_1})}{1 - \bar{g}_1\tan(k_ol_1\sqrt{n_1{}^2 - \sin^2\alpha_1})\tan(k_ol_2\sqrt{n_2{}^2 - \sin^2\alpha_1})}\right\}, \tag{4.8}$$

where

$$\bar{g}_1 = \frac{m_2\sqrt{n_2^2 - \sin^2\alpha_1}}{m_1\sqrt{n_1^2 - \sin^2\alpha_1}}, \tag{4.9}$$

$$n_j = k_j / k_o \qquad \text{and} \qquad m_j = \rho_o / \rho_j \qquad \text{with } j = 1,2 . \tag{4.10}$$

Here, ρ_o is the density of air, g_1 is a dimensionless ratio characterizing the change of media properties from the first layer to the second, R_2 is the distance between the image source and the field point, α_l is the angle of incidence of the reflected wave, and l_l and l_2 are the thickness of the first and second layers, respectively. According to the phenomenological model for porous pavement proposed by Bérengier *et al.* [8], the complex wave number and characteristic impedance can be written as

$$k = k_o q F_\mu^{1/2}[\gamma - (\gamma - 1)/F_\theta]^{1/2}, \tag{4.11}$$

$$Z_c = (\rho_o c q/\Omega) F_\mu^{1/2}[\gamma - (\gamma - 1)/F_\theta]^{-1/2}. \tag{4.12}$$

The functions

$$F_\mu = 1 + i f_\mu / f \tag{4.13}$$

and

$$F_\theta = 1 + i f_\theta / f \tag{4.14}$$

are related to the viscous and thermal dependencies, which are given respectively by

$$f_\mu = \Omega R_s /(2\pi \rho_o q^2) \tag{4.15}$$

$$f_\theta = R_s /(2\pi \rho_o N_{pr}). \tag{4.16}$$

In the above equations, γ is the specific heat ratio, N_{pr} is the Prandtl number, R_s is the airflow resistivity of the porous structure, Ω is the porosity of the air-filled connected pores, and q^2 is the tortuosity. These last three parameters can be independently determined, directly or indirectly, which makes this simple model for porous road pavements attractive. In addition, the density ratio m_l, the index of refraction n_l, and the normalized surface impedance $Z = Z_c / \rho_o c$ are related according to the following relationship:

$$\frac{1}{Z} = m_1 n_1. \tag{4.17}$$

Hence, by using Eqs. (4.7) - (4.17), we can determine the effective admittance for a given frequency and other physical parameters.

Since the scattered waves from the sphere above a ground surface are spherically spreading waves, the total scattering sound field due to the presence of a hard-backed porous ground can be calculated by

$$\phi_T^s = \phi^s + Q_2\phi_r^s, \tag{4.18}$$

where ϕ^s is the scattered sound field from a real sphere in free space and ϕ_r^s is the scattered sound field from the image sphere. The spherical wave reflection coefficient Q_2 for a scattered wave reflection on an impedance ground can be obtained in a similar formulation as Eq. (4.3). In fact, Q_2 can be computed by replacing α_1 and R_2 in Eqs. (4.3) – (4.10) with α_2 and R_3, respectively; where R_3 is the distance of separation between the center of the image sphere and the field point, and α_2 is the angle of incidence of the scattered wave on the porous layer. The total sound field above a hard-backed porous layer can now be represented in a real spherical coordinates system, which consists of four components: direct source, scattered waves from the real sphere, image source, and scattered waves from the image sphere, as follows:

$$\begin{aligned}
\phi^T &= \phi^i + Q_1\phi_r^i + \phi^s + Q_2\phi_r^s \\
&= \sum_{n=0}^{\infty}\sum_{m=0}^{n} a_{mn} h_n^{(1)}(k_oR_o) j_n(k_oR) P_n^m(\cos\theta) P_n^m(\cos\theta_o)\cos m(\varphi-\varphi_o) \\
&+ \mathrm{Q}_1 \sum_{n=0}^{\infty}\sum_{m=0}^{n} a_{mn} h_n^{(1)}(k_oR_o^{'}) j_n(k_oR) P_n^m(\cos\theta) P_n^m(\cos\theta_1)\cos m(\varphi-\varphi_o) \\
&+ \sum_{n=0}^{\infty}\sum_{m=0}^{n} b_{mn} h_n^{(1)}(k_oR_o) h_n^{(1)}(k_oR) P_n^m(\cos\theta) P_n^m(\cos\theta_o)\cos m(\varphi-\varphi_o) \\
&+ Q_2 \sum_{q=0}^{\infty}\sum_{m=0}^{q} (-1)^{m+q} b_{mq} h_q^{(1)}(k_oR_o) P_q^m(\cos\theta_o)\cdot \\
&\quad \sum_{n=m}^{\infty} A_{mn}^{mq}(k_od_o) j_n(k_oR) P_n^m(\cos\theta)\cos m(\varphi-\varphi_o)
\end{aligned}, \tag{4.19}$$

where

$$a_{mn} = \frac{i(n-m)!(2n+1)(2-\delta_{m0})k_o}{4\pi(n+m)!}, \tag{4.20}$$

and δ_{m0} is a Kronecker delta function that vanishes if $m \neq 0$. The translation coefficient $A_{mn}^{mq}(k_o d_o)$ is given in Eq. (2.14). The unknown scattering coefficient b_{mn} can be determined by imposing the rigid boundary condition on the surface of the sphere if it is regarded as acoustically hard. As a result, we can get a set of coupled linear complex equations for solving b_{mn} in a matrix form, as follows:

$$\mathbf{XB} = \mathbf{D}. \tag{4.21}$$

The diagonal elements of **X** are

$$X_{nn} = h_n^{(1)}(k_o R_o) P_n^m(\cos\theta_o) + Q_2 T_n (-1)^{m+n} h_n^{(1)}(k_o R_o) P_n^m(\cos\theta_o) A_{mn}^{mn}(k_o d_o), \tag{4.22}$$

the off-diagonal elements of **X** are

$$X_{nq} = Q_2 T_n (-1)^{m+q} h_q^{(1)}(k_o R_o) P_q^m(\cos\theta_o) A_{mn}^{mq}(k_o d_o), \tag{4.23}$$

and the elements of the vector **D** are

$$D_n = -a_{mn} T_n [h_n^{(1)}(k_o R_o) P_n^m(\cos\theta_o) + Q_1 h_n^{(1)}(k_o R_o') P_n^m(\cos\theta_1)], \tag{4.24}$$

with

$$T_n = \frac{j_n'(k_o b)}{h_n'(k_o b)}. \tag{4.25}$$

The system of complex equations in Eq. (4.21) can be truncated to an order of N; that is, the number of sums from n or $q = 0$ to N, depending on the degree of accuracy required. The complex matrix **X** has an order of $(N+1-m) \times (N+1-m)$, and the complex vectors **B** and **D** have dimensions of $(N+1-m)$ for each m, where m ranges from 0 to N.

4.3 Comparisons with published results

According to the hypothesis stated in Sec. 4.2 above, the tire belt can be replaced by a sphere for predicting the horn effect of a tire/road interaction. In order to apply this simplified model to investigate the influence of porous ground, it is important to validate the hypothesis. There are published experimental results and BEM calculations for the interaction of a tire with hard ground. In this section, these published results are compared with the predictions computed by the simplified model.

Based on the experimental configuration described in Ref. [40], the following geometrical configuration is used (unless stated otherwise) for all of the numerical calculations throughout this section. The sphere, which has a diameter of 0.64 m, is placed on the ground; and a point source is located 2.57 m from the center of the sphere and 0.72 m above the surface of the ground. In the graphs, the amplification due to the horn effect is plotted against the frequency. Throughout this section, amplification is defined as the difference in sound levels with and without the presence of the sphere. Equation (4.19) is used in the computations, with Q_1 and Q_2 set to 1 in the case of hard ground. For all of the simulations in this section, the receiver is located on the ground at a distance d from the contact point and at an offset distance o from the center of the sphere (see Fig. 4.2). The computed results are plotted for comparison with the published experimental results.

Figure 4.3, which is extracted from Fig. 11 of Ref. [40], shows the experimental measurements for a cylinder and an unloaded tire for different distances d from the contact point. In the same figure, we also show the theoretical predictions for the amplification of sound, calculated by assuming a hard sphere rested on a hard ground for the same geometrical configurations. In these measurements and numerical predictions, the receiver was located at the centerline, $o = 0$, of the respective scatter.

It can be seen from Fig. 4.3 that, according to our model, the predicted dips are shallower than those shown in the experimental measurements for the cylinder and the tire. According to Graf *et al.* with respect to the BEM results shown in Fig. 12 of Ref. [40], the effect of the rounded shoulders of the tire can broaden the dips of the acoustic interferences, reduce the maximum amplification and shift the dips to higher frequencies. This can be confirmed in our numerical predictions because a sphere has a much larger radius curvature of the round edges than an unloaded tire. Not surprisingly, the predicted amplification spectra are in closer agreement with the measured results of an unloaded tire than with the corresponding results of a cylinder. This is understandable, because the hypothesis of using a sphere to replace a tire belt is used in our numerical simulations.

The dependence of the amplification on d is plotted in Fig. 4.4. It is obvious that at low frequencies the amplification is independent of d. The amplifications give almost no differences for sufficiently small values of d (less than 40 mm). Our theoretical predictions show good qualitative agreement with the trends shown in the experimental observations found in Ref. [40], see their Fig. 4. In Fig. 4.5 of this chapter, the results of the simulation of different d at various offset distances o of the receiver away from the center of the sphere are shown for comparison with the experimental measurements obtained from Fig. 16 in Ref. [40]. Our theoretical model is consistent with this in predicting the general trend of the amplification due to the horn effect: it decreases as the offset distance increases. We note that, as shown in Figs. 4.4 and 4.5, the interference minima are less distinct in the predicted results according to the numerical model presented in this chapter. This is due to the corner effect of the sphere.

The ability of the proposed simulation model to describe the amplification of sound by a smooth tire is compared with the ray theory developed by Kuo *et al.* [69], as shown in Fig. 4.6. The numerical results predicted by the ray theory and the measurements given in Fig. 4.6 are extracted from Fig. 5 of Ref. [69]. The locations of the microphone and receiver are given in Fig. 4.6, where d is the distance of the source from the contact patch, L is the distance of the receiver from the contact patch and ø is the angle made by the receiver with the ground (see Figs. 2 and 5 of Ref. [69]). It is of interest to point out that our proposed simulation model seems to give closer agreement with the experimental data than the ray model. However, as in our previous observations, the interference dips predicted by our simulation model are consistently shallower than those obtained by the ray model and measurements.

It is worth noting that use of a sphere to represent a tire has somewhat limited the quantitative accuracy of the numerical model proposed in Sec. 4.2. Indeed, it can be seen from Fig. 4.3 that the BEM results of a cylinder and the experimental data of a tire are different from our predicted results by an order of 5 dB. However, we stress that an objective of our present study is to exploit the acoustic characteristic of porous road pavement for reducing the amplification of sound due to the horn effect. As our model has proved to be accurate in predicting the general trend of the amplification spectra at a much reduced computational time especially at high frequencies, we shall use it in a parametric study of porous road pavement, as detailed in Sec. 4.4. This detailed study can lay a foundation to optimize the design of porous road pavements for reducing noise caused by the interaction between tire and road.

Next, we verify the validity of Li's approximate analytical model [73] for the propagation of sound above a hard-backed layer of porous ground, as follows. Bérengier's published results (Fig. 7 of Ref. [8]) are compared with the numerical predictions according to the approximate model for porous ground, see Fig. 4.7. The geometrical configurations and other details of the porous pavement can be found in Ref. [8]). We can confirm that Li's prediction results are consistent with Bérengier's numerical results. Hence, our proposed sound propagation model for a spherical wave propagated above a porous road pavement can be confidently adopted to study the horn effect above a porous road pavement.

Finally, we end this section by comparing our predictions with those calculated by a 2D-BEM model for a rigid cylinder on porous ground. The predicted results of the 2D-BEM model are taken from Fig. 2 of Ref. [2]. Figure 4.8 shows the geometrical locations of a point source and receiver of the simulation. In this numerical example and other simulations shown in Sec. 4.4, unless otherwise stated, the sound source is assumed to be localized at a single point on the surface of a sphere with a radius of 0.3 m and situated at an angle of $\psi = 5^{\circ}$ measured from the vertical axis. The receiver is located at a horizontal distance of 1 m from the contact point of the sphere and situated at a height of 0.3 m above the porous pavement. The acoustical structural parameters of the porous layer are: $R_s = 20$ kN s m^{-4}, $\Omega = 15$ %, $q^2 = 3.5$ and $l_l = 0.04$ m. It is shown in Fig. 4.9 that our model gives comparable spectra as that computed by the 2D-BEM model. Again, the difference in the amplification factor is of an order of about 5 dB. This observation is consistent with the earlier simulation results for hard ground, shown in Fig. 4.3. It is worth pointing out that the discrepancies between the predictions made by our model and the 2D-BEM model for porous ground are less than that for hard ground. The differences in magnitude are less than 3 dB in the frequency range between 800 Hz to 4000 Hz in the case of the amplification of sound over porous ground.

4.4 A parametric study of porous road pavement on the horn effect

Section 4.3 presents a set of comprehensive numerical comparisons with published experimental data and theoretical predictions of horn amplification above the surface of the ground. It is reassuring to find that the numerical results of our simulation model can give a reasonable agreement with the general trend of the published experimental data and theoretical predictions based on other numerical schemes. We can now use our prediction model to explore the effect of sound propagation due to a point source located in the gaps between the tire and a porous road pavement. The road pavement has either a single layer or double layers. The influence of porous road pavement on the horn effect can be investigated by using Eq. (4.19). The phenomenological model as described in Eqs. (4.11) - (4.16) can be employed to determine the effective admittance of the porous layer by using Eq. (4.17). The horn effect considered in this section is the difference in sound pressure level due to a localized sound source on the surface of the tire with and without porous ground. The source/receiver configurations of the following examples are given in Fig. 4.8.

In Fig. 4.10, we show the influence of the thickness of a porous layer on the reduction in the horn amplification of sound radiating from tires. In these simulations, the acoustical structural parameters of the porous layer are R_s = 20 kN s m^{-4}, Ω = 15 %, q^2 = 3.5, with the thickness of the porous layer varying from 0.0 m (hard ground) to

0.04 m at a step of 0.02 m. A porous road pavement can effectively suppress the amplification of sound due to the horn effect by creating interference minima in the amplification spectrum. The interference "dips" shift to higher frequencies when the thickness of the porous layer is reduced. Obviously, the overall effectiveness of the porous road pavement in reducing noise will decrease as the thickness of the layer decreases. For instance, there is only one interference dip in the dominant frequency range of the noise of a rolling tire, i.e., 500 to 4000 Hz, at a layer thickness of 0.02 m. The noise reduction is about 28 dB at the frequency of 2500 Hz for the layer thickness of 0.02 m while a noise reduction of 22 dB and 14 dB can be achieved respectively at the frequencies of 1300 Hz and 3400 Hz for the layer thickness of 0.04 m.

Figure 4.11 presents another important piece of information for investigating the material properties of a porous layer on the horn effect. It shows the effect of the porosity of a porous layer on the horn amplification of sound. In this example, the acoustical structural parameters of the porous layer are chosen to be $R_s = 20$ kN s m^{-4}, $q^2 = 3.5$, and $l_1 = 0.04$ m. The respective porosity with $\Omega = 0$ % (for a hard ground), 15 % and 30 % are shown in the same figure for ease of comparison. As expected, a higher porosity can provide a better attenuation of the horn effect by reducing the magnitude of the sound amplification. Extra noise reduction can be obtained for frequencies greater than 1000 Hz when the porosity is doubled such that a maximum noise reduction of 17 dB can be achieved at the frequency of about 1800 Hz. The finding is consistent with the conclusion drawn in Ref. [56]. With regard to the flow resistivity of a porous layer, the change in its values does not alter too much the sound spectrum when the porosity is 15 %. However, the change in its values has a more significant effect to the sound spectrum when the porosity of the porous layer is increased to 30%, as evidenced in Fig. 4.12. The change of sound spectrum becomes noticeable for a greater value of porosity such that a noise reduction of 10 dB can be observed at the frequency of 1500 Hz when the value of flow resistivity is reduced from 20 kN s m^{-4} to 5 kN s m^{-4}.

Recent studies [58][59][68] have identified that a double layer of porous road pavement can better reduce the road traffic noise. Its application in road construction has received attention in recent years. Hence, the influence of a double layer of porous road pavement on the horn amplification of sound is worth exploring in the present study. For practical significance and numerical convenience, two different types of double-layer porous road pavement are investigated. The first type has a coarse porous surface and the second type has a fine porous surface. Both types of double-layer porous road pavement are currently used in the Netherlands [68] and are selected for the current study. Figures 4.13 and 4.14 illustrate the comparison of a double layer of porous road pavement with that of a single layer of road pavement. The spectra of sound amplification above a hard ground are also given in the figures for the purpose of comparison.

In Fig. 4.13, the acoustical structural parameters of the coarse top layer are given by $R_s = 6000$ N s m^{-4}, $\Omega = 20$ %, $q^2 = 3.5$, and $l_1 = 0.025$ m. For the bottom layer, $R_s =$ 1500 N s m^{-4}, $\Omega = 20$ %, $q^2 = 4$, and $l_2 = 0.045$ m are used in Fig. 4.13. On the other hand, the predicted amplification factors for the porous road pavement with a fine top layer are shown in Fig. 4.14. The respective acoustical structural parameters of the top and bottom layers are given as follows. For the top layer, $R_s = 24000$ N s m^{-4}, $\Omega =$

20 %, $q^2 = 2.5$, and $l_1 = 0.015$ m, and, for the bottom layer, $R_s = 1500$ N s m^{-4}, $\Omega = 25$ %, $q^2 = 4$, and $l_1 = 0.055$ m.

It is not surprising to see that a double layer of porous road pavement can provide better attenuation of the horn amplification by creating more interference dips in the frequency range of interest. The first dip shifts to the lower frequency region in the case of a double layer of porous road pavement which produces an extra noise reduction of about 20 dB.

The dependence of the horn effect on the angular position of the source on the surface of the sphere is presented in Fig. 4.15. It shows that the amplification factor is rather insensitive to changes in the angular position of the source when the angle is small, i.e. smaller than 10°, such that the maximum change in magnitude of sound amplification is about 3 dB. There is a slight tendency for the interference dips to shift to lower frequencies when the angular position of the source increases.

Finally, a general remark can be drawn by studying Figs. 4.10 – 4.15: the acoustical properties of a porous layer and the angular position of the source on the surface of a tire do not have a noticeable influence on the horn effect at the low frequency region below 300 Hz.

4.5 Summary

This chapter has presented a theoretical model to study the amplification of noise due to the propagation of sound confined to a gap between the tire and the road over a porous road pavement. The simplified model can give good predictions of the general trend of amplification spectra compared to the published numerical and experimental results for the studies of the horn effect above hard and porous types of ground. The principal aim of this simplified model is to provide a parametric study of the acoustical parameters of porous road pavements on the horn effect. In the study, the source of the noise is assumed to be a monopole point source localized on the surface of the tire. It has been shown that a porous road pavement can effectively reduce the level of sound amplification resulting from the horn geometry of the tire/road in the frequency range of interest. A decrease in the thickness of the porous layer leads to an overall increase in the sound amplification of the horn effect. A noise reduction of 22 dB and 14 dB can be achieved at two interference dips, i.e. 1300 Hz and 3400 Hz respectively, for a layer thickness of 0.04 m while there is only one interference dip at the frequency of 2500 Hz which produces a noise reduction of 28 dB for a layer thickness of 0.02 m. An increase in porosity can improve the noise reduction such that a maximum noise reduction of 17 dB at the frequency of 1800 Hz can be achieved when the porosity is doubled. The use of a double layer of porous road pavement can enhance the attenuation of sound and create more interference dips in the amplification spectrum. The interference dips shift to lower frequencies when a double layer of porous road pavement is used which produces an extra noise attenuation of 20 dB. The changes in the flow resistivity of a porous road pavement do not seem to have a significant effect on horn amplification when the porosity of the porous road pavement is relatively small. However, a maximum noise reduction of 10 dB can be observed at the frequency of 1500 Hz for a decrease in the value of flow resistivity when the porosity is 30 %. As shown in the predictions, the variations in the angular position of the source on the tire surface have no significant effect on the horn amplification of sound when the angle is smaller than 10°. The maximum change in magnitude of sound amplification is about 3 dB for a change in angle from 5° to 10°.

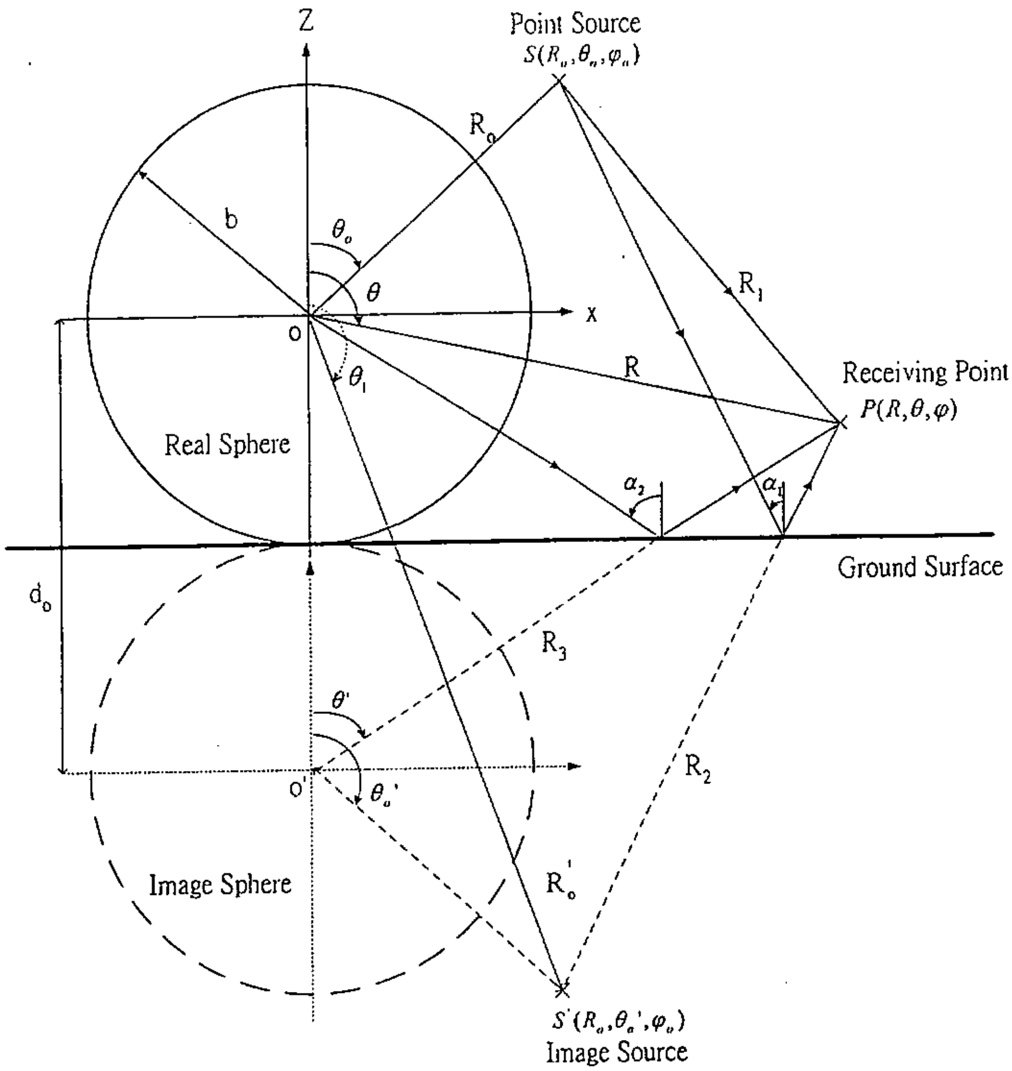

Figure 4.1. Geometrical configuration of a sphere on flat ground irradiated by a point source.

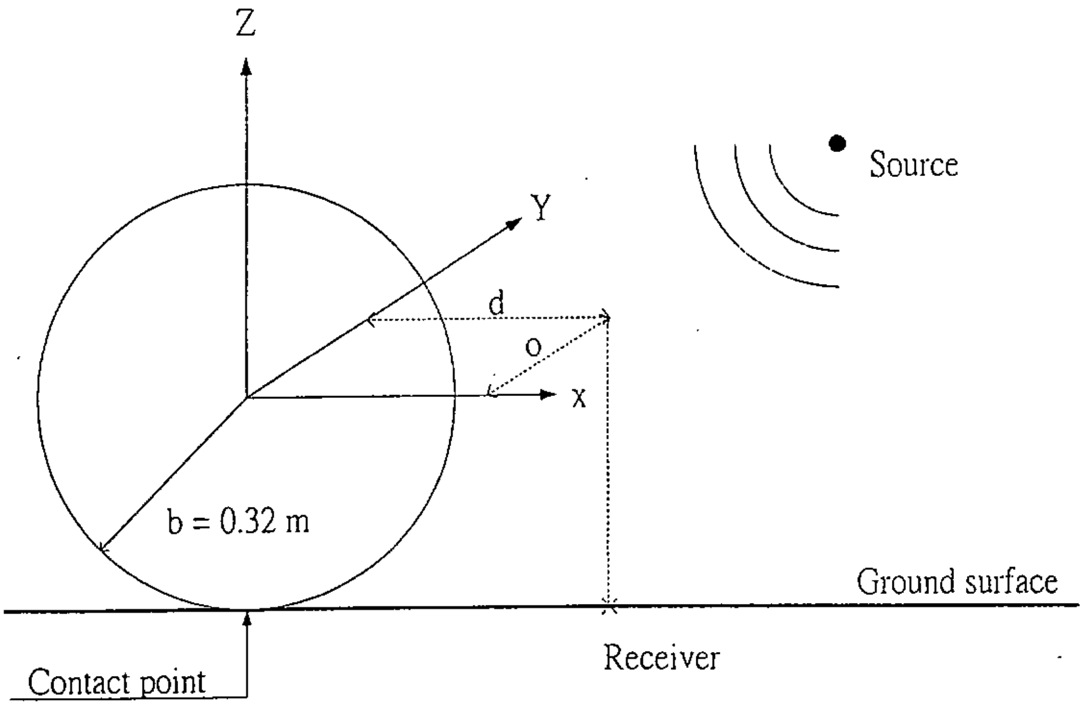

Figure 4.2. A rigid sphere on flat ground to simulate the horn effect. The receiver is located on the ground at a distance *d* from the contact point (the center of the sphere) and at an offset distance *o* from the contact point.

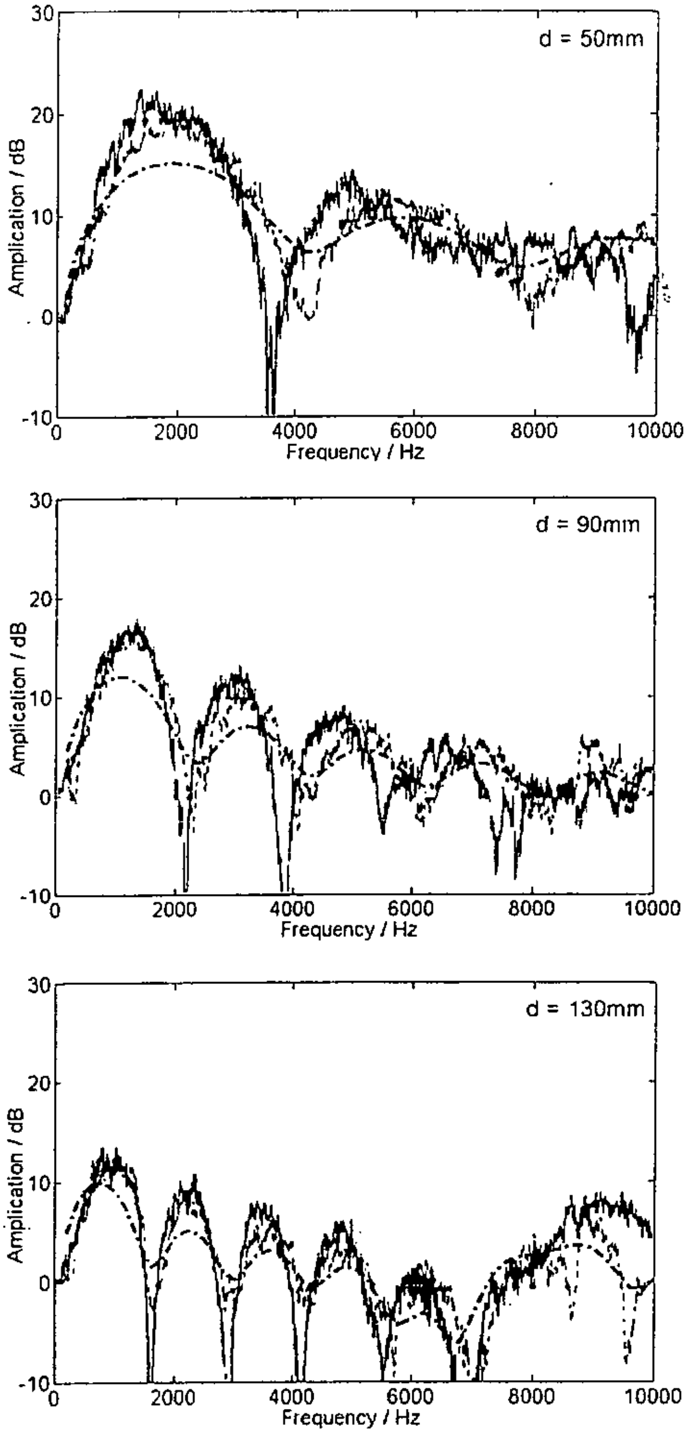

Figure 4.3. Comparison of sound amplification by a rigid sphere simulation model to the experimental measurements of cylinder/tire (Fig. 11 in Ref. [40]) on a hard ground for different distances *d*. The receiver is located at the centerline of the scatter. The solid line and dotted line represent the experimental results of a cylinder and tire respectively. The dash-dotted line represents the result predicted by the simulation model.

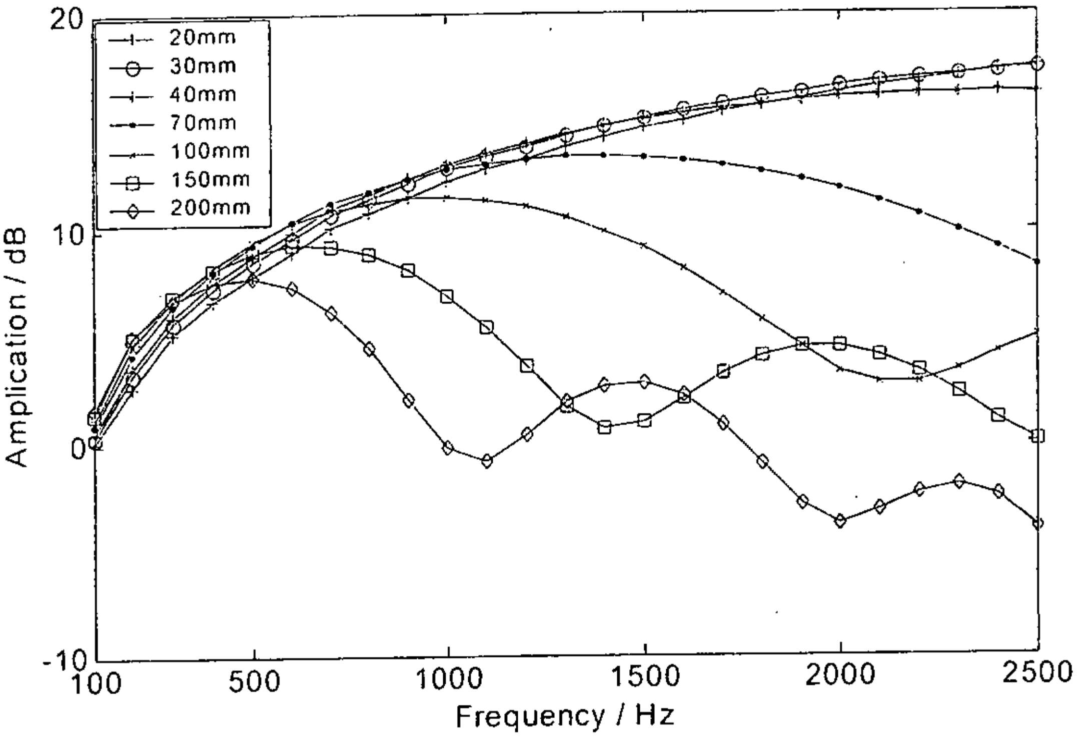

Figure 4.4. Dependence of sound amplification on *d* by a rigid sphere simulation model (compared to Fig. 4 in Ref. [40]).

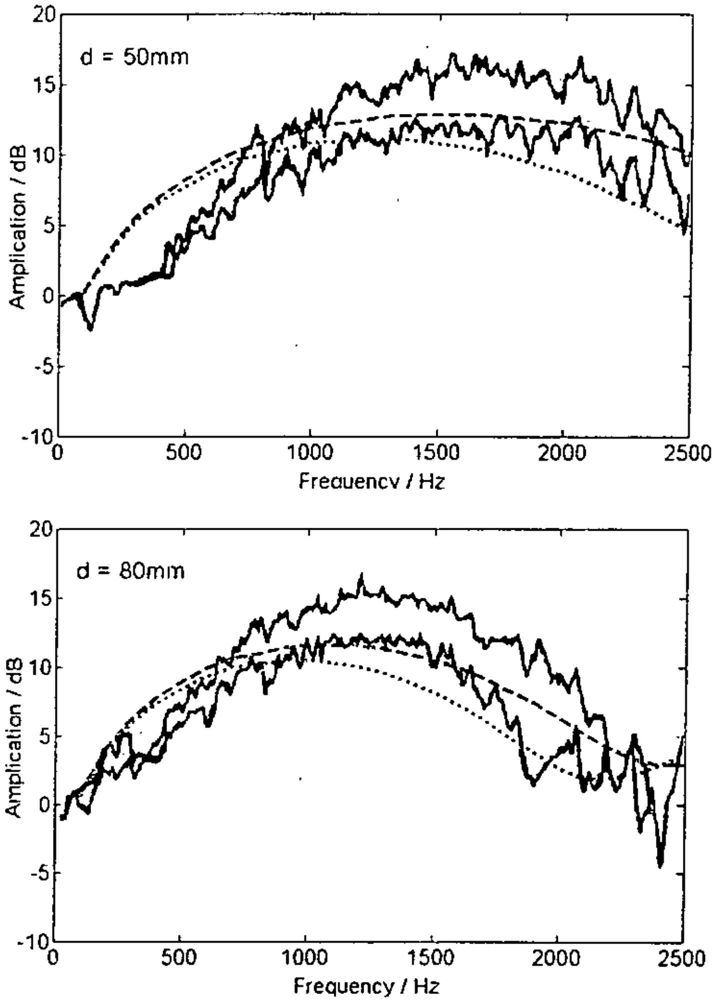

Figure 4.5. Comparison of sound amplification by a rigid sphere simulation model to the experiments for a cylinder (Fig. 16 in Ref. [40]) on a hard ground for different offset distances *o* from the centerline of the scatter. The solid lines represent the experimental results of a cylinder. The dashed line and dotted line represent the simulation results of an offset distance 5 cm and 8 cm respectively.

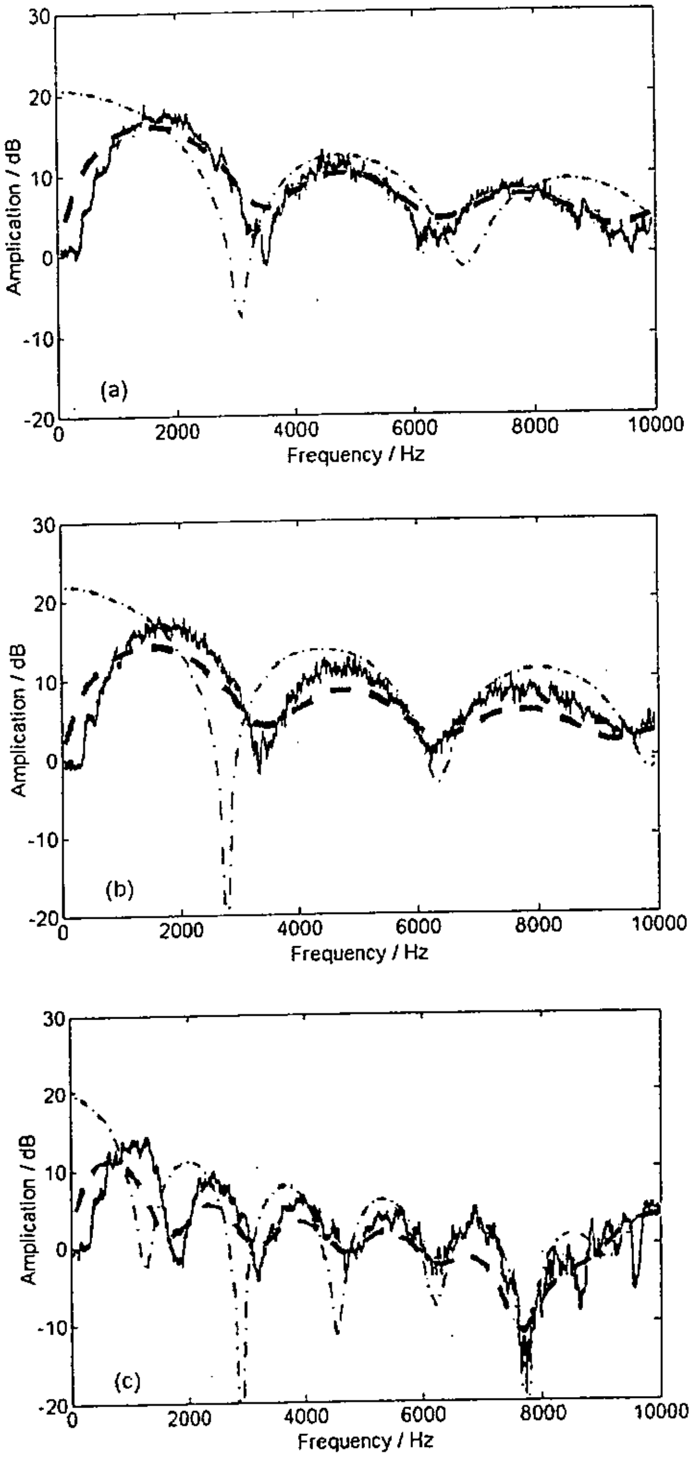

Figure 4.6. Comparison of sound amplification by a rigid sphere simulation model with smooth tire measurement and ray theory given in Fig. 5 of Ref. [69]. The solid line and dash-dotted line represent results from smooth tire measurement and ray theory respectively. The dashed line represents the simulation result. (a) d=60 mm, (L, θ)=(2.67 m, 15°); (b) d =60 mm, (L, θ)=(1.92 m, 2.4°); (c) d=120 mm, (L, θ)=(2.67 m, 15°).

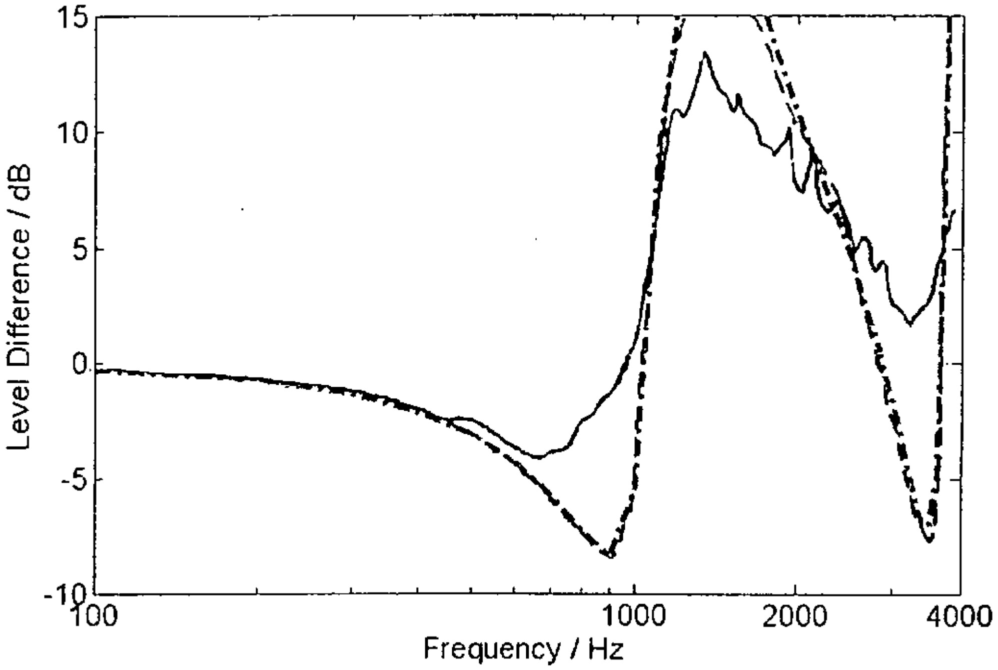

Figure 4.7. Reproduction of Bérengier's results (Fig. 7 in Ref. [8]) of level differences obtained above a porous asphalt using Li's approximate analytical model for sound propagation above a finite hard-backed layer of porous ground [73]. Solid line: measurement results by Bérengier; dashed line: results predicted by Bérengier; dash-dotted line: results predicted by Li [73].

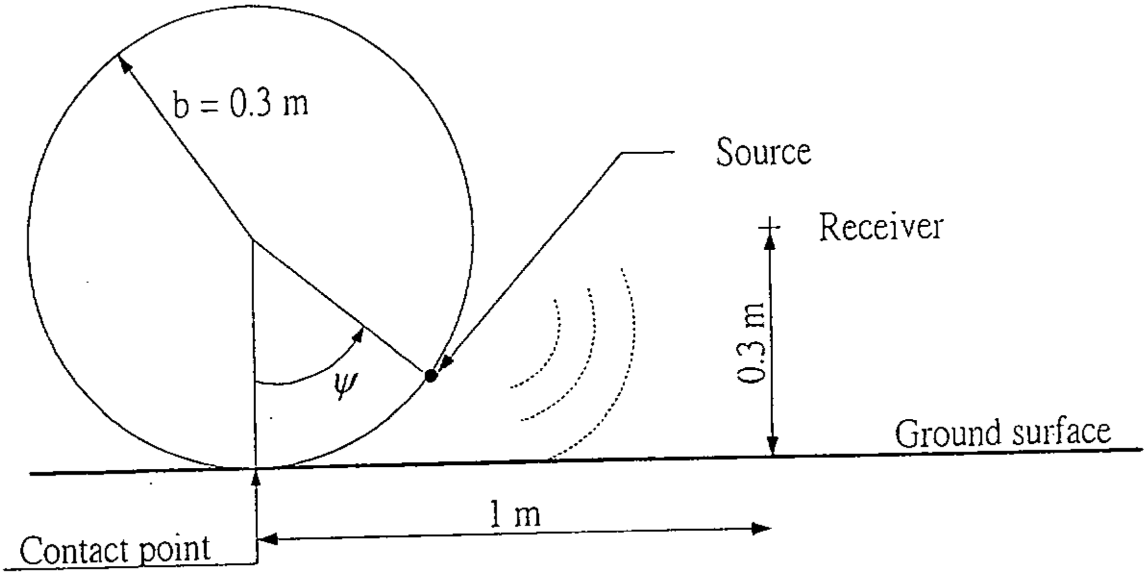

Figure 4.8. Localized sound source located on the surface of the sphere at an angle ψ measured from the vertical axis.

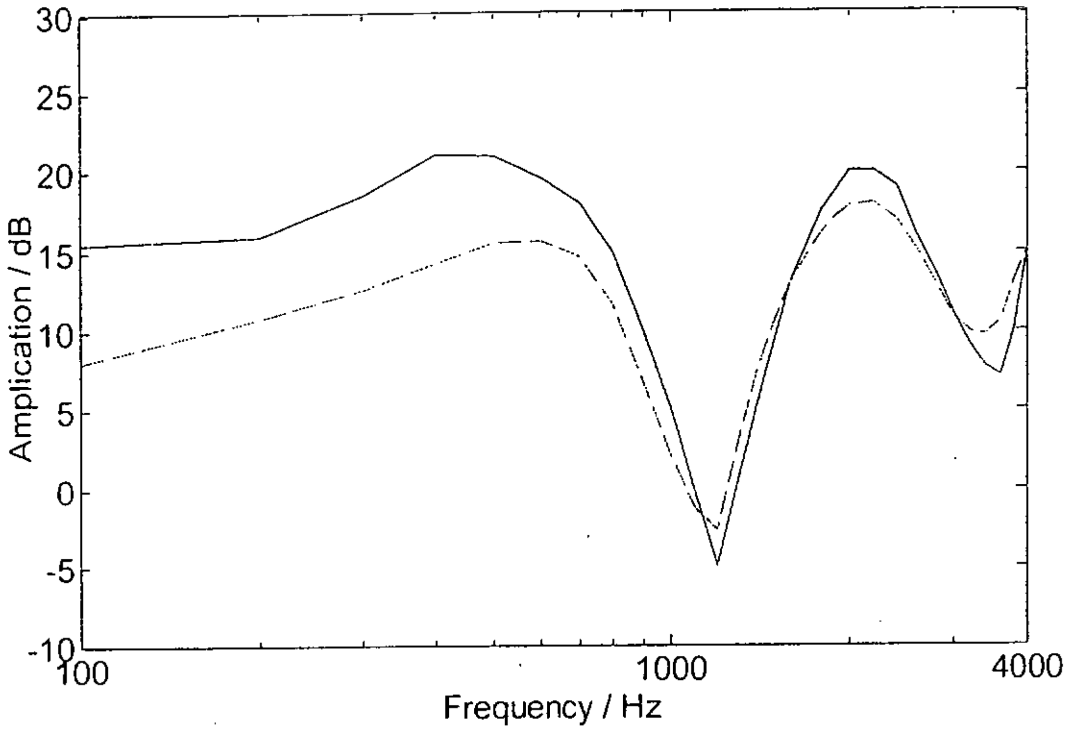

Figure 4.9. Comparison of the amplification of sound by a rigid sphere simulation model to a 2D-BEM model for a rigid cylinder on porous ground. The acoustical structural parameters of the porous layer are R_s=20000 N s m^{-4}, Ω=15 %, q^2=3.5 and l_l =0.04 m. (Solid line: 2D-BEM model; dotted line: rigid sphere simulation model)

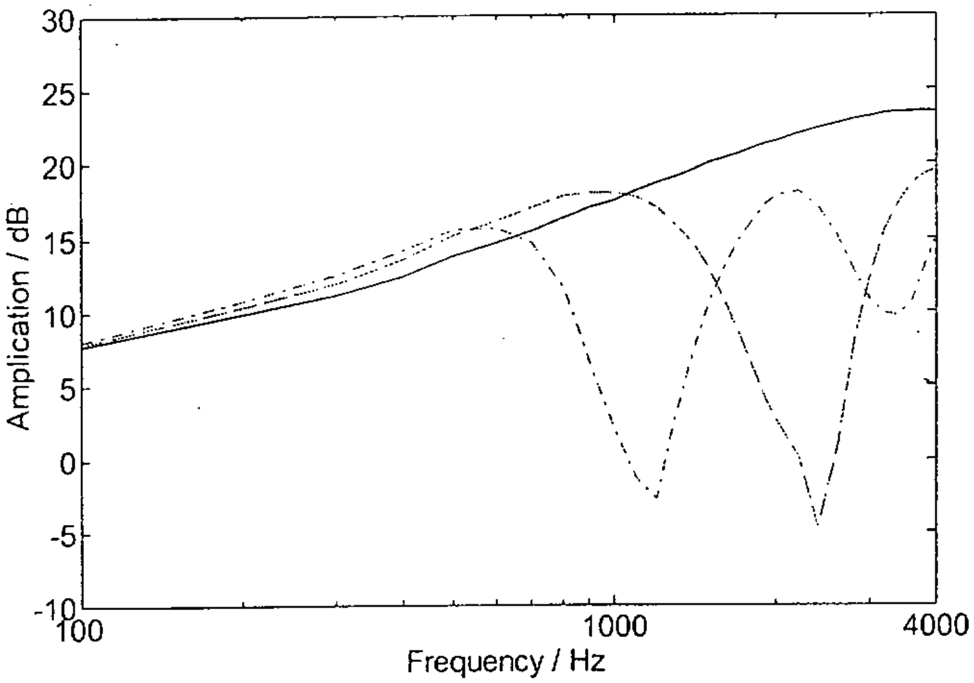

Figure 4.10. Influence of the thickness of a porous road pavement on the horn effect. The acoustical structural parameters of the porous layer: R_s=20000 N s m^{-4}, Ω=5 % and q^2=3.5. (Sold line: hard ground; dashed line: l_l = 0.02 m; dotted line: l_l =0.04 m)

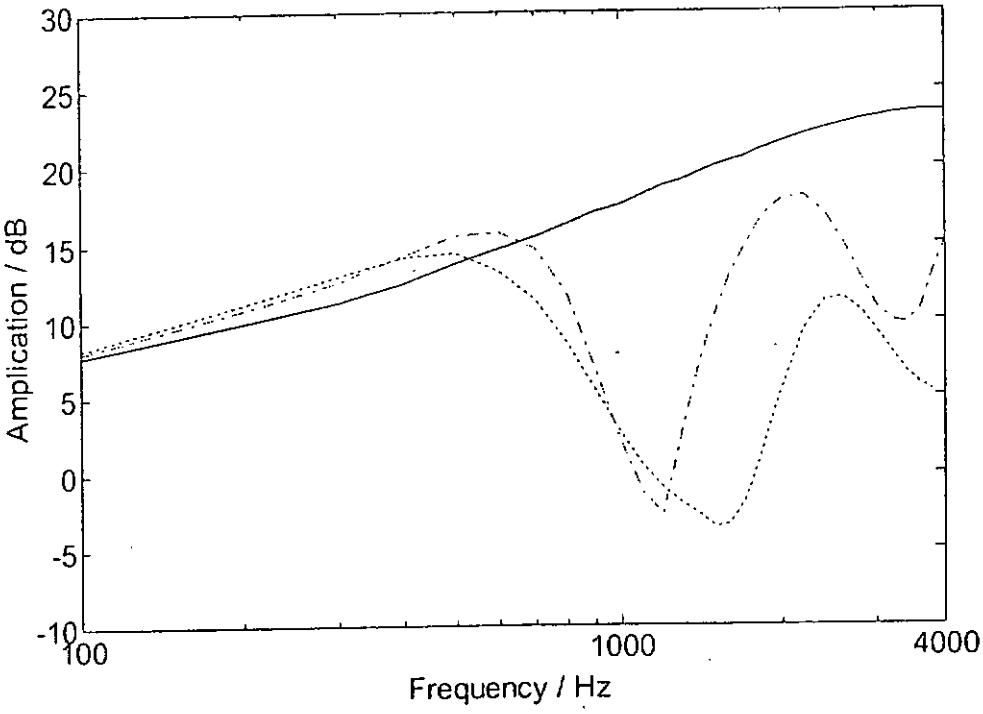

Figure 4.11. Influence of the porosity of a porous road pavement on the horn effect. The acoustical structural parameters of the porous layer: R_s=20 000 N s m^{-4}, q^2=3.5 and l_l=0.04 m. (Sold line: hard ground; dashed line: Ω=15 %; dotted line: Ω=30 %)

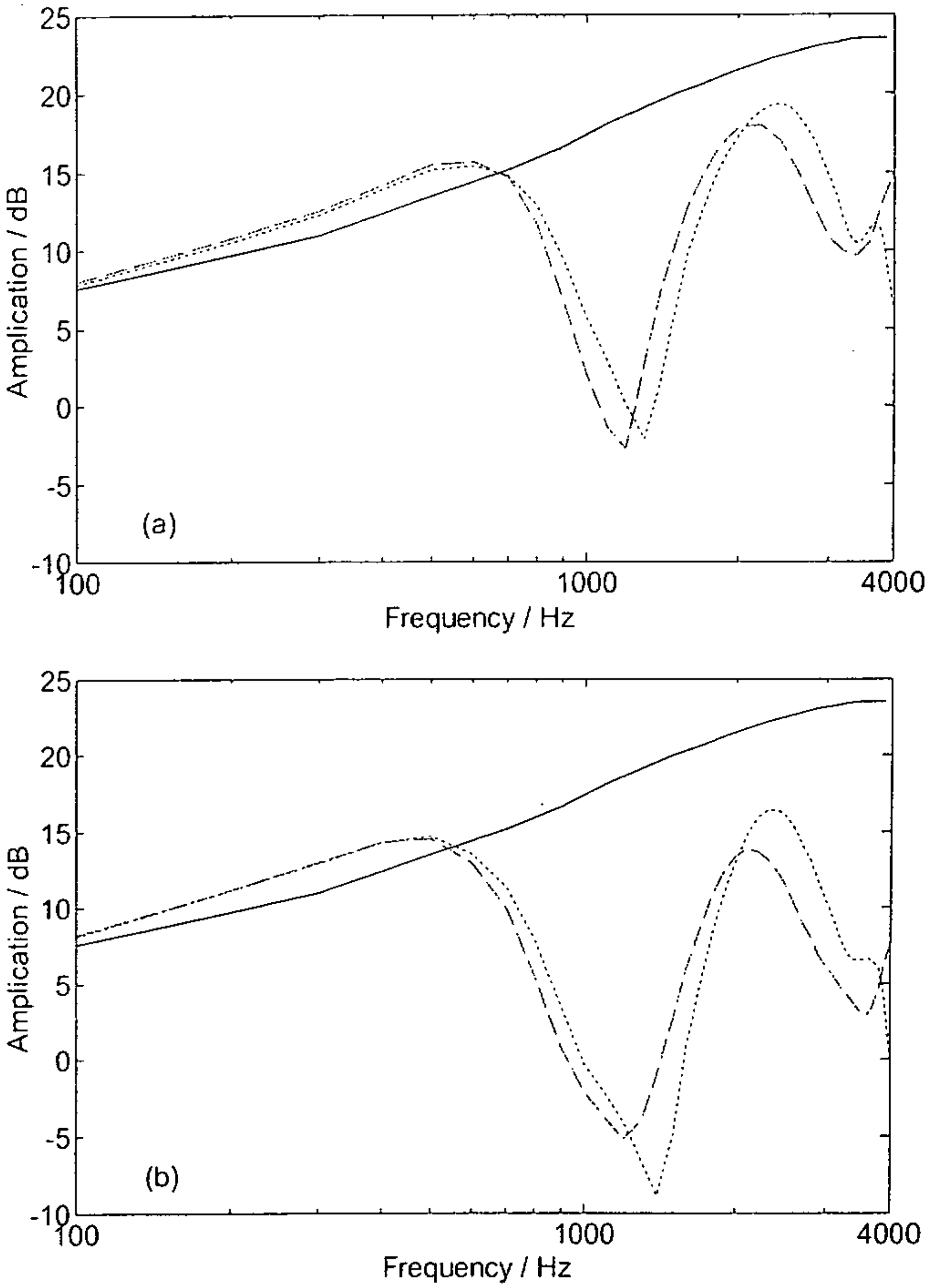

Figure. 4.12. Influence of the flow resistivity of a porous road pavement on the horn effect. The acoustical structural parameters of the porous layer, (a): Ω =15 %, q^2 =3.5 and l_f=0.04 m; (b): Ω =30 %, q^2 =3.5 and l_f=0.04 m. (Solid line: hard ground; dashed line: R_s =20 000 N s m^{-4}; dotted line: R_s =5000 N s m^{-4})

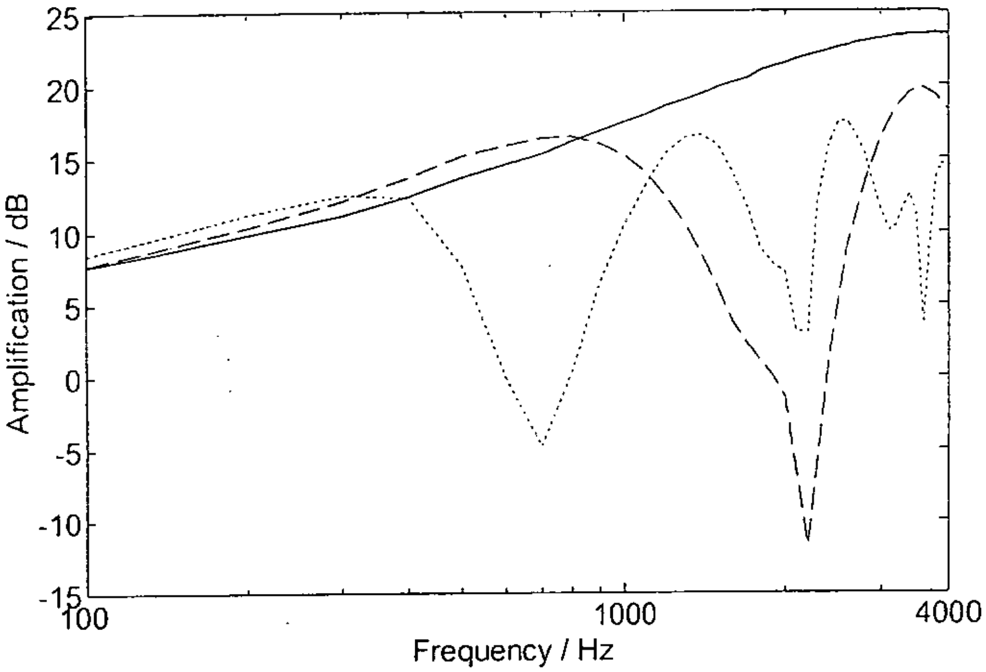

Figure 4.13. Reduction in the horn effect due to a double layer of porous road pavement - the top layer is a coarse porous surface. (Solid line: hard ground; dashed line: a coarse top layer with $R_s = 6000$ N s m^{-4}, $\Omega = 20$ %, $q^2 = 3.5$ and $l_1 = 0.025$ m; dotted line: double layers - a coarse top layer and a bottom layer with $R_s = 1500$ N s m^{-4}, $\Omega = 25$ %, $q^2 = 4$ and $l_2 = 0.045$ m).

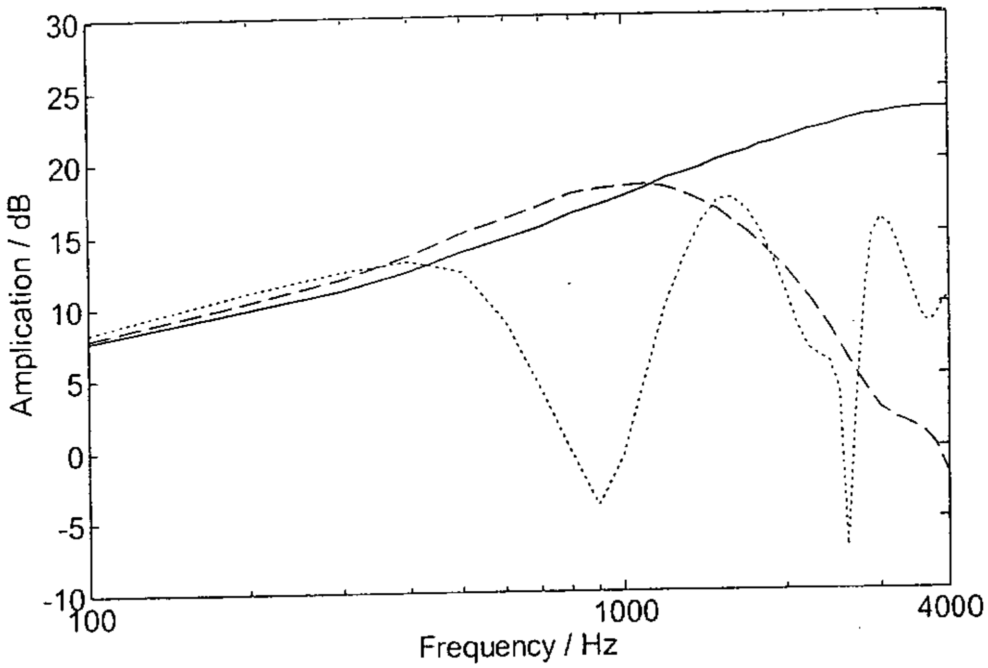

Figure 4.14. Reduction in the horn effect due to a double layer of porous road pavement - the top layer is a fine porous surface. (Solid line: hard ground; dashed line: a fine top layer with $R_s = 24000$ N s m^{-4}, $\Omega = 20$ %, $q^2 = 2.5$ and $l_1 = 0.015$ m; dotted line: double layers - a fine top layer and a bottom layer with $R_s = 1500$ N s m^{-4}, $\Omega = 25$ %, $q^2 = 4$ and $l_2 = 0.055$ m).

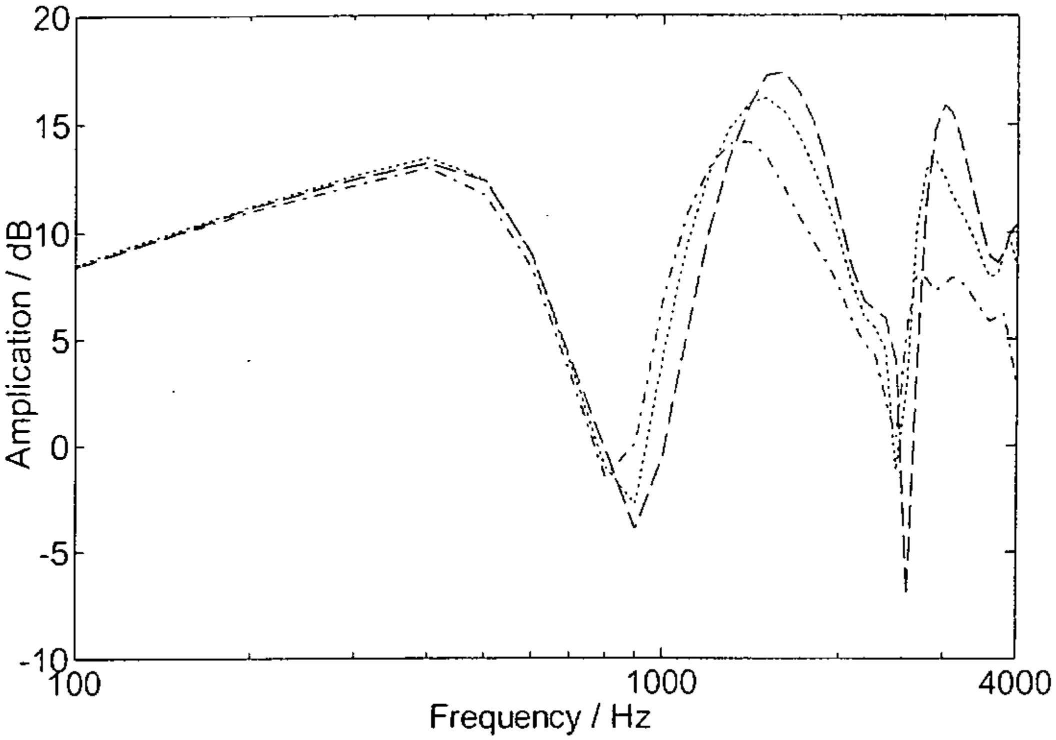

Figure 4.15. Dependence of the horn effect on the angular position of the source on the surface of the tire. A fine double layer of porous road pavement is used for the simulation. (Dashed line: source at ψ=5°; dotted line: source at ψ=10°; dash-dotted line: source at ψ=15°)

Chapter 5

Comparative Study of Different Prediction Schemes for Train Noise

5.1 Introduction

In Chapter 4, the problem of tire/road rolling noise was studied. However, like many metropolitan cities around the world Hong Kong experiences the problem of railway noise as well as the road traffic noise. The problem is even more acute around sections of railway track that run on a viaduct above the ground level in the vicinity of high-rise buildings. The reasons are simple: the scarcity of suitable land has encouraged buildings to become ever taller. It is not uncommon to find residential and commercial tower blocks of over 40 storeys, with a height of over 100 m. The lack of available land means that buildings go upwards and can be located very close to the viaducts. This inevitably causes neighborhood residents to suffer from even higher levels of noise emanating from the elevated railways.

At present, there is no established numerical scheme for predicting railway noise in high-rise cities. To tackle the problem, a reasonable approach will concentrate on reviewing exisiting prediciton schemes, that have been developed mainly for suburban districts. Many numerical schemes are available to predict railway noise. For instance, various prediction models have been developed in different European countries (see van Leeuwen [67][107] for a comprehensive review), and there is also the Greek prediction model [7] and American procedures for prediction [106]. Experimental data measured locally usually form the basis of the numerical formulation of the prediction model. This means that these models, which influence their respective national standards for prediction, are mostly empirical and aimed primarily at fullfilling local regulations, acts and laws. In addition to the various models for prediction mentioned previously, the international ISO 9613-2 standard for the propagation of outdoor sound [53][54] also supports the prediction of train noise. However, these schemes have mainly been developed for suburban situations. They may not be suitable for urban environments where many high-rise buildings and multiple reflections/scatterings of sound are detrimental to predicting overall noise levels. Moreover, these empirical schemes do not provide the prediction of train noise propagated from an elevated viaduct to its neighborhood buildings. A heuristic approach is to take the viaduct parapet as an effective barrier. Van Leeuwen [107], identified the inherent differences in various models. These differences include the assumption of source positions, the levels of noise emitted by passing trains, the characteristics of sound radiation and the correction factors to account for the effect of reflection adopted. In light of this, the predicted noise levels are invariably different for different prediction models.

Due to the current trend of heightened environmental concern, it is inevitable that more railway lines will be constructed in many cities. As a result, it is highly desirable to achieve an improved understanding of the accuracy of these prediction models for use in typical urban enviroments. In Section 5.2, an overview of the prediction models selected for numerical comparisons will be presented. In Section 5.3, details of outdoor field measurements of the noise from trains in a complex urban environment will be described. The measured data and the predicted noise levels will be presented in Section 5.4. Finally, conclusions will be drawn in Section 5.5.

5.2 An overview of models for predicting noise from trains

Four schemes for predicting noise from trains, which will be used for numerical comparisons with the outdoor noise measurements, will be reviewed in this section. These four schemes for prediction are: *Calculation of Railway Noise (CRN)* from the U.K. [29], the *Nordic Prediction Method for Train Noise (NMT)* [20] and the *French Mithra* model [1]. Two different schemes for prediction, namely, *CSTB 92 and ISO 9613-2*, are available in Mithra. Both of these methods will be used in our numerical comparisons. In addition to Mithra, there are other commercially available software for predicting the propagation of noise from trains. For instance, SoundPLAN [99] implements four different schemes for predicting noise from trains, including Schall 03 from Germany and OAL 30 from Austria, in addition to the CRN and NMT schemes for prediction. However, since the full document of the Schall 03 and OAL 30 prediction schemes are not easily accessible, and the fact that Schall 03 and OAL 30 normally do not take into account the detrimental influences of reflections from buildings on the predicted sound fields in a complex urban environment. SoundPLAN has therefore been excluded from use in the current study. It is also worth pointing out that the prediction schemes have been selected to cover a range of different methodologies used in calculating the attenuation of noise levels and different models for representing the noise source. All of these prediction schemes are some forms of energy-based models that make the numerical comparisons detailed in Sec. 5.3 meaningful.

5.2.1 Calculation of Railway Noise – U.K.

The CRN method is based on classic CRTN (Calculation of Road Traffic Noise) methodology [30], which was among the first systematic scheme developed to predict transportation noise. CRN starts by dividing the railway line into one or more segments such that the variation of noise within the track segment is less than 2 dB(A). For each segment, the reference sound exposure level SEL_{ref} in dB(A) is calculated for each type of train on each track. The source, which is treated as a line source, is taken at the railhead of near-side rail. With regard to propagation, corrections are made for the distance of the reception point from the track segment, for ground and air absorption, the effect of screening by barriers, buildings and so forth, and the angle of view at the reception point, respectively. A degraded adjustment will be applied to the barrier correction factor in a situation where the far-side barrier is more than 1.5m above the railhead of the near-side rail. The CRN model gives a correction of +2.5 dB(A) for a reflection from a nearby façade and includes a correction factor to calculate the effects of reflection from the opposite façades at opposite sides. The noise level at the reception point for each segment is determined by converting the corrected sound exposure level SEL to an A-weighted equivalent sound pressure level L_{Aeq}. The overall L_{Aeq} is finally computed by summing contributions from all segments, taking into account the possibility that different types of trains may pass the reception point.

5.2.2 Nordic prediction method for train noise - Norway

The NMT is used to calculate a 24-hour energy equivalent level. The calculations are carried out in octave bands from 63 to 4000 Hz. Based on measurements of the noise of octave band emissions for different types of trains, the sound power generated per meter of track can be determined if the speed of the train and the volume of traffic are known. The source line is then divided into elements in the direction along the track. Each element has a length of not more than 50% of the distance between the track and the reception point. The source is assumed to be located at the center of the track, with its height (measured above the rail head) varying according to the frequency of the source. Each of these source elements is treated as a point source located at the respective center. For the reception point, the contribution from each point source is calculated in turn, taking into account track conditions, distance between the source and receiver, air absorption, screening effect, ground effects and reflections from façades. The ground correction is determined by dividing the ground effect into three parts: source, receiver and central part. For prediction positions of between 0.5 to 2 meters from a building surface, a façade correction of +3 dB is used in NMT. However, the correction factors to account for the effect of reflection vary with the distance of the receiver position from the façade. No correction is required for positions of more than 20 meters from a building's façade. In cases where a hard screen is placed close to the track, a correction for the screening effect is necessary in NMT to model the reduced efficiency of the screen due to multiple reflections between the train and screen. There is no correction for the angle of view in NMT. The resultant noise level in dB(A) can be determined by adding the contributions from each source element within each octave band after adjusting for the standard A-weighting correction factor.

5.2.3 French Mithra model

Mithra is a prediction software package developed by Centre for the Science and Technology of Building in France. It has been developed to model the propagation of sound in outdoor environments. The prediction model provides the following three separate methods of calculation for predicting the propagation of sound outdoors: CSTB 92, ISO 9613-2 and NMPB 95. CSTB 92 is the only model (in Mithra) that does not include the meteorological effect in the prediction scheme. However, the prediction model of CSTB 92 implements a ray tracing technique that provides a fast algorithm for presenting the results of long-term equivalent A-weighted noise levels. The railway source is modeled as a set of equivalent point sources with a height of 0.8 m above the ballast. The octave-band source strength is expressed as the level of sound power per meter of a train's length. The method specifies a directivity index in both the horizontal and vertical planes for each noise source. The directivity index is distinct in each octave band frequency. In addition to considering the attenuations due to geometric divergence, atmospheric absorption, ground effect, diffraction effect and surface reflection, the model also takes into account the acoustic absorption of a surface, the retro-diffraction phenomenon (that is when a ray is reflecting close to the edge of a barrier) and the effect of multiple reflections of boundary surfaces such as barriers. Finally, we point out that the current Mithra software does not permit a train to run on an elevated railway viaduct. In all our calculations using Mithra, the railway track is built on a reflective embankment instead of a viaduct. The use of this simplified model should not affect the overall predicted noise levels.

5.3 Measurements of train noise over a busy road

5.3.1 Site description and measurement method

The aim of the current study is to investigate the noise radiating from a train running on a viaduct in a densely populated urban environment, as this is a very common scenario in Hong Kong that always results in complaints from residents. The study was implemented by conducting large-scale outdoor field measurements on the roof top of a residential building close to a viaduct, as shown in Fig. 5.1. The viaduct, which is located at a nominal distance of about 26 m from residential areas, is flanked on both sides by tall residential buildings. The viaduct is built with dual tracks in the vicinity of a flyover with a single traffic lane in each direction. The viaduct and the flyover are operated over a busy trunk road of five lanes in both directions. The measurements were made simultaneously with eleven microphones protruding 1 m from the façade of the building and four microphones fixed on an extension pole erected on the floor of the rooftop. The details of the experimental setup and dimensions are given in Fig. 5.1. Each measurement was started when the train came into sight and stopped when it was out of sight, as parts of the viaduct are shielded by nearby buildings. The speed of the train as it traveled through the section was about 50 km/h, and the duration of the measurement for each passing train was 17 seconds. The noise data were recorded through a 16-channel SONY digital data recorder and subsequently analyzed in the laboratory with the aid of post-processing sound analysis software.

5.3.2 Eliminating the influence of road traffic noise

Since the section of the viaduct selected for this study is in the vicinity of a busy trunk road, the measured train noise was inevitably influenced by the noise of the traffic on the road, even though we extended our measurement to midnight. In the measurement periods, the noise from the traffic on the road was monitored closely before and after the noise from a passing train was monitored. Since motor vehicles passing over the flyover and the underneath trunk road contributed to the noise from road traffic, the flow of traffic at each road was counted during the measurement period. The vehicles were classified into two classes according to the standard procedure of CRTN: heavy vehicles were those weighed more than 2.8 tonnes and light vehicles those that weighed less than 2.8 tonnes. Many control measurements were carried out to record the traffic noise under similar traffic conditions except that there were no trains passing by. The class and number of motor vehicles on each road were recorded during the "standard" 17-second measurement period. By assuming that contributions from road traffic noise at the receiver points will remain unchanged under similar road traffic conditions, the net noise from a passing train can be determined by logarithmically subtracting the traffic noise levels obtained in the control measurements from the overall noise levels when the train passed the observation station. The net levels of noise from a passing train are given by:

$$L_{Aeq} = 10\log(10^{\frac{L_{Aeq,m}}{10}} - 10^{\frac{L_{Aeq,t}}{10}}) \qquad (5.1)$$

where $L_{Aeq,m}$ is the measured overall noise level and $L_{Aeq,t}$ is the measured level of traffic noise in the control measurements. All noise levels are expressed in terms of A-weighted sound pressure level. We point out that extra precautions were taken by conducting the measurements at midnight, when the impact of the noise from road traffic was greatly minimized because of the reduced volumes of traffic at night.

5.3.3 Measurement results

Three typical sets of measurement results are presented in Fig. 5.2. Generally speaking, all of the measurements were taken during the periods when they were least affected by impact of noise from road traffic. In Fig. 5.3, we show the results of two typical control measurements of road traffic noise that can best be used to represent traffic flow conditions during the period when we were making our measurements of train noise. The measured noise spectra due to rail and road traffic noise sources are shown in Figs. 5.4 – 5.6, respectively, for noise received at heights of 6 m (shadow zone), 20 m (illuminated zone) and 27.5 m (measurement on the roof-top) above ground level. The data on the flow of traffic during the period when the measurements of noise were being made are summarized in Table 5.1. The symbol *M* represents the period of the measurement of train noise and the symbol *T* denotes the period of control noise measurements where the volume of road traffic flows was comparable to the period of the measurements of train noise.

The data "extracted" for the A-weighted noise levels due to a passing train is derived by logarithmically subtracting the road traffic noise from the measured train noise. These numerical results are shown in Fig. 5.7. As shown in Figures 5.4 – 5.6, the overall noise spectra in different measurements of noise show a consistent trend for frequencies higher than 40 Hz. The noise levels are mainly dominated by noise from rail traffic. It is reasonable to suggest that noise levels due to rail traffic can be obtained by using the logarithmic subtraction method in correcting for "unwanted" noise due to sources from road traffic (see Equation (5.1)). The average A-weighted noise levels due to passing trains are presented in the same figure. The extracted noise levels *C1*, *C2* and *C3* are derived from the logarithmic subtractions of measurements *M1*, *M2* and *M3* from the measurements *T1*, *T2* and *T1*, respectively. It is clear that the extracted levels of noise obtained from the three measurements are repeatable and that their deviations are less than 1 dB(A). As a result, the extracted train noise levels can be used as experimental data for comparison with different numerical schemes.

5.4 Comparisons with the prediction models

In this section, the four models for prediction introduced in Sec. 5.2 will be compared with the averaged levels of train noise obtained by our experimental data from an urban scenario as described in Sec. 5.3. Since the NMT and Mithra software do not offer a train model that can match our existing type, the sound power level per meter of length in octave bands were thus determined by an inversion method. The sound power level in octave bands at different source heights were found by inversely applying the method proposed in NMT to calculate the sound pressure level. In the inverse calculation, we have assumed that the sound source is omni-directional and that the measured sound pressure level of train noise at the highest measurement point after excluding the level of traffic noise was used to calculate the sound power level. The highest measurement point was chosen for the calculation because it is relatively free from the screening of reflections from parapets and façades. The distance attenuation was the only factor taken into the inversion calculation. The air absorption was not considered due to the short sound propagation distance. The reflections of sound from other surfaces were also neglected in view of the relatively large separations of the measurement point from those surfaces according to NMT. The sound power level obtained per meter of length in octave bands at different source heights were used as source input in the calculation methods NMT, CSTB 92 and ISO 9613-2. We wish to point out that although the calculation method ISO 9613-2 provides algorithms to consider the meteorological effect, the effect is less important in the present case as the propagation of noise is confined in a densely populated urban space.

In using the method of CRN, the train type Class 421 EMU passenger coaches fitted with tread brakes was chosen to calculate the reference sound exposure level in our prediction scheme. Although it may be possible to estimate the reference sound exposure level using an inversion method, no conversion from the measured data as recommended by CRN is implemented in the current study because we feel that choice of Class 421 EMU is sufficient for the present purpose. The rationale for our choice is due to the fact that the railway vehicles used in the measurements, which were made in the United Kingdom, consisted of electric multiple units fitted with tread brakes. The use of Class 421 EMU passenger coaches should be adequate in light of the assumptions made in our experimental measurements. It is also worth mentioning that in the CRN calculations we assume that the rail track is of the continuously welded type and that the trackform is made of concrete slabs.

Figure 5.8 shows the extracted levels of train noise obtained from our outdoor field measurements. The calculated levels of train noise according to different prediction schemes are also given in the same figure for numerical comparison. The measured noise levels increase gently from the minimum level at the lowest measurement point to the track level, which is about 8.8 m above the ground level. Since the average speed of the passing trains is about 50 km/h, the noise radiating from passing trains is mainly dominated by the noise of rolling wheels/rail. The noise was partially shielded by the parapet of the viaduct for these receiver points. The measured noise levels increase almost linearly with the measurement heights of 8.8 m to 15.8 m. The levels of noise increase at a relatively fast rate as the screening effect of the parapet decreases rapidly when the measurement points move from the shadow zone to the illuminated zone. Next, the measured noise levels remain relatively unchanged from a height of 17.2 m to 20 m above ground level. This is because the measurement points are directly exposed to the source and the change in the propagation distances from the source to the measurement points is relatively small; given that the horizontal distance between the viaduct and the building is about 26 m. In the next interesting region from 20 m to 28 m above ground level, the measured noise level drops abruptly as the receiver points are now located above the roof top of the building. The large drop in noise level is largely due to the fact that the measurement point is free from the reflections from the building façade at these positions. However, the measured noise levels on the roof top increase continuously by up to 1 dB(A) as the height of the receiver points increases. For an omni-directional point source, the noise levels will be reduced as the propagation distance increases. From measurements above the roof top of the building, it is possible to suggest that the source exhibits a vertical directivity characteristic, as shown by Chew [15][16][17] in his earlier studies of the propagation of noise from trains in urban districts.

From the results of the comparison, it is apparent that the numerical results predicted by CRN give the best agreement with the measurement results in terms of quantitative accuracy and the general trend of the measured noise levels as a function of the height above ground in an urban environment. However, according to CRN, the predicted noise levels below the track level are somewhat underestimated as compared with the measured data. The discrepancies between the predicted noise levels and measured data in shadow zone are probably due to the fact that the measured data are severely contaminated with traffic noise resulting in unpredicted errors. As shown in the CRN calculations, the predicted noise levels over the roof top decreases as heights above ground increase. This is in contrast with the measurement results because the CRN does not take into account the directivity effect of a passing train.

For the NMT numerical scheme, the prediction results are rather similar to that of CRN in terms of the general trend of predicted noise levels. Nevertheless, the prediction results of NMT are consistently about 3 dB(A) higher than that of CRN for receiver points that are 1 m from the façades of buildings, and only 1 dB(A) higher for receivers located above the roof. We note that the prediction results of NMT at the highest receiver point should be the same as the measurement data because the measured A-weighted noise at this point was used as the datum for calculating the sound power level of the passing train. The main reason for the apparent deviation between these two prediction schemes over the roof top are due to the intrinsic difference in the estimation of the source strength of the passing train. The relatively large deviations in predictions for measurements taken in front of the building's façade are due to the cumulative effects of estimating the source strength, the difference in the use of the façade correction (2.5 dB(A) for CRN but 3 dB(A) for NMT) and to lesser screening correction factors adopted by the NMT scheme as compared to the CRN methodology.

Comparing with measured data, the prediction results given by the methods of CSTB 92 and ISO 9613 as built in the Mithra software have greatly overestimated the noise levels to a maximum deviation of about 8 dB(A). Moreover, the methods are unable to provide a reasonable agreement on the general trend of the measured noise levels. The large difference in predictions may be due to the fact that the railway is built on a reflective embankment instead of on a viaduct as in the numerical modeling by

Mithra. As a result, the noise levels may build up due to the existence of multiple reflections in the confined environment between the "artificial" embankment and the building's façade. Although the Mithra numerical scheme provides an algorithm for calculating the vertical directivity of a passing train, it is not observable for predictions made on the roof top.

5.5 Summary

The noise measurement data of a passing train running on a viaduct in an urban environment have been compared with different models of predicting noise from trains. The method of *Calculation of Railway* (CRN) from U.K. gives the best agreement, in terms of quantitative accuracy and general trend of prediction, with the measured data. However, the CRN methodology cannot predict the vertical directivity characteristic of noise from a passing train that is evident in our study. The *Nordic Prediction Method for Train Noise* (NMT) also provides a good agreement with the general trend of the measured noise levels, despite the fact that the predicted results overestimate the noise levels. The prediction results of NMT are consistently about 3 dB(A) higher than that of measured data for receiver points that are 1 m from the façades of buildings and the maximum deviation is about 1 dB(A) higher for receivers located above the roof. The prediction methods of CSTB 92 and ISO 9612-2 are relatively inferior compared with the current set of measured data such that the maximum deviation is about 8 dB(A).

	Flyover		Far side road		Near side road	
Measurement	Heavy Vehicle	Light Vehicle	Heavy Vehicle	Light Vehicle	Heavy Vehicle	Light Vehicle
M1	0	3	1	0	1	6
M2	0	1	2	2	3	0
M3	1	0	1	2	1	4
T1	0	0	2	3	3	1
T2	0	2	1	3	1	5

Table 5.1. Traffic flow data on measurements of train noise (mixed with traffic noise) and control measurements. The symbols M1 - M3 represent the 1st, 2nd and 3rd measurement for the mixed noise. The symbols T1 – T2 represent the 1st and 2nd control measurement for the road traffic noise. The numerical value in the table is the number of individual cars/trucks passing by during the acquisition of a measurement.

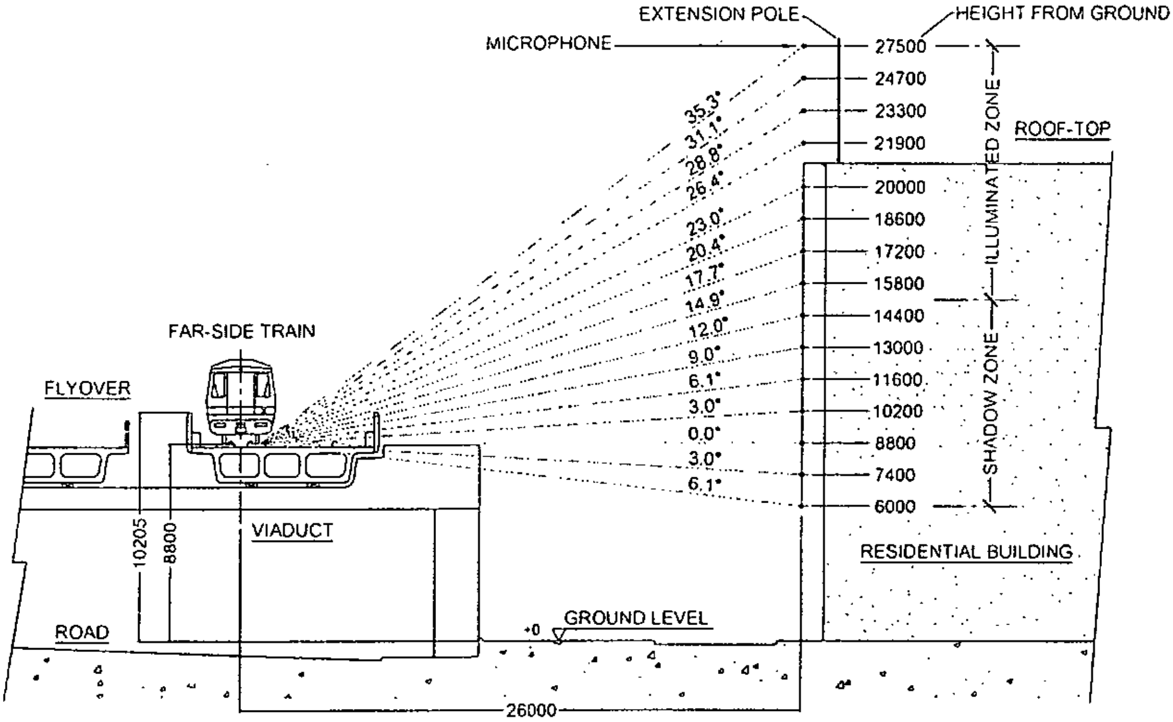

Figure 5.1. Illustration of the measurement of the noise from a train running on a viaduct.

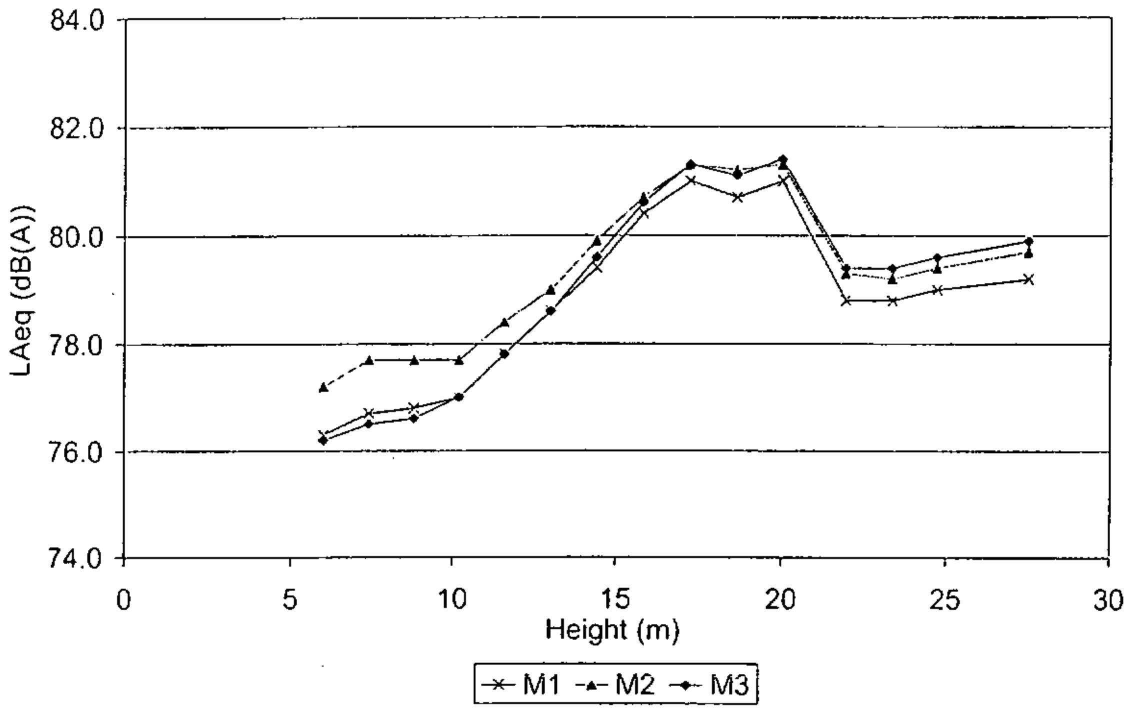

Figure 5.2. Results of measurements of train noise. The symbols M1, M2 and M3 represent the 1st, 2nd and 3rd measurement of train noise.

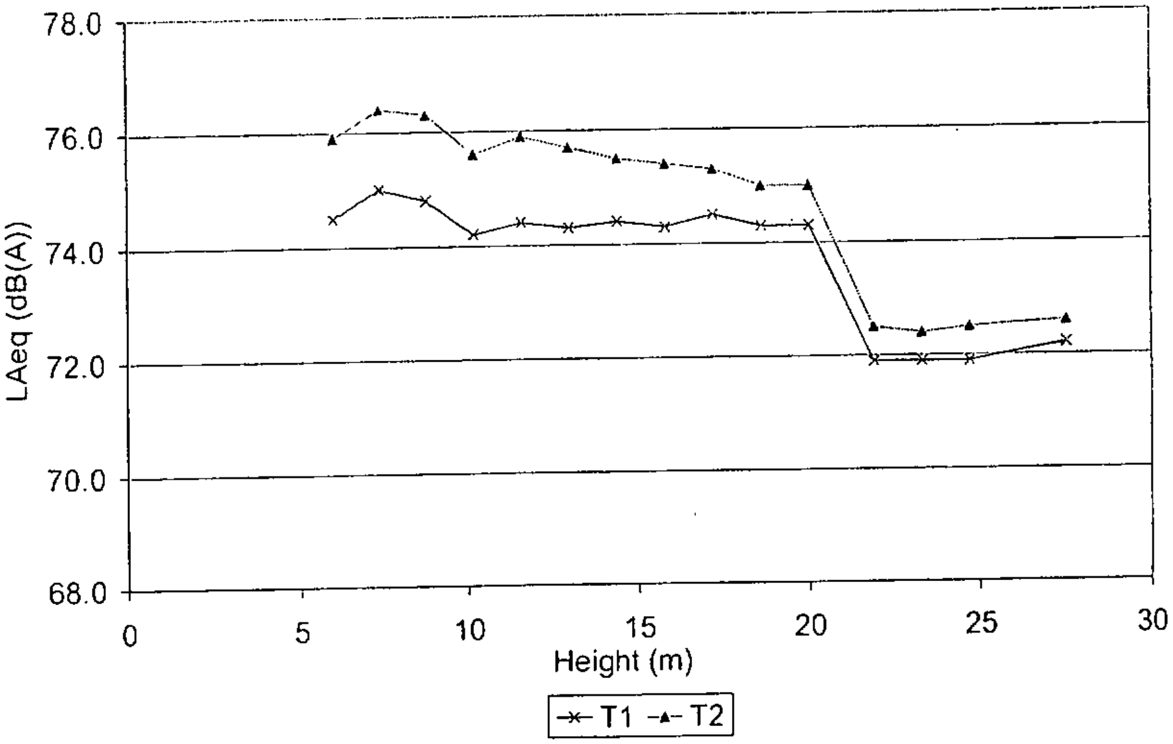

Figure 5.3. Results of control measurements of noise from road traffic. The symbols T1 and T2 represent the 1st and 2nd control measurement of road traffic noise.

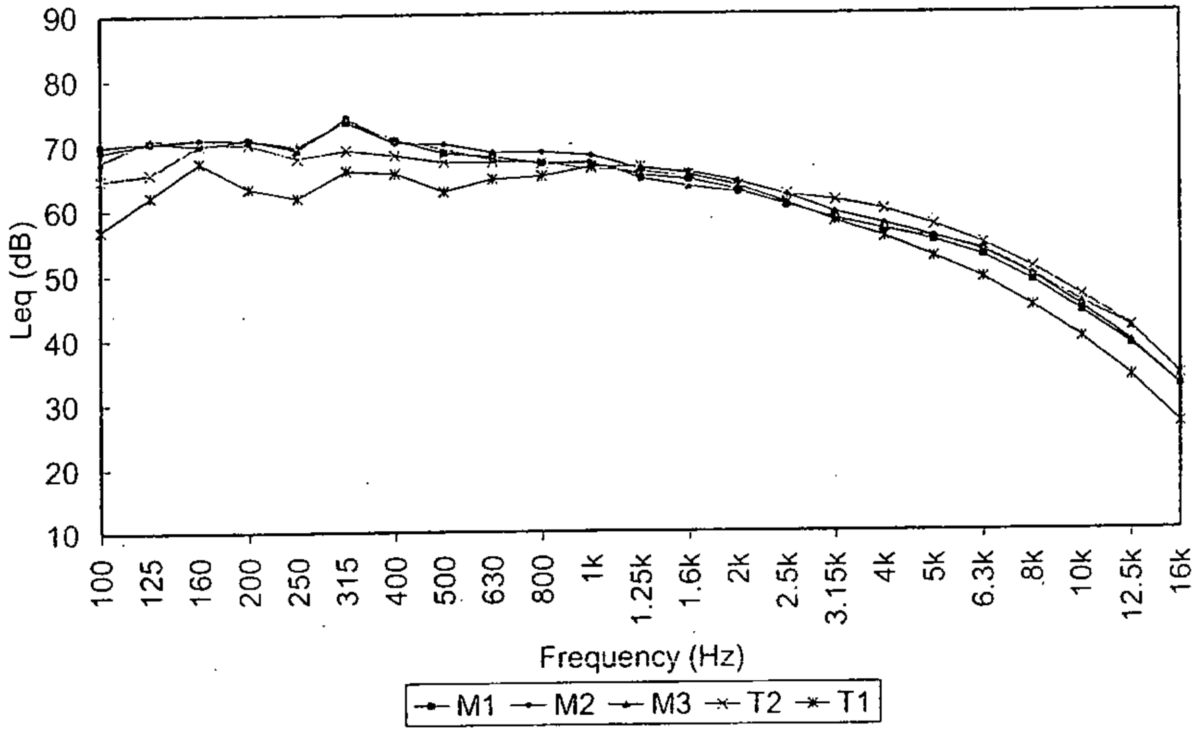

Figure 5.4. One-third octave bands spectra of mixed noise levels and road traffic noise at 6 m above the ground level. The symbols M1 - M3 represent the 1st, 2nd and 3rd measurement for the mixed noise. The symbols T1 – T2 represent the 1st and 2nd control measurement for the road traffic noise.

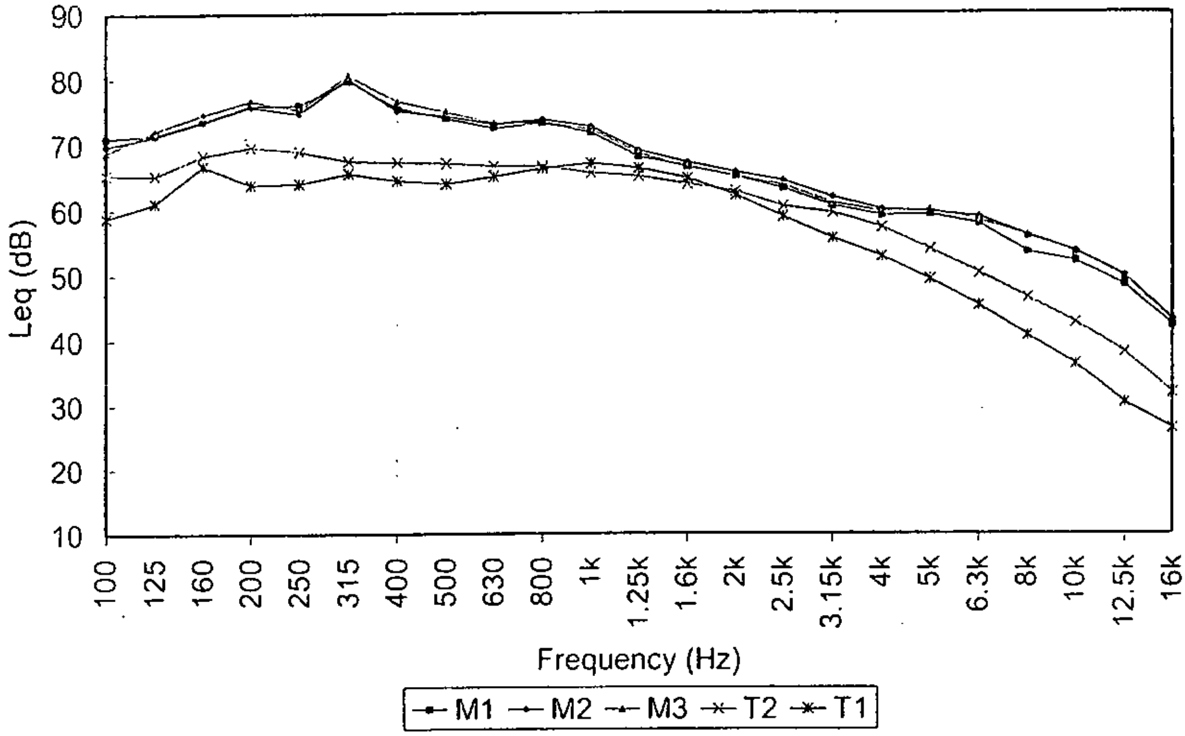

Figure 5.5. One-third octave bands spectra of mixed noise levels and road traffic noise at 20 m above the ground level. The symbols M1 - M3 represent the 1st, 2nd and 3rd measurement for the mixed noise. The symbols T1 – T2 represent the 1st and 2nd control measurement for the road traffic noise.

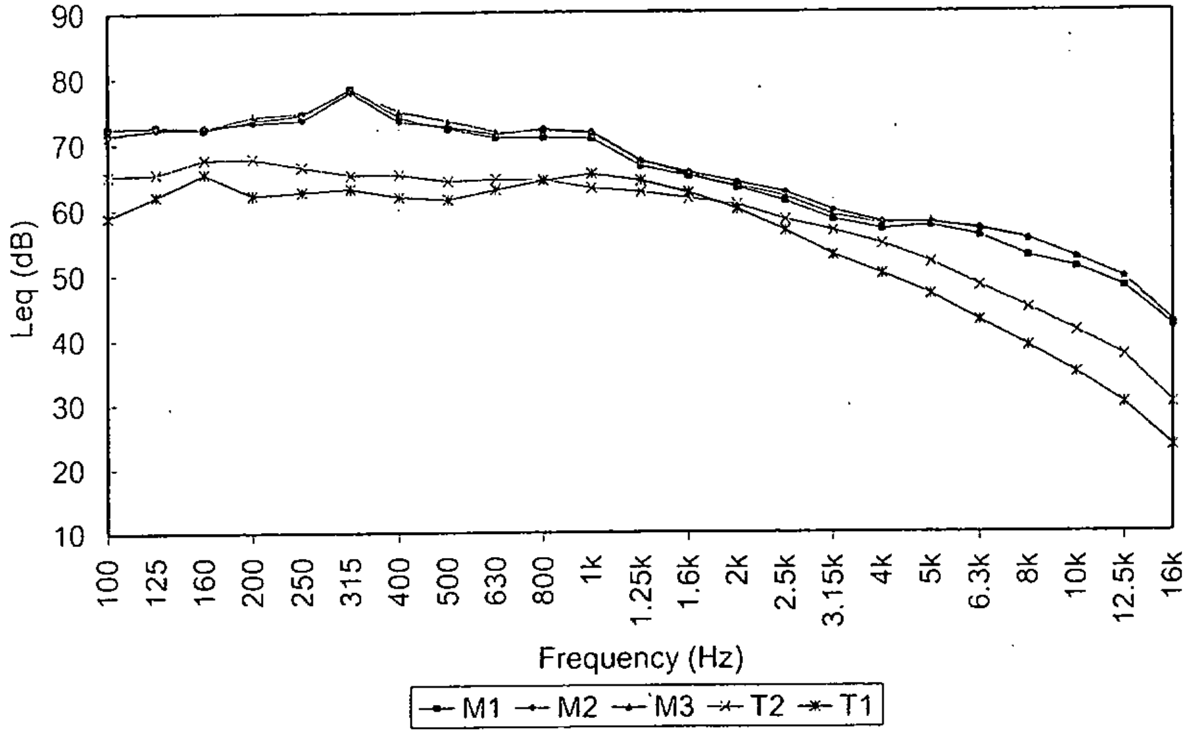

Figure 5.6. One-third octave bands spectra of mixed noise levels and road traffic noises at 27.5 m above ground level. The symbols M1 - M3 represent the 1st, 2nd and 3rd measurement for the mixed noise. The symbols T1 – T2 represent the 1st and 2nd control measurement for the road traffic noise.

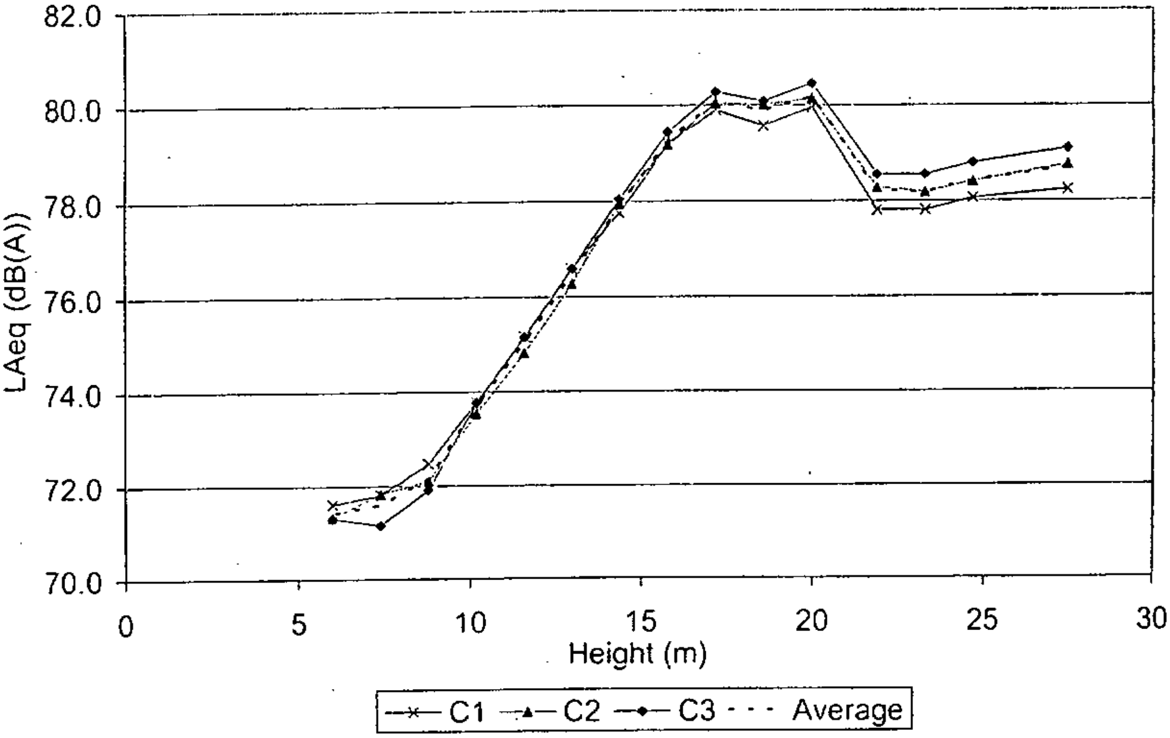

Figure 5.7. Extracted levels of train noise after the logarithmic subtraction of road traffic noise from the measured train noise.

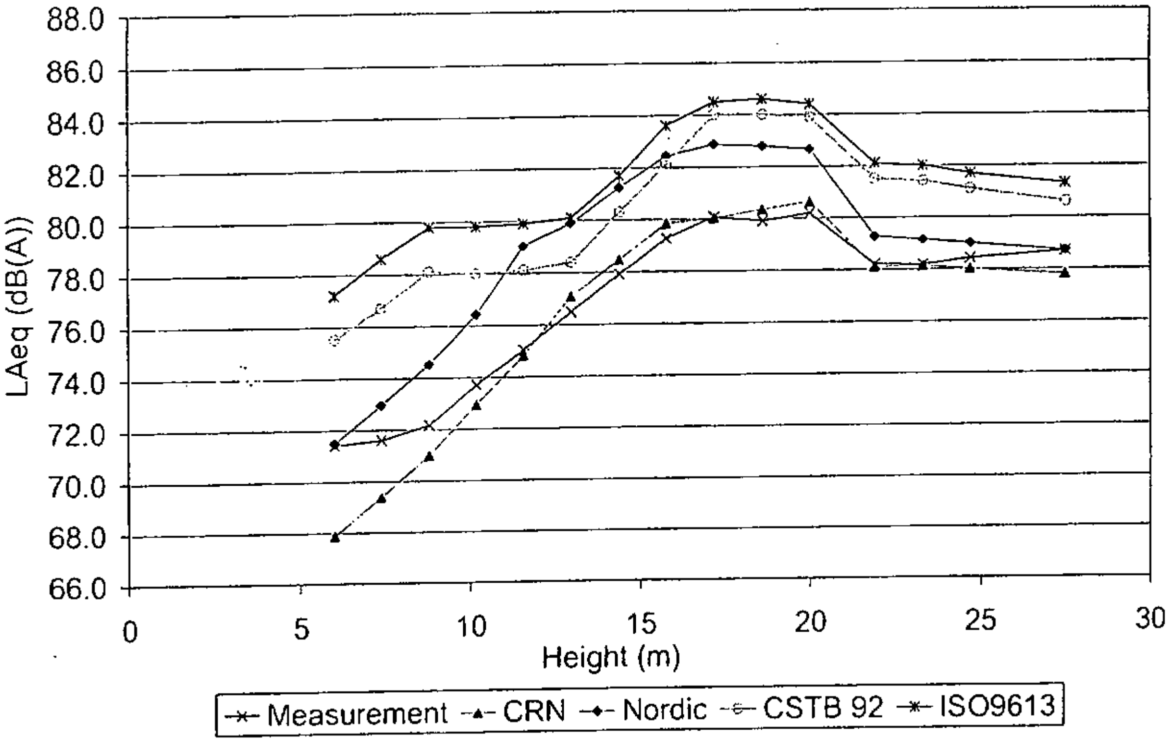

Figure 5.8. Comparison of the extracted levels of train noise using different prediction models.

Chapter 6

Modeling the Characteristics of Wheel/Rail Rolling Noise

6.1 Introduction

The Mass Transit Railway in Hong Kong currently operates a railway network route of 87 kilometres. With a daily capacity of over 2.3 million passengers, the system is one of the most intensively utilized systems in the world. The railway provides 19 hours of passenger service daily from 6 a.m. in the morning to 1 a.m. the following day. Each of the Urban Lines is capable of running 34 trains per hour in each direction. The frequency of the services, together with high-rise developments along the lines, have brought noise disturbances to nearby residential buildings in open sections that may be just 20 meters or so from the elevated railway. These constraints have led to many complaints, commonly lodged from residents on the higher floors.

In the last chapter, the applicability of different models for predicting the noise from a passing train running on a viaduct in a high-rise city have been assessed. Despite the fact that the method of *Calculation of Railway* (CRN) from U.K. gives the best prediction compared to other models, it does not provide an algorithm to count for the vertical directivity of the radiated train noise that is obvious in our study. Though it is widely accepted that the main source of noise from railway operations is the wheel/rail rolling noise that is dominant at speeds of below 220 km/h. The aerodynamic noise from the body of the vehicle is important and can dominate overall noise levels if the speed of a train is above 250 km/h. Other sources such as equipment, gear boxes, and air-conditioners are generally less important as far as the generation of noise is concerned in most situations [31][46][67][88][102][106][107] [113]. However, there is no consistent view on the pattern of vertical directivity due to a passing train. This is understandable, because the directivity of train noise changes according to the type of rolling stock and the methods of rail fixation and support [67]. This has prompted the current study on the sound radiation characteristics of modern electric multiple units.

In Sec. 6.2 of this chapter, we discuss theoretical models that are capable of modeling the sound energy radiating from a passing train. It is proposed that a semi-empirical factor is added to the prediction models to account for the vertical directivity. Noise measurements for different types of trains running under different operational conditions are reported in Sec. 6.3. The measured noise profiles will then be compared with those obtained using the prediction schemes to determine the models that best fit the measured data. An empirical formula to determine the vertical directivity will be discussed in Sec. 6.4.

6.2 Modeling train noise

A host of sources contribute to the overall level of noise emitted by a train. However, wheel/rail rolling noise is the dominant source of noise from mass transit trains operating at speeds of between 50 km/h and 130 km/h [31][46][67][88][102][106] [113]. A simpler model is the use of an incoherent line source for predicting wheel/rail rolling noise. The line source can be treated as a row of point sources that incoherently radiate sound. Suppose a receiver *P* is located at a height of *h* above the origin *O*. Figure 6.1 shows the geometrical configuration of an incoherent line source that is used to model a passing train of length *d*. In the figure, *S* is the nearest point of the source line to *P*, *n* is the normal distance from the source line to *P*, *R* is the slant distance from *S* to *P*, and ψ is the polar angle made with the *z*-axis and the line joining points *S* and *P*. The angle of elevation θ (where $\theta = \pi/2 - \psi$), which is measured at point *S*, is more commonly used to represent the vertical directivity of the train. It will be used instead of ψ in our analysis. The center of the train is located at a distance *l* from the point *S*. Let us consider a small train segment *dx* at a distance *x* from *S* along the source line, where *r* is the shortest distance from the train segment to *P* and ϕ is the azimuthal angle subtended from the train segment to *S*.

In the following paragraphs, the spherical radiation model for predicting the noise profile of train wheel/rail rolling noise will be used together with the radiation model developed by Hohenwarter [46]. In his cosine and dipole radiation model, Hohenwarter used the total angle, which is the angle between the vertical axis and the line joining the incoherent source with the receiver (see Fig. 6.1 for the angle marked ψ'). Consequently, in these earlier models, the radiation characteristic of train noise is only dependent on ψ'. In the present study, we propose the following somewhat different approach. The radiation characteristic of train noise can be decomposed into two independent parts: a horizontal and a vertical component. The horizontal directivity, which is assumed to be dependent only on the azimuthal angle ϕ, is the time signature (noise profile) of the passage of a train. A close examination of the situation suggests that the dominant contribution of the overall noise level comes from the segment of incoherent line sources located closest to the receiver. It is marked with *S* in Fig. 6.1. Since the level of sound exposure is used in our subsequent analysis for determining the noise level of a passing train, we therefore suggest that the function of the vertical directivity is dependent only on the angle of elevation θ instead of on the total angle ψ'.

We use an energy approach to estimate the sound field from a row of effective sources located at the center of the track. The A-weighted sound intensity received at P from the incoherent source of an elemental length dx can be modeled by

$$dI = \frac{(W/d)}{4\pi r^2} f(\phi) g(\theta) dx \tag{6.1}$$

where W is the total A-weighted sound power radiated by the train, d is the length of the train, and the distance r between source and receiver is given by

$$r^2 = n^2 + h^2 + x^2 \quad . \tag{6.2}$$

The dimensionless functions $f(\phi)$ and $g(\theta)$ denote the factors characterizing, respectively, the horizontal and vertical directivities of noise radiated due to the passage of a train. Here, the effect of ground reflection has been incorporated in the single term, W, the total sound radiated by the train. It is independent of the angles ϕ and θ, but is dependent on the speed of the passing train and other site conditions, such as the roughness of the track. Substituting Eq. (6.2) into Eq. (6.1) and evaluating the resulting expression, the total sound intensity yields

$$I = \frac{(W/d)}{4\pi} g(\theta) \left[F(l + d/2) - F(l - d/2) \right] \ , \tag{6.3}$$

where the integral function, $F(X)$, of the above equation is given by

$$F(X) = \int^{X} \frac{f(\phi)}{r^2} dx \, . \tag{6.4}$$

The A-weighted sound pressure level can then be expressed in terms of the functions of the horizontal and vertical directivity by noting that

$$L = 10\lg\left[\frac{I}{I_o}\right], \tag{6.5}$$

where I_o is the reference sound intensity given by 10^{-12} watts/m². In order to study the characteristics of noise radiating from trains, L is split into three parts: the source strength L_w, the radiation pattern due to the horizontal directivity L_h, and the vertical directivity L_v. Substituting Eq. (6.3) into Eq. (6.5), we can rewrite L as

$$L = L_w + L_h + L_v, \tag{6.6}$$

where

$$L_w = 10\lg\left[\frac{(W/d)}{4\pi I_o}\right], \tag{6.7}$$

$$L_h = 10\lg\left[F(l+d/2) - F(l-d/2)\right], \tag{6.8}$$

and $$L_v = 10\lg\left[g(\theta)\right]. \tag{6.9}$$

In the case of horizontal directivity showing a spherical radiation pattern, we have $f(\phi)=1$. The integral function, $F(X)$, can then be evaluated to give

$$F(X) = \frac{\tan^{-1}\left(\frac{X}{\sqrt{n^2+h^2}}\right)}{\sqrt{n^2+h^2}}, \tag{6.10}$$

For a cosine and a dipole radiation pattern, the horizontal directivity function, $f(\phi)$ can be written as $\cos\phi$ and $\cos^2\phi$, respectively. Using the cosine and dipole radiation patterns in Eq. (6.4) and integrating the resulting expressions, the respective integral functions can be written in closed forms as follows:

$$F(X) = \frac{n}{2h\sqrt{n^2+h^2}}\tanh^{-1}\left[\frac{2Xh(X^2+n^2)^{\frac{1}{2}}(n^2+h^2)^{\frac{1}{2}}}{h^2(X^2+n^2)+n^4+X^2(n^2+h^2)}\right] \tag{6.11}$$

and

$$F(X) = \frac{n^2}{h^2}\left[\frac{1}{n}\tan^{-1}\left(\frac{X}{n}\right) - \frac{1}{\sqrt{n^2+h^2}}\tan^{-1}\left(\frac{X}{\sqrt{n^2+h^2}}\right)\right]. \tag{6.12}$$

The vertical directivity exhibits a more intricate pattern than the horizontal directivity due to the combined effects of noise generated by the interaction between wheel and rail and the shielding effect of the carriage. The sound field contributed by the vertical radiation can be considered to be composed of multipole sources. Pierce [90] gave a detailed description of methods for calculating the sound field due to the multipole expansion. Here, we limit our analysis of the multipole expansion to the third order only; i.e., where the sound field is composed of a combination of a monopole, a dipole, and a quadrupole. The multipole expansion can be expressed in a rather compact form [90] as

$$p = S\frac{e^{ikR}}{R} - J\cdot\nabla\left(\frac{e^{ikR}}{R}\right) + \sum_{\mu,\nu} Q_{\mu\nu}\frac{\partial^2}{\partial\mu\partial\nu}\left(\frac{e^{ikR}}{R}\right), \tag{6.13}$$

where S, J and $Q_{\mu\nu}$ are the monopole source strength, dipole source strength, and quadrupole source strength, respectively. The dipole source strength can be expressed in vector form as

$$J = \begin{pmatrix} J_x & J_y & J_z \end{pmatrix}, \tag{6.14}$$

and the source strength of the quadrupole can be conveniently written in tensor form as

$$Q_{\mu\nu} = \begin{pmatrix} Q_{xx} & Q_{xy} & Q_{xz} \\ Q_{yx} & Q_{yy} & Q_{yz} \\ Q_{zx} & Q_{zy} & Q_{zz} \end{pmatrix}. \tag{6.15}$$

Restricting our attention to the field due to a monopole, a vertical dipole, and a longitudinal quadrupole aligned along the z-axis at P, the sound pressure can be simplified to yield

$$p = \left\{ S - J_z k \left(i - \frac{1}{kR} \right) \cos\psi + Q_{zz} k^2 \left[\left(1 - 3\cos^2\psi\right) \left(\frac{i}{kR} - \frac{i}{k^2 R^2} + \frac{1}{3} \right) - \frac{1}{3} \right] \right\} \frac{e^{ikR}}{R} . \quad (6.16)$$

Considering the time average intensity $\frac{1}{2}|p|^2 / \rho c$ in far fields ($kR >> 1$) and after some tedious calculations, we can show that the vertical directivity of the mean sound intensity at P can be modeled by the multipole expansion as a fourth-order polynomial in terms of $\sin\theta$ as follows:

$$g(\theta) = A_4 \sin^4\theta + A_3 \sin^3\theta + A_2 \sin^2\theta + A_1 \sin\theta + A_0 , \quad (6.17)$$

where the coefficients A_0 to A_4 are determined empirically from the measured data.

For the center of the train located closest to the receiver (i.e., at point S in Fig. 6.1) at time $t = 0$, the A-weighted sound exposure level can be evaluated using

$$SEL = 10\lg\left[\int_{-\infty}^{\infty} \frac{I}{I_o} dt \right], \quad (6.18)$$

Transforming the integral variable from the temporal domain to the spatial domain, the A-weighted sound exposure level can be integrated in the case where a passing train has a constant speed v. The sound exposure level can be written as

$$SEL = 10\lg\left[\int_{-\infty}^{\infty} \frac{I}{I_o} \frac{dx}{v} \right], \quad (6.19)$$

where the range of integration extends along the track to infinity at both ends. Similar to the case of computing sound pressure level, the A-weighted sound exposure level can be divided into three parts: the source strength SEL_0 at the reference position $(0, n, h_0)$, the normalized horizontal directivity D_h, and the normalized vertical directivity D_v, as follows:

$$SEL = SEL_0 + D_h + D_v , \quad (6.20)$$

where

$$SEL_0 = 10\lg\left[\frac{(W/d)g_0 H_0}{4\pi I_0 v}\right], \tag{6.21}$$

$$D_h = 10\lg[H(n,h,d)/H_0], \tag{6.22}$$

$$D_v = 10\lg[g(\theta)/g_0], \tag{6.23}$$

$H_0 \equiv H(n,h_0,d)$, and $g_0 \equiv g(\theta_0)$ are the respective horizontal and vertical directivities at the reference position where the receiver is located at $(0,n,h_0)$ with $\cos\theta_0 = h_0/\sqrt{n^2+h_0^2}$. The use of SEL_0, D_h , and D_v becomes apparent in the following section when we analyze the experimental data. The definite integral, $H(n,h,d)$, in Eq. (6.22) is a function of the position P and the length of the train, d. It is given by

$$H(n,h,d) = \int_{-\infty}^{\infty}[F(l+d/2) - F(l-d/2)]dl. \tag{6.24}$$

Applying Taylor's expansion for $F(l+d/2)$ and $F(l-d/2)$, and noting that the property of $F(l) = -F(l)$, we can show that

$$H(n,h,d) = 2d \cdot \lim_{l\to\infty}[F(l)]. \tag{6.25}$$

The respective integral functions $H(n,h,d)$ for the horizontal directivity with spherical, cosine, and dipole radiation patterns can be evaluated analytically to closed form solutions. They are given as follows:

$$H(n,h,d) = \frac{d\pi}{\sqrt{n^2+h^2}}, \tag{6.26}$$

$$H(n,h,d) = \frac{dn}{h\sqrt{n^2+h^2}}\tanh^{-1}\left(\frac{2h\sqrt{n^2+h^2}}{2h^2+n^2}\right), \tag{6.27}$$

and

$$H(n,h,d) = \frac{dn\pi}{h^2\sqrt{n^2+h^2}}\left(\sqrt{n^2+h^2} - n\right). \tag{6.28}$$

Using Eqs. (6.20) to (6.23), it is possible to calculate sound exposure levels as long as the relative sound power level, normalized horizontal directivity, and the normalized vertical directivity are determined. In the following sections, we describe an experimental study for validating the theoretical model detailed above.

6.3 Noise measurements

In Hong Kong, all rolling stock consists of electric multiple units that are fed via a pantograph to an overhead power line. Most sections of the Mass Transit Railway are operated underground in populated urban areas, but about one-third of rail tracks are built on concrete viaducts or on ballast grounds. Their operations at the exposed sections are sources of nuisance to neighborhood communities, especially in the early hours of the day.

The Mass Transit Railway operates two main types of railway vehicles. The first type of rolling stock, which was designed in the mid-1970s, is operated in all Urban Lines. All wheels are fitted with tread brakes. The second type of rolling stock is used in the Lantau Airport Railway (LAR), which consists of the Airport Express Line (AEL) and the Tung Chung Line (TCL). The LAR, came into service in 1997, is operated with more modernized rolling stock, where all wheels are fitted with disc brakes. All rails in both the Urban Lines and the LAR are the continuously welded type and most of the trackform is built with a concrete slab track. Since the MTR trains are operated at speeds of well below 130 km/h, the noise that they radiate is mainly dominated by the interaction between wheels and rail, which exhibits different radiation characteristics. In fact, their noise levels depend on the type of trains, bogies, and wheels that are used, together with characteristics of the railway system including the rails, sleepers, and track beds.

In the current study, we endeavor to develop a simple numerical model to predict the directivity pattern of train noise, which can be applied to different types of trains. Initially, the normalized vertical directivity of the AEL trains was determined from the measurement data. Two sets of measurements were carried out in two different sites in order to construct a complete pattern of the normalized vertical directivity of the AEL trains. This normalized vertical directivity pattern would then be used to compare the measured data of the TCL and Urban Line trains. A total of four different sets of measurements were carried out in three different sites in order to study the directivity of the train noise from different types of trains. This experimental data permitted an extensive study of the characteristics of the noise radiated by different types of trains.

In all of the measurements, the noise levels were recorded by a digital data recorder through free-field microphones with matching preamplifiers and wind shields. The recording system (microphone, preamplifier, and the digital data recorder) was carefully calibrated before and after any measurements of train noise to ensure that there was no significant drifting error in electronic equipment. The recorded data were subsequently analyzed in the laboratory using 01dB-Stell post-processing software.

6.3.1 Test trains of the AEL at Siu Ho Wan

To study the directivity of train noise at various speeds, a seven-car AEL test train 158 m in length was recruited for measurements. The noise levels at angles of elevation of between 4° and 86° were measured through 14 microphones attached to the portal bracing, as shown in Fig. 6.2. The experiments were conducted from 1:00 a.m. to 5:00 a.m. at Siu Ho Wan (SHW) during the non-traffic hours when no other passenger trains were in operation. As a result, the test trains were allowed to run at various speeds for the study. Since Siu Ho Wan is located in a suburban area and the experiments were conducted in the early hours of the morning, the lowest possible level was lower than that from passing trains by at least 20 dB throughout the measurement period. The test train was run on the ballast track at the following three different speeds: 60 km/h, 80 km/h, and 100 km/h. There was only a single measurement for each train speed because time was limited during the testing period. Since the test train was the same type of vehicle as that used for AEL passenger trains, three extra measurements for AEL passenger trains running on the same track at a nominal speed of 110 km/h were also made during the routine period in the evening immediately before the day of the field measurements. The measured data were subsequently analyzed for A-weighted sound pressure levels and A-weighted sound exposure levels in order to construct a noise profile for the horizontal and vertical directivities. The measured sound exposure levels were normalized such that the lowest measured sound exposure level at the smallest elevation angle (approximately 4° in this case) was used as the reference point. The normalized sound exposure levels for different speeds are plotted in Fig. 6.3. In the same figure, the variation in the measured data for the AEL passenger trains was also shown, indicating the repeatability of the measured data. The curves for the normalized sound exposure levels at different speeds show a similar trend in variation with the angle of elevation. The amplitude of the sound exposure level appears to be dependent on the speed of the train. Nevertheless, the sound exposure levels show large fluctuation at angles of elevation of less than 44°. This was largely due to the effect of the ground topography of the measurement site. The effect was particularly noticeable for the field points located close to the ballast track.

6.3.2 Test trains of the AEL at the LAR depot

Since the measured data at lower angles of elevation in the previous measurements were possibly influenced by the topographical effect of the measurement site, supplementary measurements were carried out at the LAR depot to fill the gap in the data within this range. An AEL test train 68 m in length, and consisting of three carriages, was used in the second set of noise measurements. The train was run at the maximum allowable speed of 60 km/h. The measurements were made 7.5 m from the center of the track as shown in Fig. 6.4. An array of thirteen microphones was mounted on a vertical pole with a maximum height of 7 m. The pole was erected on concrete ground in the vicinity of the test track. In this set of measurements, three separate measurements were made for the angles of elevation varied between 4.9° and 40.7°. The depot was located a few kilometres from the test site of the last set of experiments and, again, it was located in a suburban area about 500 m away from trunk roads. The level of background noise at the depot was 60 dB(A). The measured sound exposure levels were normalized such that the lowest measured sound exposure level at the smallest elevation angle (4.9° in this case) was set to zero. The normalized sound exposure levels at various angles of elevation are presented in Fig. 6.5. The variations in the measured noise levels for different test runs are also shown.

In this set of measured data, they show good repeatability, as the deviations in the measured levels are generally less than 1 dB(A).

6.3.3 AEL and TCL tests on the mainline track

The noise measurements of the AEL and TCL trains running passenger services on a ballast track were conducted at exactly the same location as in the previous section (see Fig. 6.6.) The same experimental set-up was also used. The AEL and TCL trains are 158 m in length and consist of seven-car electrical multiple units. The AEL and TCL service trains travel at a nominal speed of 120 km/h when passing the monitoring station. The measurement points were located at a horizontal distance of 26 m from the center of the track and their respective angle of elevation varied from 1.7° to 14°. In this set of experimental data, five noise measurements for the TCL trains and one noise measurement for the AEL trains are shown. In presenting the data, the sound exposure levels are normalized at the minimum noise level measured at the lowest angle of elevation, i.e. 1.7°, in this set of data. The sound exposure levels against elevation angles are plotted in Fig. 6.7 for the TCL trains as well as for the AEL trains.

All measured data at different runs for different trains demonstrate a consistent trend. This is reasonable because the AEL and TCL trains have basically the same principal features: they have the same bogies but differ in coach design. We expected the noise profiles of the AEL and TCL trains to be rather similar. However, at all measuring points, the mean noise levels of the AEL trains were about 1 dB(A) higher than that of the TCL trains. This is due to the different sound power levels for these two different types of trains. This is understandable because, according to their respective maintenance records, the AEL trains have a better wheel truing schedule than the TCL trains. This results in a quieter operation for the AEL trains.

6.3.4 Mainline service trains at the Urban Lines

To demonstrate the validity of the model in a more complex environment, a fourth set of noise measurements was conducted in an urban setting for the mainline service trains operating in the Urban Lines. The trains of the Urban Lines, which consisted of electrical multiple units of eight carriages with a total length of 180 m, were operated on a concrete viaduct in a busy trunk road with many road traffic vehicles contributing to the overall noise levels in the neighborhood communities. The trains travelled at a nominal speed of about 50 km/h. Measurements were taken at a residential building about 26 m away from the center of the track, as shown in Fig. 6.8. The measurements were conducted around midnight, so that the influence of the noise from road traffic would be much reduced because of a significant reduction in the volume of traffic. All measurements were made with receivers placed in the illuminated zone; i.e., the measurement points and the track were in direct-line-of-sight contact. Four microphones were placed 1 m from the façade of the building by suspending them from the rooftop of the building. An extension pole mounted with microphones was erected above the floor of the rooftop to provide four extra measurement points. The effect of sound reflecting from the façade of the building was corrected by subtracting 2.5 dB(A) (as adopted by CRN [29]) from the measured sound exposure level. Three separate measurements were taken for this set of data. In Fig. 6.9, we present the normalized sound exposure levels plotted against the angle of elevation. The experimental results show a reasonable trend and, hence, they will be used in our subsequent analysis.

6.4 Analysis of experimental data and discussions

The noise profile of a passing train is a time history of the measured levels of noise at a given reception point. It can be treated as the "signature" of the noise levels during the period of the passing of the train. The rise and decay of the sound level during the passing of a train is influenced by the characteristics of the component sources. Transforming from the temporal to spatial domain, the directivity pattern in a horizontal plane can be determined by comparing the predicted A-weighted sound pressure level with the measured noise profile of a passing train. Many previous theoretical and experimental studies [12][46][88][94] have suggested that the noise profiles of a railway train can be predicted reasonably well by using monopole, dipole, or cosine models. However, the total angle ψ' is used in these earlier models where the effect of the vertical directivity is inseparable from that of the horizontal directivity pattern. In the present formulation, their respective effects are handled separately through the use of the azimuthal angle ϕ and the angle of elevation θ in favor of the total angle ψ'. The advantage of our choice is that $H(n,h,d)$ and, hence, the normalized horizontal directivity D_h [(see Eq. (6.22)] can be expressed in simple analytical solutions. As the overall sound exposure level can be expressed in terms of the radiation characteristics in the vertical plane, consequently, the effect of the vertical directivity can be isolated and determined in a straightforward manner from measurements.

Although Cato [12] has published a comprehensive set of data comparing the measured noise profiles with the theoretical predictions, we display fives sets of typical measurements in Figs. (6.10) to (6.14) for future reference. The abscissa of these figures is the distance l between S and the centre of source line. In all these figures, the sound pressure levels are normalized such that the maximum noise levels are set to zero. It is worth stressing that our measured noise profiles generally agree well with the predicted A-weighted sound pressure levels at all angles of elevation in different measurement sites.

The principal aim of the current study is to derive an empirical formula for the vertical directivity of the noise radiated by a railway train. The model is based on a physical model, where the radiated noise is composed of a combination of monopole, dipole, and quadrupole sources. In the following paragraphs, we endeavor to describe a method of deducing the empirical formula for determining the vertical directivity pattern of the noise made by a passing train.

The best way of evaluating the sound energy radiated by a passing train is to measure the sound exposure level [67] that describes a receiver's cumulative noise exposure from a single noise event. This is represented by the total A-weighted sound energy during the noise event normalized to a period of one second. The vertical directivity of train noise can be determined by rearranging Eq. (6.20) to yield

$$D_v = SEL - SEL_0 - D_h , \tag{6.29}$$

where the source strength is generally unknown, as it is dependent on the characteristics of the wheel/rail interaction and the likely shielding effect of the train carriages. It is convenient to establish a "reference" point where all measured data are compared and the data is then corrected by the factor of the normalized horizontal directivity, D_h. The term D_h can be evaluated by using Eq. (6.22), where $H(n,h,d)$ is given by Eq. (6.26) if the horizontal directivity is modeled as a point source with monopole radiating characteristics. The term $H(n,h,d)$ is calculated by invoking either Eq. (6.27) or (6.28) if the horizontal directivity is modeled as a point source with radiating characteristics of a dipole or a cosine function, respectively. However, it is worth pointing out that the noise profile rises to the maximum level when the head of train approaches *S* and is maintained at almost this level until the end of the train completely retreats from this point. In other words, this period is the time required for the center of train *l* travels from *–d/2* to *d/2* (see Figs. (6.10) to (6.14)). In this case, the cumulative noise exposure at *P* during this period dominates the total sound energy received by *P* in the noise event. Either one of the three horizontal radiation models, i.e. monopole, dipole, and cosine, allows for a reasonable prediction of the maximum level of the noise profile. According to any of these different models, the predicted sound exposure level differs by a factor of no more than 0.5 dB(A), which is well within the measurement errors. Hence, in our subsequent analysis, we choose the monopole model for the sake of simplicity to evaluate D_h in Eq. (6.29).

In our analyses, an empirical formula of the directivity factor $g(\theta)$ for the AEL train will be determined initially. The applicability of this empirical formula for use in other electrical railway systems will then be validated by comparing it with the measured data at other measurement sites.

The normalized vertical directivity D_v of the AEL test trains at the LAR depot were calculated and normalized with the reference noise measurements at $\theta = 4.9°$ (see Fig. 6.15). In the present calculations and all subsequent calculations, averaged sound exposure levels were used in cases where there were separate measurements for the same conditions of operation. The noise exposure levels of the AEL passenger trains at Siu Ho Wan were also used to determine the empirical formula. Again, the vertical directivities were normalized at $\theta = 4.9^\circ$. This set of data was used in conjunction with data obtained at the LAR depot for the test train. It is possible to obtain a complete pattern of the vertical directivity against angles of elevation of 0° to 90°. We note that the data measured at the lower angles of elevation were strongly affected by the complex topography of the site at Siu Ho Wan. These data are shown in Fig. 6.15 but are not used to determine the empirical formula for $g(\theta)$, described as follows.

Since the sound power W radiated by the train is generally not known, it is more convenient to find out the normalized directivity factor $g(\theta)/g_o$ rather than $g(\theta)$. Assume that the directivity pattern for $g(\theta)/g_o$ is given by Eq. (6.17) with the coefficients replaced by A_0' – A_4', respectively. The normalized coefficients can be determined by the least-squares method. Suppose there are n set of data points. The total "error" between theoretical predictions and experimental measurements can be determined by

$$E = \sum_{i=1}^{n}\left[(A_4'\sin^4\theta_i + A_3'\sin^3\theta_i + A_2'\sin^2\theta_i + A_1'\sin^3\theta_i + A_0') - 10^{\frac{D_v(\theta_i)}{10}}\right]^2, \quad (6.30)$$

where θ_i is the angle of elevation of the data point and $D_v(\theta_i)$ is the measured data for the normalized vertical directivity that has been corrected according to Eq. (6.29). The coefficients A_0' – A_4' are allowed to vary in order to minimize E. The best-fit curve for $g(\theta)/g_o$ is obtained as

$$g(\theta)/g_o = 28.1\sin^4\theta - 59.1\sin^3\theta + 35.6\sin^2\theta - 5.6\sin\theta + 1.3\,. \quad (6.31)$$

It is interesting to observe that the normalized vertical directivity increases with the angles of elevation to its maximum level at about 30°, and then reduces to its minimum level at 90°. The reduction in noise levels is largely due to the partial screening effect of the rail carriages as they provide shielding from wheel/rail rolling noise. It is reasonable to expect that the noise level reduces to the minimum level at 90° because the source of the noise is completely shielded when the reception point is located right over the rail carriages.

In Fig. 6.15, we also display the experimental results of other measurement sites to explore any similarities that may exist with the vertical directivity pattern. In addition to our measured result for the Urban Lines, we also use Chew's measurement results summarized in Table 1 of Ref. [15] for further comparison. In his experiment, Chew measured the maximum noise levels of a passing train with a running speed of 80 km/h to compute the levels of noise from a passing train. The measured noise levels were averaged and normalized. They were then compared with the normalized vertical directivity based on the empirical model given in Eq. (6.31). It is enlightening to observe that Chew's data and other noise measurements agree reasonably well with the empirical formula. The current study for a passing train reveals the fact that the vertical directivity pattern is possibly dominated by the shielding effect of train carriages. Although different rail systems may operate at different conditions in different sites, their respective vertical directivity patterns are surprisingly similar and can be represented by the same empirical formula.

6.5 Summary

This study reveals that the noises radiating from different electrical train systems display a rather similar vertical directivity pattern where the noise levels increase with the angle of elevation up to about 30°. The directivity pattern reaches a maximum level and then reduces to a minimum level at 90°. It has also been demonstrated that train noise can be modeled by a combination of monopole, dipole, and quadrupole sources. Based on this physical model, the vertical radiation characteristic can be modeled by a fourth-order polynomial in terms of $\sin\theta$, where θ is the angle of elevation. With the proposed model, see Eqs. (6.20) to (6.23), it is possible to compute the short-distance propagation of train noise in urban districts with high-rise buildings. The model is particularly useful because it provides an empirical scheme for estimating the vertical directivity of train noise in high-rise cities.

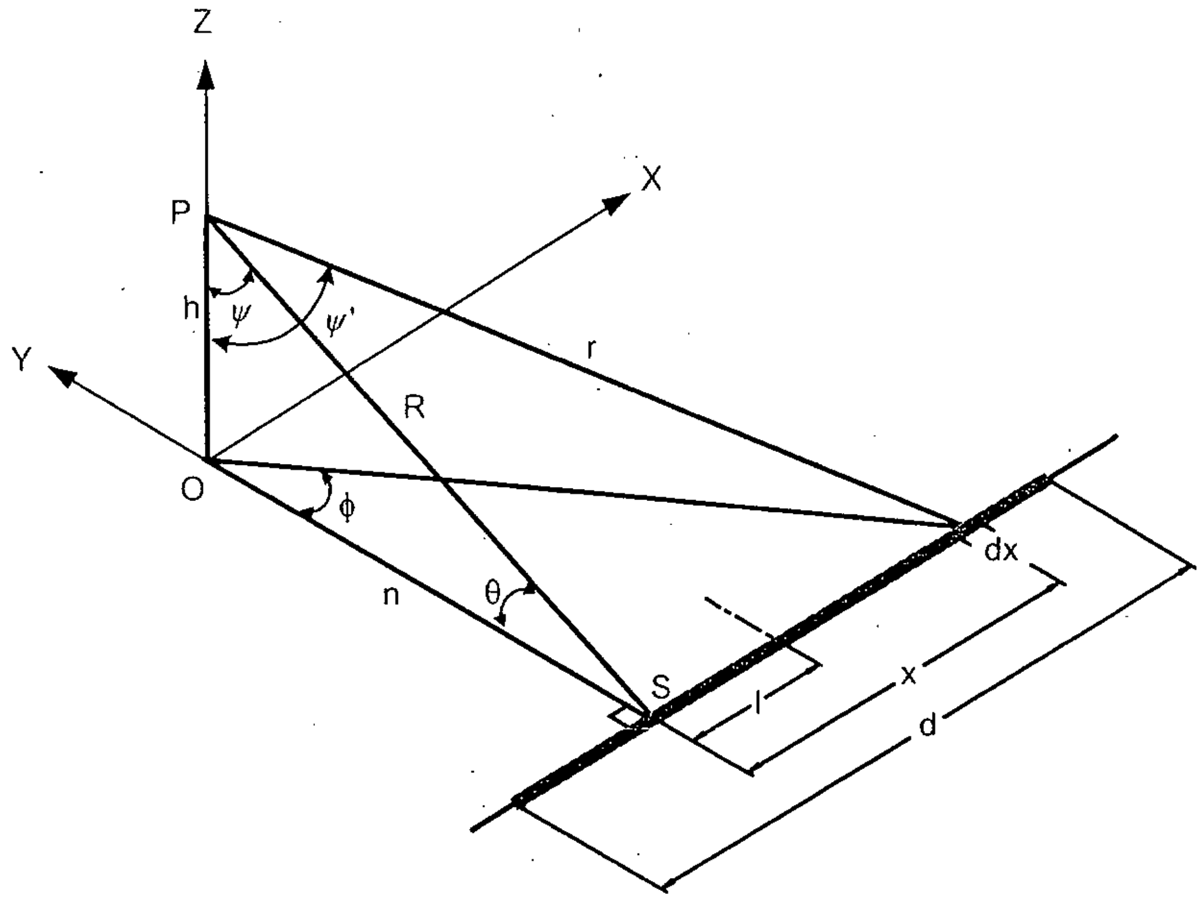

Figure 6.1: Illustration shows the geometrical parameters for the computation of the noise of a passing train.

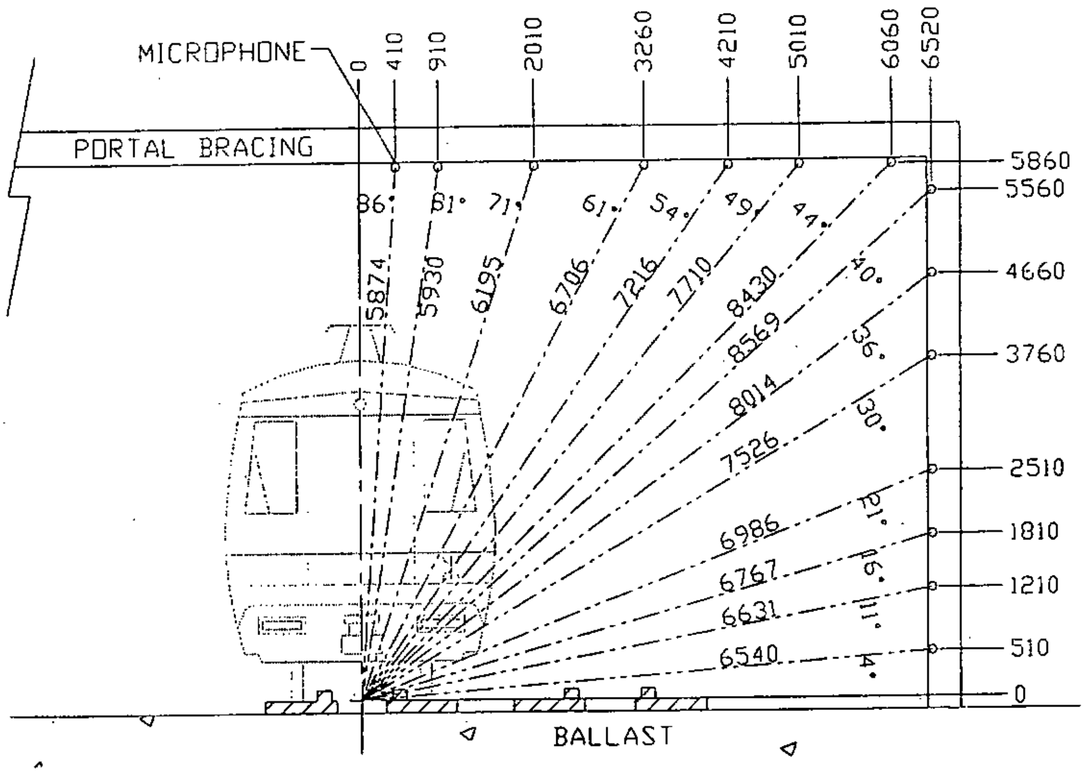

Figure 6.2: Noise measurement for AEL trains (7-cars) at Siu Ho Wan.

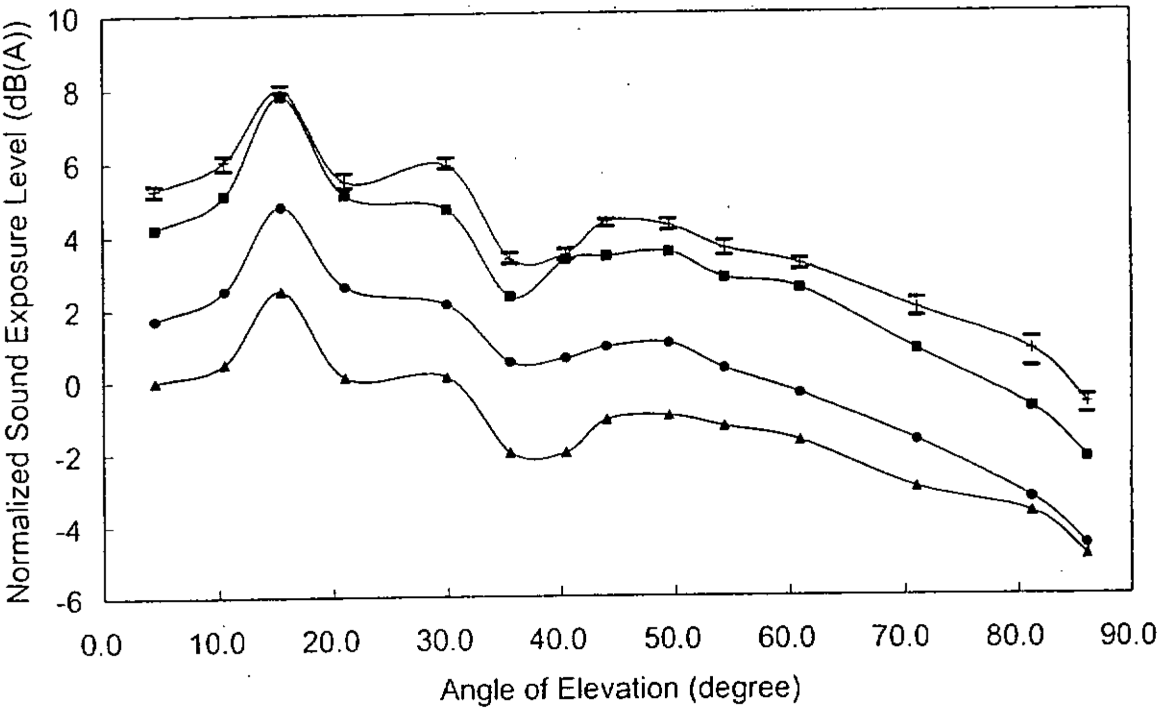

Figure 6.3: The normalized sound exposure levels for the AEL test train running at different speeds (▲ – 60 km/h; ● – 80 km/h; ■ – 100 km/h). The means (marked with "+") and normalized sound exposure levels for the AEL passenger trains running at 110 km/h.

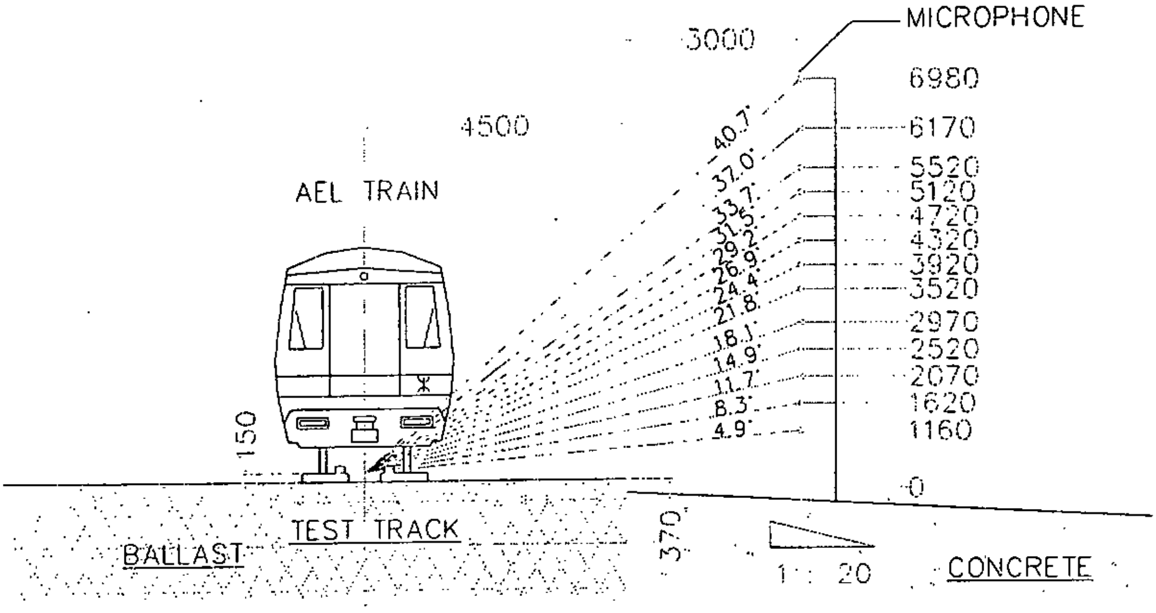

Figure 6.4: Noise measurement for the AEL test train (3-cars) at the LAR depot.

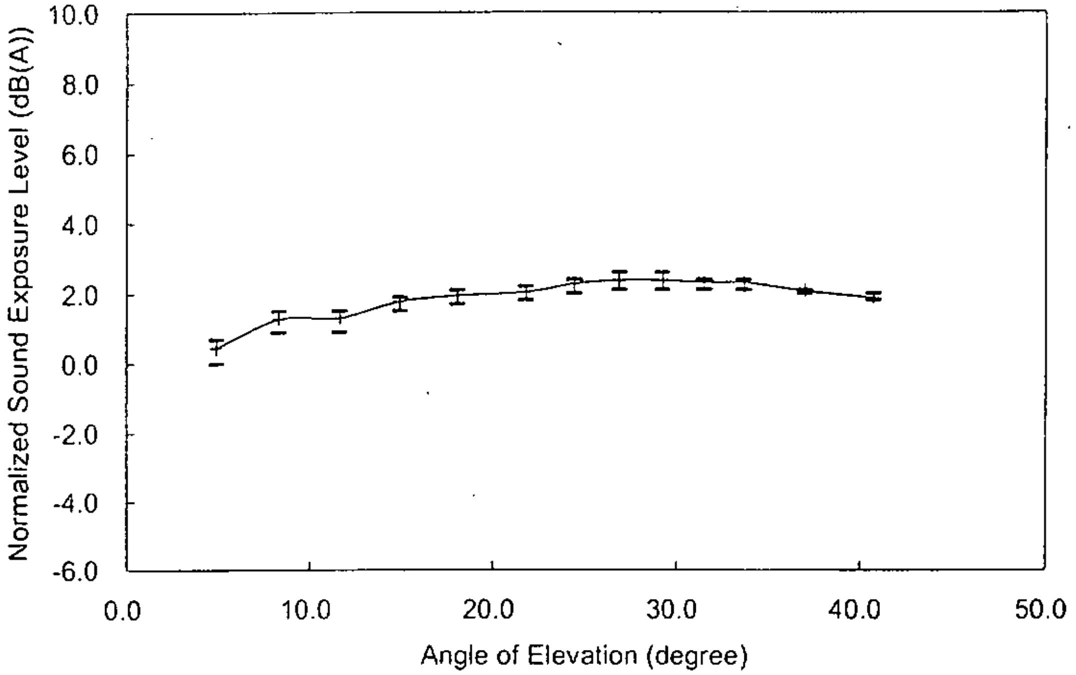

Figure 6.5: The means and normalized sound exposure levels for the AEL test train running at 60 km/h at the LAR depot.

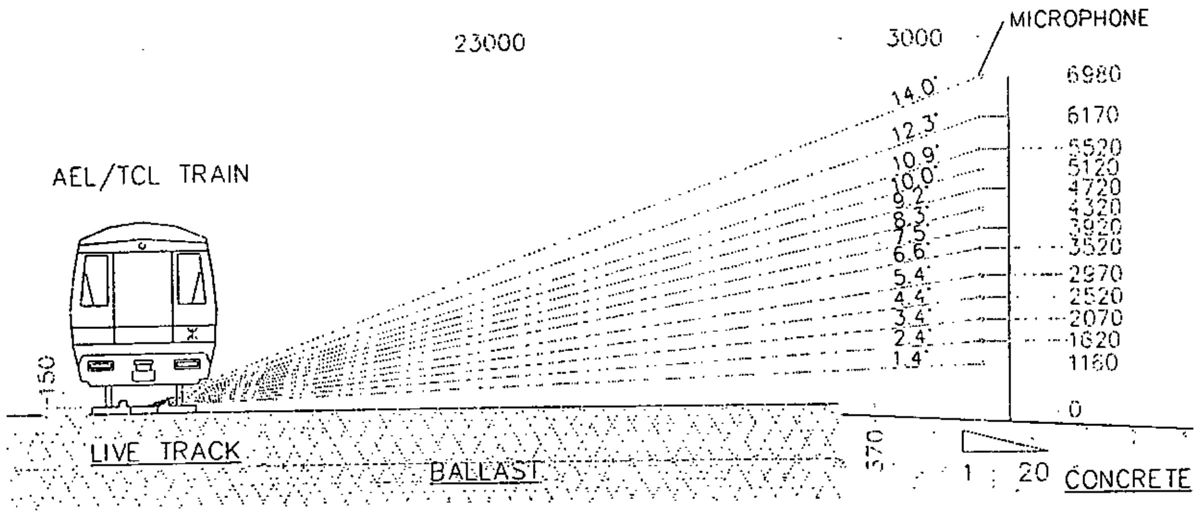

Figure 6.6: Noise measurement for the AEL/TCL passenger train at the LAR depot.

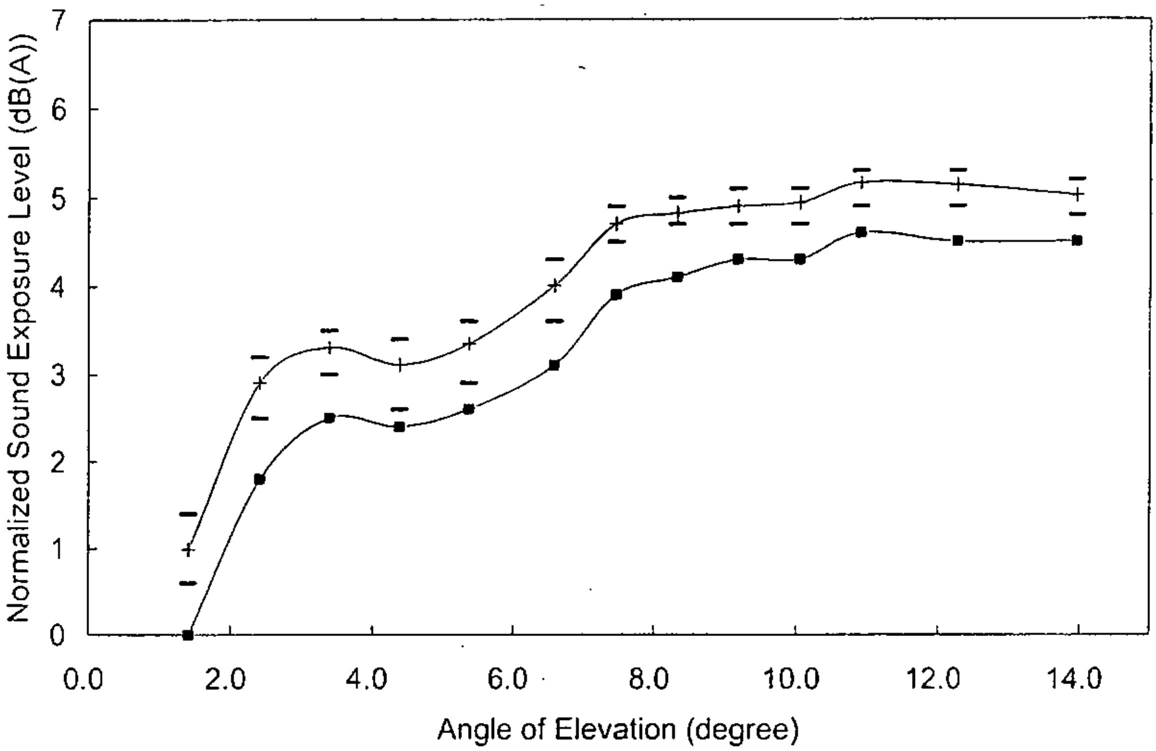

Figure 6.7: The means (marked with "+") and normalized sound exposure levels for the TCL passenger trains running at the LAR depot. The normalized sound exposure levels for the AEL passenger train running at the LAR depot are marked with "■."

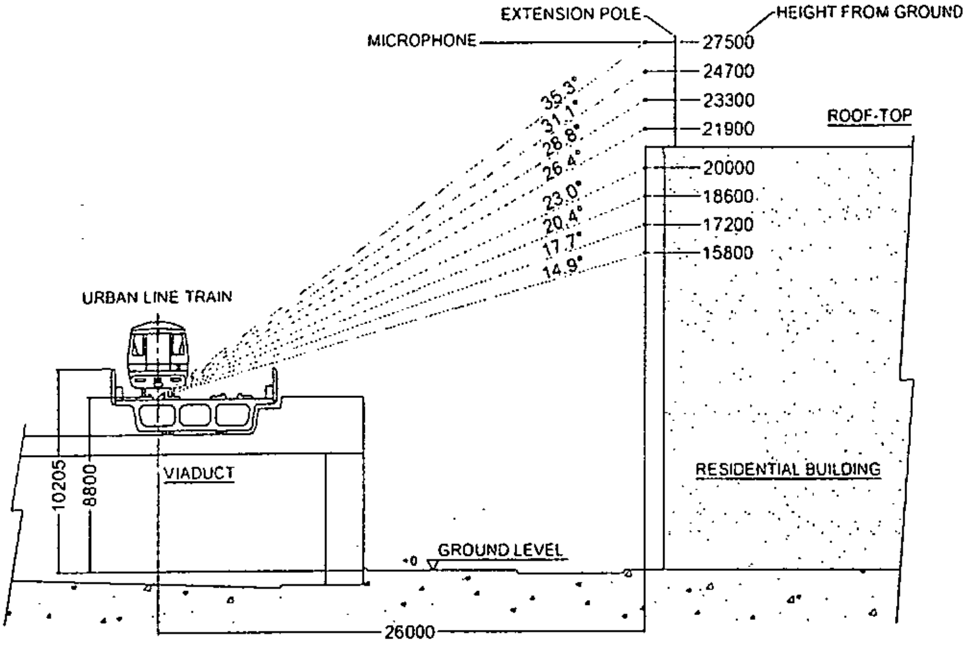

Figure 6.8: Noise measurement for Urban Line trains running on a viaduct.

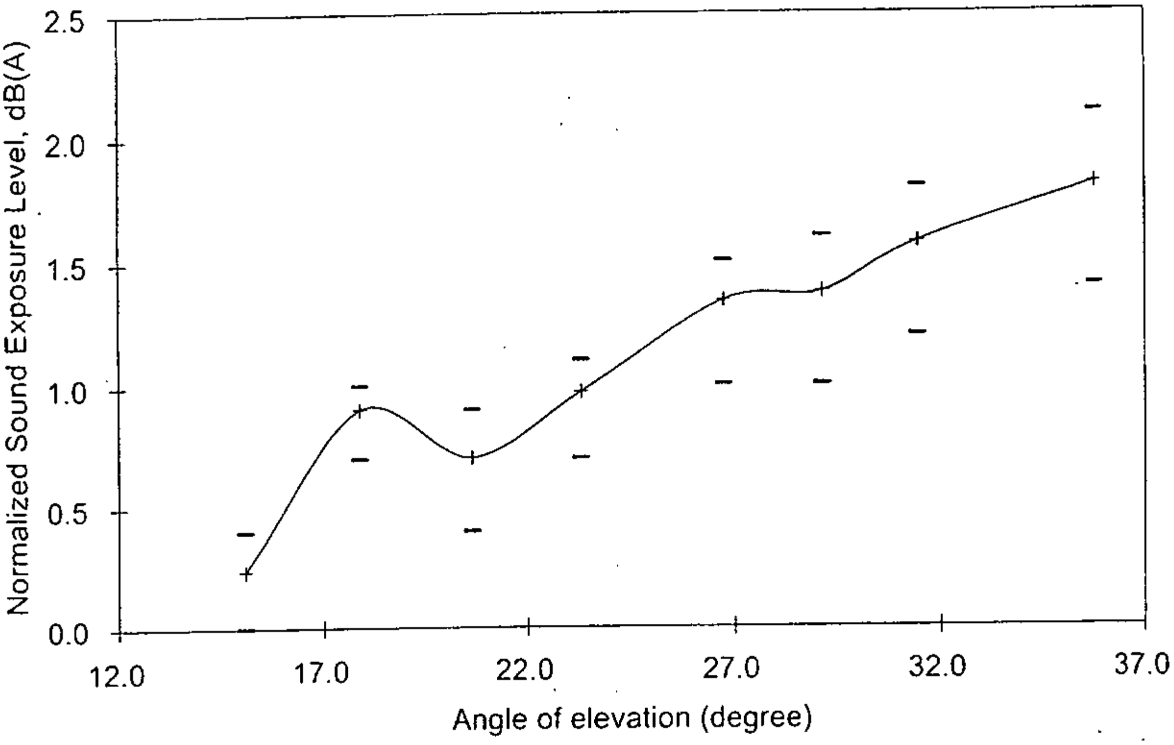

Figure 6.9: The means and normalized sound exposure levels for Urban Line trains running on a viaduct.

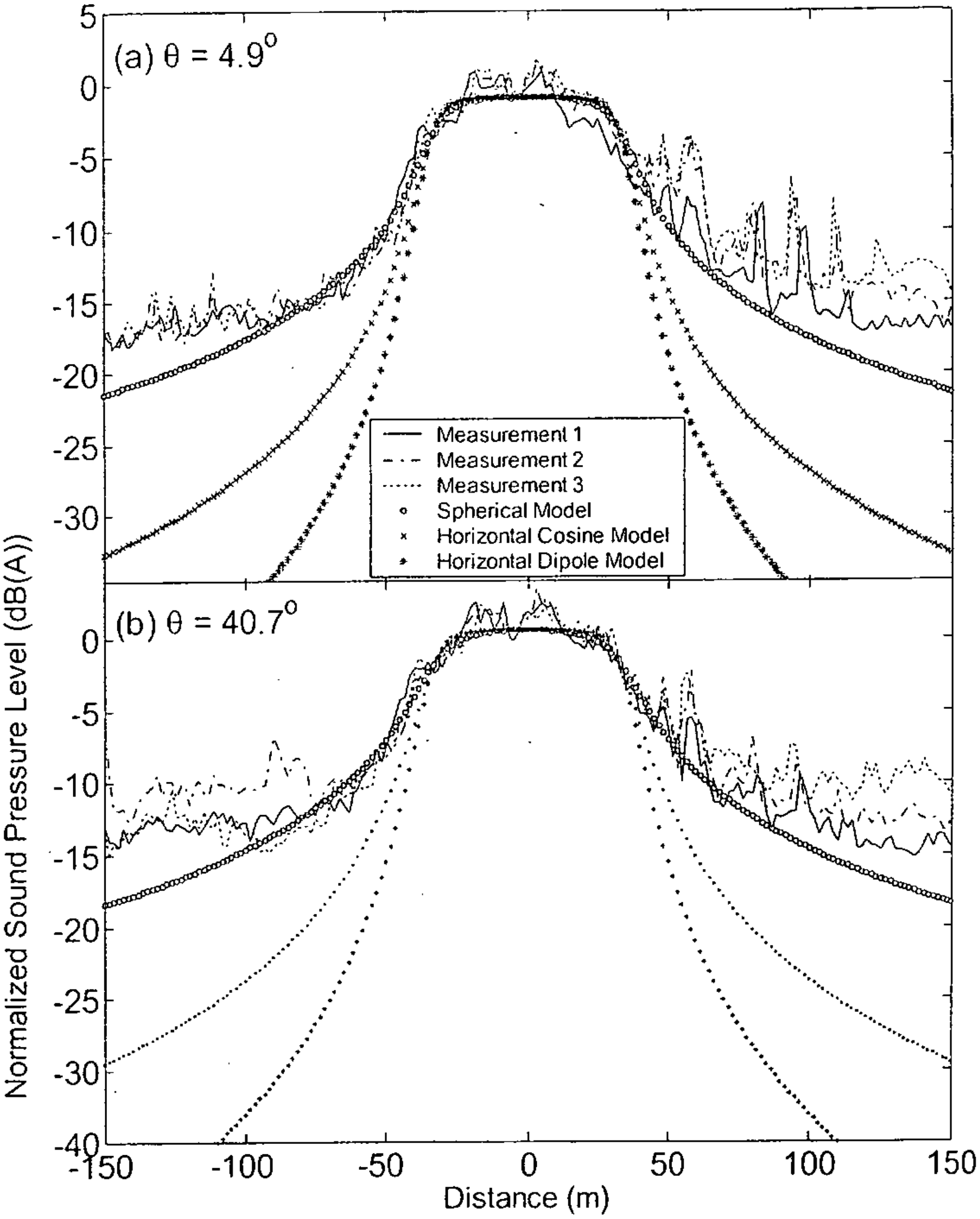

Figure 6.10: Measured and predicted noise profiles for an AEL test train running at 60km/h at the LAR depot.

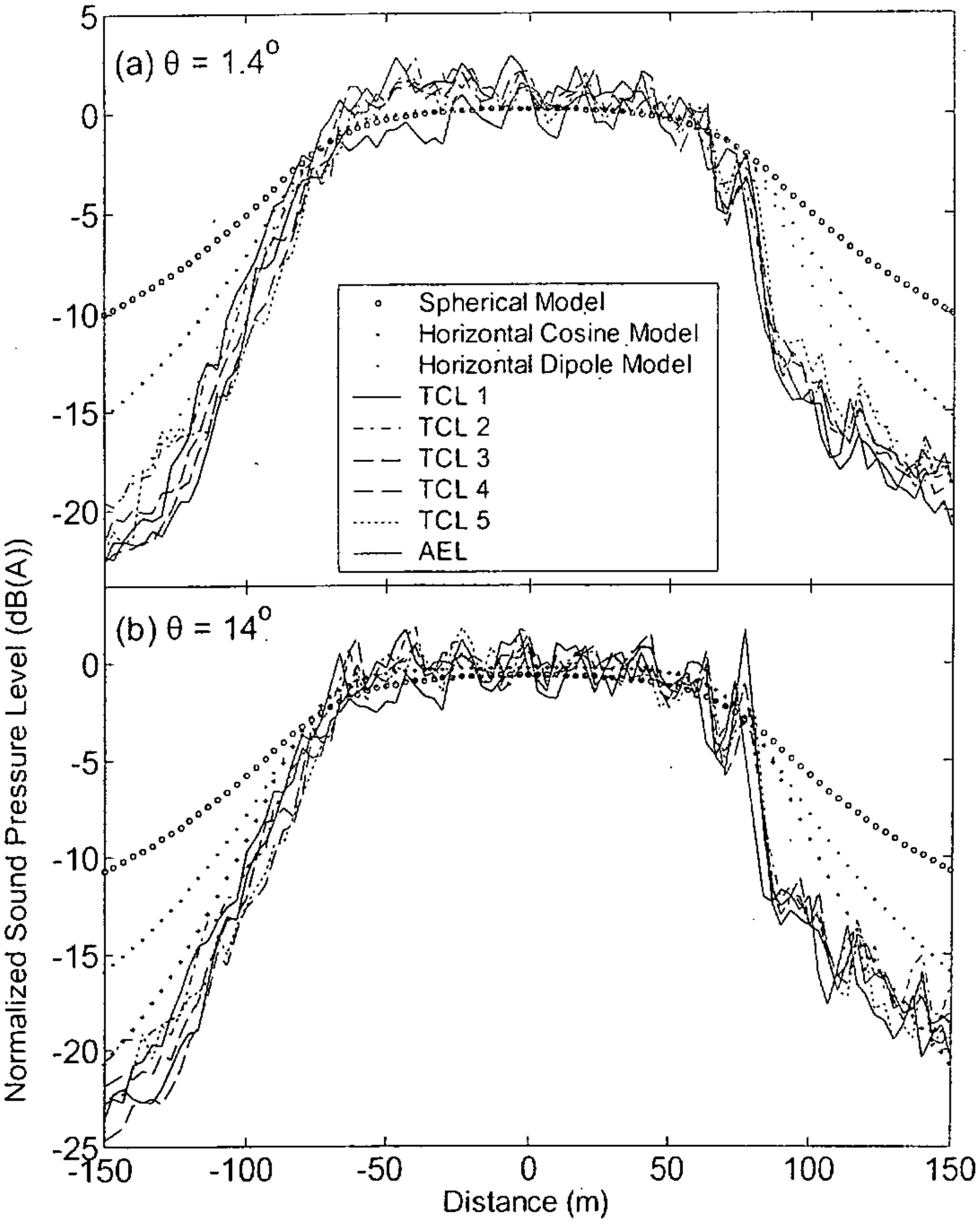

Figure 6.11: Measured and predicted noise profiles of the passenger trains running at 120 km/h at the LAR depot.

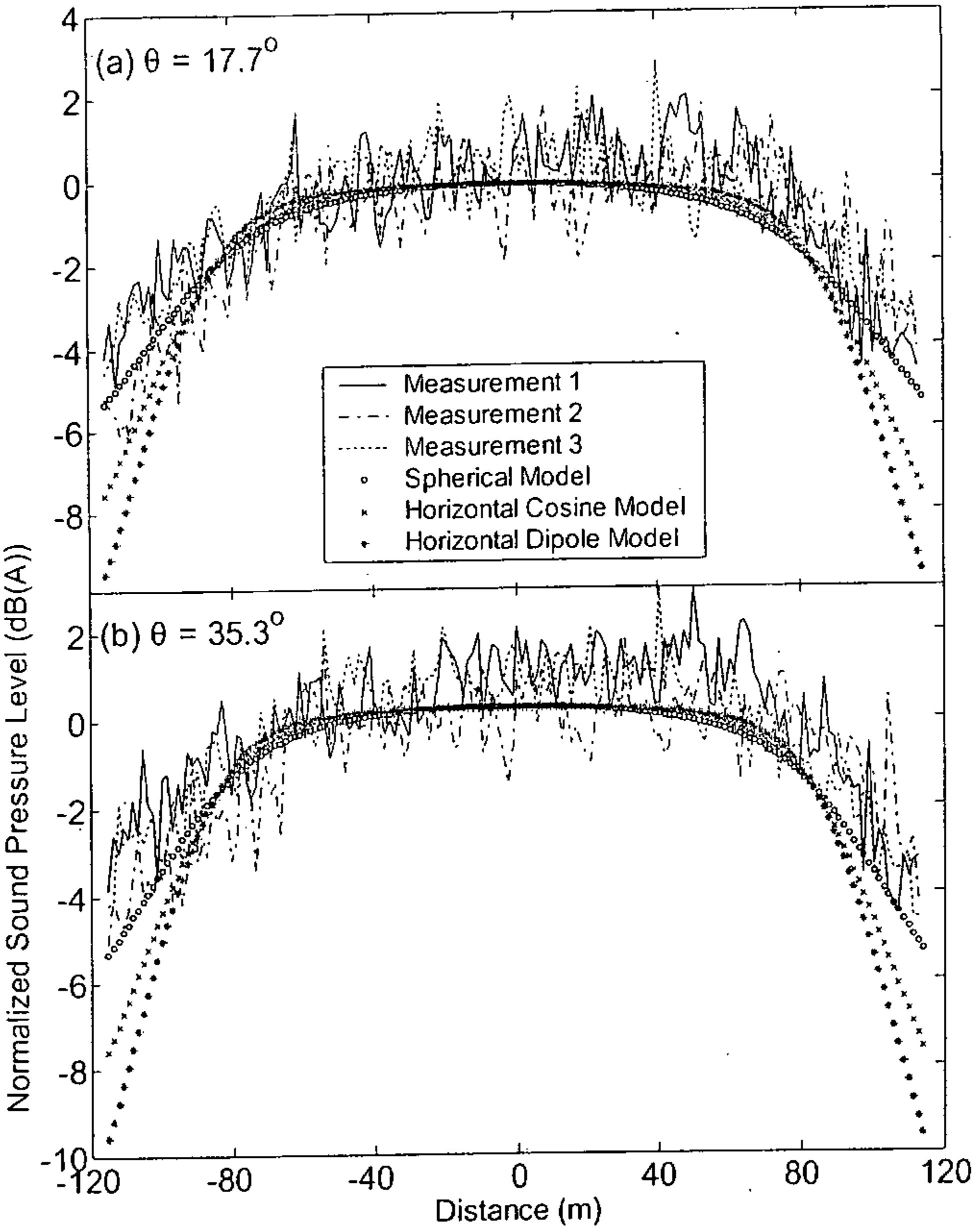

Figure 6.12: Measured and predicted noise profiles for an Urban Line train travelling at 50 km/h on a viaduct.

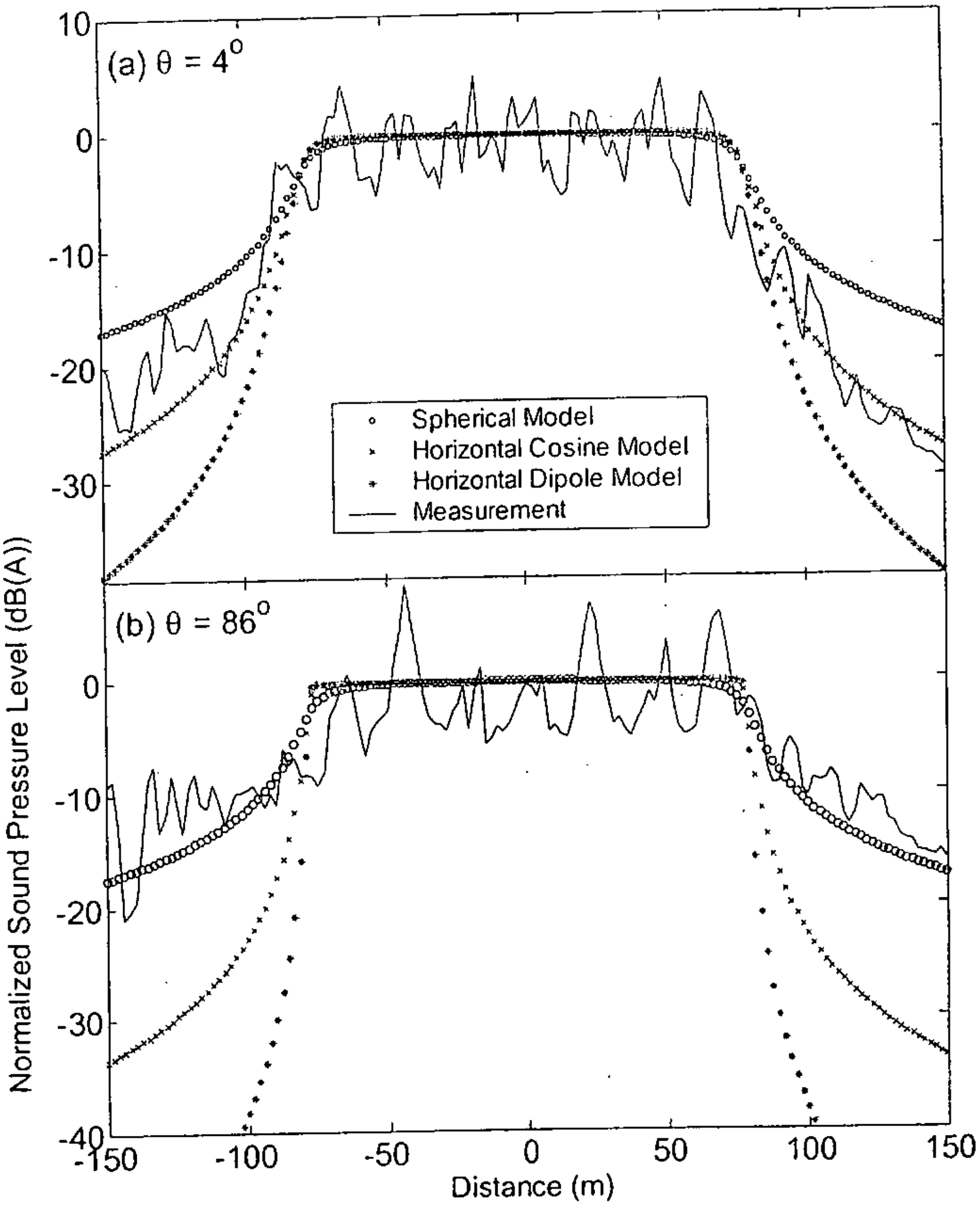

Figure 6.13: Measured and predicted noise profiles for an AEL test train travelling at 60 km/h at Siu Ho Wan.

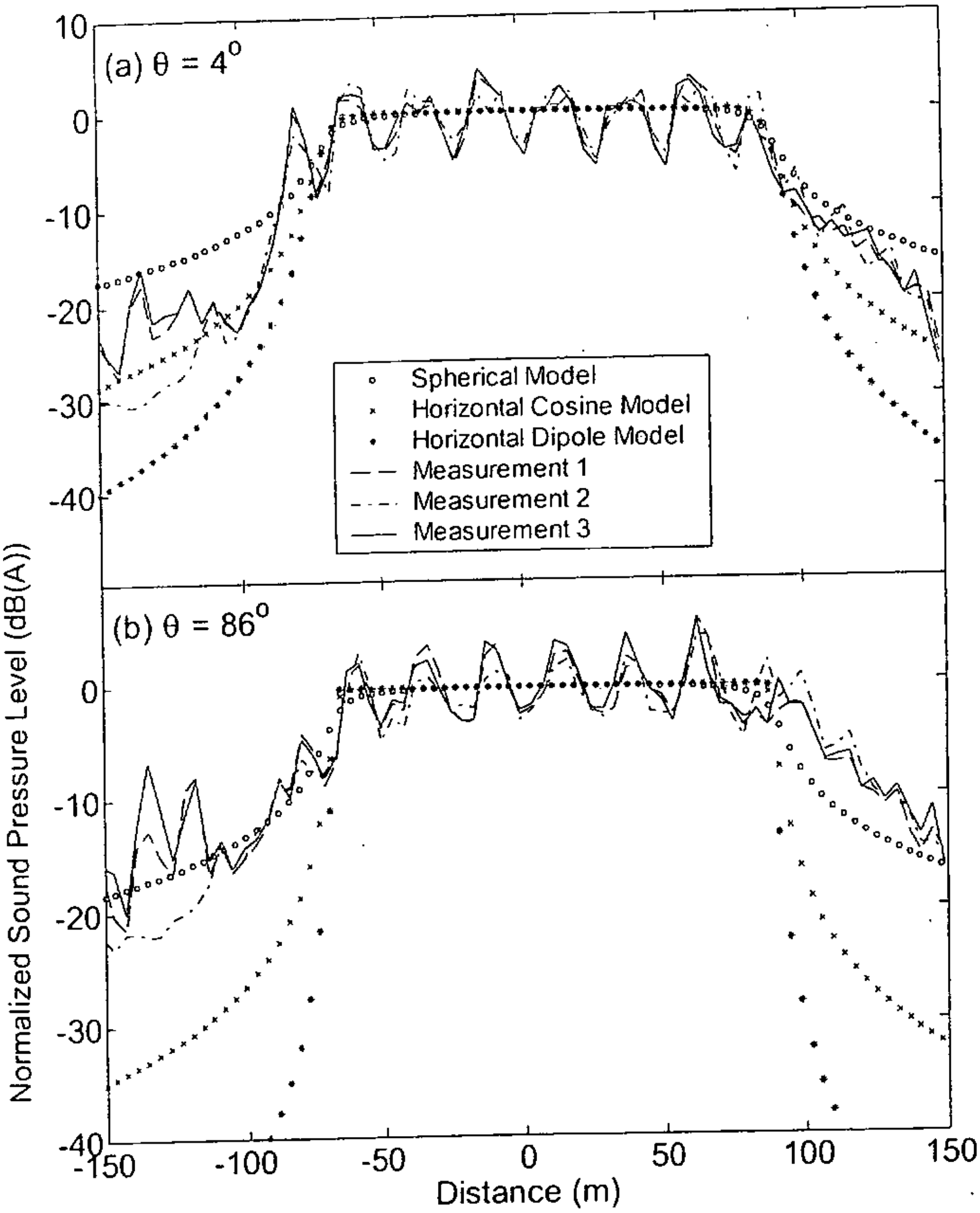

Figure 6.14: Measured and predicted noise profiles for the AEL mainline service trains travelling at 110 km/h at Siu Ho Wan.

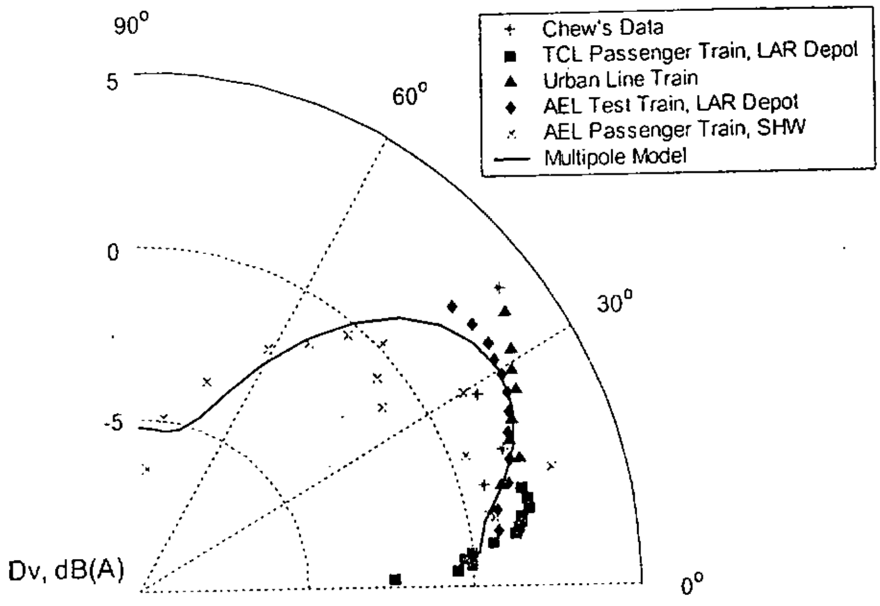

FIG. 15: The vertical directivity of the noise radiation from different electrical railway systems and the multipole model.

Chapter 7

Prediction of Traffic Noise Levels inside a Balcony

7.1 Introduction

In the previous chapters, attention has been paid to look into the problem accruing from the tire/road and wheel/rail rolling noise. In this chapter, the attention has been turned to explore the possible abatement measures that can be used to alleviate the land transportation noise in an urban environment. Noise tolerant buildings or structures such as car parks, commercial complexes or podium structures below residential levels have been used as a tactical means to prevent road traffic noise from reaching residential blocks. However, these measures have only limited application or uses in a dense high-rise city where residential blocks are unavoidably placed very close or even next to a road, due to overriding site constraints. Under such circumstances, balconies may be considered as a possible measure as the noise screening effect is there even with the balcony door opened for ventilation.

However, relatively little attention has been focused on studies pertaining to the propagation of traffic noise from a road into a balcony, although there has been a surge of interest recently in research on sound propagation in urban environments (see, for example, [39][41][55][62][89][109][110][111]). Despite the fact that studies based on indoor scale model experiments [41][82], full-scale field experiments [80][104], boundary element method [50], three-dimensional theoretical model [64][65] and averaged sound energy method [60] have been carried out to investigate the sound field inside the balconies, the methodologies described above are either experimental or not possible to incorporate in any of the simple yet accurate prediction models (such as CRTN) currently in use for the assessment of road traffic noise. Therefore, it is preferable to establish a specific methodology that is based on the source levels of road traffic noise obtained as per the road traffic noise prediction scheme, to model the propagation of traffic noise from a road into a balcony. We note that the "Calculation of Road Traffic Noise (CRTN)" [30] and other similar prediction schemes are commonly used in many different countries for noise impact assessments in projects for infrastructure development and housing construction. It is rational to adopt one of these simple numerical schemes as a basis for predicting noise levels in complex urban environments, that is, dependent on the noise emission levels from traffic and other physical factors such as the propagation, scattering, diffraction and attenuation of sound in the atmosphere. In the present study, we choose the CRTN model as the prediction scheme to illustrate the principles for the development of a new methodology for predicting noise levels inside a balcony. It should be straightforward to apply the same principles to other numerical schemes for the prediction of road traffic noise. In fact, the same principles can also be incorporated in the numerical schemes for the prediction of train noise such as "Calculation of Railway Noise (CRN)" from UK [29].

In the present study, we aim to predict the noise levels inside a balcony by incorporating the image source method in the CRTN model for a more refined scheme. As a result, the insertion loss that quantifies the noise screening effect of a balcony can be better assessed. The proposed refinement on the CRTN model is validated by comparing it with extensive field measurements conducted at two separate sites.

7.2 Methodology for prediction

Without a balcony, the CRTN works reasonably well for the prediction of road traffic noise at the window façades of a building, even in cases where the propagation path between the segment source line and a reception point is interrupted by an obstacle such as a noise barrier. In these classic urban situations, the traffic noise level is expected to be relatively constant across a window and, hence, the exact location of an assessment point is not critical so long it is 1 m from the façade. In predicting road traffic noise levels on a balcony, the CRTN cannot be applied straightforwardly. It is because reception points are partially shielded by the balcony parapets (barriers) and a complex sound field is setup due to the possible reverberant ray paths between the balcony ceiling, floor, parapets and façades.

7.2.1 Factors influencing the road traffic noise levels on a balcony

There are abrupt changes in the predicted noise levels for shifting the receiver positions inside the balcony. This is because, according to the ray theory, even a small shift in position may result in the reception point falling into the illuminated zone or lying in the shadow zone, as balcony parapets are normally close to the receivers inside the balcony. Noise levels inside the balcony will be sensitive to whether the receiver is in the illuminated or shadow zone of the parapet. The height of the receiver and orientation of the parapet in relation to the road segment are two most important factors affecting the overall noise levels. In addition, noise levels inside a balcony may be augmented by the presence of reflecting surfaces such as parapets, external building façades, balcony ceilings and floors because all these surfaces are good reflectors of sound. Another significant factor affecting the total sound fields, which should also be included in the proposed model, is the sound waves diffracted at the edges of the balcony parapets.

7.2.2 Road sub-segmentation

In accordance with the CRTN, the road should be divided into smaller segments when the generated noise along the length of a road varies considerably due to changes in traffic conditions, road gradients, and road curvatures, or due to the progressive change in screening. This procedure ensures that the variation of noise levels within any one segment is not more than 2 dB(A). Each segment is treated as a separate noise source, and its contribution to the total noise level is evaluated according to the standard CRTN procedures. However, noise from each segment may reach a receiver through different propagation paths in the presence of a balcony and its parapets. This is because sound waves, which come from the road segment, may either reach the receiver directly or diffract at different parts of the parapets before reaching the receiver. In this paper, we consider a balcony of the type shown in Fig. 7.1 for the purpose of illustration. It should be fairly straightforward to extend the proposed methodology to other balcony configurations. In our example, the balcony, which has a parapet at the front, a full-height sidewall on the right side and railings on the left side, is backed on an acoustically hard building façade. We further assume that the railings are acoustically 'transparent' – they offer no diffraction or reflection of sound.

To illustrate the principle, let us further assume that the orientation of a typical road is shown in Fig. 7.2. We assume that there is a full-height wall at one side of the balcony in this illuminated example. It is apparent that the noise can intrude into one side of the balcony through the railings without any obstruction (in some situations the diffraction of sound at the edge of floor need to be considered according to the CRTN procedures), and the sound waves can also reach the receiver by diffraction at the parapet edge in the front. In this circumstance, a reception point in the balcony receives both direct and diffracted waves from a source segment simultaneously. Further sub-division of the road segments is necessary for modeling the noise propagated from a road segment into a balcony. Not only do we require a constant noise level in each road segment, we also have to ensure that the noise contributions from each propagation path (either direct path, diffracted path or reflected path) within a sub-segment are constant. For instance, as shown in Fig. 7.2, the noise from the road segment intruding into the balcony has two propagation paths: the first path links the source and receiver through the left side of the balcony, and the second path connects them through the balcony front. In this example, the boundary of one sub-segment passes through the junctions of the left railings and the front parapet, see sub-segments A and B in Fig. 7.2.

7.2.3 Geometrical-acoustic theory

In the proposed methodology, the prediction of road traffic noise in a balcony is based on the source levels obtained as per the CRTN methodology. The predicted traffic noise level is highly dependent on the noise levels of the direct ray as well as the reflected ray reaching the receiver. The underlying principle for our approach is the theory of geometrical acoustics (see Sec. 9.8 of Ref. [90]). Using a simple ray tracing technique, we include the noise level due to a direct wave if a ray can be constructed linking the source and receiver. Similarly, the total noise level is comprised of a reflected wave contribution if a ray passing through an *interception* *plane* can be found connecting the source and the corresponding "image" receiver (see Fig. 7.1 for an example). More details for the reflected wave will be elaborated in the next section. Depending on its location – whether the receiver is situated in an illuminated zone or in a shadow zone – we adopt two approaches for the prediction of road traffic noise levels on a balcony. In the following sections, we will demonstrate the application of geometrical acoustic theory in the proposed approaches. In order to simplify the calculations, we have made further assumptions. First, the contribution from the reflected ray due to the floor can be neglected because the location of receiver is deep in the shadow zone that leads to a large attenuation of sound due to the diffraction at the top edge of a parapet. Secondly, the contribution due to the sound diffraction around vertical edges such as the ends of the parapet is ignored.

7.2.4 Prediction in an illuminated zone

In Fig. 7.1, the balcony is designed with a cantilever, a front parapet, side railings, a full-height sidewall and a ceiling. In this case, image receivers I_c, I_b, and I_s of the reception point R can be identified immediately in the balcony ceiling, back wall and full-height sidewall respectively, in accordance with the geometrical acoustic theory. The image receivers I_c and I_s are not shown in Fig. 7.2 for clarity. Here, we also assume that all surfaces in the balcony are perfectly flat and smooth.

If we can construct a ray linking the effective source point S of a sub-segment and the reception point R (ray SR in Fig. 7.2) without any obstruction, R is said to fall on the illuminated zone. However, the barrier correction factor for the illuminated zone will still be applied, where appropriate, as per the standard CRTN procedures. The effective source point and its direct noise level can be found by following CRTN methodology, and the details will not be repeated here.

Similarly, if we can construct a ray from a *bisecting point* on a sub-segment source line to the image receiver $\boldsymbol{I_b}$ of $\boldsymbol{R}$, and the ray also passes through an *interception plane* as shown in Fig. 7.1, then there is a contribution to the overall noise levels at the receiver $\boldsymbol{R}$ due to the façade reflection from the back wall. The bisecting point is the intersection point of the sub-segment source line and the line bisecting the sub-segment angle, as shown in Fig. 7.2. An interception plane is a plane through which the direct wave propagates from a bisecting point to the image receiver. For instance, the interception plane at the front of balcony marked with JKLM as shown in Fig. 7.1 is bounded vertically by the balcony ceiling, line KL, and the top edge of the intervening parapet (or floor if it is only a cantilever-type balcony), line JM. It is also bounded longitudinally by the boundaries, lines JK and ML, of the intervening parapet/floor. The interception plane at the side of the balcony can be defined in a similar way, i.e. bounded vertically by the edge of ceiling and the floor, and bounded longitudinally by the back wall and the edge of the front parapet.

Due to the close proximity of the reception point and its image receiver, the noise contribution due to the reflected ray cannot be ignored because its magnitude is of the same order of the direct ray. This is because the propagation path lengths of the direct and reflected rays are nearly identical, but the sound energy of the reflected ray is normally less than that of the direct ray due to the finite absorption of building façades. It is worth noting that not all the effective noise sources have contributions due to the reflected waves. The approach as described above should be used to identify all possible reflections in a balcony. We also assume that there should be no façade reflection from the back wall if ***R*** is located in front of the open balcony door. The overall noise level $\wp$ at ***R*** contributed by a sub-segment is readily obtainable by combining contributions of the direct ray and all reflected rays to yield

$$\wp = 10\log_{10}(10^{\frac{L_0}{10}} + \sum_{i}^{n} 10^{\frac{\overline{L}_i}{10}}), \tag{7.1}$$

where L_0 is the direct noise level, and $\overline{L}_i$ where $i = 1, 2, \ldots n$ is the noise level of each reflected ray due to the balcony ceiling, back wall and full-height sidewalls. Again, all surfaces are assumed to be perfectly hard and smooth. The direct noise level can be calculated by following the procedures described in CRTN [30] (e.g. basic noise level calculation, distance correction, barrier correction, angle of view and others). The noise contribution of a reflected ray is set to zero if it cannot be established by the proposed method. The magnitude of $\overline{L}_i$ can be assumed of the same magnitude as L_o if the sound wave is reflected from an acoustically hard surface due to the close proximity of the reception point and its image receiver.

In case of the surface material of the reflecting façade is finished with some sound absorption material, the noise contribution from the image receiver should be corrected in accordance with equation

$$\overline{L}_i = L_i + 10\log_{10}(1-\alpha), \tag{7.2}$$

where L_i is the incident noise level. It is taken to be the noise level at ***R*** without the barrier correction, and α is the sound absorption coefficient of the reflecting surface.

7.2.5 Prediction in shadow zone

When a reception point is shielded from the sub-segment source line by a parapet of a balcony, the receiver is located in the shadow zone (see Fig. 7.3). In fact, the balcony in Fig. 7.3 is the same as that in Fig. 7.1, except that the railings are not shown for clarity. The image receivers of ***R*** in the balcony ceiling, back wall and sidewall can be readily located by using a simple ray tracing technique. The noise contribution by the reflection from the floor is considered negligible as compared with other contributions. There should also be no contribution from the back wall if the receiver ***R*** is located in front of the open balcony door. Again, the direct ray contribution from the sub-segment can be estimated by following the CRTN methodology and the noise levels of the reflected rays $\overline{L}_i$ can be obtained by Eq. (7.2). However, L_i corresponding to the reflection by the back wall and side wall should be taken as the noise level with barrier correction at ***R*** (i.e. L_o). In the shadow zone, the total noise level $\wp$ at ***R*** is obtained by summing the noise contribution from the direct and reflected rays in the analogous form as shown in Eq. (7.1).

7.2.6 Combining contributions from sub-segments

After obtaining the overall noise level at a reception point due to a sub-segment source, we move on to calculate contributions from other sub-segments individually. For a road with a single segment, of course, no further adjustment is required. But, for a road segment consisting of more than one sub-segment, the combined noise level L_s at the reception point due to the road segment shall be calculated by combining the contributions from all sub-segments using the following formula

$$L_S = 10\lg\left(\sum_{1}^{N} 10^{\frac{\wp_i}{10}}\right), \tag{7.3}$$

where $\wp_i$ is the contribution from each sub-segment and N is number of sub-segments within a road segment.

7.3 *In-situ* measurements

In-situ field measurements on four different types of balconies at two different sites were conducted to validate the proposed methodology. The sites were distinct, with the road alignments at different angles and distances to the balcony façades. In each site, three balconies on low, medium and high floors in the same building or adjacent buildings were selected, such that these balconies had similar orientation in relation to the road from which the traffic noise was measured.

7.3.1 Road orientations and building layouts

Figure 7.4 shows the layout of Site 1. In this test site, the measurements were conducted on balconies on the 3rd, 4th and 5th floors respectively in two adjacent buildings (due to accessibility constraints) with similar orientations to the roads. The third floor was approximately 9 m above the road surface, and the floor-to-floor height was about 3 m. The selected balconies were affected by traffic noise from two roads with orientations of about 0° and 90° to the balcony façades respectively. The balconies featured a front parapet and a side parapet of 1 m height, a full-height sidewall, and a ceiling with dimensions as shown in Fig. 7.5. The distances of balconies from the parallel road is about 35 m, and from the perpendicular road are about 25m (3rd balcony), 35m (5th balcony) and 60m (4th balcony) respectively.

At site 2, see Fig. 7.6, the measurements were conducted at balconies on the 5th, 9th and 11th floors of the same building respectively. The 5th floor was estimated to be about 3.6 m above the elevated road surface, and the floor-to-floor height was measured to be about 2.64 m. The selected balconies were affected by traffic noise from a single road, with an orientation of about 0° to the balcony façade. The distance of balconies from the road is about 37 m. The balconies featured a front parapet and railings on both sides of 1 m height, with dimensions as shown in Fig. 7.7. Except for the balcony on the 11th floor, which was the top floor, the selected balconies were built with ceilings. At site 2, two sets of extra measurements were made on the selected balconies, as both sides of the balconies had been built with temporary parapets of 1 m height and full-height sidewalls respectively by using 12 mm-thick plywood boards. These sets of control measurements were used to explore the effectiveness of parapets for shielding road traffic noise.

7.3.2 Measurement method

For each selected balcony, measurements were conducted at 0.5, 1.0, 1.5 & 2.0 m above the balcony floor along the vertical lines, at the locations shown in Figs. 7.5 and 7.7 respectively. For each setup, three readings were recorded and analysed in order to minimize the random measurement errors. During the measurements at the locations described, measurements were also taken at a control point *A* that was located 1 m outside the balcony. The control point in each site was not screened off from the road by the balcony, i.e. a direct line-of-sight was established throughout the measurement periods.

For the measurements at Site 1, a Sony 16 Channels Sensor Input High Speed Digital Data Recorder was used. Noise data at four locations, namely points ***B*** – ***E*** as shown in Fig. 7.5, were recorded simultaneously together with the control point *A*. Four different levels, ranging from 0.5 m to 2.0 m above the balcony floor, were recorded. The measured data were then analyzed in the laboratory using a B&K Pulse Multi-analyzer System Type 7700. For the measurements at Site 2, the noise levels at the five locations *A* - *E*, were recorded simultaneously by 5 Rion sound level meters at heights 0.5, 1, 1.5 and 2 m above the balcony floor respectively. The assessment point *E* was located at the plane of the balcony door-frame at both sites. The sliding door in Site 1 was fully open and the door in Site 2 was pushed to lean to the back-wall when measurements were carried out such that the point *E* was clear from any door and back wall reflection.

The traffic flow data was recorded by counting the number of light and heavy vehicles during each measurement period as per the CRTN model. The CRTN methodology was used in the calculation of basic noise levels, with the traffic speed taken as the corresponding speed limits of the road. The speed limits were 50 km h^{-1} and 70 km h^{-1} for Sites 1 and 2 respectively. Three independent measurements were recorded for each assessment point. The average noise levels were obtained for subsequent interpretations. Strictly speaking, it is not necessary to calculate the basic noise level if the insertion loss is only required for the interpretation of results. However, the information for the basic noise levels is provided for sake of completeness.

7.4 Results and discussion

First of all, the predicted traffic noise levels on a balcony are determined according the modified CRTN model as described in Sec. 7.2. They are subsequently used to derive the balcony insertion losses (IL) at different locations, where IL is defined as the difference in noise levels at an assessment point with and without the presence of a balcony.

Next, we need to measure the free field noise level due to the noise sources from road traffic, because this is required for the determination of the balcony insertion loss. It is understood that a common method of obtaining the free field level which avoids the problem of the reflected sound is to place a microphone on a hard reflecting surface and subtract 6 dB from the measured results. It is not practicable in the present situation because of site constraints. Preliminary experiments were conducted at the control point *A* to assess the noise levels. Simultaneous measurements were conducted with four microphones protruding at different locations outside a balcony. Experimental results have suggested that the noise levels vary with an average value of 1.0 dB(A) outside the balcony. In addition, the measured noise levels agree reasonably well with those predicted by the CRTN model, in which no façade correction is added. Consequently, we assume that the control point *A* may be regarded as a reference noise level corresponding to the free field value at an equivalent distance in our prediction model. Indeed, the assumption is justifiable because the dimension of the reflection surface (front parapet) is small such that only a negligibly small portion of the sound energy from the road segment can reach *A* by reflection from the front parapet. As a result, the contribution of noise levels from this reflection path is negligible in comparison with the direct ray. Ideally, the control point *A* should be located as far away from the balcony as possible in order to minimize the reflection from the front parapet. In our measurements, the control point *A* was fixed at a distance 1 m from the front parapet for safety reasons. Nevertheless, the control point has provided a useful reference noise levels in our measurements, as shown below.

Knowing the corresponding free field noise level, the measured insertion loss at an assessment point (Point ***B*** to Point ***E***) on the balcony can be found by subtracting the traffic noise level at the control point ***A*** by the traffic noise level at the assessment point. The insertion loss is used in the presentation of experimental data as it gives useful information for assessing the noise shielding effect of a balcony. The experimental data are used for comparison with the predicted noise levels for the validation of the theoretical model.

The measured insertion losses are obtained and compared with the predicted insertion losses at each assessment point. Since the insertion losses at locations ***B*** to ***D*** are of rather similar values, only the insertion losses at locations *C* and *E* are presented in Figs. 7.8 – 7.11 for brevity. Figure 7.12 demonstrates that measured results at points ***B*** to ***D*** have suggested a similarity of the insertion losses for these two assessment points. These figures demonstrate the effectiveness of balconies in reducing noise at different positions of the balcony, and the accuracy of adopting the proposed methodology. In Fig. 7.8, we display the results for measurements and predictions of the balcony insertion loss at Site 1. We show the comparison results of the balcony insertion loss at Site 2 in Fig. 7.9. As discussed in Sec. 7.3, two extra sets of measurements were conducted to explore the effectiveness of parapets for shielding road traffic noise at Site 2. Plywood boards were used to construct temporary parapets of 1 m and full height respectively, and the results are shown in Figs. 7.10 and 7.11. In general, the insertion loss is often over predicted especially when the measurement is at the shadow zone in the lower part of the balcony. These differences range between 0.5 dB(A) and 3 dB(A) for most of the measurements at 1.5 m and 2 m above the balcony floor. There is a single measurement point which shows a difference exceeding 3 dB(A). For the measurements at 0.5 m and 1 m above the balcony floor, the discrepancies are in the range of 0.5 dB(A) and 6 dB(A). Again, there are a few isolated instances where the deviations are about 7 dB(A). The observable deviations for the measurements at the lower part of the balcony will be explained in the following paragraphs.

As demonstrated in Figs. 7.9 – 7.11, the balconies of different features at Site 2 all provide a noise-screening effect for the low, middle and high floors. Balconies on high floors can give better insertion losses at all assessment points than those at lower floors, regardless of the balcony structure. This is reasonable because the path difference of a diffracted ray (diffracted at the parapet or floor of a balcony) and a direct ray increases with the relative height of a balcony to a road. Moreover, since the road at Site 2 is almost parallel to the balconies, at the lower floors, the sound rays penetrating into the balconies can undergo a reflection from the back wall of the building when the angle of incidence are moderate. This leads to an increased noise level and lessen the screening effect at the lower floors. For the assessment points at 2 m above the balcony floor (in the illuminated zone of the balcony), the insertion losses at these points on the 11th floor were found to be greater than those on the lower floors. This is because the receivers were located deeper in the shadow zone than those located at lower floors. In addition, there is no ceiling reflection at 11th floor. These lead to a lower noise level and hence a greater insertion loss, as revealed in our prediction results. It is also obvious that the balcony insertion loss decreases, with an increase in the height of the assessment points in a balcony. This is mainly due to the fact that these assessment points can observe the road without screening at a higher level, leading to a decreased screening effect of the balcony.

By comparing the insertion losses provided by an open-type balcony (built with a front parapet and acoustical transparent railings, see Fig. 7.9), with those of closed-type balconies (enclosed with parapets and side walls, Figs. 7.10 and 7.11) at Site 2, it seems that closed-type balconies do not offer a significant increase in screening effect when the road is parallel to the balconies. This is understandable, because most of the traffic noise intruding into a balcony is through the front opening, such that the side parapets and sidewalls do not play a significant role in screening road traffic noise from intruding onto the balcony. Moreover, the noise contributions from sidewall reflections can cause degradation of the balcony effectiveness in shielding against the road traffic noise, as revealed in our calculation results.

The balcony insertion losses obtained by measurements at the levels of 0.5 m and 1 m above the floor are found to be less than the predicted values to some extent for the closed-type balconies (see Figs. 7.10 and 7.11) but the difference diminishes for the relatively open-type balcony (see Fig. 7.9). As shown in Figs. 7.10 and 7.11, there are noticeable discrepancies between the predicted and measured results in the case when the receiver is at the lower part of the balcony. This is possibly due to the effect of multiple reflections between parapet and façade and this effect has not been taken into account in our prediction model. The difference between the predicted and measured results in Fig. 7.9 is possibly due to the sound diffracted at the end of the parapet which has been omitted in the prediction model. The reverberation effect and diffraction around the edges of parapet generally increases the noise level and lead to degradation of the overall balcony effectiveness against the intruding noise. Moreover, the assumption of effective source line located at 3.5m from the road kerb of nearside carriageway of a road in the CRTN scheme can lead to prediction error especially for estimating the screening effect of noise barrier. Under this assumption, the measured traffic noise level is always higher than that predicted by the CRTN as the barrier cannot actually screen the traffic noise from the farside carriageway but the CRTN scheme assume that it can do so. The insertion losses obtained by measurement and calculation for assessment levels at or over 1.5 m above the balcony floor are reasonably close, and the maximum difference between predicted and measured IL is close to 3.5 dB(A).

In general, assessment point ***E*** obtains the best insertion loss compared to point ***C*** at the same assessment level, as it is in a better shielding position as well as there is no façade reflection at the assessment point ***E***. For the assessment points ***E*** at the upper floors which are clear of ceiling reflection, the noise reductions (by measurements) provided by the balconies are between 8 dB(A) and 10 dB(A) at and below 1 m; the noise reductions are between 3 dB(A) and 8 dB(A) for the measurement levels over 1 m from the balcony floor. For the assessment points ***E*** at the middle and lower floors, the noise reductions provided by the balconies are between 3 dB(A) and 7 dB(A) for the measurement levels at and below 1 m; the noise reductions are between 0 dB(A) and 5 dB(A) for the measurement levels over 1 m from the balcony floor.

Figure 7.8 shows that the balconies at Site 1 provide a considerable noise screening effect for most of the assessment points in a balcony. In this case, the insertion losses at all assessment points at the higher floor do not show a significant increase in values compared to the lower floors, as the height differences relative to the affecting roads are quite small. Generally, the balcony insertion losses become smaller with an increase in the height of assessment points in a balcony such that the balcony does not provide a screening effect for assessment points at 2 m above the balcony floor, except for those at the plane of balcony door. We note that there is no insertion loss for point *C*, located at 2 m above the balcony floor. This can be attributed to the fact that the assessment point is directly exposed to the traffic noise sources.

Similar to the observations at Site 2, for the assessment levels at and over 1.5 m above the balcony floor, the maximum difference between predicted and measured IL is close to 3.5 dB(A). The measured insertion losses at the lower part of the balconies at this site are found to be less than the predicted values to some extent. The reasons are as explained earlier. Finally, as expected, assessment points ***E*** get the best protection from the road traffic noise for all the balconies selected at this site. For the assessment points ***E*** at the upper floor, the measured noise reductions are 8 dB(A) and 7 dB(A) at 0.5 m and 1 m above the floor respectively; and the measured noise reductions are 5 dB(A) and 4 dB(A) at 1.5 m and 2 m above the floor respectively. For the assessment points ***E*** at the middle and lower floors, the measured noise reductions are between 5 dB(A) and 7dB(A) for the measurement levels at and below 1 m; the measured noise reductions are between 2 dB(A) and 6 dB(A) for the measurement levels over 1m from the balcony floor.

7.5 Summary

A brief literature review was conducted to examine the current models pertaining to the propagation of road traffic noise from a road onto a balcony. *In-situ* measurements for four different types of balcony were conducted at two sites. Insertion loss was used to quantify the noise-reducing effect of a balcony: with the new methodology proposed in this study, insertion losses at levels over 1 m above the balcony floor can give a reasonable prediction at most of the time for the assessment points. For these heights, the average discrepancies between predicted and measured results vary between 0 and 3 dB(A). However, for the measurements at the lower part of the balcony, the average differences vary from 0 and 6 dB(A). These large deviations can attribute to the multiple reflections inside the lower part of the balcony and diffraction around the edges of parapet which generally increase the noise level. These effects have not been accounted for in this simple prediction model. Moreover, the position of the effective source line as assumed in the CRTN scheme can also lead to an over-prediction of the screening effect provided by a noise barrier.

It has been shown that points at the plane of the balcony door-frame have the best protection in terms of insertion loss for all balcony constructions and levels above the balcony floor. The measured insertion loss provided by a balcony without a ceiling at this position can be as high as 10 dB(A) on the high floors and at least 3 dB(A) on the low floors. The noise levels at the balcony door can also be used to represent the amount of noise energy entering the room. In addition to the more reliable predictions that can be obtained, noise levels at the upper part of the balcony are also more dominant than those at the lower part. Hence, these points can be used for evaluating the effectiveness of a balcony in protecting a dwelling against road traffic noise.

The experimental data also suggest that balconies offer considerable screening effects in protecting dwellings against excessive road traffic. In conclusion, regardless of the balcony type, on the high floors when the incident angle is large (such that no sound reflection from the back wall) and without ceiling reflection, a balcony on the high floors can provide at most 7 dB(A) extra noise reduction compared to the balcony on the low floors. As expected, the noise screening effects decrease with an increase of height above the balcony floor such that a maximum of 6 dB(A) deviation in the noise reduction on a balcony can be observed .

It is expected that a balcony with a closed construction (built with parapets or side walls) offers a more considerable reduction of noise than the open (cantilever) type. However, the effectiveness of a parapet or side wall against road traffic noise depends on their orientations with the affecting roads. A parapet or side wall can provide an effective screening effect if it is parallel to the affecting road, but the noise reducing effect becomes less significant when it is perpendicular to the road. This conclusion is drawn from the noise surveys at Site 2, in which the addition of side parapets and walls to the original balcony construction did not show significant improvement in the noise-reducing effect. This is because the road was parallel to the balconies, and the side screening effect becomes less significant when most of the noise entering into a balcony is through the front opening.

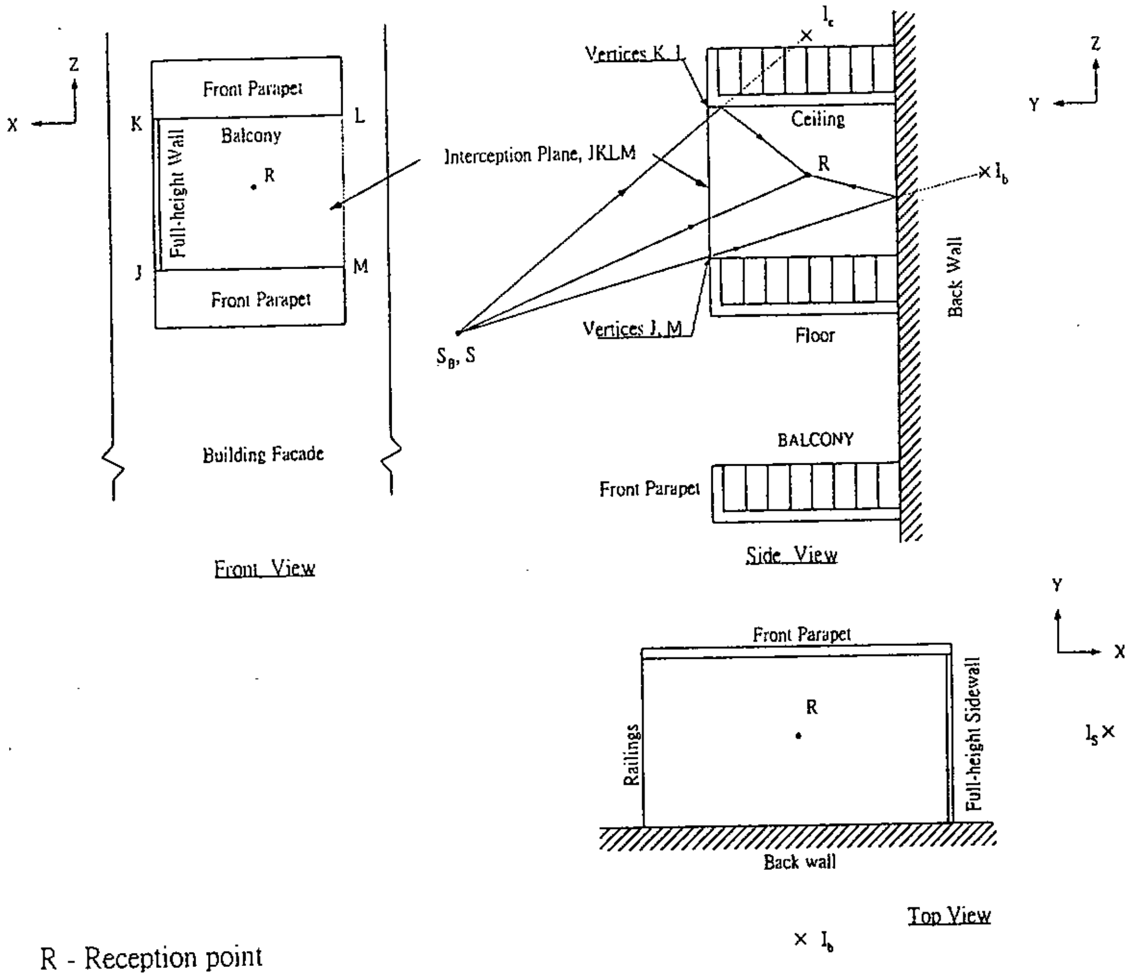

R - Reception point
S - Effective source point on a source line
S_B - Bisecting point on sub-segment B (see Figure 2)
I_c - Image receiver in the ceiling
I_b - Image receiver in the back wall
I_s - Image receiver in the full-hight sidewall
JKLM - Vertices of the interception plane

Figure 7.1. Schematic representation of the reception point and image receivers on a balcony, only the direct and reflected sound rays are shown for clarity.

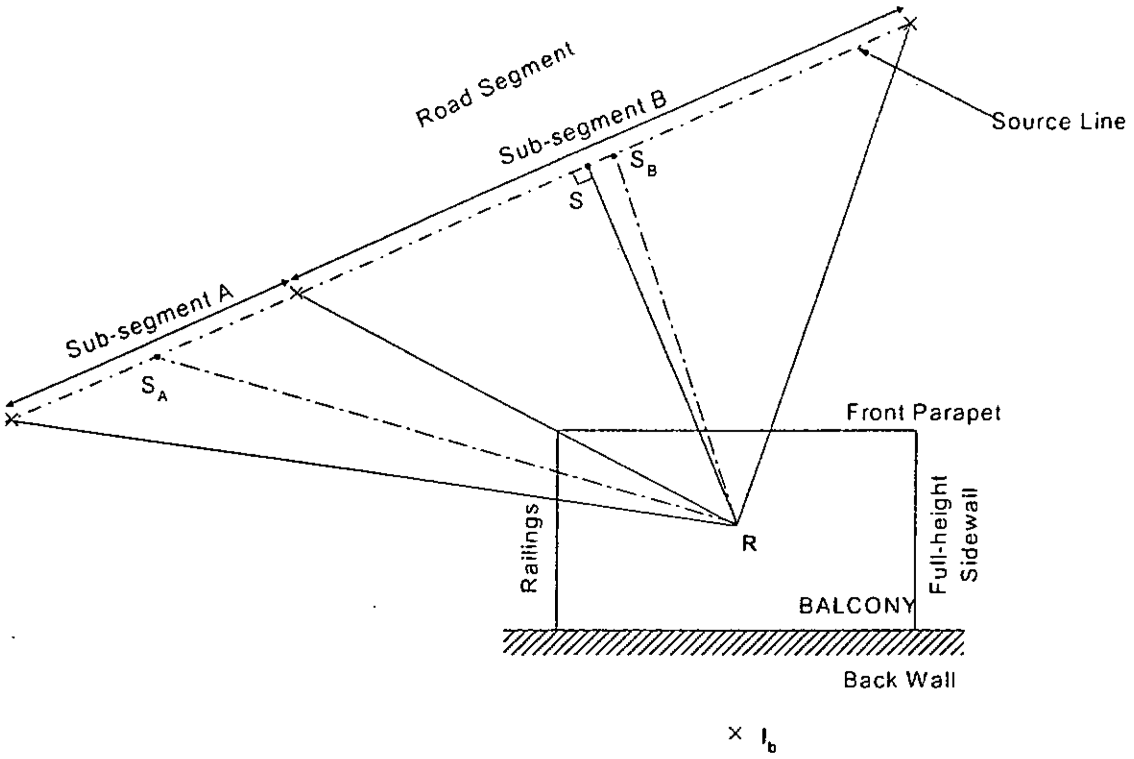

R - Reception point
S - Effective source point on a source line
S_B - Bisecting point on sub-segment B
S_A - Bisecting point on sub-segment A
I_b - Image receiver in the back wall
SR - Shortest slant line from the source line to the reception point
S_BR - Bisector of sub-segment B
S_AR - Bisector of sub-segment A

Figure 7.2. Diagram demonstrating road sub-segmentation and bisecting points on the sub-segments.

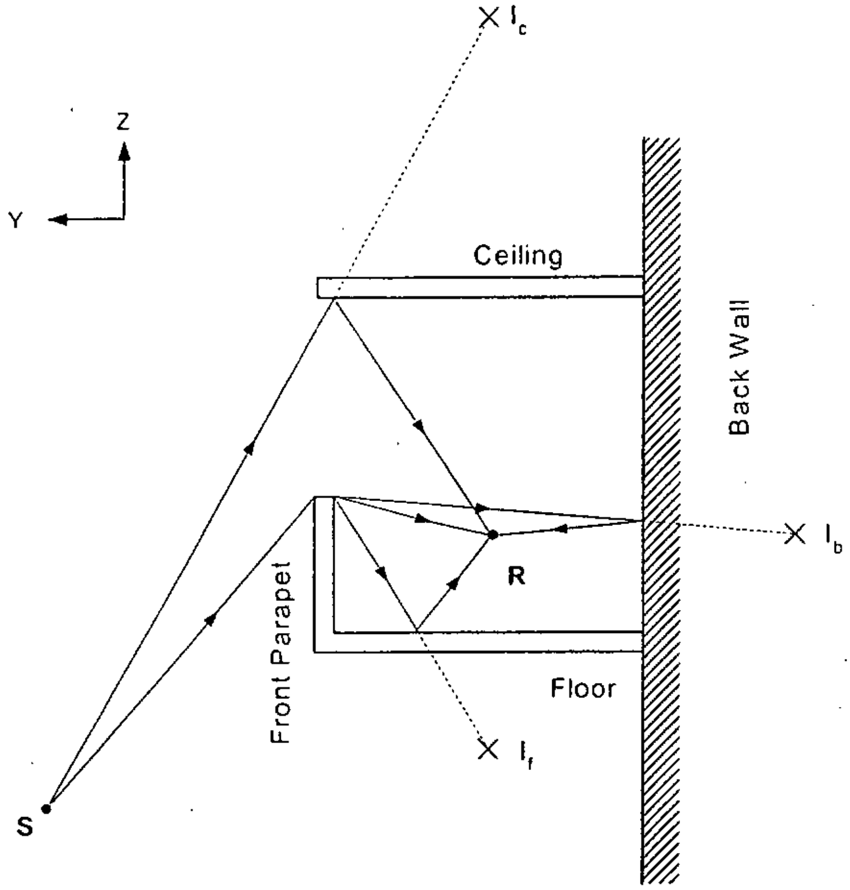

R - Reception point
S - Effective source point on a source line
I_f - Image receiver in the floor
I_b - Image receiver in the back wall
I_c - Image receiver in the ceiling

Figure 7.3. Diagram showing the reception point *R*, which is shielded from the source line by a front parapet on a balcony.

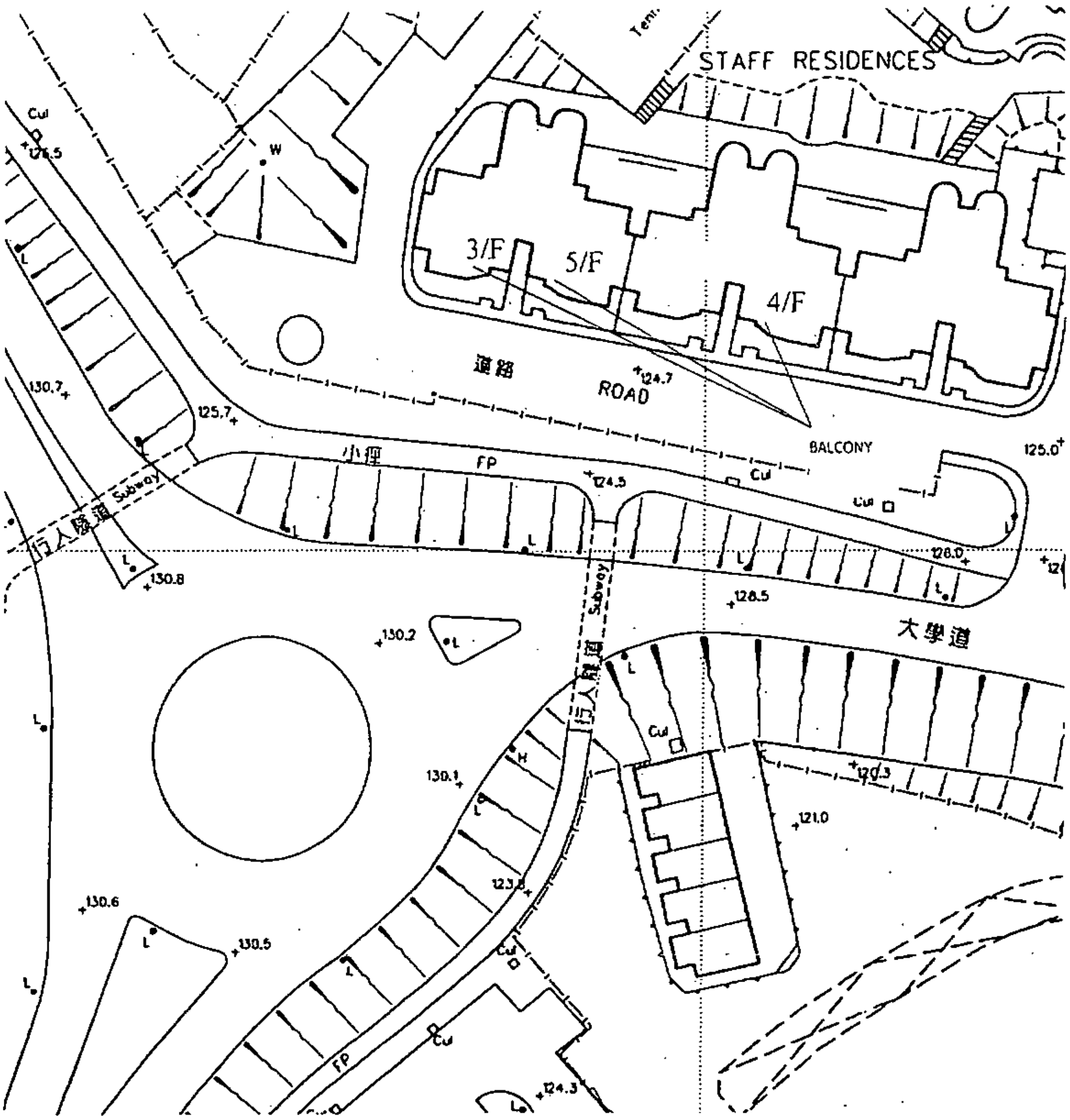

Figure 7.4. Survey map showing the orientation of the investigated buildings and roads layout at Site 1.

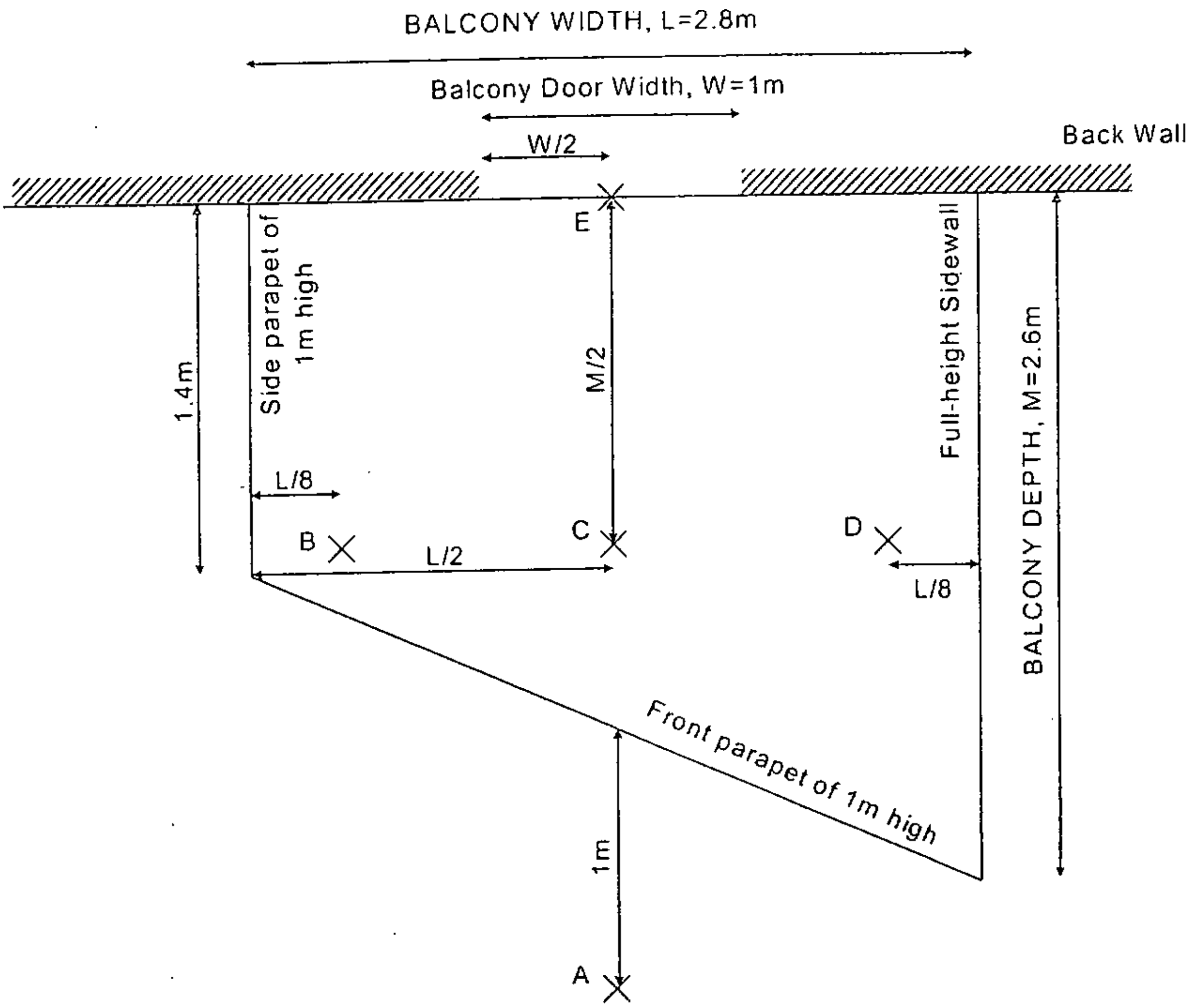

Figure 7.5. The layout and dimensions of the balconies at Site 1. The measurement points are marked A – E, where A is the control point.

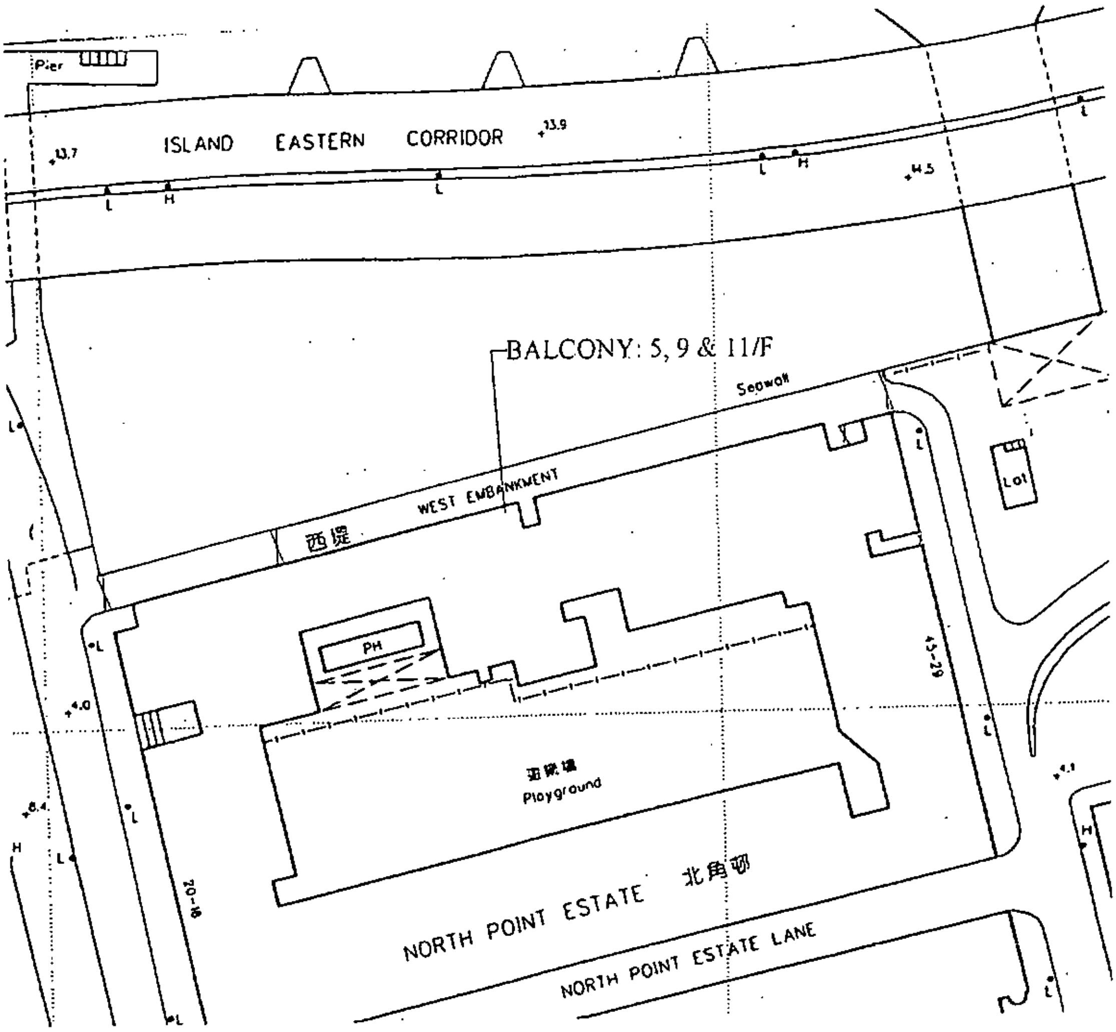

Figure 7.6. Survey map showing the orientation of the investigated building and road layout at Site 2.

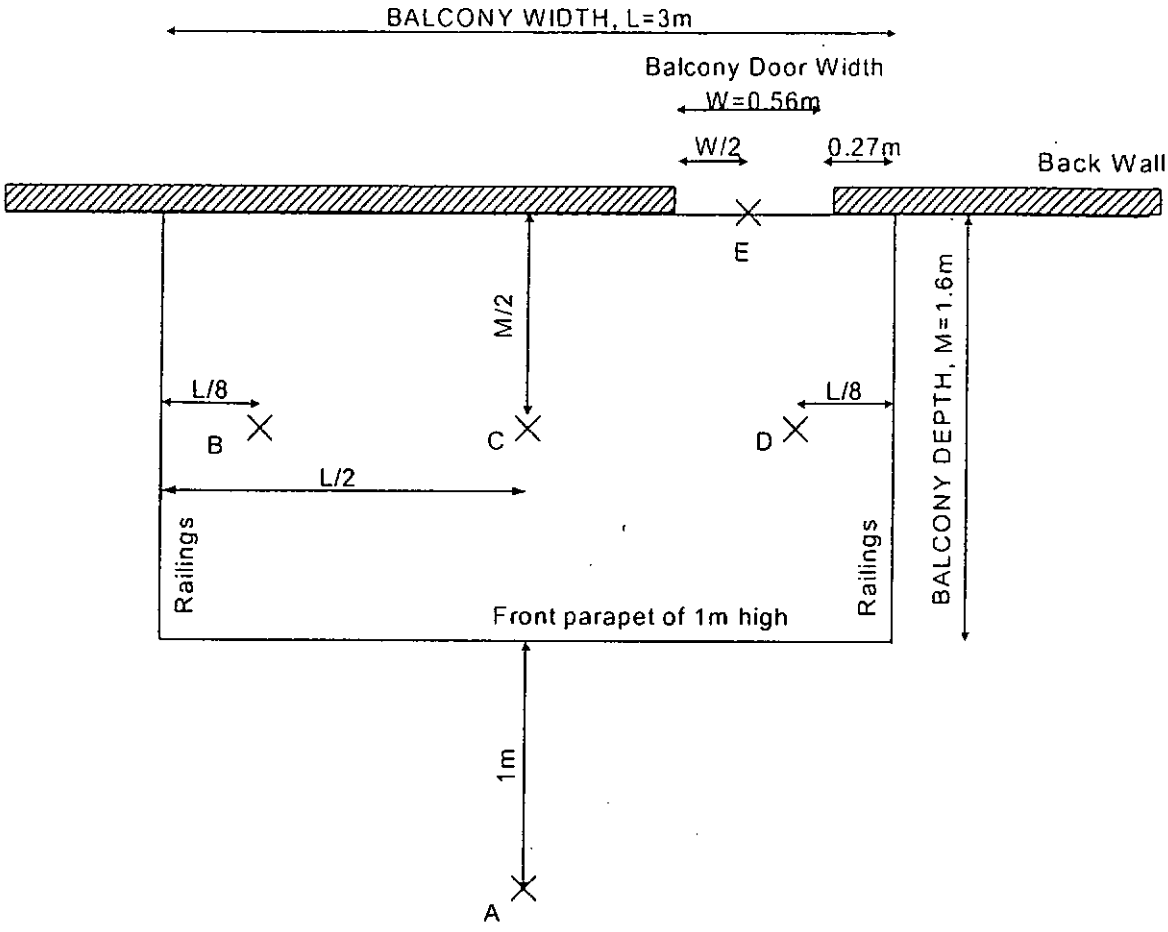

Figure 7.7. The layout and dimensions of the balconies at Site 2. The measurement points are marked **A** – **E**, where **A** is the control point.

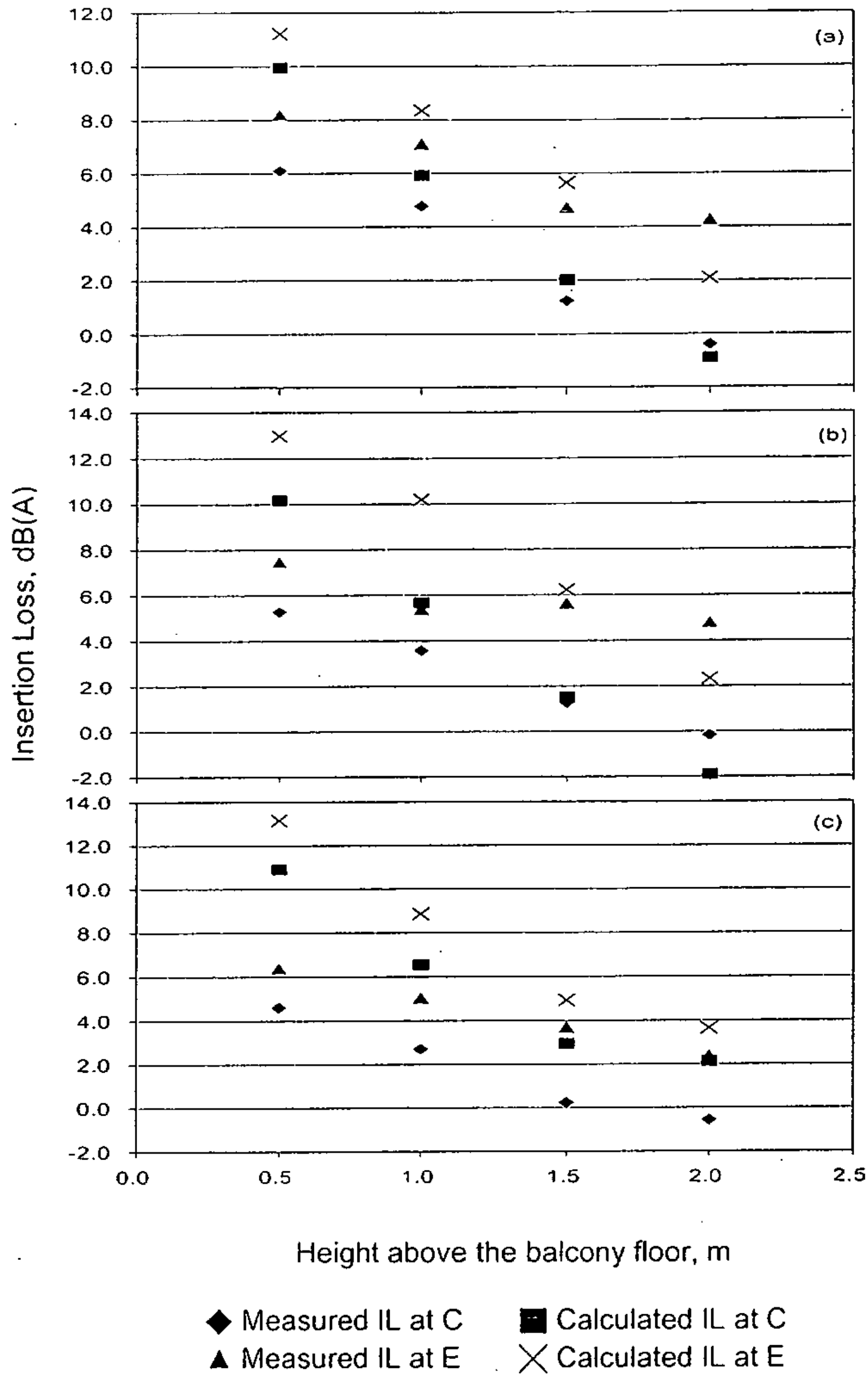

Figure 7.8. Comparison between the measured and calculated barrier insertion losses at Site 1 for balconies on (a) the 5th floor, (b) the 4th floor, and (c) the 3rd floor.

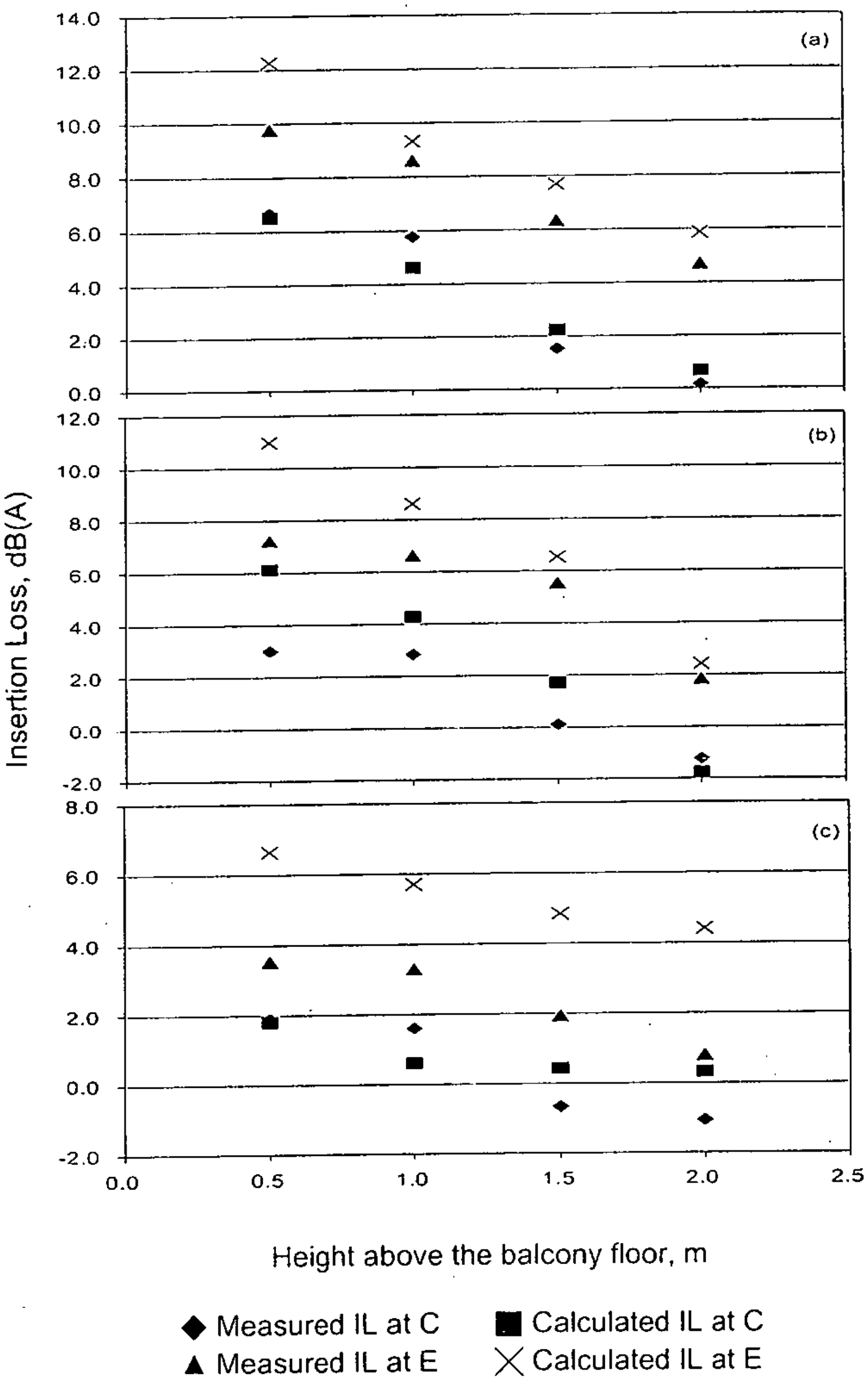

Figure 7.9. Comparison between the measured and calculated barrier insertion losses at Site 2 for balconies of original structure on (a) the 11th floor, (b) the 9th floor, and (c) the 5th floor.

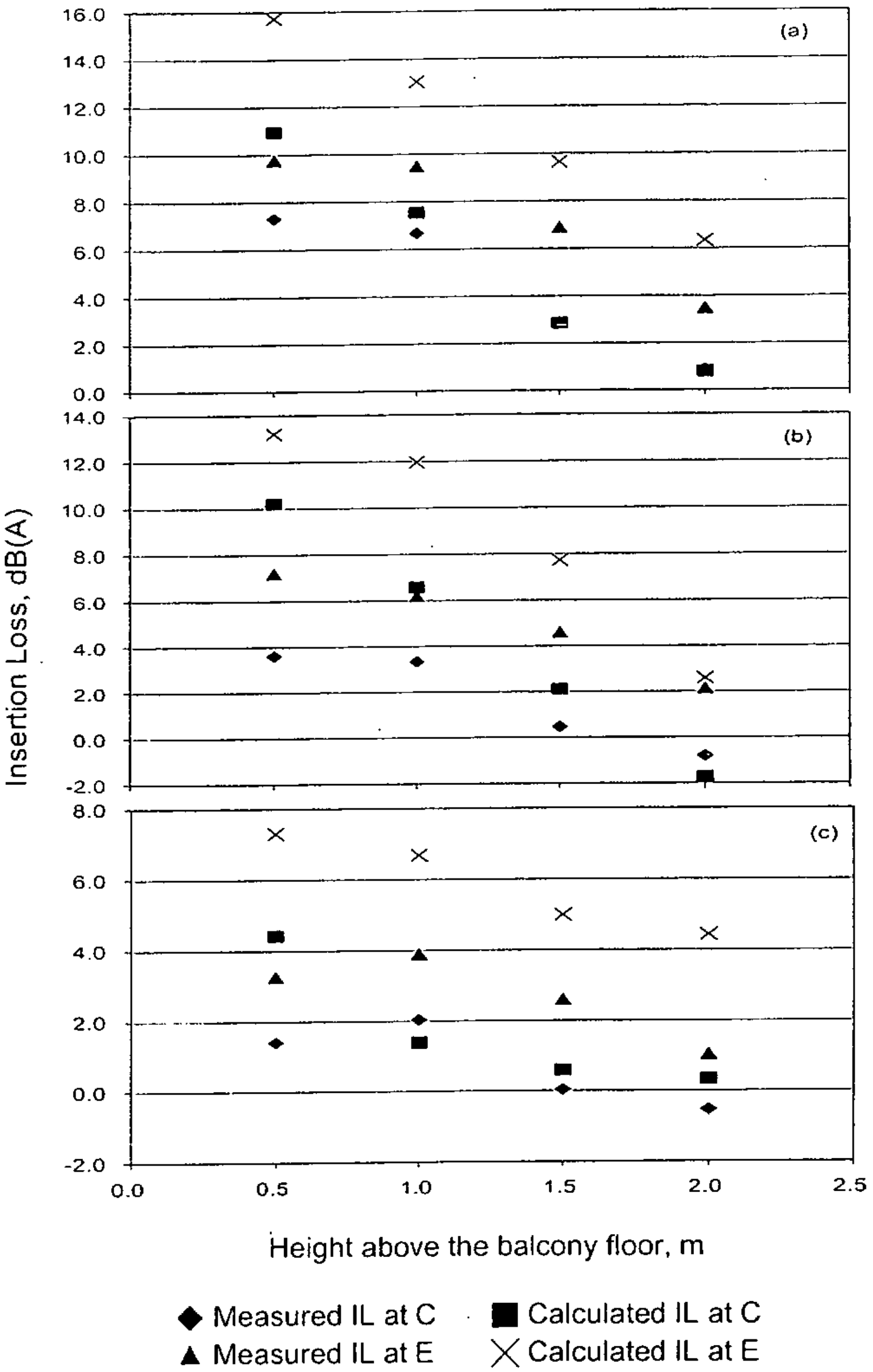

Figure 7.10. Comparison between the measured and calculated barrier insertion losses at Site 2 for balconies with 1 m high side boards on (a) the 11th, (b) 9th, and (c) 5th floors.

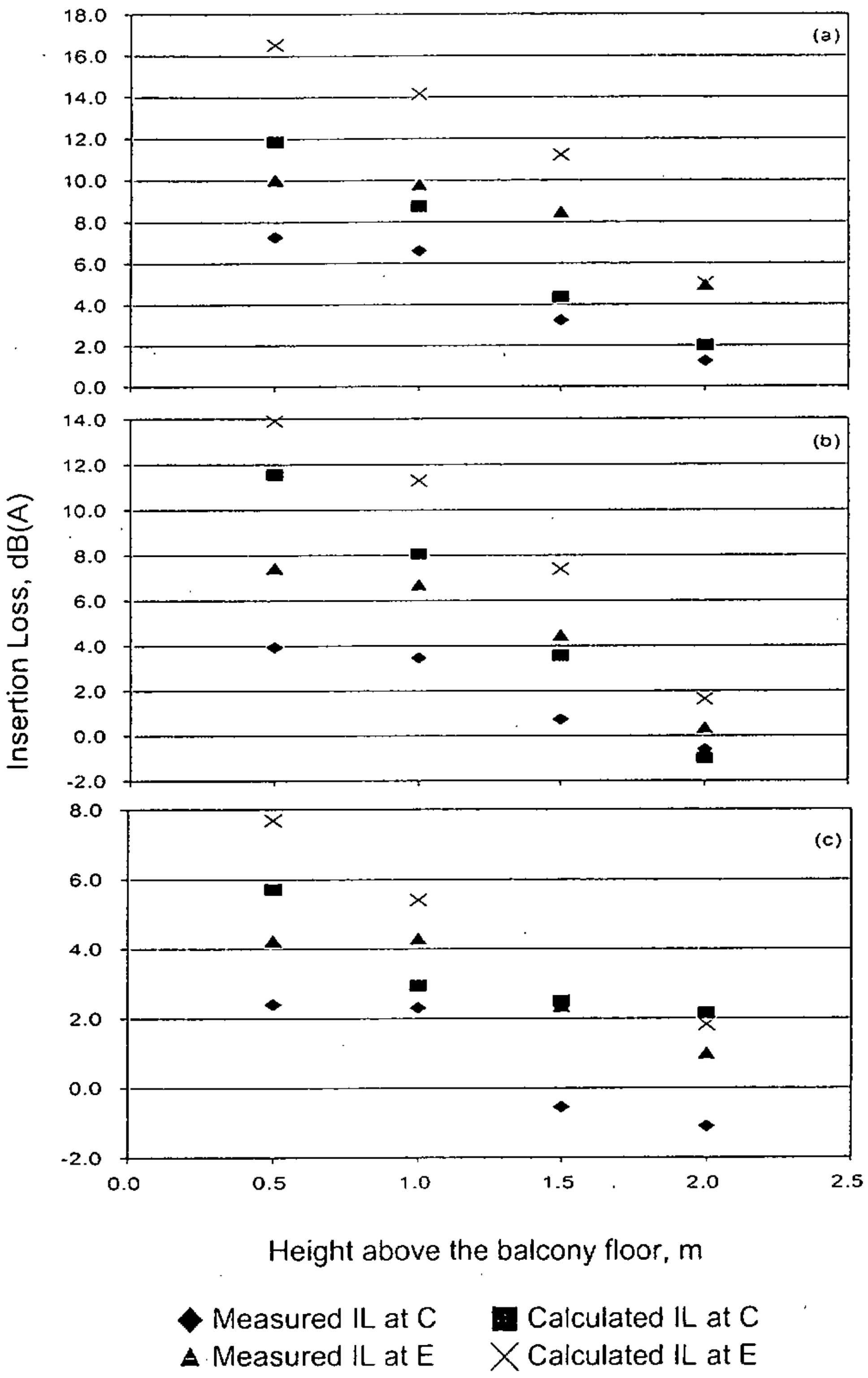

Figure 7.11. Comparison between the measured and calculated barrier insertion losses at Site 2 for balconies with full-height side boards on (a) the 11th, (b) 9th, and (c) 5th floors.

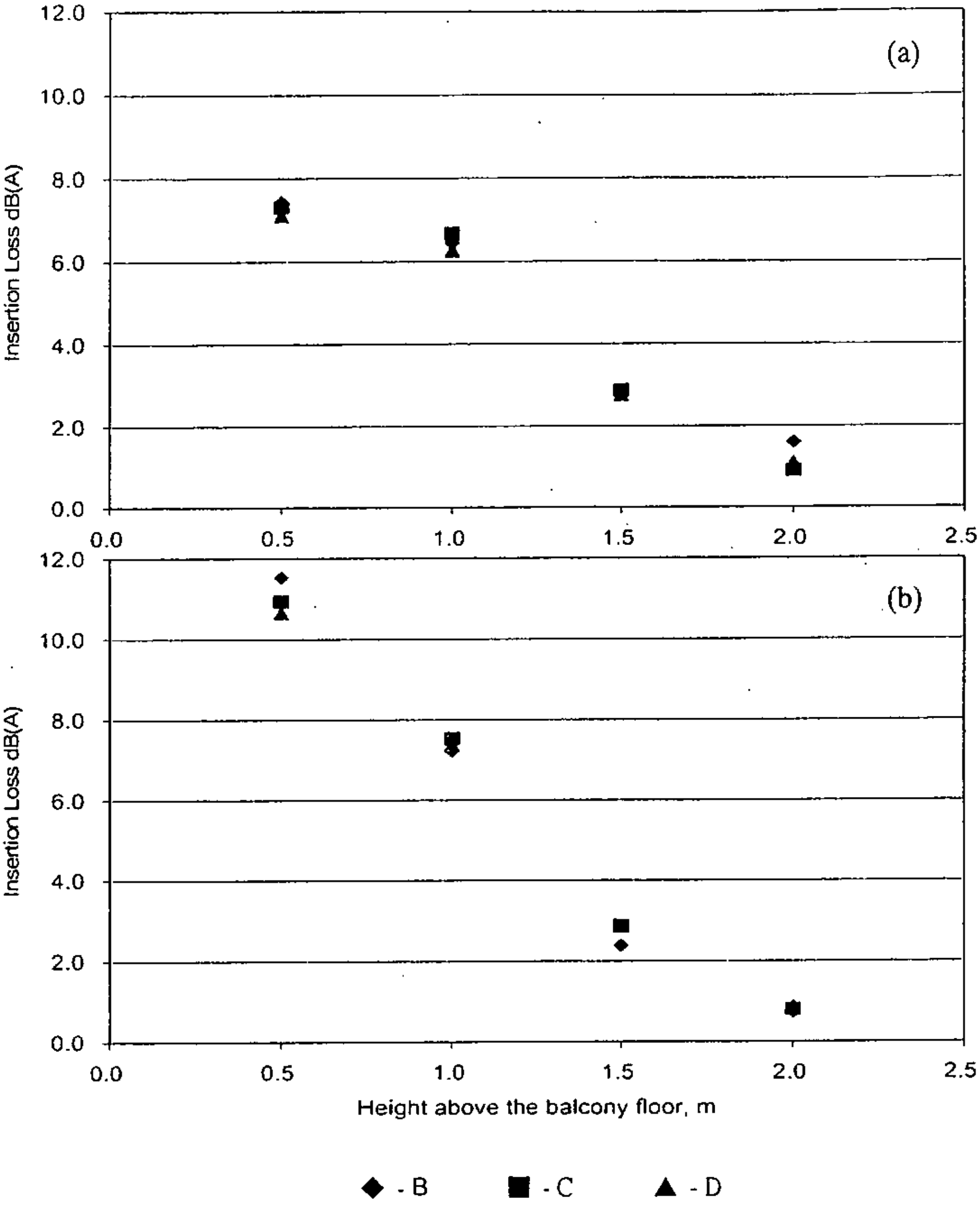

Figure 7.12. A typical demonstration on the similarity of the insertion losses at points B to D. The balcony with 1m high side boards on the 11th floor at Site 2 is selected for demonstration: (a) measured insertion loss and (b) predicted insertion loss.

Chapter 8

Conclusions and Suggestions for Future Research

8.1 Conclusions

A comprehensive review of literatures has been carried out to study the acoustical problems that arise from the propagation of urban transportation noise. Theoretical and numerical models have been developed to account for these physical problems. Experimental measurements have also been conducted for these studies and the measured data have been used to validate the models developed in this thesis.

Initially, the classical problem of acoustic diffraction by an acoustically hard sphere irradiated by a point source has been reviewed. The problem of sound diffraction by an absorbing sphere due to a monopole point source has also been investigated. The theoretical models have been extended to consider the case of sound diffraction by a hard sphere and an absorbing sphere with a locally reacting boundary or an extended reaction boundary placed above an outdoor ground surface of finite impedance. The solutions to the problems are analyzed in an exact fashion using the technique of separation of variables and appropriate wave field expansions. Incorporating the image method, the numerical solutions can be generated by systematically analyzing the multi-scattering interaction between the sphere and the image sphere above a hard and an impedance ground. The effect of ground impedance on the reflected sound fields is taken into account by using the approximate analytical solution known as the Weyl-van der Pol formula. Based on these theoretical analyses on a sphere, a simplified model is developed to investigate the influence of a porous road pavement on the sound amplification due to the horn-like geometry enveloped by the tire belt and road surface. In a parametric study, a point monopole source is assumed to be localized on the surface of a tire. In the frequency range of interest, a porous road pavement is found to reduce effectively the level of amplified sound due to the horn effect. The increase of thickness and porosity in a porous layer, or the use of a double layer porous road pavement can enhance the attenuation of horn amplification. However, the decrease of flow resisitivity of a porous layer does not provide substantial attenuation of horn amplification. It has been shown that the position of the source on the circumference of the tire does not show significant influence on the sound amplification.

Since it is not uncommon to find that railway tracks in Hong Kong are built above ground level and close to dense high-rise dwellings, the applicability of oversea empirical schemes for prediction of train noise in these situations is doubtful. Comparative studies have been conducted to investigate the accuracy of these oversea prediction schemes against the experimental data obtained from field measurements. The octave-band sound power levels of a passing train, required as input parameters for the *Nordic Prediction Method for Train Noise* (NMT), and the methods of CSTB 92 and ISO 9613, are determined by an inversion method of *in-situ* measurement. The method of *Calculation of Railway Noise* (CRN) from the U.K. gives the best agreement with the measured results, although it does not provide a term for correcting the vertical directivity characteristic of a passing train. The NMT prediction scheme also provides a good prediction of the general trend of the experimental data, but it always overestimates the measured noise levels. As far as the quantitative agreement with experimental data is concerned, the CSTB 92 and ISO 9612-2 prediction schemes are less satisfactory; nevertheless, these two schemes do provide reasonable predictions that agree with the measured data.

In view of the results obtained from the comparative study of different schemes for the prediction of train noise, the theoretical models for predicting sound radiation characteristic from a passing train have been reviewed. The radiation characteristic of wheel/rail rolling noise from a passing train is proposed to be modeled by using an energy approach and to be consisting of two independent parts: a horizontal and a vertical component. The horizontal directivity, which is the time signature (noise profile) of the passage of a train, is assumed to be dependent only on the azimuthally angle. The vertical directivity, which can be deduced from the measured sound exposure levels, is assumed to be dependent only on the angle of elevation. The time signatures are computed by the modified horizontal radiation models. The vertical radiation directivity is modeled by a multipole expansion model which is composed of a combination of monopole, dipole and quadrupole sources. Based on this physical model and experimental data, an empirical formula is derived to account for the vertical radiation directivity of the train noise. This study reveals that the noise radiated from an electrical train system displays eminent vertical radiation characteristic such that the noise levels increase with angles of elevation up to about 30° and reduces to a minimum level at 90°.

Lastly, the viable measure of protecting high-rise dwellings from land transportation noise is discussed. Since, it has been accepted that a balcony can provide acoustical protection to high-rise dwellings from the road traffic noise. Due to the lack of a practical model, a new methodology is developed. It focuses on the prediction of traffic noise levels inside a balcony by incorporating geometrical acoustic principles into a well-known prediction model – Calculation of Road Traffic Noise (CRTN). The source level of road traffic noise is obtained in accordance to CRTN methodology. However, a revised scheme is proposed to subdivide a road segment into sub-segments and new approaches based on geometrical acoustics are used to calculate the noise levels for a receiver at an illuminated zone and at a shadow zone inside a balcony. Field measurements in four different types of balcony have been conducted to validate the proposed methodology. It is found that the proposed method can provide better predictions for assessment points over 1m above the balcony floor. The calculated insertion losses are always over-estimated because the multiple reflections on the reflecting surfaces of the balcony and diffraction at the edges are neglected in the calculation. Moreover, the assumption of effective source line as adopted in the CRTN scheme can lead to over-estimation of screening effect provided by a noise barrier. In general, a balcony can provide considerable screening effect regardless of the balcony type. On the high floors when the incident angle is large and without ceiling reflection, a balcony provides a better noise-reducing effect for the dwelling. However, the noise screening effects decrease with an increase of height above the balcony floor. A balcony with a closed construction (built with parapets or side walls) can offer more considerable reduction of noise than the open (cantilever) type. However, the effectiveness of a parapet or side wall against road traffic noise depends on their orientations with the affecting roads. A parapet or side wall can provide an effective screening effect only if it is parallel to the affecting road, However, its noise reducing effect becomes less significant when it is perpendicular to the road. The results of this study may inspire the developers and architects to use balconies as an architectural feature for the protection of dwellings from land transportation noise.

8.2 Suggestions for Future Research

While the theoretical works, numerical simulations, indoor and outdoor experiments carried out in this research have provided us with an insight into the noise problems caused by the sound amplification due to horn effect and by the wheel/rail interaction of a moving train, there are still some other research problems awaiting to be explored. The works implemented in the present research can further be extended in many ways in search of the solutions.

In the present research, the sound amplification due to horn effect is studied by taking the noise source as a stationary object. In a more realistic modeling, the overall effect of horn amplification over a road pavement due to a moving source passing by a noise sensitive receiver should be considered. In this case, the sound waves radiating from different source positions along the moving path have to undergo different propagating paths before reaching the receiver and give the overall noise level at the receiver. Therefore, the amplified noise level at the receiver in this case should be different from that of taking the source as a stationary object.

The energy approach has been used to model the characteristics of wheel/rail rolling noise. It would be advantageous to extend the investigation, based on the current method, for the spectral analysis on the source radiation characteristics of wheel/rail rolling noise. The results of this research would be especially useful for the effective design of trackside barriers or viaducts in terms of shape and sound absorption materials used in the design as a means of mitigation measures to abate the wheel/rail rolling noise impact to high-rise dwellings.

The noise screening effects provided by conventional types of balconies have been studied. A simplified prediction model has been proposed. The accuracy of the prediction scheme can be improved by incorporating the reverberation effect due to the multiple reflections inside the balcony and the diffraction effect at the edges in the new prediction methodology by using the Ray Tracing Method. Moreover, the assumed position of effective source line as adopted in the CRTN scheme should be reassessed so as to improve the prediction accuracy for the screening effect provided by a noise barrier. With an improved model, more research work is recommended to explore the viable designs for the balcony elements so as to improve the sound attenuation ability, for instance, the use of an inclined ceiling to reduce the sound reflection and the use of top-bended parapet walls to provide a better screening effect. The optimum use of sound absorption materials in combination to the innovative designs on the elements can further enhance the acoustical protection of a balcony from intruding noise. The prediction model developed in this research can be extended to include an inclined ceiling and top-bended parapet in the calculation.

References

[1] 01dB-Stell MVI Technologies Group, Mithra Environmental Prediction Software version 5.0: User Manual, 1998.

[2] Anfosso-Ledee F., Klein P., Fadavi A. and Duhamel D., "Tire/road noise: comparison of 2D and 3D models for horn effect", Inter-noise 2000, Nice, France, 2000.

[3] Attenborough K., "Acoustical characteristics of rigid fibrous absorbents and granular materials," J. Acoust. Soc. Am. **73**, 785-799 (1983).

[4] Attenborough K., "Ground parameter information for propagation modeling," J. Acoust. Soc. Am. **92**, 418-427 (1992).

[5] Attenborough K., "Review of ground effects on outdoor sound propagation from continuous broadband sources," Appl. Acoust. **24**, 289-319 (1988).

[6] Attenborough K., Taherzadeh S., Bass H. E., Di X., Raspet R., Becker G. R., Gudesen A. , Chrestman A., Daigle G. A., Lesperance A., Gabillet Y., Gilbert K. E., Li Y. L., White M. J., Naz P., Noble J. M., H. A. J. M. Van Hoof, "Benchmark cases for outdoor sound-propagation models," J. Acoust. Soc. Am. **97**, 173-191 (1995).

[7] Bamnios Y. and Trochides A., "Railway noise in Greece: measurement and prediction", InterNoise 2000, IN2000/135, (2000).

[8] Bérengier M. C., Stinson M. R., Daigle G. A. and Hamet J. F., "Porous road pavements: Acoustical characterization and propagation effects", J. Acoust. Soc. Am. **101**, 155-162 (1997).

[9] Born M., Principles of optics: electromagnetic theory of propagation, interference, and diffraction of light (Pergamon Press, Oxford, 5th ed., 1975).

[10] Bruning J. H. and Lo, Y., "Multiple scattering of electromagnetic waves by

spheres I," IEEE Trans. Antenn. Propagat. **AP-19**, 378-400 (1971).

[11] Bruning J. H., Multiple scattering by spheres, PhD Thesis, University of Illinois, 1969.

[12] Cato D. H., "Prediction on environmental noise from fast electric trains," J. Sound Vib. **46**, 483-500 (1976).

[13] Chandler-Wilde S. N. and Hothersall D. C., "Efficient calculation of the Green function for acoustic propagation above a homogeneous impedance plane". J. Sound Vib. **180,** 705-724 (1995).

[14] Cheung A., Chan K. O. and Ng K. K., "Road traffic noise on balcony," The 6th Western Pacific Regional Acoustics Conference, Hong Kong, 32-38 (1997).

[15] Chew C. H., "Directivity of train noise in the vertical plane," Bldg. Acoust. **16,** 41-56 (2000).

[16] Chew C. H., "Vertical directivity of train noise," Appl. Acoust. **51**, 157-168 (1997).

[17] Chew C. H., "Vertical directivity pattern of train noise," Appl. Acoust. **55,** 243-250 (1998).

[18] Chien C. F. and Soroka W. W., "A note on the calculation of sound propagation along an impedance plane," J. Sound Vib. **69**, 340-343 (1980).

[19] Chien C. F. and Soroka W. W., "Sound propagation along an impedance plane". J. Sound Vib. **43**, 9-20 (1975).

[20] Copenhagen [Denmark]: Nordic Council of Ministers, Railway traffic noise: the Nordic prediction method, 1996.

[21] Copenhagen [Denmark]: Nordic Council of Ministers, Road traffic noise: Nordic prediction method, 1996.

[22] Crocker M. J., Handbook of Acoustics (Wiley, New York, 1998).

[23] Cruzan O. R., "Translational addition theorems for spherical vector wave functions," Quart. Appl. Math. **20**, 33-40 (1962).

[24] Cullinane S. L., "Hong Kong's low car dependence: lessons and prospects," Journal of Transport Geography 11, 25-35 (2003).

[25] Cullinane S. L., "The relationship between car ownership and public transport provision: a case study of Hong Kong," Transport Policy 9, 29-39 (2002).

[26] Dassios G. and Kleinman R., Low Frequency Scattering, Oxford University Press/Clarendon Press, Oxford, 2000.

[27] Dassios G., Hadjinicolaou M. and Kamvyssas G., "The penetrable coated sphere embedded in a point source excitation field," Wave Motion **32**, 319-338 (2000).

[28] Delaney M. E. and Bazley E. N., "Acoustical properties of fibrous materials," Appl. Acoust. **3**, 105-116 (1970).

[29] Department of Transport, Calculation of Railway Noise 1995, London: HMSO, 1995.

[30] Department of Transport, Calculation of Road Traffic Noise 1988, London: HMSO, 1988.

[31] Dittrich M. G. and Janssens M. H. A., "Improved measurement methods for railway rolling noise", J. Sound Vib. **231**, 595-609 (2000).

[32] Edmunds A., Angular Momentum in Quantum Mechanics (Princeton U.P., NJ, 1957).

[33] Embleton T. F. W., "Tutorial on sound propagation outdoors," J. Acoust. Soc. Am. **100**, 31-48 (1996).

[34] Environmental Resources Management, "Draft Report: Environmental Assessment for LAR 4-Tracking and Mei Foo Interchange: Tsing Yi Viaduct Noise Survey", 4 January 1999.

[35] Fadavi A., Duhamel D., Klein P. and Anfosso-Ledee F., "Tire/road noise: 3D model for horn effect", Inter-noise 2000, Nice, France, 2000.

[36] Gaunaurd G. C. and Huang H., "Acoustic scattering by a spherical body near a plane boundary," J. Acoust. Soc. Am. **96**, 2526-2536 (1994).

[37] Gaunaurd G. C. and Huang H., "Acoustic scattering by an air-bubble near the sea surface," IEEE J. Ocean Eng. **20**, 285-292 (1995).

[38] Gaunaurd G. C. and Huang H., "Sound scattering by a spherical object near a hard flat bottom," IEEE transactions on ultrasonics, ferroelectrics, and frequency control **43**, 690-697 (1996).

[39] Godinho L. et al., "Sound propagation around rigid barriers laterally confined by tall buildings," Appl. Acoust. **63**, 595-609 (2002).

[40] Graf R. A. G., Kuo C.-Y., Dowling A. P. and Graham W. R., "On the horn effect of a tire/road interface, Part I: experiment and computation," J. of Sound Vib. **256**, 417-431 (2002).

[41] Hammad R. N. S. and Gibbs B. M., "Building facades in hot climate: part 2," Appl. Acoust. **16**, 441-454 (1983).

[42] Hampton L. D. and McKinney C. M., "Experimental study of the scattering of acoustic energy from solid metal spheres in water", J. Acoust. Soc. Am. **33**, 664-673 (1961).

[43] Harbold M. L. and Steinberg B. N., "Direct experimental verification of creeping waves", J. Acoust. Soc. Am. **45**, 592-603 (1961).

[44] Hasheminejad S. M., "Modal acoustic force on a spherical radiator in an acoustic halfspace with locally reacting boundary," Acta Acustica **87**, 443-453 (2001).

[45] Heckl M., "Tire noise generation," Wear **13**, 157-170 (1986).

[46] Hohenwarter D., "Railway noise propagation models," J. Sound Vib. **141**, 17-41 (1990).

[47] Hossam El-Dien H. and Woloszyn P., "Balcony form: an approach to reduce sound pressure level into the building façade," In: Cadiz: Third International Conference on modeling and experimental measurements in acoustics. Acoustics 2003, 349-358.

[48] Hossam El-Dien H. and Woloszyn P., "Prediction of the sound field into high-rise building facades due to its balcony ceiling form," Appl. Acoust. **65**, 431-440 (2004).

[49] Hossam El-Dien H., "Acoustic performance of high rise building facades due to its balconies form," In: Naples: Fifth European Conference on noise control. Euronoise 2003.

[50] Hothersall D. C., Horoshenkov K. V., Mercy, S. E., "Numerical modeling of sound field near a tall building with balconies near a road," J. Sound Vib. **198**, 507-515 (1996).

[51] Huang H. and Gaunaurd G. C., "Acoustic point source scattering by a spherical elastic shell submerged beneath a free surface," J. Acoust. Soc. Am. **99**, 2720-2726 (1996).

[52] Ingard U., "On the reflection of a spherical sound wave from a finite plane", J. Acoust. Soc. Am. **23**, 329-335 (1951).

[53] International Organization for Standardization. Acoustics – Attenuation of Sound During Propagation Outdoors – Part 1: Calculation of the Absorption of Sound by the Atmosphere. ISO, Geneva, 1996, ISO 9613-1.

[54] International Organization for Standardization. Acoustics – Attenuation of Sound During Propagation Outdoors – Part 2: General Method of Calculation.

ISO, Geneva, 1996, ISO 9613-1.

[55] Iu K. K. and Li K. M., "The propagation of sound in narrow street canyons," J. Acoust. Soc. Am. **112**, 537-550 (2002).

[56] Iwai S., Miura Y., Koike H. and Levy G., "Influence of porous asphalt pavement characteristics on the horn amplification of tire/road contact noise", Inter-noise 94, Yokohama, Japan, 1994.

[57] Iwao K. and Yamazaki I., "A study on the mechanism of tire/road noise," JSAE Rev. **17**, 139-144 (1996).

[58] Iwase T., "Acoustic properties of porous pavement with double layers and its reduction effects for road traffic noise", Inter-noise 2000, Nice, France, 2000.

[59] Iwase T., "Measurements of basic acoustical properties of the porous pavement and their applications to the estimation of road traffic noise reduction", J. Acoust. Soc. Jpn. **20**, 63-74 (1999).

[60] Jiang G., Lau Stephen S.Y., Wang J., "A study of noise reduction by high-rise balcony," Applied Acoustics, Beijing: Sinica Academia, **19**, 20-24 (2000).

[61] Jones D. S., Acoustic and electromagnetic waves (Oxford University Press, 1986), 441-442. (Note that in this textbook, the time dependent factor $e^{i\omega t}$ is used.).

[62] Kang J., "Sound propagation in street canyons: Comparison between diffusely and geometrically reflecting boundaries," J. Acoust. Soc. Am. **107**, 1394-1404 (2000).

[63] King W. F., "On the role of aerodynamically generated sound in determining the radiated noise levels of high speed train," J. Sound Vib. **54**, 361-378 (1977).

[64] Kropp W. and Berillon J., "A theoretical model to consider the influence of absorbing surfaces inside the cavity of balconies," Acustica **86**, 485-494

(2000).

[65] Kropp W. and Berillon J., "A theoretical model to investigate the acoustic performance of building facades in low and middle frequency range," Acustica, **84**, 681-688 (1998).

[66] Kropp W., Becot F.-X. and Barrelet S., "On the sound radiation from tyres", Acta Acust. **86**, 769-779 (2000).

[67] Krylov Victor V., Noise and vibration from high-speed trains (London: Thomas Telford, c2001).

[68] Kuijpers A. and Van Blokland G., "Modeling and optimization of two-layer porous asphalt roads", Inter-noise 2000, Nice, France, 2000.

[69] Kuo C. Y., Graf R. A. G., Dowling A. P. and Graham W. R., "On the horn effect of a tire/road interface, Part II: asymptotic theories", J. of Sound Vib. **256**, 433-445 (2002).

[70] Kurze U. J., "Tools for measuring, predicting and reducing the environmental impact from railway noise and vibration," J. Sound Vib. **193**, 237-251 (1996).

[71] Larsson K., Barrelet S. and Kropp W., "The modeling of the dynamic behaviour of tyre tread blocks", Appl. Acoust. **63**, 659-677 (2002).

[72] Lawhead R. B. And Rudndick I., "Acoustic waves propagation along a constant normal impedance boundary", J. Acoust. Soc. Am. **23**, 546-549 (1951).

[73] Li K. M., Fuller T. W. and Attenborough K., "Sound propagation from a point source over extended-reaction ground", J. Acoust. Soc. Am. **104**, 679-685 (1998).

[74] Li K. M., Lui W. K. and Frommer G. H., "The diffraction of sound by an impedance sphere in the vicinity of a ground surface", J. Acoust. Soc. Am. **115**, 42-56 (2004).

[75] Li K. M., Lui W. K. and Frommer G. H., "The scattering of sound by a hard sphere above an impedance ground", Acta Acust. **90**, 251-262 (2004).

[76] Lui W. K. and Li K. M., "A theoretical study of the horn amplification of sound radiated from tires above a porous road pavement", J. Acoust. Soc. Am. **116**, 313-322 (2004).

[77] Makarewicz R. and Jarzecki J., "Prediction of train noise in open terrain," J. Acoust. Soc. Jpn. (E) **12**, 195-201 (1991).

[78] Makarewicz R., "The influence of refraction and turbulence on railway noise," J. Sound Vib. **210**, 367-374 (1998).

[79] Makarewicz R., Yoshida M., "Railroad noise in an open space," Appl. Acoust. **49**, 291-306, (1996).

[80] May D. N., "Freeway noise and high rise balconies," J. Acoust. Soc. Am. **65**, 699-704 (1979).

[81] Medwin H., Fundamentals of acoustical oceanography (Academic Press, Boston, 1998).

[82] Mohsen E. A. and Oldham D. J., "Traffic noise reduction due to screening effect of balconies on a building façade," Appl. Acoust. **10**, 243-257 (1977).

[83] Morse P. M. and Ingard K. U., Theoretical Acoustics (McGraw-Hill, New York, 1968).

[84] NMPB96, New French method for road traffic noise prediction including meteorological effects, 1996.

[85] Ochmann M., "The source simulation technique for acoustic radiation problems," Acustica **81**, 512-526 (1995).

[86] Okumura Yohzoh and Kuno Kazuhiro, "Multiple regression analysis of railway noise based on finite line source models including the excess attenuation," J.

Acoust. Soc. Jpn. (E) **13**, 161-169 (1992).

[87] Perisse J., "A study of radial vibrations of a rolling tire for tire-road noise characterization", Mech. Syst. and Signal Process **16**, 1043-1058 (2002).

[88] Peters S., "The prediction of railway noise profiles," J. Sound Vib. **32**, 87-99 (1974).

[89] Picaut J., Simon L., and Hardy J., "Sound field modeling in streets with a diffusion equation," J. Acoust. Soc. Am. **106**, 2638-2645 (1999).

[90] Pierce A. D., Acoustics: An Introduction to its physical principles and applications. (Acoustical Society of America, New York, 1989).

[91] Piercy J. E., Embleton T. F. W., Sutherland L. C., "Review of noise propagation in the atmosphere," J. Acoust. Soc. Am. **61**, 1403-1418 (1997).

[92] Pirinchieva R. K., "Model study of sound propagation over ground of finite impedance", J. Acoust. Soc. Am. **90**, 1191-2682 (1991).

[93] Pirinchieva R. K., Erratum: "Model study of sound propagation over ground of finite impedance", J. Acoust. Soc. Am. **94**, 1722 (1993).

[94] Rathe E. J., "Railway noise propagation," J. Sound Vib. **51**, 371-388 (1977).

[95] Rayleigh Lord [Strutt J. W.], The theory of sound (Dover publications, New York, 2nd ed., 1945).

[96] Rudnick I., "The propagation of an acoustic wave along a boundary", J. Acoust. Soc. Am. **19**, 348-356 (1947).

[97] Schaaf K. and Ronneberger D., "Noise radiation from rolling tires – sound amplification by the horn effect", Inter-Noise **82**, San Francisco, CA, pp.131-134.

[98] Shenderov E. L., "Diffraction of sound by an elastic or impedance sphere located near an impedance or elastic boundary of a halfspace," Acoust. Physics.

48, 607-617 (2002).

[99] SoundPLAN LLC, SoundPLAN version 6.1: User Manual, 2003.

[100] Stein S., "Addition theorems for spherical wave functions," Quart. Appl. Math. **19**, 15-24 (1961).

[101] Tang S. H. and Li K. M., "The prediction of façade effects from a point source above an impedance ground," J. Acoust. Soc. Am. **110**, 278-288 (2001).

[102] Ten Wolde T. and van Ruiten C.J.M., "Sources and mechanisms of wheel/rail noise: state-of-the-art and recent research," J. Sound Vib. **87**, 147-160 (1983).

[103] Thompson D. J. and Jones C. J. C., "A review of the modeling of wheel/rail noise generation," J. Sound Vib. **231**, 519-536 (2000).

[104] Tzekakis E. G., "On the Noise Reducing Properties of Balconies," Acustica **52**, 117-121 (1982/1983).

[105] U.S. Department of Transportation, Federal Highway Administration, FHWA Traffic Noise Model Technical Manual, 1998.

[106] U.S. Department of Transportation, High-speed ground transportation noise and vibration impact assessment, Federal Railroad Administration, Office of Railroad Development Washington, D.C. 20590, Report No. 293630-1.

[107] Van Leeuwen H. J. A, "Railway noise prediction models: A comparison," J. Sound Vib. **231**, 975-987 (2000).

[108] Van Leeuwen J. J. A., "Noise prediction models to determine the effect of barriers placed alongside railway lines," J. Sound Vib. **231**, 975-987 (2000).

[109] Walerian E., Janczur R. and Czechowicz M., "Sound level forecasting for city-centers. Part I: Sound level due to a road within an urban canyon," Appl. Acoust. **62**, 359-380 (2001).

[110] Walerian E., Janczur R. and Czechowicz M., "Sound level forecasting for

city-centers. Part II: Effect of source model parameters on sound level in built-up area," Appl. Acoust. **62**, 461-492 (2001).

[111] Walerian E., Janczur R. and Czechowicz M., "Sound level forecasting for city-centers. Part III: a road lane structure influence on sound level within an urban canyon," Appl. Acoust. **62**, 493-512 (2001).

[112] Wiener Francis M., "Sound diffraction by rigid spheres and circular cylinders", J. Acoust. Soc. Am. **19**, 444-451 (1947).

[113] Zhang Xuetao, Jonasson Hans and Holmberg Kjell, Source modelling of train noise – Literature review and some initial measurements, SP Report 2000:36 Physics and Electrotechnics Boras 2000.